Bogolyubov Institute for Theoretical Physics
National Academy of Science of Ukraine (Kiev)
Joint Institute for Nuclear Research (Dubna)

# NEW TRENDS IN HIGH-ENERGY PHYSICS

**Proceedings of the Conference held in Alushta (Crimea) on September 3-10, 2011**

Edited by
*P.N. Bogolyubov and L.L. Jenkovszky*

Kiev 2011

# FOREWORD

The XXII-d Intrenational Conference on ***New Trends in High-Energy Physics***, co-organized by the Bogolyubov Institute for Theoretical Physics, National Academy of Sciences of Ukraine and the Joint Institute for Nuclear Research (Dubna), was held in Alushta, Crimea on September 3-10, 2011.

The present Proceedings contain written versions of the invited talks, grouped in two sections: 1. ***Experiment*** and 2. ***Phenomenology & Theory***. Within each section, the talks are ordered alphabetically, by the first author. The Book contains also contributions by H. Terazawa, who was invited but could not come, and by G. Stelmakh. To speed up the publication, we minimized the editorial intervention.

We thank the Authors for their invaluable contributions and apologize for the black-and-white reproduction of the color figures (due to the limited budget of the Conference). This omission is fully compensated at our WEB page: http://crimea.bitp.kiev.ua/, where all papers of the present Proceedings appear in full color.

The next conference of this series is scheduled to be held in 2013 (late spring or autumn); Novy Svet (Crimea) is a candidate site for the future conference.

**ISBN 978-966-02-6199-0**

# CONTENTS

## 2. PHENOMENOLOGY AND THEORY

# CONFERENCE PROGRAM

## September 4 (Sunday)

| | |
|---|---|
| 10.00 | Opening |
| | ***The standard model and beyond; heavy quarks*** |
| | **Chairperson: V.A. Matveev** |
| 10.15 | K. Sumisawa |
| 10.50 | F. Derue |
| 11.20 | J. Lellouch |
| 11.45 | *Coffee break* |
| | **Chairperson: L.D. Faddeev** |
| 12.00 | Yu. Uchiyama |
| 12.30 | V.N. Bolotov |
| 13.00 | G.A. Kozlov |
| | ***The standard model and beyond; heavy quarks (continued):*** |
| | **Chairperson: S. Costantini** |
| 15.00 | M. Hasinoff |
| 15.30 | N. Gromov |
| 15.55 | V.V. Khruschov |
| 16.20 | *Coffee break* |
| | **Chairperson: T. Ibragimova** |
| 16.40 | S. Gevorkya |
| 17.10 | I. Denysenko |
| 17.35: | M. Bondarenco |
| | *Wine-tasting: after dinner* |

## September 5 (Monday)

| | |
|---|---|
| | ***Physics at the LHC and at the Tevatron*** |
| | **Chairperson:M. Hasinoff** |
| 9.00 | A. Ventura |
| 9.35 | S. Costantini |
| 10.10 | E. Scapparone |
| 10.45 | *Coffee break and Conference picture* |
| | **Chairperson:R. Lednicky** |
| 11.15 | V. Sharyy |

| | |
|---|---|
| 11.55 | N. Ruckstuhl |
| 12.25 | A. Pozzobon |
| 13.30 | *Excursion to Alupka (the Vorontsov palace), Swallow's Nest and Yalta (by boat)* |
| | **Chairperson: J. Lellouch** |
| 20.00: | M. Krammer |
| 20.25 | S. Uzunyan |
| 20.50 | A. Branca |
| 21.15 | L. Jenkovszky |

## September 6 (Tuesday)

***Non-accelerator physics, cosmic rays, gravity, and neutrino physics***

**Chairperson: M. Krammer**

| | |
|---|---|
| 9.00 | R. Bernabei |
| 9.35 | P. Giusti |
| 10.05 | V. Gavrin |
| 10.35 | *Coffee break* |
| | **Chairperson: M. Turcato** |
| 10.50 | C. Broggini |
| 11.20 | K. Grzelak |
| 11.45: | M. Khabibullin |
| 13.30 | *Excursion to the Livadia palace in Yalta* |

***Non-accelerator physics, cosmic rays, gravity, and neutrino physics (continued)***

**Chairperson: R. Bernabei**

| | |
|---|---|
| 20.00 | L. Gironi |
| 20.25 | T. Katori (2 talks) |
| 21.15 | K. Hamada |
| 21.45 | L Tkachev |
| 22.10 | A. Flanchik |

## September 7 (Wednesday)

***New trends in quantum field theories***

**Chairperson: D. Pontecorvo**

| | |
|---|---|
| 9.00 | L.D. Faddeev |
| 9.35 | A.A. Slavnov |
| 10.10 | N.S.M. Borstniak |

***DIS, nucleon structure, parton distributions***
**Chairperson: K. Yip**

15.00 M. Turcato
15.35 S. Levonian
16.00 A. Bakulev

16.30 *Coffee break*

**Chairperson: F. Derue**

16.45 G. Calucci
17.15 K. Yip
17.40 H. Marukyan

20.00 ***Round-table discussion on Future Trends (to be continued on Saturday, Sept. 10; more names and items are welcome!)***
1. Mass spectrum of the elementary fermions. How many flavors? Do sterile neutrinos exist? (Rita Bernabei, V. Gavrin, Norma Mankoc)
2. "Higgsless" standard model, what beyond? (A. Slavnov, ALICE, ATLAS, CMS)
3. Is QCD the ultimate strong interaction theory, without any alternative? (L. Faddeev, A. Bakulev, E. Strokovsky)
4. Does anything like QGP exist? Expected signatures from FAIR and NICA/Nuclotron? (V.A. Matveev, R. Lednicky, Yu. Sinyukov)

## September 8 (Thursday)

***Collective properties of the nuclear matter, heavy ion collisions***
**Chairman: T. Katori**

9.00 R. Lednicky
9.35: E. Kistenev
10.10 Yu. Sinyukov

10.40 *Coffee break*

***Collective properties of the nuclear matter, heavy ion collisions (c'ntd)***
**Chairperson: N.S.M Borstniak**

11.00 V.A. Nikitin
11.30 I.. Vassiliev
12.00 P. Zarubin
12.25 I. Zarubina

*Afternoon: Free time*

## September 9 (Friday)

***Future facilities***
**Chairperson: T. Keri**

9.00 A. Ratti
9.35 P. Kostka

10.10 *Coffee break*

**Chairperson: Yu. Stelmakh**

10.30 T. Katori
11.00 E. Strokovsky
11.30 T. Keri

*Afternoon: Free time*

19.00 *Conference dinner*

## September 10 (Saturday)

9.00 Continuation of the ***Round-Table discussion*** and ***closing the Conference***

# I. EXPERIMENT

# DAMA/LIBRA AT GRAN SASSO

R. Bernabei[1], P. Belli[1], F. Cappella[2], R. Cerulli[3], C.J. Dai[4], A. d'Angelo[2], A. Di Marco[1], H.L. He[4], A. Incicchitti[2], X.H. Ma[4], F. Montecchia[1,5], D. Prosperi[2,+], X.D. Sheng[4], R.G. Wang[4], Z.P. Ye[4,6]

[1] *Dip. Fisica, Università di Roma "Tor Vergata" and INFN, sez. Roma Tor Vergata, Rome, Italy*
[2] *Dip. Fisica, Università di Roma "La Sapienza" and INFN, sez. Roma, Rome, Italy*
[3] *Laboratori Nazionali del Gran Sasso, I.N.F.N., Assergi, Italy*
[4] *IHEP, Chinese Academy, P.O. Box 918/3, Beijing, China*
[5] *Lab. Sperim. Policentrico di Ingegneria Medica, Università di Roma "Tor Vergata"*
[6] *University of Jing Gangshan, Jiangxi, China*
[+] *deceased*

**Abstract**

The DAMA/LIBRA experiment is mainly devoted to the investigation of the presence of Dark Matter (DM) particles in the Galactic halo by exploiting the model independent DM annual modulation signature. The present DAMA/LIBRA and the former DAMA/NaI (exposed masses: $\simeq$ 250 kg and $\simeq$ 100 kg of highly radiopure NaI(Tl), respectively) experiments have released so far a total exposure of 1.17 ton $\times$ yr collected over 13 annual cycles. They have obtained a positive model independent result for the presence of DM particles in the galactic halo at 8.9 $\sigma$ C.L. Some of the obtained results are shortly summarized and future perspectives mentioned.

## 1. Introduction

The DAMA project is an observatory for rare processes located deep underground at the Gran Sasso National Laboratory of the I.N.F.N. It

is based on the development and use of low background scintillators; profiting of the low background features of the realized set-ups, many rare processes are studied [1–19].

The main apparatus, DAMA/LIBRA, is investigating the presence of Dark Matter (DM) particles in the galactic halo by exploiting the model independent DM annual modulation signature.

In fact, as a consequence of its annual revolution around the Sun, which is moving in the Galaxy traveling with respect to the Local Standard of Rest towards the star Vega near the constellation of Hercules, the Earth should be crossed by a larger flux of Dark Matter particles around ∼2 June (when the Earth orbital velocity is summed to the one of the solar system with respect to the Galaxy) and by a smaller one around ∼2 December (when the two velocities are subtracted). Thus, this signature has a different origin and peculiarities than the seasons on the Earth and than effects correlated with seasons (consider the expected value of the phase as well as the other requirements listed below). This DM annual modulation signature is very distinctive since the effect induced by DM particles must simultaneously satisfy all the following requirements: (1) the rate must contain a component modulated according to a cosine function; (2) with one year period; (3) with a phase that peaks roughly around ∼ 2nd June; (4) this modulation must be present only in a well-defined low energy range, where DM particles can induce signals; (5) it must be present only in those events where just a single detector, among all the available ones in the used set-up, actually "fires" (*single-hit* events), since the probability that DM particles experience multiple interactions is negligible; (6) the modulation amplitude in the region of maximal sensitivity has to be $\lesssim$7% in case of usually adopted halo distributions, but it may be significantly larger in case of some particular scenarios such as e.g. those in refs. [20, 21]. Only systematic effects or side reactions able to simultaneously fulfill all the six requirements given above and to account for the whole observed modulation amplitude might mimic this DM signature; no one has been found or suggested by anyone over more than a decade. At present status of technology it is the only model independent signature available in direct Dark Matter investigation that can be effectively exploited.

The DAMA/LIBRA data released so far correspond to six annual cycles for an exposure of 0.87 ton×yr [17, 18]. Considering these

data together with those previously collected by DAMA/NaI over 7 annual cycles (0.29 ton×yr), the total exposure collected over 13 annual cycles is 1.17 ton×yr; this is orders of magnitude larger than the exposures typically collected in the field.

## 2. DAMA/LIBRA Results

The DAMA/NaI set up and its performances are described in ref. [1, 3–5], while the DAMA/LIBRA set-up and its performances are described in ref. [16, 18]. The sensitive part of the DAMA/LIBRA set-up is made of 25 highly radiopure NaI(Tl) crystal scintillators placed in a 5-rows by 5-columns matrix; each crystal is coupled to two low background photomultipliers working in coincidence at single photoelectron level. The detectors are placed inside a sealed copper box flushed with HP nitrogen and surrounded by a low background and massive shield made of Cu/Pb/Cd-foils/polyethylene/paraffin; moreover, about 1 m concrete (made from the Gran Sasso rock material) almost fully surrounds (mostly outside the barrack) this passive shield, acting as a further neutron moderator. The installation has a 3-levels sealing system which excludes the detectors from environmental air. The whole installation is air-conditioned and the temperature is continuously monitored and recorded. The detectors' responses range from 5.5 to 7.5 photoelectrons/keV. Energy calibrations with X-rays/$\gamma$ sources are regularly carried out down to few keV in the same conditions as the production runs. A software energy threshold of 2 keV is considered.

Several analyses on the model-independent DM annual modulation signature have been performed (see Refs. [17, 18] and references therein). Fig. 1 shows the time behaviour of the experimental residual rates of the *single-hit* events collected by DAMA/NaI and by DAMA/LIBRA in the (2–6) keV energy interval [17, 18]. The superimposed curve is the cosinusoidal function: $A\cos\omega(t-t_0)$ with a period $T=\frac{2\pi}{\omega}=1$ yr, with a phase $t_0=152.5$ day (June $2^{nd}$), and modulation amplitude, $A$, obtained by best fit over the 13 annual cycles. The hypothesis of absence of modulation in the data can be discarded [17, 18] and, when the period and the phase are released in the fit, values well compatible with those expected for a DM

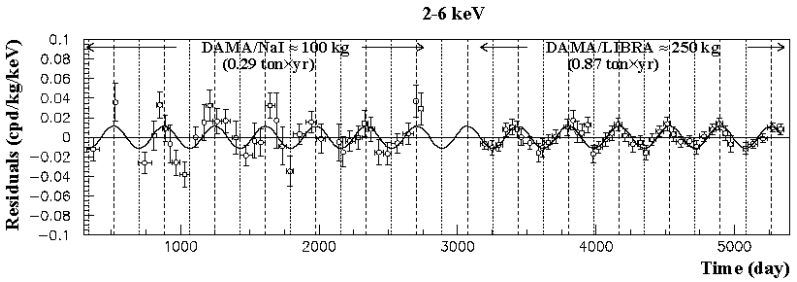


Fig. 1: Experimental model-independent residual rate of the *single-hit* scintillation events, measured by DAMA/NaI over seven and by DAMA/LIBRA over six annual cycles in the (2–6) keV energy interval as a function of the time [4,5,17,18]. The zero of the time scale is January $1^{st}$ of the first year of data taking. The experimental points present the errors as vertical bars and the associated time bin width as horizontal bars. The superimposed curve is $A\cos\omega(t-t_0)$ with period $T=\frac{2\pi}{\omega}=1$ yr, phase $t_0=152.5$ day (June $2^{nd}$) and modulation amplitude, $A$, equal to the central value obtained by best fit over the whole data: cumulative exposure is 1.17 ton $\times$ yr. The dashed vertical lines correspond to the maximum expected for the DM signal (June $2^{nd}$), while the dotted vertical lines correspond to the minimum. See Refs. [17,18] and text

particle induced effect are obtained [18]; for example, in the cumulative (2–6) keV energy interval: $A=(0.0116\pm0.0013)$ cpd/kg/keV, $T=(0.999\pm0.002)$ yr and $t_0=(146\pm7)$ day. Summarizing, the analysis of the *single-hit* residual rate favours the presence of a modulated cosine-like behaviour with proper features at 8.9 $\sigma$ C.L. [18].

The same data of Fig.1 have also been investigated by a Fourier analysis, obtaining a clear peak corresponding to a period of 1 year [18]; this analysis in other energy regions shows instead only aliasing peaks. Moreover, in order to verify absence of annual modulation in other energy regions and, thus, to also verify the absence of any significant background modulation, the energy distribution in energy regions not of interest for DM detection has also been investigated: this allowed the exclusion of a background modulation in the whole energy spectrum at a level much lower than the effect found in the lowest energy region for the *single-hit* events [18]. A further relevant investigation has been done by applying the same hardware and software procedures, used to acquire and to analyse the *single-hit* residual rate, to the *multiple-hits* events in which more than one detector "fires". In fact, since the probability that a DM particle interacts

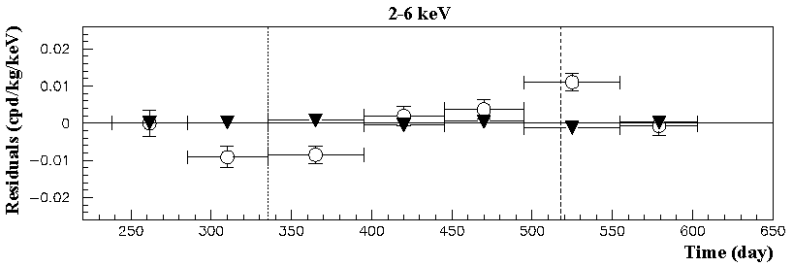


Fig. 2: Experimental residual rates over the six DAMA/LIBRA annual cycles for *single-hit* events (open circles) (class of events to which DM events belong) and for *multiple-hit* events (filled triangles) (class of events to which DM events do not belong). They have been obtained by considering for each class of events the data as collected in a single annual cycle and by using in both cases the same identical hardware and the same identical software procedures. The initial time of the figure is taken on August $7^{th}$. The experimental points present the errors as vertical bars and the associated time bin width as horizontal bars. See text and Refs. [17, 18]

in more than one detector is negligible, a DM signal can be present just in the *single-hit* residual rate. Thus, this allows the study the background behaviour in the same energy interval of the observed positive effect. The result of the analysis is reported in Fig. 2 where it is shown the residual rate of the *single-hit* events measured over the six DAMA/LIBRA annual cycles, as collected in a single annual cycle, together with the residual rates of the *multiple-hits* events, in the same considered energy interval. A clear modulation is present in the *single-hit* events, while the fitted modulation amplitudes for the *multiple-hits* residual rate are well compatible with zero [18]. Similar results were previously obtained also for the DAMA/NaI case [5]. Thus, again evidence of annual modulation with proper features, as required by the DM annual modulation signature, is present in the *single-hit* residuals (events class to which the DM particle induced events belong), while it is absent in the *multiple-hits* residual rate (event class to which only background events belong). Since the same identical hardware and the same identical software procedures have been used to analyse the two classes of events, the obtained result offers an additional strong support for the presence of a DM particle component in the galactic halo further excluding any side effect either from hardware or from software procedures or from background.

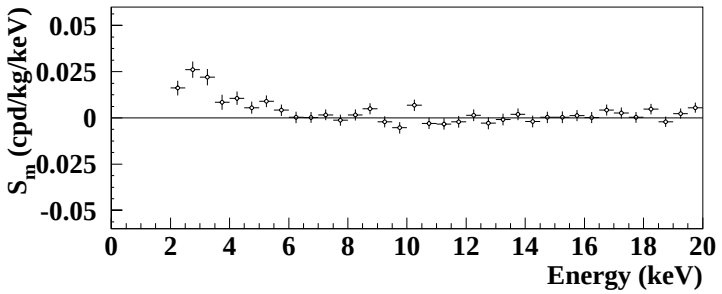


Fig. 3: Energy distribution of the modulation amplitudes $S_m$ for the total cumulative exposure 1.17 ton×yr. The energy bin is 0.5 keV. A clear modulation is present in the lowest energy region, while $S_m$ values compatible with zero are present just above. In fact, the $S_m$ values in the (6–20) keV energy interval have random fluctuations around zero with $\chi^2$ equal to 27.5 for 28 degrees of freedom. See Refs. [17, 18]

The annual modulation present at low energy has also been analyzed by depicting the differential modulation amplitudes, $S_m$, as a function of the energy; the $S_m$ is the modulation amplitude of the modulated part of the signal obtained by maximum likelihood method over the data, considering $T = 1$ yr and $t_0 = 152.5$ day. The $S_m$ values are reported as function of the energy in Fig. 3. It can be inferred that a positive signal is present in the (2–6) keV energy interval, while $S_m$ values compatible with zero are present just above; in particular, the $S_m$ values in the (6–20) keV energy interval have random fluctuations around zero with $\chi^2$ equal to 27.5 for 28 degrees of freedom. It has been also verified that the measured modulation amplitudes are statistically well distributed in all the crystals, in all the annual cycles and energy bins; these and other discussions can be found in ref. [18].

It is also interesting the results of the analysis performed by releasing the assumption of a phase $t_0 = 152.5$ day in the procedure of maximum likelihood to evaluate the modulation amplitudes from the data of the seven annual cycles of DAMA/NaI and the six annual cycles of DAMA/LIBRA. In this case alternatively the signal has been written as: $S_{0,k} + S_{m,k} \cos\omega(t - t_0) + Z_{m,k} \sin\omega(t - t_0) = S_{0,k} + Y_{m,k} \cos\omega(t - t^*)$, where $S_{0,k}$ and $S_{m,k}$ are the constant part and the modulation amplitude of the signal in $k$-th energy interval.

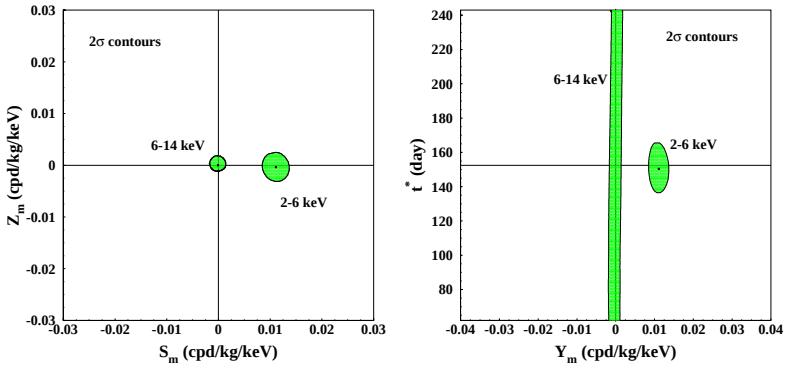


Fig. 4: $2\sigma$ contours in the plane $(S_m, Z_m)$ (*left*) and in the plane $(Y_m, t^*)$ (*right*) for the (2–6) keV and (6–14) keV energy intervals. The contours have been obtained by the maximum likelihood method, considering the cumulative exposure of 1.17 ton $\times$ yr. A modulation amplitude is present in the lower energy intervals and the phase agrees with that expected for DM induced signals

Obviously, for signals induced by DM particles one would expect: i) $Z_{m,k} \sim 0$ (because of the orthogonality between the cosine and the sine functions); ii) $S_{m,k} \simeq Y_{m,k}$; iii) $t^* \simeq t_0 = 152.5$ day. In fact, these conditions hold for most of the dark halo models; however, it is worth noting that slight differences in the phase could be expected in case of possible contributions from non-thermalized DM components, such as e.g. the SagDEG stream [7] and the caustics [22]. The $2\sigma$ contours in the plane $(S_m, Z_m)$ for the (2–6) keV and (6–14) keV energy intervals and those in the plane $(Y_m, t^*)$ are reported in Fig. 4 [18]. The best fit values for the (2–6) keV energy interval are ($1\sigma$ errors): $S_m = (0.0111 \pm 0.0013)$ cpd/kg/keV; $Z_m = -(0.0004 \pm 0.0014)$ cpd/kg/keV; $Y_m = (0.0111 \pm 0.0013)$ cpd/kg/keV; $t^* = (150.5 \pm 7.0)$ day; while for the (6–14) keV energy interval are: $S_m = -(0.0001 \pm 0.0008)$ cpd/kg/keV; $Z_m = (0.0002 \pm 0.0005)$ cpd/kg/keV; $Y_m = -(0.0001 \pm 0.0008)$ cpd/kg/keV and $t^*$ obviously not determined. These results confirm those achieved by other kinds of analyses. In particular, a modulation amplitude is present in the lower energy intervals and the period and the phase agree with those expected for DM induced signals. For more detailed discussions see ref. [18]

Both the data of DAMA/LIBRA and of DAMA/NaI fulfil all the requirements of the DM annual modulation signature.

Sometimes naive statements were put forwards as the fact that in nature several phenomena may show some kind of periodicity. It is worth noting that the point is whether they might mimic the annual modulation signature in DAMA/LIBRA (and former DAMA/NaI), i.e. whether they might be not only quantitatively able to account for the observed modulation amplitude but also able to contemporaneously satisfy all the requirements of the DM annual modulation signature; the same is also for side reactions.

Careful investigations on absence of any significant systematics or side reaction able to account for the measured modulation amplitude and to simultaneously satisfy all the requirements of the signature have been quantitatively carried out (see e.g. ref. [4,5,16–18,23], refs therein). No systematics or side reactions able to mimic the signature (that is, able to account for the measured modulation amplitude and simultaneously satisfy all the requirements of the signature) has been found or suggested by anyone over more than a decade.

The obtained model independent evidence is compatible with a wide set of scenarios regarding the nature of the DM candidate and related astrophysical, nuclear and particle Physics. For examples some given scenarios and parameters are discussed e.g. in Refs. [2, 4–11] and in Appendix A of Ref. [17]. Further large literature is available on the topics [24]; other possibilities are open. Here we just recall the recent paper [25] where the DAMA/NaI and DAMA/LIBRA results, which fulfill all the many peculiarities of the model independent Dark Matter annual modulation signature, are examined under the particular hypothesis of a light-mass Dark Matter candidate particle interacting with the detector nuclei by coherent elastic process; comparison with recent possible positive hint [26] is also given.

It is worth noting that no other experiment exists, whose result can be directly compared in a model-independent way with those by DAMA/NaI and DAMA/LIBRA. Moreover, concerning those activities claiming model dependent exclusion under some largely arbitrary assumptions (see for example discussions in [4, 5, 17, 27, 28]) and generally using marginal exposures, it is worth noting that often important critical points exist in some of their experimental aspects (energy threshold, energy scale, multiple selection procedures, disuniformity of the detectors response, absence of suitable periodical calibrations in the same running conditions and in the claimed low

energy region, stabilities, etc.); in addition existing experimental and theoretical uncertainties are not considered.

Finally, as regards the indirect detection searches, let us note that no direct model-independent comparison can be performed between the results obtained in direct and indirect activities, since it does not exist a biunivocal correspondence between the observables in the two kinds of experiments. Anyhow, if possible excesses in the positron to electron flux ratio and in the $\gamma$ rays flux with respect to an assumed simulation of the hypothesized background contribution, which is expected from standard sources, might be interpreted in terms of Dark Matter (but huge and still unjustified boost factor and new interaction types are required), this would also be not in conflict with the effect observed by DAMA experiments.

## 3. Upgrades and Perspectives

A first upgrade of the DAMA/LIBRA set-up was performed in September 2008. One detector was recovered by replacing a broken PMT and a new optimization of some PMTs and HVs was done. The transient digitizers were replaced with new ones, having better performances and a new DAQ with optical read-out was installed.

A further and more important upgrade has been performed in the end of 2010. In fact, all the PMTs have been replaced with new ones with higher quantum efficiency; this will allow lower software energy threshold and, hence, the improvement of the performance and of the sensitivity for deeper corollary information on the nature of the DM candidate particle(s) and on the various related astrophysical, nuclear and particle Physics scenarios. Since January 2011 the DAMA/LIBRA experiment is again in data taking in the new configuration. In the future DAMA/LIBRA will also study several other rare processes as done by the former DAMA/NaI apparatus in the past [12] and by itself so far [19].

1. R. Bernabei *et al.*, Il Nuovo Cim. A **112**, 545 (1999).

2. R. Bernabei *et al.*, Phys. Lett. B **389**, 757 (1996); Phys. Lett. B **424**, 195 (1998); Phys. Lett. B **450**, 448 (1999); Phys. Rev. D **61**, 023512 (2000); Phys. Lett. B **480**, 23 (2000); Phys. Lett. B **509**, 197 (2001); Eur. Phys. J. C **23**, 61 (2002); Phys. Rev. D **66**, 043503 (2002).

3. R. Bernabei *et al.*, Eur. Phys. J. C **18**, 283 (2000).

4. R. Bernabei *el al.*, La Rivista del Nuovo Cimento **26** n.1, 1 (2003).

5. R. Bernabei *et al.*, Int. J. Mod. Phys. D **13**, 2127 (2004).

6. R. Bernabei *et al.*, Int. J. Mod. Phys. A **21**, 1445 (2006).

7. R. Bernabei *et al.*, Eur. Phys. J. C **47**, 263 (2006).

8. R. Bernabei *et al.*, Int. J. Mod. Phys. A **22**, 3155 (2007).

9. R. Bernabei *et al.*, Eur. Phys. J. C **53**, 205 (2008).

10. R. Bernabei *et al.*, Phys. Rev. D **77**, 023506 (2008).

11. R. Bernabei *et al.*, Mod. Phys. Lett. A **23**, 2125 (2008).

12. R. Bernabei *et al.*, Phys. Lett. B **408**, 439 (1997); P. Belli *et al.*, Phys. Lett. B **460**, 236 (1999); R. Bernabei *et al.*, Phys. Rev. Lett. **83**, 4918 (1999); P. Belli *et al.*, Phys. Rev. C **60**, 065501 (1999); R. Bernabei *et al.*, Il Nuovo Cimento A **112**, 1541 (1999); Phys. Lett. B **515**, 6 (2001); F. Cappella *et al.*, Eur. Phys. J.-direct C **14**, 1 (2002); R. Bernabei *et al.*, Eur. Phys. J. A **23**, 7 (2005); Eur. Phys. J. A **24**, 51 (2005); Astrop. Phys. **4**, 45 (1995); in *The identification of Dark Matter* (World Sc. Pub., Singapore, 1997), pp. 574.

13. P. Belli *et al.*, Astropart. Phys. **5**, 217 (1996); Nuovo Cim. C **19**, 537 (1996); Phys. Lett. B **387**, 222 (1996); Phys. Lett. B **389**, 783 err. (1996); R. Bernabei *et al.*, Phys. Lett. B **436**, 379 (1998); P. Belli *et al.*, Phys. Lett. B **465**, 315 (1999); Phys. Rev. D **61**, 117301 (2000); R. Bernabei *et al.*, New J. of Phys. **2**, 15.1 (2000); Phys. Lett. B **493**, 12 (2000); Nucl. Instr. & Meth A **482**, 728 (2002); Eur. Phys. J. direct C **11**, 1 (2001); Phys. Lett. B **527**, 182 (2002); Phys. Lett. B **546**, 23 (2002); in the volume *Beyond the Desert 2003* (Springer, Berlin, 2003), pp. 365; Eur. Phys. J. A **27**, s01 35 (2006).

14. R. Bernabei *et al.*, Astropart. Phys. **7**, 73 (1997); Nuovo Cim. A **110**, 189 (1997); P. Belli *et al.*, Astropart. Phys. **10**, 115 (1999); Nucl. Phys. B **563**, 97 (1999); R. Bernabei *et al.*, Nucl. Phys. A **705**, 29 (2002); P. Belli *et al.*, Nucl. Instr. & Meth A **498**, 352 (2003); R. Cerulli *et al.*, Nucl. Instr. & Meth A **525**, 535 (2004); R. Bernabei *et al.*, Nucl. Instr. & Meth A **555**, 270 (2005); Ukr. J. Phys. **51** 1037 (2006); P. Belli *et al.*, Nucl. Phys. A **789**, 15 (2007); Phys. Rev. C **76**, 064603 (2007); Phys. Lett. B **658**, 193 (2008); Eur. Phys. J. A **36**, 167 (2008); Nucl. Phys. A **826**, 256 (2009). Nucl. Instr. & Meth. A **615**, 301 (2010); Nucl. Instr. & Meth. A **626-627**, 31 (2011); J. Phys. G: Nucl. Part. Phys. **38**, 015103 (2011).

15. P. Belli *et al.*, Nucl. Instr. & Meth. A **572**, 734 (2007); Nucl. Phys. A **806**, 388 (2008); Nucl. Phys. A **824**, 101 (2009); in the *Proceed. of the Int. Conf. NPAE 2008*, ed. INR-Kiev, Kiev, 2009, pp. 473; Eur. Phys. J. A **42**, 171 (2009); Nucl. Phys. A **846**, 143 (2010); Nucl. Phys. A **859**, 126 (2011). Phys. Rev. C **83**, 034603 (2011); Eur. Phys. J. A **47**, 91 (2011).

16. R. Bernabei *et al.*, Nucl. Instr. & Meth. A **592**, 297 (2008).

17. R. Bernabei *et al.*, Eur. Phys. J. C **56**, 333 (2008).

18. R. Bernabei *et al.*, Eur. Phys. J. C **67**, 39 (2010).

19. R. Bernabei *et al.*, Eur. Phys. J. C **62**, 327 (2009).

20. D. Smith and N. Weiner, Phys. Rev. D **64**, 043502 (2001); D. Tucker-Smith and N. Weiner, Phys. Rev. D **72**, 063509 (2005).

21. K. Freese *et al.*, Phys. Rev. D **71**, 043516 (2005); Phys. Rev. Lett. **92**, 111301 (2004).

22. F. S. Ling, P. Sikivie and S. Wick, Phys. Rev. D **70**, 123503 (2004).

23. R. Bernabei *et al.*, AIP Conf. Proceed. **1223**, 50 (2010) [arXiv:0912.0660]; J. Phys.: Conf. Ser. **203** 012040 (2010) [arXiv:0912.4200]; http://taup2009.lngs.infn.it/slides/jul3/nozzoli.pdf, talk given by F. Nozzoli; Can. J. Phys. **89**, 11 (2011); SIF Atti Conf. **103**, (2011) [arXiv:1007.0595]; pre-print ROM2F/2011/12 to appear in the *Proc. of TIPP2011 Conf., Baltimore, USA*.

24. A. Bottino *et al.*, Phys. Rev. D **81**, 107302 (2010); N. Fornengo *et al.* Phys. Rev. D **83**, 15001 (2011); A.L. Fitzpatrick *et al.*, [arXiv:1003.0014]; D. Hooper *et al.*, [arXiv:1007.1005v2]; A.V. Belikov *et al.*, [arXiv:1009.0549]; E. Kuflik *et al.*, [arXiv:1003.0682]; S. Chang *et al.*, Phys. Rev. D **79**, 043513 (2009); S. Chang *et al.*, [arXiv:1007.2688]; R. Foot, [arXiv:1001.0096]; Y. Bai, P.J. Fox, [arXiv:0909.2900]; J. Alwall *et al.*, [arXiv:1002.3366]; M.Yu. Khlopov *et al.*, [arXiv:1003.1144]; S. Andreas *et al.*, [arXiv:1003.2595]; J. Kopp *et al.*, [arXiv:0912.4264]; V. Barger *et al.*, [arXiv:1005.3328]; J. L. Feng *et al.*, [arXiv:1102.4331];

25. P. Belli *et al.*, Phys. Rev. D **84**, 055014 (2011).

26. C.E. Aalseth *et al.*, [arXiv:1002.4703; arXiv:1106.0650].

27. R. Bernabei *et al.*, *Liquid Noble gases for Dark Matter searches: a synoptic survey*, Exorma Ed., Roma, ISBN 978-88-95688-12-1, 2009, pp. 1–53 [arXiv:0806.0011v2].

28. J.I. Collar and D.N. McKinsey, [arXiv:1005.0838]; [arXiv:1005.3723]; J.I. Collar, [arXiv:1006.2031]; [arXiv:1010.5187]; [arXiv:1103.3481]; [arXiv:1106.0653]; [arXiv:1106.3559].

# STUDY OF ULTRARARE DECAYS $K^0 \to \pi^0\nu\nu$(BAR) (Search of $K^0 \to \pi^0\nu\nu$(bar) decay at IHEP, project KLOD)

V.N. Bolotov[1]
on behalf of the collaboration
JINR, IHEP and INR RAS

*INR RAN, Moscow*

## Motivation of Experiment

The main goal of the presented project consists in the search and measurement of the branching ratio of $K_L^0 \to \pi^0\nu\tilde{\nu}$ decays. The experimental setup is optimized for the main purpose but opens some additional opportunities for researches of neutral modes of $K_L^0$-decays. The $K_L^0 \to \pi^0\nu\tilde{\nu}$ decay is $CP$-violation decay [1]. In the frame of Standard Model (SM) the branching ratio of $K_L^0 \to \pi^0\nu\tilde{\nu}$ decay is proportional to Im $(V_{td}\ V_{ts})$, which represents the height of the Unitarity Triangl [e2] (Fig. 1).

The measurement of this height allows to determine the quark mixing matrix parameter $\eta$, which is responsible for CP-violation [3, 4]. The theoretical ambiguities in calculations of branching ratio of $K_L^0 \to \pi^0\nu\tilde{\nu}$ decay are very small, $\sim 1 \div 2\%$. Using the current values of the Cabibo-Kaboyashi-Maskawa (CixKM) matr parameters, the branching ratio is equal to $(2.8\pm0.4)\times10^{-11}$ [5], and even small deviation of the measured value from the theoretically predicted one will give a direct indication for the existence of "New Physics".

The most strict upper limit of branching ratio derived from isotopic invariance is the model-independent theoretical limit Br$(K_L^0 \to$

$$V_{\rm CKM} = \begin{pmatrix} V_{ud} & V_{us} & V_{ub} \\ V_{cd} & V_{cs} & V_{cb} \\ V_{td} & V_{ts} & V_{tb} \end{pmatrix} \approx$$

$$\approx \begin{pmatrix} 1-\lambda^2/2 & \lambda & A\lambda^3(\rho - i\eta) \\ -\lambda & 1-\lambda^2/2 & A\lambda^2 \\ A\lambda^3(1-\rho-i\eta) & -A\lambda^2 & 1 \end{pmatrix} + O(\lambda^4),$$

$$\lambda = \sin(\theta_c) = 0.22 \pm 0.002, \quad \text{“}\eta\text{”}(\mathrm{Im}(V_{td}))$$

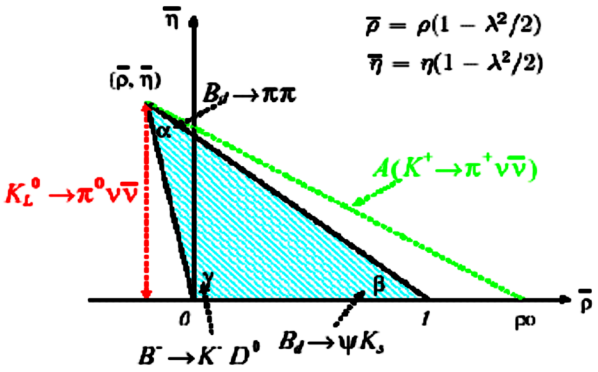


Fig. 1: The Cabibo-Kaboyashi-Maskawa (CKM) matrix and Unitarity Triangl

$\pi^0\nu\tilde\nu) < 4.37\ \mathrm{Br}(K^+ \to \pi^+\nu\tilde\nu)$, the so-called Grossman-Nir limit (GN) [6]. The decay $K^+ \to \pi^+\nu\tilde\nu$ was observed in experiments BNL E-787 (2 events) and E-949 (1 event). Common analysis of the data from these experiments results in the branching ratio to be in a range of $0.27\times10^{-10} < \mathrm{Br}(K^+ \to \pi^+\nu\tilde\nu) < 3.84\times10^{-10}$ (90% C.L.) [7]. The model-independent GN upper limit for $K_L^0 \to \pi^0\nu\tilde\nu$ decay is $\mathrm{Br}(K_L^0 \to \pi^0\nu\tilde\nu|_{\rm GN} < 1.68\times10^{-9}$ (90% C.L.) and is about 300 times more sensitive than current direct measurements.

## Experimental methods

The experimental setup us shown on Fig. 2.

Experimental difficulties in searches of extremely rare decays are not only achievement of sufficient efficiency of registration, but also

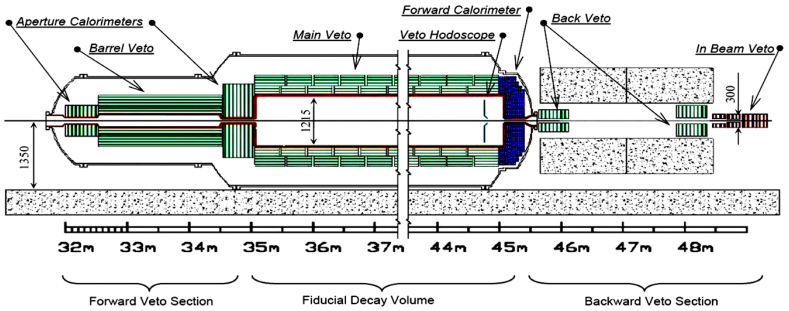


Fig. 2: The KLOD setup

control and understanding of systematic errors. The $K_L^0 \to \pi^0\nu\tilde{\nu}$ decay is to be identified by the signature of $\pi^0(\pi^0 \to \gamma\gamma)$ + "nothing", where gammas are measured by the electromagnetic calorimeter and "nothing" is the absence of the signal in the veto-system. The sought-for decay contains only 2 gammas with the effective mass of $\pi^0$ in the final state. At the same time, having considered all decay modes of $K_L^0$ listed in PDG [8], one can see that 34% of $K_L^0$ decays have $\pi^0$ in the final state. On the other hand, all decays, except $K_L^0 \to \gamma\gamma$, have at least 2 charged particles or 4 gammas in the final state. Thus, the basic condition for the search is the requirement of presence of only 2 gammas and absence of any other registered particles. The most dangerous backgrounds are decays of $K_L^0$ to $2\pi^0$, $3\pi^0$ or $2\gamma$.

The $K_L^0$-mesons basically decay to multi-particle final states, which results in small momenta of decay products in the $K_L^0$ rest system. On the contrary, a spectrum of $\pi^0$ momenta in the $K_L^0 \to \pi^0\nu\tilde{\nu}$ decay is harder due to V-A interaction. Since the momentum in the rest system corresponds to the transverse momentum $\mathbf{P}_T$ in the laboratory system, the signal/background ratio can be improved by selection of $\pi^0$ with high $\mathbf{P}_T$. Serious background sources, which are not connected with decays, are interactions of halo and core beam particles with the material of the setup. As a result, either a single $\pi^0$ or a $\Lambda$ hyperon with subsequent decay $\Lambda \to \pi^0 n$ can be produced.

Thus, the decay region of the proposed setup must be in a high vacuum and be surrounded by a highly efficient veto system. The distant wall is an electromagnetic calorimeter with a good energy and position resolution. Non-decayed $K_L^0$ leave the decay region through

the beam hole at the center of the calorimeter. A special veto detector able to efficiently detect gammas from background decays in the presence of a large flow of beam core particles is installed at the end.

The measurement strategy is to record events with 2 neutral clusters in the calorimeter without a signal from the veto system. The reconstruction of two clusters into the $\pi^0$ mass on the assumption of the infinitely narrow beam allows one to calculate the decay vertex along the beam axis and $\mathbf{P}_T$ of $\pi^0$, the cutoff of which is the strongest factor in background suppression. One more important factor of background suppression is the requirement that the decay vertex be inside the fiducial volume.

Requirements to the neutral beam following from the proposed measurement strategy are rather severe:

- the beam must be narrow ($R < 5$ cm) and well collimated;
- the beam must have small angle deviation, that is be well balanced in transverse momentum $\mathbf{P}_T$;
- the beam must have high intensity ($\sim 10^8$ $K_L^0$/cycle) at the mean $K_L^0$ energy $\sim 10$ GeV;
- the beam must have small contamination by other undesired neutral particles. Especially, the neutron/$K_L^0$ ratio should be as small as possible.

The full version of the proposal shows the possibility of constructing a neutral beam at IHEP (Protvino) on the basis of the existing magnets and accommodating it into the existing beam channel system. The beam channel providing a well-collimated highly intense beam is designed and the calculation of the main parameters of $K_L^0$ and other components of the beam is presented.

The geometry of the detector (Figure 1) is dictated by the requirement of air-tightness for good efficiency of gamma registration [9].

## Comparison with Other Experiments

Now only one experiment on registration of the$K_L^0 \to \pi^0\nu\tilde{\nu}$ decay is under way. The best upper limit of $5.7\times10^{-7}$ (90% C.L.) (as of the

**T a b l e 1: Particle fluxes per spill**

| | $K_L$ | $n$ | $\gamma$ |
|---|---|---|---|
| Without Pb | $7.7\times10^7$ | $8.3\times10^8$ | $3.1\times10^{10}$ |
| With Pb | $5.4\times10^7$ | $5.2\times10^8$ | $7.4\times10^8$ |
| | $n/K_L$ | $\gamma/K_L$ | $\gamma/n$ |
| Without Pb | 11 | 402 | 37 |
| With Pb | 10 | 14 | 1.4 |

beginning of 2006) was obtained by the KTeV-E799 experiment [10] through observing the Dalitz-decay $\pi^0 \to e^+e^-\gamma$. An advantage of this method is a possibility of measuring the decay vertex, which does not require a narrow beam. The disadvantages are a small probability of the Dalitz-decay and the background from $K_{e3}$-decays ($K_L^0 \to \pi^\pm e^\mp\gamma\nu$) due to misidentification of $\pi^\pm$ as $e^\pm$. Table 1 shows the parameters of the running and planned experiments on the given subjects. After closure of the KOPIO (BNL) [i] and KAMI (FNAL) [11] projects the parameters of the KLOD setup can be compared only with the running E-391A (KEK) experiment [12] which will also finish soon. The last two-month data-taking run (RUN-III) was carried out at the end of 2005. The sensitivity is limited by the intensity of the 12 GeV proton accelerator and might ideally reach the level of $10^{-10}$. Recently the authors have announced a new upper limit $2.1\times10^{-7}$ (90% CL) [13] based on $\sim10\%$ RUN-I statistics. Data processing continues and the analysis of the full data set will probably allow the level of the Grossman-Nir limit to be reached.

The goal of the E391a experiment was to show the reliability of the method and to understand the background sources. This is the first step for the high beam intensity experiment with a sensitivity level of $\sim10^{-13}$ at the proton accelerator J-Park [14]. But now it is clear that moving the E391a setup to a new accelerator, as was initially intended, does not solve this problem. The global modification or a completely new setup will be required.

Recently the proposal of the experiment has been published [15]. They proposed the step-by-step approach. The goal of the first step is to observe the decay ($\sim3.5$ events at the level of SM). In view of target share with other experiments, a non-optimal extraction angle and a low-energy $K_L^0$ beam, it will require three years of data taking. At this stage the E391a setup with some modifications will be used.

For example, it is considered to replace the CsI calorimeter with its big cells and inadequate radiation length by a more suitable CsI calorimeter from the KTeV experiment.

At the next (main) step it is proposed to construct a new optimized neutral beam line, to use a higher-energy beam, and to construct a new setup. Three more years of data taking will allow a detailed study of the $K_L^0 \to \pi^0\nu\tilde{\nu}$ decay by collecting $\sim 100$ events with a good S/N ratio. Considering the delay in the construction of the J-Park and high priority of the neutrino program, the results of the first step can be expected not earlier than 2013 [16].

Our experiment will have the following features and advantages:

1. The primary proton beam energy as high as 60–70 GeV provides a higher $K_L^0$ yield and allows a larger extraction angle of the secondary beam, which improves the $K_L^0$/neutron ratio.

2. A higher energy of the $K_L^0$ beam (the mean energy of the neutral beam is considered to be $\sim 10$ GeV) decreases the inefficiency of the veto-system for soft gammas from background decays. Moreover, to retain acceptance at low energy, the setup should be located near the target, which deteriorates the background conditions. On the other hand, higher energy results in increasing size and cost of the setup.

3. The ability of the calorimeter to measure the incident angle of gammas helps to suppress backgrounds.

4. A high visible ratio of deposited energy in the veto detectors due to thin converter layers allows a decrease in the veto threshold to 1 MeV.

5. The veto system of independent cells can be used not only for background suppression but also for gamma measurements, which may increase acceptance for $K_L^0 \to \pi^0\nu\tilde{\nu}$. In addition, calibration of the main detectors is simplified and their inefficiency can be monitored using the real events.

It is worth mentioning that the proposed setup is generally a set of calorimeters. The collaborating institutes have rich experience in designing, constructing and operating such detectors in home and foreign experiments.

## Estimation of Background Suppression and Sensitivity of Experiment

Characteristics of the complete experimental setup were also studied independently using GEANT-3 and GEANT-4. The results were compared and verified. The beam profile and the spectra, obtained from the beam line simulation, and the inefficiency functions of detectors were used in the simulation.

The following cuts were used for estimation of the contribution from the main background $K_L^0$-decays:

- The reconstructed energy of each gamma is larger than 0.15 GeV.
- The reconstructed energy of each gamma is smaller than 6 GeV.
- The reconstructed transverse momentum of $\pi^0$ is larger than 120 MeV/c.
- The reconstructed decay vertex must be inside the decay volume.
- The decay vertex reconstructed from the clusters using gamma angles must agree within $\pm$ 0.5 m with the decay vertex reconstructed from the cluster on the assumption of the $\pi^0$ mass.
- The center of gravity of 2 clusters in the calorimeter must be at a distance more than 20 cm from the beam axis.
- The distance between the gamma clusters must be larger than 15 cm.

Table 2 shows the contribution of the most essential background decays. The estimation was done by generating the number of events for the given decay 10 times (100 times for $K_L^0 \to 2\pi^0$ decay) larger than required for observation of one $K_L^0 \to \pi^0\nu\tilde{\nu}$ event with the given acceptance. No events of any background decay (except $K_L^0 \to 2\pi^0$) were observed in the simulation. The limit for $K_L^0 \to \pi^+e^-\nu$ was obtained from the simulation of $K_L^0 \to \pi^-e^+\nu$ with allowance for the difference in registration inefficiency between $\pi^\pm$ and $e^\pm$. The major part of $K_L^0 \to 2\pi^0$ backgrounds comes from events with 2 gammas in the beam veto.

**Table 2**

| Background source | Number of backgrounds normalized to SES (single event sensitivity) at SM level |
|---|---|
| $K_L^0$ decays, yielding at least one gamma. Caused by inefficiency for gammas | 0.26 ($\pi^0\pi^0$)<br>$< 0.1$ ($\gamma\gamma$)<br>$< 0.1$ ($\pi^0\pi^0\pi^0$) |
| $K_L^0$ decays, yielding charged particles. Caused by inefficienc y for charged particles | $< 0.1$ ($\pi^- e^+ \nu$)<br>$< 0.01$ ($\pi^+ e^- \nu$) |

The acceptance for the $K_L^0 \to \pi^0\nu\tilde{\nu}$ decay with the above cuts was estimated to be $\sim$18%. In the decay region 4.8% of $K_L^0$ decays occurred. Thus, with the beam of intensity $10^8$ $\{5.4\times10^7\}$ $K_L^0$/spill, the sensitivity of the experiment for 10 days of data taking ($\sim 10^4$ spills/day) can be calculated as:

$$1\times(10^4)\times(10^8\{5.4\times10^7\})\times(4.8\times10^{-2})\times(18\times10^{-2})\times\mathrm{Br}(2.8\times10^{-11})\approx$$

$2.4\{1.1\}$ events.

## Setup Construction Stages

A beam with the required characteristics is the basic condition for the success of the experiment. Therefore, realization of the project must begin with design and construction of the beam line with detailed simulation and optimization of all its elements. Under favorable conditions this work can be completed within 1-1.5 years. By that time the equipment for measurement of beam characteristics and their comparison with the design parameters should be prepared.

Most detectors of the setup are well-studied calorimetric structures and do not demand detailed researches of their prototypes. In particular, for making a decision on creation of the step veto-system of the main decay volume only one counter should be assembled for optimization of manufacturing technology and for demonstration of a possibility of creating self-supported modules. The only exception is the beam veto and, probably, the forward electromagnetic calorimeter. If they are similar in design, it is possible to create a common prototype which will also be necessary for studying beam characteristics. This means that it should be made simultaneously with the

beam line, whose operation should comply with the accelerator beam time schedule.

Mass production of all detectors should start 0.5-1 year after accomplishment of the beam line construction. This delay is assumed to be used for beam survey. Also, detailed simulation carried out in parallel allows us to simplify the design of the detectors before their production.

The total time from the beam line designing to the beginning of the experiment is expected to be 4-4.5 years. Two years of data taking should allow measuring or, at least, observing $K_L^0 \to \pi^0\nu\tilde{\nu}$ decay.


1. L. Littenberg, Phys. Rev. ??; G. Buchalla, G. Isidori, Phys. Rev. D **39**, 3322 (1989); Phys. Lett. B **440**, 170 (1998).
2. G. Buchalla, A.J. Buras, Phys. Lett. B **333**, 221 (1994).
3. G. Buchalla, A.J. Buras, Phys. Rev. D **54**, 6782 (1996).
4. A.J. Buras *et al.*, hep-ph/0603079.
5. Y. Grossman, Y. Nir, Phys. Lett. B **398**, 163 (1997).
6. V.V. Anisimovsky *et al.*, Phys. Rev. Lett. **93**, 031801004.
7. W.-M. Yao *et al.*, J. Phys. Rev. G **33**, 1 (2006).
8. F. Novoskoltsev *et al.*, *$K_L$ beam line at Institute For High Energy Physics (U-70 Accelerator, Protvino), Calculated Parameters*, RuPAC 2004 – Contributions to the Proceedings 2004. Joint Accelerator Conferences Website (JACOW), http://accelconf.web.cern.ch/AccelConf/r04/papers/THLP09.PDF.
9. A. Alavi-Harati *et al.*, Phys. Rev. D **61**, 072006 (2000).
10. Full RSVP MRE Proposal, *Rare Symmetry Violating Processes*, RSVP Collaboration, November 1, 1999, http://www.kopio.bnl.gov/.
11. *A Proposal for a Precision Measurement of the Decay $K_L^0 \to \pi^0\nu\tilde{\nu}$ and Other Rare Processes at Fermilab Using The Main Injector – KAMI*, April 2, 2001, http://kpasa.fnal.gov:8080/public/kami/kami.html.
12. T. Inagaki *et al.*, *KEK-E391 Proposal 1996*, KEK-Internal 96-13 (1996); K. Abe *et al.*, KEK Preprint 2000-89 (2000).
13. J.K. Ahn *et al.*, Phys. Rev. D **74**, 051105(R) (2006).
14. *Letters of Intent for Nuclear and Particle Physics Experiments at the J-PARC, LO5*, http://www-ps.kek.jp/jhf-np/LOIlist/LOIlist.html.
15. *Proposal for $K_L^0 \to \pi^0\nu\tilde{\nu}$ Experiment at J-Park*, April 28, 2006, P14, http://j-parc.jp/NuclPart/Proposal_0606_e.html.

# LUNA, THE SUN AND THE OTHER STARS

C. Broggini[1] (the LUNA Collaboration)

[1]*INFN, Sezione di Padova, Italy*

**Abstract**

One of the main ingredients of nuclear astrophysics is the knowledge of the thermonuclear reactions responsible for the stellar luminosity and for the synthesis of the chemical elements. Deep underground in the Gran Sasso Laboratory the cross section of the key reactions of the proton-proton chain and of the Carbon-Nitrogen-Oxygen (CNO) cycle have been measured right down to the energies of astrophysical interest.

## 1. Introduction

Only hydrogen, helium and lithium are synthesized in the first minutes after the big-bang. All the other elements of the periodic table are produced in the thermonuclear reactions taking place inside the 'cosmic cauldrons'. i.e. the stars [1]. Nuclear astrophysics studies all the reactions which provide the energy to the stars and realize the transmutation of the chemical elements. In particular, the knowledge of the reaction cross-section at the stellar energies is the heart of nuclear astrophysics. The reaction rate in the hot plasma of a star, with temperatures in the range of tens to hundreds of millions Kelvin, is obtained by weighting the reaction cross section $\sigma(E)$ with the energy distribution of the colliding nuclei: a Maxwell-Boltzmann $\phi(E)$ peaked at energies of 1-10 keV. The product between $\sigma(E)$ and $\phi(E)$ identifies the energy window where the reaction occurs in the star: the Gamow peak. Inside the Gamow peak, which is far below the Coulomb energy arising from the repulsion between nuclei, the

reaction can take place only due to the quantum mechanical tunnel effect:

$$\sigma(E) = \frac{S(E)}{E} \exp(-2\,\pi\,\eta), \tag{1}$$

where $S(E)$ is the astrophysical factor (which contains the nuclear physics information) and $\eta$ is the Sommerfeld parameter, given by $2\,\pi\,\eta = 31.29\,Z_1\,Z_2(\mu/E)^{1/2}$. $Z_1$ and $Z_2$ are the nuclear charges of the interacting particles, $\mu$ is the reduced mass (in units of amu), and $E$ is the center of mass energy (in units of keV).

At these energies the cross sections are extremely small. Such smallness makes the star life-time of the length we observe, but it also makes impossible the direct measurement in the laboratory. The rate of the reactions, characterized by a typical energy release of a few MeV, is too low, down to a few events per year, in order to stand out from the laboratory background. Instead, the observed energy dependence of the cross-section at high energies is extrapolated to the low energy region, leading to substantial uncertainties. LUNA, Laboratory for Underground Nuclear Astrophysics, started twenty years ago to run nuclear physics experiments in an extremely low-background environment, the Gran Sasso Laboratory (LNGS), to reproduce in the laboratory what Nature makes inside the stars.

In particular, we have installed two electrostatic accelerators underground in LNGS: a compact 50 kV "home-made" machine and a commercial 400 kV one. Common features of the two accelerators are the high beam current, the long term stability and the precise beam energy determination. The dolomite rock of Gran Sasso provides a natural shielding equivalent to at least 3800 meters of water which reduces the muon and neutron fluxes by a factor $10^6$ and $10^3$, respectively.

## 2. The Resonance and the Solar Neutrino Problem

The initial activity of LUNA has been focused on the $^3$He($^3$He,2p)$^4$He cross section measurement within the solar Gamow peak (15-27 keV). Such a reaction is a key one of the hydrogen burning proton-proton chain, which is responsible for more than 99% of the solar luminosity.

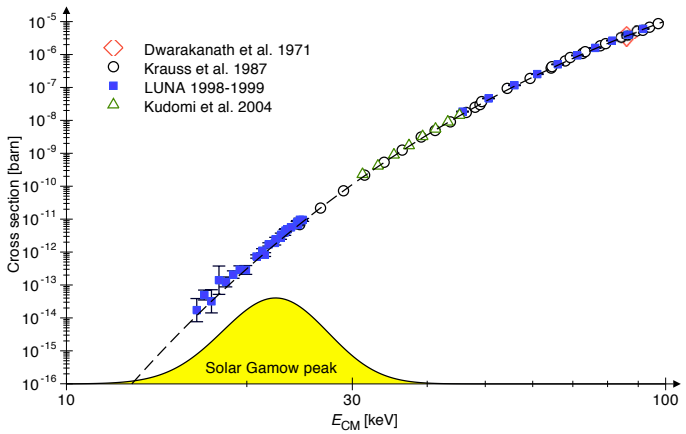


Fig. 1: The cross section of $^3$He($^3$He,2p)$^4$He. Data from LUNA and from other experiments

A resonance in its cross section at the thermal energy of the Sun was suggested long time ago to explain the observed $^8$B solar neutrino flux. As a matter of fact, such a resonance would decrease the relative contribution of the alternative reaction $^3$He$(\alpha,\gamma)^7$Be, which generates the branch responsible for $^7$Be and $^8$B neutrino production in the Sun.

The experimental set-up was made of eight 1 mm thick silicon detectors of $5\times5\,\mathrm{cm}^2$ area placed around the beam inside the windowless target chamber filled with $^3$He at the pressure of 0.5 mbar. The simultaneous detection of two protons has been the signature which unambiguously identified a $^3$He($^3$He,2p)$^4$He fusion reaction ($Q$-value: 12.86 MeV). Fig. 1 shows the results from LUNA [2,3] together with higher energy measurements [4–6] which stop just at the upper edge of the thermal energy region of the Sun. For the first time a nuclear reaction has been measured in the laboratory at the energy occurring in a star. At the lowest energy of 16.5 keV the cross section is 0.02 pbarn, which corresponds to a rate of about 2 events/month, rather low even for the "silent" experiments of underground physics. No narrow resonance has been found and, as a consequence, the astrophysical solution of the $^8$B and $^7$Be solar neutrino problem based on its existence has been definitely ruled out.

$^3$He($\alpha$,$\gamma$)$^7$Be ($Q$-value: 1.586 MeV), the competing reaction for $^3$He burning, has been precisely measured by LUNA both by detecting the prompt $\gamma$ rays and by counting of the decaying $^7$Be nuclei. Thanks to our small error, the total uncertainty on the $^7$Be flux went from 9.4 to 5.5% [7].

## 3. The Composition of the Sun Core and the Age of the Universe

$^{14}$N(p,$\gamma$)$^{15}$O ($Q$-value: 7.297 MeV) is the slowest reaction of the CNO cycle and it rules its energy production rate. In particular, it is the key reaction to know the $^{13}$N and $^{15}$O solar neutrino flux, which depends almost linearly on its cross section.

In the first phase of the LUNA study, data have been obtained down to 119 keV energy with solid targets of TiN and a 126% germanium detector. This way, the five different radiative capture transitions which contribute to the $^{14}$N(p,$\gamma$)$^{15}$O cross section at low energy were measured. The total cross section was then studied down to very low energy in the second phase of the experiment by using the $4\pi$ BGO summing detector placed around a windowless gas target filled with nitrogen at 1 mbar pressure. At the lowest center of mass energy of 70 keV a cross section of 0.24 pbarn was measured, with an event rate of 11 counts/day from the reaction.

The results obtained first with the germanium detector [8,9] and then with the BGO set-up [10] were about a factor two lower than the existing extrapolation [11,12] from previous data [13,14] at very low energy (Fig.2). As a consequence, the CNO neutrino yield in the Sun is decreased by about a factor two.

In order to provide more precise data for the ground state capture, the most difficult one to be measured because of the summing problem, we performed a third phase of the $^{14}$N(p,$\gamma$)$^{15}$O study with a composite germanium detector. This way the total error on the S-factor has been reduced to 8%: $S_{1,14}(0)$=1.57$\pm$0.13 keV barn [15]. This is significant because, finally solved the solar neutrino problem, we are now facing the solar composition problem: the conflict between helioseismology and the new metal abundances (i.e. the amount of elements different from hydrogen and helium) that emerged from im-

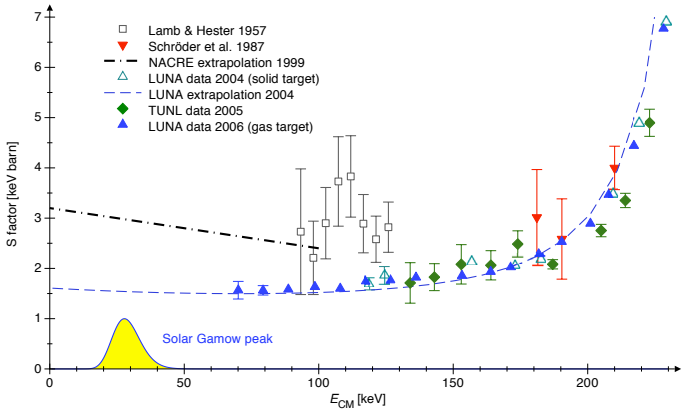


Fig. 2: Astrophysical S(E)-factor of the $^{14}$N(p,$\gamma$)$^{15}$O reaction. The errors are statistical only (the systematic ones are similar)

proved modeling of the photosphere [16]. Thanks to the relatively small error, it will be possible in the near future to measure the carbon and nitrogen content of the Sun core by comparing the predicted CNO neutrino flux with the measured one. As a matter of fact, the CNO neutrino flux is decreased by about 30% in going from the high to the low metallicity scenario. This way it will be possible to test whether the early Sun was chemically homogeneous [17], a key assumption of the standard Solar Model.

The lower cross section is affecting also stars which are more evolved than our Sun. In particular, the lower limit on the age of the Universe inferred from the age of the oldest stellar populations, the globular clusters, is increased by 0.7-1 billion years [18] up to 14 billion years and the dredge-up of carbon to the surface of asymptotic giant branch stars is more efficient [19].

## 4. Hydrogen Burning at High Temperature

The solar phase of LUNA has reached the end. A new and rich program of nuclear astrophysics mainly devoted to CNO, Mg-Al and Ne-Na cycles has already started with the measurement of $^{15}$N(p,$\gamma$)$^{16}$O [20] and $^{25}$Mg(p,$\gamma$)$^{26}$Al [21]. Due to the higher Coulomb barrier of

the reactions involved, these cycles become important at temperature higher than the one of our Sun: hydrogen burning in the shell of massive stars and Novae explosions. Relatively unimportant for energy generation, these cycles are essential for the synthesis of the different isotopes. In particular, LUNA is now measuring $^{17}$O(p,$\gamma$)$^{18}$F, the bridge reaction connecting the second to the third CNO cycle and $^{2}$H($\alpha$,$\gamma$)$^{6}$ Li, the key reaction of big-bang nucleosynthesis which determines the amount of primordial $^{6}$Li in the Universe.

## 5. Helium Burning

LUNA has shown the advantages of the low background environment on the study of the hydrogen burning processes at the stellar energies. Natural evolution is the exploitation of the underground environment to study the next step in the fusion chain towards $^{56}$Fe (the element with the highest binding energy per nucleon): the helium burning. In particular, $^{12}$C($\alpha$,$\gamma$)$^{16}$O, the "Holy Grail" of nuclear astrophysics, which determines the abundance ratio between carbon and oxygen, the two key elements to the development of life. This abundance ratio shapes the nucleosynthesis in massive stars up to the iron peak and the properties of supernovae. Of great significance are also $^{13}$C($\alpha$,n)$^{16}$O and $^{22}$Ne($\alpha$,n)$^{25}$Mg, the stellar sources of the neutrons which synthesize most of the trans-iron elements through the S-process: neutron captures followed by $\beta$ decays. This exciting and ambitious program requires a dedicated space of about 150 m$^2$ where to install a 3.5 MV accelerator in an underground laboratory. A letter of intent has been submitted to LNGS in 2007, a possible place to host the accelerator has been identified and a proposal will be ready soon. We are confident that the study of helium burning will be the next step of underground nuclear astrophysics.

## 6. Conclusions

LUNA started underground nuclear astrophysics twenty years ago in the core of Gran Sasso, below 1400 meters of dolomite rock. The extremely low background has allowed nuclear physics experiments with very small count rate, down to a few events per year. The impor-

tant reactions responsible for the hydrogen burning in the Sun have been studied for the first time down to the relevant stellar energies. In particular, the measurement of $^3$He($^3$He,2p)$^4$He has shown that nuclear physics was not the origin of the solar neutrino puzzle. The cross section of $^3$He$(\alpha,\gamma)^7$Be has been measured with two different experimental approaches and with a 4% total error. Thanks to this small error, the total uncertainty on the $^7$Be solar neutrino flux has been reduced to 5.5%. Finally, the study of $^{14}$N(p,$\gamma$)$^{15}$O has shown that the expected CNO solar neutrino flux has to be decreased by about a factor two, with an error small enough to pave the way to the measurement of the central metallicity of the Sun. When applied to stars more evolved than the Sun our cross section measured has increased by 0.7-1 billion years the age of the Universe and made more efficient the dredge-up of carbon to the surface of asymptotic giant branch stars. Over the years LUNA has experienced the important progress achievable in the comprehension of the hydrogen burning thanks to the underground environment. In the next two decades underground nuclear astrophysics will try to improve the picture of stellar nucleosynthesis by studying the key processes of the helium burning inside the stars.


1. C.E. Rolfs and W.S. Rodney, *Cauldrons in the Cosmos* (The Univ. of Chicago Press, 1988).
2. M. Junker *et al.*, Phys. Rev. C **57**, 2700 (1998).
3. R.Bonetti *et al.*, Phys. Rev. Lett. **82**, 5205 (1999).
4. A. Krauss *et al.*, Nucl. Phys. A **467**, 273 (1987).
5. M. Dwarakanath and H. Winkler, Phys. Rev. C **4**, 1532 (1971).
6. N. Kudomi *et al.*, Phys. Rev. C **69**, 015802 (2004).
7. F. Confortola *et al.*, Phys. Rev. C **75**, 065803 (2007).
8. C.Formicola *et al.*, Phys. Lett. B **591**, 61 (2004).
9. G. Imbriani *et al.*, Eur. Phys. J.A **25**, 455 (2005).
10. A. Lemut *et al.*, Phys. Lett. B **634**, 483 (2006).
11. E.G. Adelberger *et al.*, Rev. Mod. Phys. **70**, 1265 (1998).
12. C. Angulo *et al.*, Nucl. Phys. A **656**, 3 (1999).
13. W.A.S. Lamb and R.E. Hexter, Phys. Rev. **108**, 1304 (1957).
14. U. Schroder *et al.*, Nucl. Phys. A **467**, 240 (1987).
15. M. Marta *et al.*, Phys. Rev. C **78**, 022802 (2008).

16. C. Pena-Garay and A.M. Serenelli, arXiv: 0811.2424
17. W.C. Haxton and A.M. Serenelli, arXiv: 0902.0036
18. G. Imbriani *et al.*, Astronomy and Astrophysics **420**, 625 (2004).
19. F. Herwig and S.M. Austin, Astrophysical Journal **613**, L73 (2004).
20. D. Bemmerer *et al.*, J. Phys. G: Nucl. Part. Phys. **36**, 045202 (2009).
21. B. Limata *et al.*, Phys. Rev. C **82**, 015801 (2010).

# OVERVIEW OF THE CMS EXPERIMENT RESULTS

Silvia Costantini
on behalf of the CMS Collaboration

*Departement of Physics and Astronomy, University of Ghent, Ghent, Belgium*
*Postal address: CERN-PH-EP, CH-1211 Geneva 23, Switzerland*

**Abstract**

The CMS experiment at the Large Hadron Collider has collected more than 2 $fb^{-1}$ at the center-of-mass energy of 7 TeV, with peak values of the instantaneous luminosity reaching $2 \times 10^{33}$ $cm^{-2}\,s^{-1}$. Recent running has seen an increase in the average number of interactions per bunch crossing, testing the capabilities of the acquisition and trigger systems. Selected CMS results are presented from the proton-proton run, with approximately 1 $fb^{-1}$, including results on high cross-section Standard Model processes and on searches for new physics.

## 1. Introduction

The Large Hadron Collider (LHC) has become operational in 2009. High-energy physics runs took place in 2010 and 2011 [1], with proton-proton collisions at a center-of-mass energy of 7 TeV and peak values of the instantaneous luminosity reaching, at the time of this conference, $2 \times 10^{33}$ $cm^{-2}\,s^{-1}$. Six experiments are currently operating at the LHC: two so-called omni-purpose detectors, ATLAS [2] and CMS [3, 4], which are performing a general research program, two dedicated detectors, ALICE [5] and LHCb [6], specifically designed for heavy-ion physics and b-physics, respectively, and two special purpose experiments: TOTEM [7] and LHCf [8]. The CMS Collaboration consists of over 3000 scientists, engineers and graduate students from 173 institutes spanning 40 Countries.

Heavy Flavour physics, Top physics and Higgs searches are not discussed in this note as they have been reported in separated talks and can be found elsewhere in these proceedings [9]. Public CMS results are available at [10]. Only a selection will be discussed in the following.

## 2. The CMS Detector

The central feature of the CMS detector [4] is a superconducting solenoid, of 6 m internal diameter, providing a field of 3.8 T. Within the field volume are the silicon pixel and strip tracker, the lead-tungstate crystal electromagnetic calorimeter (ECAL), and the brass-scintillator hadron calorimeter (HCAL). Muons are measured in gas-ionization detectors embedded in the steel return yoke. In addition to the barrel and endcap detectors, CMS has extensive forward calorimetry, assuring very good hermeticity with pseudorapidity coverage up to high values ($|\eta| < 5$).

The electromagnetic calorimeter (ECAL) contains 75 848 lead tungstate ($PbWO_4$) crystals (25.8 $X_0$ long in the barrel, 24.7 $X_0$ long in the endcaps). Scintillating crystals are the most precise calorimeters for energy measurements and they provide excellent energy resolution over a wide range, as well as high detection efficiency for low energy electrons and photons. The ECAL has an energy resolution of better than 0.5% above 100 GeV. The 15K-channel HCAL, when combined with the ECAL, measures jets with a resolution $\Delta E/E \sim 100\%/\sqrt{E} \oplus 5\%$.

Muons with pseudorapidity in the range $|\eta| < 2.4$ are measured with detection planes made of three technologies: Drift Tube chambers (DT), Cathode Strip Chambers (CSC) and Resistive Plate Chambers (RPC). The readout has nearly 1 million electronic channels. Matching the muons to the tracks measured in the silicon tracker should result in a transverse momentum ($p_T$) resolution between 1 and 5 %, for $p_T$ values up to 1 TeV.

The inner tracker measures charged particles within the $|\eta| < 2.5$ pseudorapidity range. It consists of 1440 silicon pixel and 15 148 silicon strip detector modules, chosen for their radiation hardness and small amount of material, corresponding to about 30% of the radia-

tion length $X_0$. The tracking system provides an impact parameter resolution of the order of 5 $\mu$m and a transverse momentum resolution of about 1.5% for 100 GeV particles.

## 3. Recent Operation

As of the end of August 2011, CMS has recorded 2.27 $fb^{-1}$out of 2.52 $fb^{-1}$delivered by the LHC, for an efficiency of 90%. Roughly 90% of the recorded data has been certified as "golden" for all physics analysis. An average of 98% of the subdetector channels are operational and in the readout. One of the key challenges for the LHC experiments is reducing the O(10 MHz) collision rate to O(100 Hz). At CMS, the first-level (L1) trigger is implemented in hardware, and it combines information from the calorimeters and muon systems to accept less than 100 kHz of events. The High Level Trigger (HLT) system is implemented in software, allowing an enormous flexibility, and selects roughly 300 Hz of events to store for offline physics analysis. The number of bunches in the LHC was slowly increased over the 2011 run, culminating in $\sim$ 1300 bunches colliding in CMS. Since July 2011, the luminosity has been steadly increased, resulting in an increase of the number of proton-proton interactions per bunch crossing ("pile-up"), with more than 10 interactions per bunch crossing at the luminosities of Summer 2011.

CMS finds that the mean number of reconstructed vertices stays linear as a function of luminosity per bunch. The efficient reconstruction of vertices separated by as little as 1 mm allows for offline objects such as jets and isolated leptons to be corrected event-by-event for pileup effects by removing contamination from vertices not associated with the physics process of interest. To ensure a high level of physics performance, it is important to maintain low trigger thresholds even with increasing pileup. This is achieved also by forming triggers from combinations of multiple objects, for example multiple leptons and isolated leptons, instead of a single lepton.

## 4. Soft QCD and Jet Physics

Using minimum bias events CMS has measured the average transverse momentum and pseudo-rapidity distributions of charged tracks down

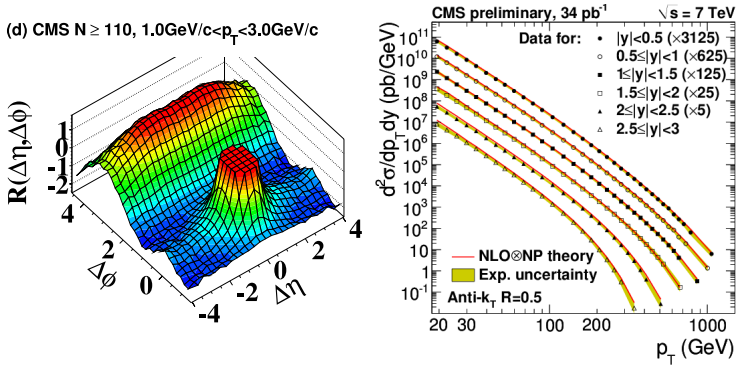


Fig. 1: Left: Two-dimensional two-particle correlation function, for $\sqrt{s} = 7$ TeV, for high multiplicity ($N > 110$) events with $1 < p_{\mathrm{T}} < 3$ GeV. The sharp near-side peak from jet correlations is cut off in order to better illustrate the structure outside that region. Right: Inclusive jet differential cross section, as a function of $p_{\mathrm{T}}$, for six different rapidity intervals, scaled by the factors shown in the legend for easier viewing. The next-to-leading-order (NLO) theoretical predictions, corrected for nonperturbative (NP) effects via multiplicative factors, are superimposed. The statistical uncertainties are smaller than the symbol used to represent each data point

to very low transverse momentum ($p_{\mathrm{T}} \simeq 50$ MeV), in a large pseudo-rapidity interval ($|\eta| < 2.5$) for three different collision energies (0.9, 2.36 and 7 TeV) [13]. The data are corrected for trigger and event selection efficiency, for effects of tracking inefficiency and secondary tracks originating from the decay of long-lived particles and for products of interactions with the beam pipe and the detector material. At higher energies we observe an increase in the density of particles in data stronger than in model predictions. In high multiplicity events, a pronounced structure [14] emerges in the two-dimensional correlation function for particle pairs with intermediate $p_{\mathrm{T}}$ of 1-3 GeV, $2.0 < |\Delta\eta| < 4.8$ and $\Delta\phi \sim 0$. This is the first observation of such a long-range, near-side feature in two-particle correlation functions in pp or $p\bar{p}$ collisions. (Fig. 1, left).

Inclusive jet $p_{\mathrm{T}}$ spectra have been produced for all three jet approaches used in CMS, i.e. based on the purely calorimetric information; based on the information of the charged particles associated to jets, as reconstructed by the tracker, to improve the measurements of

the calorimeters; combining all information available from the various sub-detectors (Particle-Flow or PF). The measured cross sections are found to be in agreement with next-to-leading order perturbative QCD calculations, within the experimental and theoretical uncertainties [15]. With the PF approach the distributions can be extended to a low $p_{\mathrm{T}}$ value of 18 GeV (Fig. 1, right).

## 5. Electroweak Bosons and Di-bosons

The production of the electroweak gauge bosons in pp collisions proceeds mainly via the weak Drell-Yan (DY) process consisting of the annihilation of a quark and an antiquark. The production process pp $\rightarrow$ W + X is dominated by $u\bar{d} \rightarrow W^+$ and $d\bar{u} \rightarrow W^-$, while pp $\rightarrow$ Z + X is dominated by $u\bar{u}$ and $d\bar{d} \rightarrow$ Z. Events containing W and Z bosons produce very clean signals and provide unique samples to calibrate and understand the CMS detector response to leptons, jets and missing energy. In addition, the excellent level of theoretical and experimental understanding of these processes allows electroweak tests at the LHC at an unprecedented level of precision. CMS uses a wide range of final states to measure cross sections, asymmetries, polarizations and differential distributions in general.

### 5.1. W and Z production

W events are selected [12] by using a loose single-lepton (electron or $\mu$) trigger. Leptons are required to have $p_{\mathrm{T}} > 25$ GeV and pseudorapidity $\eta$ within the trigger fiducial volume. Lepton isolation is enforced by requiring low tracker and calorimeter activities within a cone of $\Delta R = \sqrt{(\Delta\eta)^2 + (\Delta\phi)^2} < 0.3$. Events with a second lepton are vetoed to suppress the Drell-Yan background. The W signal yield is extracted from a fit to the missing transverse energy ($E_{\mathrm{T}}$) distributions of the events passing the selection criteria. Separate fits to missing $E_{\mathrm{T}}$ spectra in events containing positive and negative leptons allow to extract $\sigma(W^+)$ and $\sigma(W^-)$. Luminosity uncertainties cancel in their ratio. The selection of Z events [12] requires pairs of isolated leptons with $p_{\mathrm{T}} > 20\,(25)$ GeV for $Z \rightarrow \mu^+\mu^-$ or $Z \rightarrow e^+e^-$, respectively, and $\eta$ within the fiducial detector and trigger acceptances. The invariant mass of the two leptons is required to be in

the range 60–120 GeV for signal extraction, which is performed via a simultaneous fit of the Z signal yield and efficiencies. Theoretical uncertainties affect acceptance determinations. In particular, the PDF uncertainty, the modeling of initial-state radiation, higher-order QCD effects, electroweak corrections, final-state radiation, and factorization and renormalization scale.

The inclusive W and Z production cross sections times branching ratios (B) at a center-of-mass energy of 7 TeV are determined as:

$$\sigma(pp \to WX) \times B(W \to \ell\nu) = 10.31 \pm 0.02(\text{stat.}) \pm 0.09(\text{syst.}) \pm 0.10(\text{th.}) \pm 0.41(\text{lumi.}) \text{ nb}, \quad (1)$$

$$\sigma(pp \to ZX) \times B(Z \to \ell^+\ell^-) = 0.974 \pm 0.007(\text{stat.}) \pm 0.007(\text{syst.}) \pm 0.018(\text{th.}) \pm 0.039(\text{lumi.}) \text{ nb}. \quad (2)$$

Good overall agreement of the inclusive cross section measurements and their ratios with theoretical predictions at NNLO is found.

The Berends-Giele scaling has been tested measuring the ratios $\sigma(V + n\text{jets})/\sigma(V + (n-1)\text{jets})$, confirming that the ratio is approximately independent on the number of jets $n$. The ratio as a function of n has been parametrized as $\alpha + \beta \times n$. The fitted values for $\alpha$ and $\beta$ give the latter close to zero, as expected.

### 5.2. Diboson production

First measurements of the WZ and ZZ production cross sections at 7 TeV, and updated measurements of the WW cross section have been performed with 2011 data.Results are based on data corresponding to an integrated luminosity of 1.1 fb$^{-1}$. The leptonic decay modes of the W and Z bosons are considered and the final states include electrons, muons, taus and missing transverse energy. The following cross sections are determined:

$$\sigma(pp \to W^+W^- + X) = 55.3 \pm 3.3(\text{stat.}) \pm 6.9(\text{syst.}) \pm 3.3(\text{lumi.}) \text{ pb}, \quad (3)$$

$$\sigma(pp \to WZ + X) = 17.0 \pm 2.4(\text{stat.}) \pm 1.1(\text{syst.}) \pm 1.0(\text{lumi.}) \text{ pb}, \quad (4)$$

$$\sigma(pp \to ZZ + X) = 3.8 \pm 1.5(\text{stat.}) \pm 0.2(\text{syst.}) \pm 0.2(\text{lumi.}) \text{ pb}. \quad (5)$$

The measured cross sections are found to be consistent with the Standard Model.

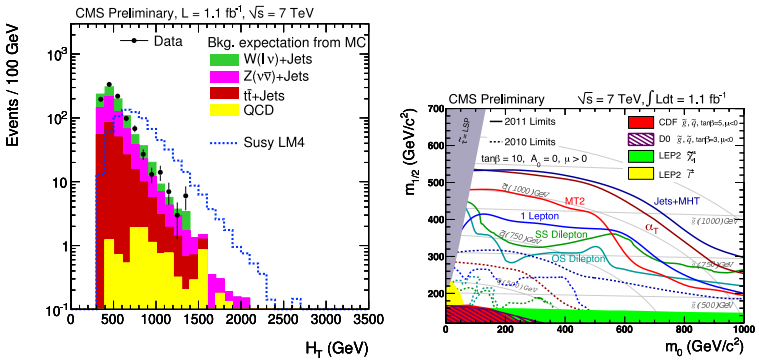


Fig. 2: Left: Distribution of the missing transverse energy in the inclusive hadronic SUSY search. Right: Summary of the excluded regions at 95% C.L. in the $m_{1/2} - m_0$ plane of the CMSSM, with $\tan\beta = 10$, $A_0 = 0$ and positive $\mu$

## 6. Searches for New Physics

Plenty of new CMS results are available with a data sample of about 1 fb$^{-1}$ [16]. Searches in CMS focus on very different topologies and emphasize complementarity between analyses, with a large variety of signatures. The use of several kinematic observables and well understood "objects" (leptons, photons, jets, missing transverse energy) allows to exploit the detector strong assets and drive the search strategies.

### 6.1. SUSY Searches

Results include hadronic searches and signatures with one or more (same-sign or opposite-sign) leptons, or photons. Data-driven background estimation is emphasized, to avoid reliance on the tails of SM MC distributions. A variety of methods are used, although they generally involve using a control sample for each background to extract an estimate for the search region. All SUSY searches find data in agreement with the SM background expectations. A representative distribution from SUSY searches is shown in Fig. 2 (left), while Fig. 2 (right) shows a combined summary of several searches in the $m_{1/2} - m_0$ plane of CMSSM.

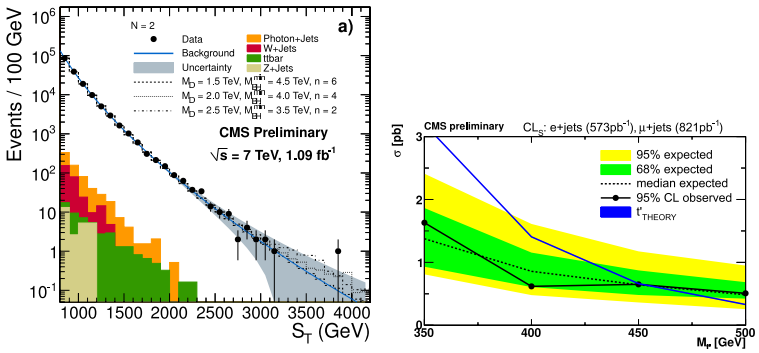


Fig. 3: Left: Total transverse energy ST, for events with the multiplicity of N = 2 objects in the final state. The shaded band is the background prediction obtained from data (solid line) with its uncertainty. Non-multijet backgrounds are shown as colored histograms. Also shown is the predicted black hole signal for three different parameter sets. Right: Observed and expected limits, at 68% and 95% C.L., for e+jets and mu+jets channels combined. The integrated luminosity is 573 $pb^{-1}$for the electron channel and 821 $pb^{-1}$for the muon channel

## 6.2. Exotica Searches

Among the large variety of exotica analyses, the searches for microscopic Black Holes are performed by requiring the spectacular presence presence of multiple energetic jets. leptons, and photons, plus large total transverse energy (Fig. 3, left). A good agreement with the expected Standard Model backgrounds, dominated by QCD multijet production, has been observed for various multiplicities of the final state. Stringent model-independent limits on new physics production in high-multiplicity energetic final states have been set, along with model-specific limits on semi-classical black hole masses in the 4-5 TeV range for a variety of model parameters.

The existence of a fourth generation of elementary fermions, a new replica of the known three generations of chiral matter, may provide a sufficiently large CP violation and may account as well for the asymmetry between matter and antimatter. Provided the mass difference between the fourth generation quarks $t'$ and $b'$ is lower than the W mass, their existence is not excluded by precision electroweak measurements. Furthermore, within the framework of the Standard Model, the $t'$ and $b'$ masses are constrained to be below approximately

550 GeV by unitarity conditions. The possible phenomenology of fourth generation quarks is discussed in [17].

Fourth generation $b'$ and $t'$ quarks are extensively searched for in CMS. The $t'$ quarks are assumed to decay to a W boson and a $b$ quark, with subsequent semileptonic or dileptonic decays of the WW pair. Assuming strong pair production of $t'$ quarks, lower limits are set on the $t'$ quark mass in the range 420-450 GeV at 95% confidence level.

## 7. Conclusions

The CMS experiment is in good operating conditions and has proved to be able to cope well with the challenge of instantaneous luminosity values higher than $10^{33}$ cm$^{-2}$ s$^{-1}$. No evidence of new physics has been obtained so far. Plenty of new results are being published by the CMS Collaboration.

### Acknowledgments

Acknowledgments of support of all CMS are given in Ref. [4] and [12–15].

1. The Large Hadron Collider home page: http://lhc.web.cern.ch/lhc/ contains also general and outreach information. The LHC schedule can be found here: http://lhc-commissioning.web.cern.ch/lhc-commissioning/.
2. A Toroidal LHC Apparatus, Technical Proposal, CERN/LHCC 94-43 (1994).
3. The Compact Muon Solenoid, Technical Proposal, CERN/LHCC 94-38 (1994).
4. CMS Collaboration, "The CMS Experiment at the CERN LHC, 2008 JINST 3 S08004, http://iopscience.iop.org/1748-0221/3/08/S08004; CMS Physics TDR Volume 1, Detector Performance and Software, CERN/LHCC 2006-001.
5. F. Carminati *et al.*, J. Phys. G: Nucl. Part. Phys. **30**, 1517 (2004) and references therein.
6. The Large Hadron Collider beauty experiment, Technical Proposal, CERN/LHCC 98-04 (1998).
7. Total Cross Section, Elastic Scattering and Diffraction Dissociation at the LHC, The TOTEM Collaboration, "The TOTEM Experiment at the CERN Large Hadron Collider", http://iopscience.iop.org/1748-0221/3/08/S08007.

8. Forward production of neutral particles in proton-proton collisions at extremely low angles. The LHCf Collaboration, "The LHCf detector at the CERN Large Hadron Collider", http://iopscience.iop.org/1748-0221/3/08/S08006.

9. Antonio Branca, Higgs searches at CMS, these proceedings; Jérémie Lellouch, Top quark pair cross-section measurement using CMS data at 7 TeV, *ibid.*; Nicola Pozzobon, Heavy-Flavour Physics with the CMS Experiment, *ibid.*.

10. CMS public Physics Results are available at: http://twiki.cern.ch/twiki/bin/view/CMSPublic/PhysicsResults.

11. K. Nakamura *et al.* (Particle Data Group), J. Phys. G **37**, 075021 (2010) and 2009 web edition on http://pdg.lbl.gov/.

12. CMS Collaboration, arXiv:1107.4789, CMS-EWK-10-005, J. High Energy Phys. **10**, 132 (2011).

13. CMS Collaboration, arXiv:1105.3299, CMS-QCD-10-006, Phys. Rev. Lett. **105**, 022002 (2010).

14. CMS Collaboration, arXiv:1009.4122, CMS-QCD-10-002, J. High Energy Phys. **09**, 091 (2010).

15. CMS Collaboration, arXiv:1106.0208, CMS-QCD-10-011, Phys. Rev. Lett. **107**, 132001 (2011).

16. Public CMS results on searches for New Physics are available at: http://twiki.cern.ch/twiki/bin/view/CMSPublic/PhysicsResultsSUS and http://twiki.cern.ch/twiki/bin/view/CMSPublic/PhysicsResultsEXO.

17. G.D. Kribs, T. Plehn, M. Spannowsky, and T.M.P. Tait, Phys. Rev. D **76**, 075016 (2007); P.H. Frampton, P.Q. Hung, and M. Sher, Phys. Repts. **330**, 263 (2000). P.Q. Hung, and M. Sher, Phys. Rev. D **77**, 037302 (2007).

# RESULTS OF THE BES-III EXPERIMENT

I. Denysenko[1,2]

[1] *Joint Institute for Nuclear Research,*
[2] *Bogolyubov Institute for Theoretical Physics, Kiev, Ukraine*

**Abstract**

The BES-III experiment successfully takes data since 2009. For at least next ten years it will remain the world leading experiment in the $\tau$-charm domain. Here the status of the BES-III experiment is presented and the recent results in charmonium physics and light hadron spectroscopy are reviewed.

## 1. The BEPC-II/BES-III Project

BEPC-II/BES-III is a major upgrade of the BES-II experiment at the Institute of High Energy Physics CAS in Beijing. The BEPC-II is a double-ring $e^+e^-$ collider providing $e^+e^-$ beams in the energy range of $\sqrt{s} = (2 - 4.6)$ GeV and a design peak luminosity of $10^{33}$ cm$^{-2}$s$^{-1}$. The BES-III apparatus [1] is a new high performance general purpose detector for measurements in the $\tau$-charm energy region. It consists of the following main components: a helium-based Main Drift Chamber, a plastic scintillator Time-of-Flight system, a CsI(Tl) Electromagnetic Calorimeter, and a Muon Counter. Acceptance of charged particles and photons is 93% of $4\pi$, and the charged particle momentum and photon energy resolutions at 1 GeV are 0.5% and 2.5% respectively.

The physics data taking started in March of 2009 and so far BES-III has collected the world largest data samples of $J/\psi$ data (225M events), $\psi'$ data ($106M$ events), $\psi(3770)$ data (2.9 fb$^{-1}$) data and a

unique sample of $\psi(4010)$ data (0.5 fb$^{-1}$). The achieved peak luminosity is $0.65 \times 10^{33}$ cm$^{-2}$s$^{-1}$.

The main goals of the experiment are precision measurements in the $\tau$-charm domain that are possible with unprecedentedly high statistics to be accumulated [2].

The most interesting results are discussed in the next section.

## 2. Physics Results

### 2.1. Light hadron spectroscopy

#### *2.1.1. The $p\bar{p}$ near threshold enhancement in $J/\psi \to \gamma p\bar{p}$*

The anomalously strong enhancement in the $p\bar{p}$ invariant mass was first observed by BES-II collaboration in $J/\psi \to \gamma p\bar{p}$ [3]. Its important peculiarity is that it is not clearly seen in $\psi(2S) \to \gamma p\bar{p}$, $\Upsilon \to \gamma p\bar{p}$ and $\psi(2S) \to \omega p\bar{p}$, making unlikely a possibility for it to be a pure final state interaction (FSI) effect. There are different speculations on its nature and the most intriguing one is that it comes from a $p\bar{p}$ bound state, sometimes called baryonium.

The huge statistics of the BES-III experiment allows to perform a detailed study of this structure. The first published results [4] on $\psi(2S) \to \pi^+\pi^- J/\psi(J/\psi \to \gamma p\bar{p})$ confirms BES-II observation (see Fig. 1). In the analysis the data are fitted under assumption that the enhancement is produced by a S-wave state, giving $M = 1861^{+6\ +7}_{-13-26}$ MeV, $\Gamma \leq 38$ MeV at 90% C.L.

Recently a study of $J/\psi \to \gamma p\bar{p}$ has been performed. The preliminary results of partial wave analysis show that preferable quantum numbers are $0^{-+}$ and that the data description is significantly improved if FSI corrections are taken into account. The preliminary fit results are: $M = 1832.5 \pm 5(\text{stat})^{+15}_{-17}(\text{syst}) \pm 19(\text{mod})$ MeV and $\Gamma < 45$ MeV at 90% C.L.

#### *2.1.2. X(1835), X(2120) and X(2370) in $J/\psi \to \gamma\pi^+\pi^-\eta'$*

The state X(1835), decaying to $\pi^+\pi^-\eta'$, was discovered by the BES-II collaboration in the $J/\psi$ radiative decay [5]. The study was motivated by an observation of the $p\bar{p}$ near threshold enhancement dis-

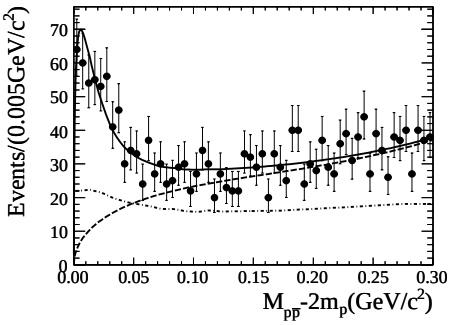


Fig. 1: The $p\bar{p}$ invariant mass for $\psi' \to \pi^+\pi^- J/\psi$, $J/\psi \to \gamma p\bar{p}$ is shown. The solid line is the fit result, the dashed line is a background function and the dash-dotted indicates variation of an acceptance

cussed above. Its possible interpretations include a $p\bar{p}$ bound state, a glueball, a radial excitation of $\eta'$ meson etc.

The BES-III analysis of this channel [6] confirms BES-II and reports an observation of two new states X(2120) and X(2370). The results of the fit to the $\pi^+\pi^-\eta'$ invariant mass spectrum are given in the Table 1. An important note is that the fit doesn't take into account a possible interference. The photon angular distributions for X(1835) are consistent with expectations for a pseudoscalar, but other possibilities are not excluded.

To determine spins, parities and to get more precise measurements of these states a partial wave analysis is needed, which will be possible as much higher statistics is available.

### *2.1.3. X(1870) and $\eta(1405)$ in $J/\psi \to \omega(\pi^+\pi^-\eta)$*

The decay $J/\psi \to \omega(\pi^+\pi^-\eta)$ can be used to study $\eta(1405)$ production mechanism and a possible production of $X(1835)$ that is important for a glueball search.

**T a b l e 1: Analysis results for $J/\psi \to \gamma\pi^+\pi^-\eta'$**

| resonance | $M$(MeV) | $\Gamma$(MeV) | stat. sign. |
|---|---|---|---|
| X(1835) | $1836.5 \pm 3.0^{+5.6}_{-2.1}$ | $190.1 \pm 9.0^{+38}_{-36}$ | $20\sigma$ |
| X(2120) | $2122.4 \pm 6.7^{+4.7}_{-2.7}$ | $83 \pm 16^{+31}_{-11}$ | $7.2\sigma$ |
| X(2370) | $2376.3 \pm 8.7^{+3.2}_{-4.3}$ | $83 \pm 17^{+44}_{-6}$ | $6.4\sigma$ |

The BES-III collaboration reports an observation of new process $J/\psi \to \omega X(1870)$, $X(1870) \to a_0^{\pm}\pi^{\mp}$ with the statistical significance more than $7.2\sigma$ [7]. Also in the lower $\pi^+\pi^-\eta$ mass region clear signals of $f_1(1285)$ and $\eta(1405)$ are seen and corresponding branching ratios measured for the first time. The $\pi^+\pi^-\eta$ mass spectra fit is performed under assumption of no interference resulting in $M = 1877.3 \pm 6.3^{+3.4}_{-7.4}$ MeV and $\Gamma = 51 \pm 12^{+19}_{-4}$ MeV. With the current statistics it is impossible to distinguish whether X(1870) is due to $X(1835)$, $\eta_2(1870)$, interference of both or is a new state. Further study using PWA will be performed as more $J/\psi$ data are accumulated.

## 2.2. Charmonium spectrum and transitions

The charmonium spectrum and transitions are a perfect laboratory to test various QCD models and phenomenological mechanisms. Due to an interplay of perturbative and non-perturbative effects they allow one to study QCD beyond the perturbative regime.

### *2.2.1. $h_c$ in $\psi' \to \pi^0 h_c$*

The $h_c$ is the least studied charmonium state below $D\bar{D}$ threshold. The precise measurement of its mass allows one to calculate a hyperfine 1P mass splitting $\Delta M_{hf} = \langle M(^3P_J)\rangle - M(^1P_1)$, where $\langle M(^3P_J)\rangle = \frac{1}{9}(M_{\chi_{c0}} + 3M_{\chi_{c1}} + 5M_{\chi_{c2}})$. This may give a hint to a spin-spin interaction of heavy quarks. Also the $Br(\psi' \to \pi^0 h_c)$ is a measure of an isospin violation in hadronic decays.

At BES-III $\psi' \to \pi^0 h_c$ is studied both exclusively and inclusively via registeration of a E1 photon from the $h_c \to \gamma\eta_c$ decay [8]. Fits to the $\pi^0$ recoil mass (see Fig. 2) allow one to measure a branching ratio for the $\psi' \to \pi^0 h_c$ decay and width of $h_c$ for the first time. Combining results of inclusive and exclusive channels one obtains the first measurement of $Br(h_c \to \gamma\eta_c)$. These values a found to be $Br(\psi' \to \pi^0 h_c) = (8.4 \pm 1.3 \pm 1.0) \times 10^{-4}$, $\Gamma(h_c) = 0.73 \pm 0.45 \pm 0.28$ MeV and $Br(h_c \to \gamma\eta_c) = (54.3 \pm 6.7 \pm 5.2) \times 10^{-2}$.

### *2.2.2. $\eta_c$ resonance parameters from $\psi' \to \gamma\eta_c$*

Despite $\eta_c$ has been known for a long time its mass and width are known by an order of magnitude worser then for $J/\psi$, $\psi'$ and $\chi_{cJ}$. Be-

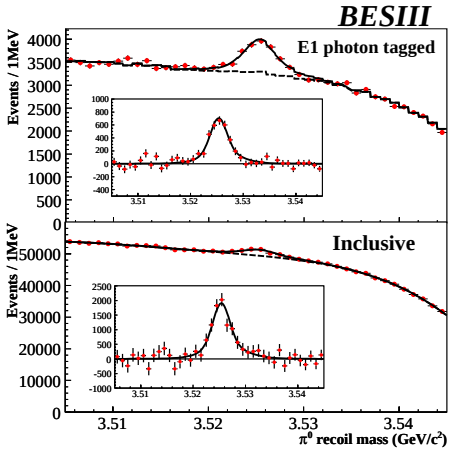


Fig. 2: The $\pi^0$ recoil mass (top – inclusive analysis, bottom – exclusive analysis). Fits are shown with a solid line and backgrounds with a dashed one

sides there are significant discrepancies in the $\eta_c$ mass measurements between earlier experiments with radiative $J/\psi$ transitions and recent studies with two photon processes.

In the BES-III inclusive analysis $\eta_c$ is reconstructed from six hadron modes $K_S K\pi$, $KK\pi^0$, $2K2\pi\pi^0$, $\pi\pi\eta$, $K_S K3\pi$, $6\pi$. The simultaneous fit to the mass spectrum takes into account the interference between $\eta_c$ signal and non-$\eta_c$ decays (treated as $0^{-+}$ component). The interference phases for different modes are found to be consistent with the same value and a single parameter is used in the final fit. Two solutions of relative phase are found, one for constructive interference and the other for destructive, however $\eta_c$ mass and width remain unchanged regardless which solution is taken. It yields $M = 2984.3 \pm 0.6 \pm 0.6\,\text{MeV}$, $\Gamma = 32.0 \pm 1.2 \pm 1.0\,\text{MeV}$ that is currently the world best measurement, being consistent with two-photon production and $J/\psi \to \gamma\eta_c$ result by CLEO collaboration. This result is preliminary.

### *2.2.3. M1 transition $J/\psi \to \gamma\eta_c(2S)$*

The $\eta_c(2S)$ state is observed for the first time in charmonium decays at BES-III. The $K_S K\pi$ invariant mass spectrum (see Fig. 3) is

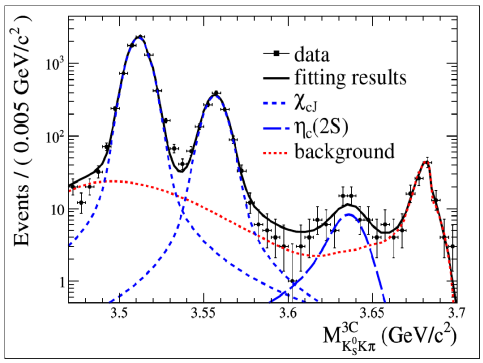


Fig. 3: The $\eta_c(2S)$ signal from the $K_S K\pi$ invariant mass spectrum

fitted with $\chi_{cJ}$, $\eta_c(2S)$ and background contributions. The $\eta_c(2S)$ significance is found to be greater $5\sigma$. This result is preliminary.

## 2.3. Charmonium decays

### *2.3.1. $\psi' \to \gamma P$, $(P = \pi^0, \eta, \eta')$*

The radiative decay $\psi'$ to a pseudoscalar is important for testing various phenomenological mechanisms like vector meson dominance, the $\eta_c - \eta^{(\prime)}$ mixing, two-gluon couplings $q\bar{q}$ states and a final state radiation by light quarks.

The BES-III reports the first evidence for $\psi' \to \gamma\pi^0$, $\psi' \to \gamma\eta$ and a new measurement of $\psi' \to \gamma\eta'$ [9] (see Table 2).

The ratio $R_X = \frac{Br(X\to\gamma\eta)}{Br(X\to\gamma\eta')}$, where $X$ is $J/\psi$ or $\psi'$, can be predicted from the first order perturbation theory: it is expected that $R_{\psi'} \approx R_{J/\psi}$. Recently, CLEO collaboration reported $R_{\psi'} \ll R_{J/\psi}$, with $R_{\psi'} \leq 1.8\%$ at 90% C.L. and $R_{J/\psi} = (21.1 \pm 0.9)\%$ [10]. The BES-III analysis yields $R_{\psi'} = (1.10 \pm 0.38 \pm 0.07)\%$, confirming the CLEO result. Such a small $R_{\psi'}$ value challenges our understanding of charmonium states.

**Table 2: $\psi' \to \gamma P$ $(P = \pi^0, \eta, \eta')$**

| decay channel | $Br(\times 10^{-6})$ | $Br^{\rm PDG}(\times 10^{-6})$ [14] | sign. |
|---|---|---|---|
| $\psi' \to \gamma\pi^0(\gamma\gamma)$ | $1.58 \pm 0.40 \pm 0.13$ | $\leq 5$ | $4.6\sigma$ |
| $\psi' \to \gamma\eta(3\pi)$ | $1.38 \pm 0.48 \pm 0.09$ | $\leq 2$ | $4.3\sigma$ |
| $\psi' \to \gamma\eta(\pi^+\pi^-\eta, \gamma\pi^+\pi^-)$ | $126 \pm 3 \pm 8$ | $121 \pm 8$ | |

### 2.3.2. $\chi_{cJ} \to \gamma V$, $V = (\rho, \omega, \varphi)$

Doubly radiative decays $\psi' \to \gamma\chi_{cJ}$, $\chi_{cJ} \to \gamma V$, where $V$ is one of $\rho^0$, $\phi$ and $\omega$ mesons, provide information on the flavour content of $\chi_{cJ}$ states and on the gluon hadronization dynamics in this process. Remarkably the branching ratios of these channels measured by CLEO collaboration [11] appeared to be much larger than ones predicted by the theory.

The BES-III collaboration presents [12] new measurements of $Br(\chi_{c1} \to \gamma\rho^0)$ and $Br(\chi_{c1} \to \gamma\omega)$, the first observation of $\chi_{c1} \to \gamma\varphi$ and upper limits for $\chi_{c0}$ and $\chi_{c2}$ decays to these final states. The branching ratios measured by BES-III are in agreement with CLEO results. It is also shown that decays $\chi_{c1} \to \gamma V$ are dominated by the longitudial component. The branching ratios of $\chi_{c1} \to \gamma V$ are shown in Table 3.

### 2.3.3. $\chi_{cJ} \to VV$, $V = (\omega, \varphi)$

Several modes of $\chi_{cJ}$ decays have been reported by BES-III: the first observation of $\chi_{c1} \to \varphi\varphi$, $\chi_{c1} \to \omega\omega$ and $\chi_{c0} \to \omega\varphi$; $4\sigma$ evidence for $\chi_{c1} \to \omega\varphi$ [13]. The precision of branching ratio measurements have been improved compared to the current world average values [14] (see Table 4).

The unexpectedly high branching ratios $\chi_{c1} \to VV$ indicate a significant violation of the helicity selection rule. In addition the measurements for $\chi_{cJ} \to \omega\varphi$ provides the first indication of the rate of doubly OZI suppressed $\chi_{cJ}$ decays.

## 3. Future Prospects

The BES-III running plan for 2012 is to collect 1 billion $J/\psi$ events and 0.7 billion $\psi'$. The preliminary program for 2013-2015 includes

**Table 3: $\psi' \to \gamma V$ ($V = \rho, \omega\, \varphi$)**

| decay channel | $Br(\times 10^{-6})$ | sign. |
|---|---|---|
| $\chi_{c1} \to \gamma\varphi$ | $25.8 \pm 5.2 \pm 2.3$ | $6\sigma$ |
| $\chi_{c1} \to \gamma\rho$ | $228 \pm 13 \pm 22$ | $> 10\sigma$ |
| $\chi_{c1} \to \gamma\omega$ | $69.7 \pm 7.2 \pm 6.6$ | $> 10\sigma$ |

**Table 4:** $\chi_{cJ} \to \varphi\varphi, \omega\omega, \omega\varphi$

| decay channel | $Br(\times 10^{-6})$ | $Br^{\rm PDG}(\times 10^{-6})$ [14] |
|---|---|---|
| $\chi_{c0} \to \varphi\varphi$ | $8.0 \pm 0.3 \pm 0.8$ | $9.2 \pm 1.9$ |
| $\chi_{c1} \to \varphi\varphi$ | $4.4 \pm 0.3 \pm 0.5$ | – |
| $\chi_{c2} \to \varphi\varphi$ | $10.7 \pm 0.3 \pm 1.2$ | $14.8 \pm 2.8$ |
| $\chi_{c0} \to \omega\omega$ | $9.5 \pm 0.3 \pm 1.1$ | $22.0 \pm 7.0$ |
| $\chi_{c1} \to \omega\omega$ | $6.0 \pm 0.3 \pm 0.7$ | – |
| $\chi_{c2} \to \omega\omega$ | $8.9 \pm 0.3 \pm 1.1$ | $19.0 \pm 6.0$ |
| $\chi_{c0} \to \omega\varphi$ | $1.2 \pm 0.1 \pm 0.2$ | – |
| $\chi_{c1} \to \omega\varphi$ | $0.22 \pm 0.06 \pm 0.02$ | – |
| $\chi_{c2} \to \omega\varphi$ | $< 0.2$ at 90% C.L. | – |

taking data at higher energies ($\psi(4170)$, R-scan), accumulating more than 20 fb$^{-1}$ data at $\psi(3770)$, acquiring data for $\tau$-physics.


1. M. Ablikim *et al.*, Nucl. Instrum. Meth. A **614**, 345 (2010).
2. D. M. Asner, T. Barnes, J. M. Bian, I. I. Bigi, N. Brambilla, I. R. Boyko, V. Bytev, K. T. Chao *et al.*, arXiv:0809.1869.
3. J.Z. Bai *et al.* (BES Collaboration), Phys. Rev. Lett. **91**, 022001 (2003).
4. M. Ablikim *et al.* (BES-III Collaboration), Chinese Physics C **34**(4) (2010).
5. M. Ablikim *et al.* (BES Collaboration), Phys. Rev. Lett. **95**, 262001 (2005).
6. M. Ablikim *et al.* (BES-III Collaboration), Phys. Rev. Lett. **106**, 072002 (2011).
7. M. Ablikim *et al.* (BESIII Collaboration), Phys. Rev. Lett. **107**, 182001 (2011).
8. M. Ablikim *et al.* (The BES-III Collaboration), Phys. Rev. Lett. **104**, 132002 (2010).
9. M. Ablikim, M. N. Achasov, L. An, Q. An, Z. H. An, J. Z. Bai, R. Baldini, Y. Ban *et al.*, Phys. Rev. Lett. **105**, 261801 (2010).
10. T. K. Pedlar *et al.* (CLEO Collaboration), Phys. Rev. D **79**, 111101 (2009).
11. J. V. Bennett *et al.* (CLEO Collaboration), Phys. Rev. Lett. **101**, 151801 (2008).
12. M. Ablikim *et al.* (BES-III Collaboration), Phys. Rev. D **83**, 112005 (2011).
13. M. Ablikim, M. N. Achasov, L. An, Q. An, Z. H. An, J. Z. Bai, R. Baldini, Y. Ban *et al.*, Phys. Rev. Lett. **107**, 092001 (2011).
14. K. Nakamura *et al.* (Particle Data Group), J. Phys. G **37**, 075021 (2010).

# RESULTS ON STANDARD MODEL AND HEAVY IONS PHYSICS OF ATLAS AT THE LHC

Frédéric Derue (on behalf the ATLAS Collaboration)

*LPNHE (UPMC, Université Paris-Diderot CNRS/IN2P3, Paris, France)*

**Abstract**

This document presents results of the ATLAS collaboration at the Large Hadron Collider at CERN on Standard Model and Heavy Ions physics. Proton-proton collisions were recorded at an energy $\sqrt{s} = 7$ TeV with a total integrated luminosity of 45 pb$^{-1}$ in 2010 and up to 1.1 fb$^{-1}$ in 2011. Several analysis are presented: the inclusive production cross sections of leptons, photons and jets, the production cross sections for $W^{\pm} \to l\nu$, $Z/\gamma^* \to ll$ and cross section measurements of dibosons. Results are compared to the predictions of perturbative QCD calculations and are in good agreement. Lead-lead collisions were recorded at an energy $\sqrt{s_{NN}} = 2.76$ TeV in 2010 with an integrated luminosity of 9.17 $\mu$b$^{-1}$. The document reports on the production of $W$ and $Z$ bosons and on an asymmetry in dijet production.

## 1. The ATLAS Detector and Data Taking

The ATLAS (A Toroidal LHC ApparatuS) detector [1][1] consists of an inner detector (ID) tracking system surrounded by a superconducting solenoid providing a 2 T magnetic field, electromagnetic and hadronic calorimeters, and a muon spectrometer (MS). The ID consists of pixel

[1] ATLAS uses a right-handed coordinate system with its origin at the nominal interaction point (IP) in the centre of the detector and the $z$-axis along the beam pipe. The $x$-axis points from the IP to the centre of the LHC ring, and the $y$ axis points upward. Cylindrical coordinates $(r, \phi)$ are used in the transverse plane, $\phi$ being the azimuthal angle around the beam pipe. The pseudorapidity is defined in terms of the polar angle $\theta$ as $\eta = -\ln\tan(\theta/2)$.

and silicon microstrip detectors inside a transition radiation tracker. The electromagnetic calorimeter is a lead liquid-argon (LAr) detector in the barrel ($|\eta| < 1.475$) and the endcap ($1.375 < |\eta| < 3.2$) regions. Hadron calorimetry is based on two different detector technologies. The barrel ($|\eta| < 0.8$) and extended barrel ($0.8 < |\eta| < 1.7$) calorimeters are composed of scintillator/steel, while the hadronic endcap calorimeters ($1.5 < |\eta| < 3.2$) are LAr/copper. The forward calorimeters (3.1 $|\eta| < 4.9$) are instrumented with LAr/tungsten and LAr/copper, providing electromagnetic and hadronic energy measurements, respectively. The MS consists of three large superconducting toroids and a system of three stations of trigger chambers and precision tracking chambers.

In the year 2010 the ATLAS experiment has collected 45 $\text{pb}^{-1}$ of data (in 2011 up to June, 1.1 $\text{fb}^{-1}$) from p-p collisions at a center-of-mass energy of 7 TeV. The data used in the Heavy Ions analyses were recorded during the LHC Pb-Pb run at collision energy of $\sqrt{s}_{NN} = 2.76$ TeV in the fall of 2010 and correspond to 9.17 $\mu\text{b}^{-1}$ integrated luminosity. Monte Carlo (MC) simulated event samples with full detector simulation are used to model the signal and the backgrounds [2].

## 2. Standard Model Results

An understanding of electron, muon, photon and jet production in p-p collisions is a prerequisite for measurements and searches including these particles in the final state. Moreover, the inclusive production of these particles can be used to constrain theoretical predictions.

At low $p_T$ the inclusive electron and muon spectra are dominated by decays of charm and beauty hadrons. The electron and muon cross sections are measured in the range $7 < p_T < 26$ GeV and $|\eta| < 2.0$ with respectively integrated luminosities of 1.3 $\text{pb}^{-1}$ and 1.4 $\text{pb}^{-1}$ [3]. After subtraction of the $\text{W}/Z/\gamma^*$ contribution, the differential cross sections (see Fig. 1) are found to be in good agreement with predictions of NLO+NLL and NLO calculations using the program FONLL [4, 5]. Comparisons are also made to the NLO predictions from the POWHEG [6, 7] program and the Leading Order expectations from PYTHIA [8].

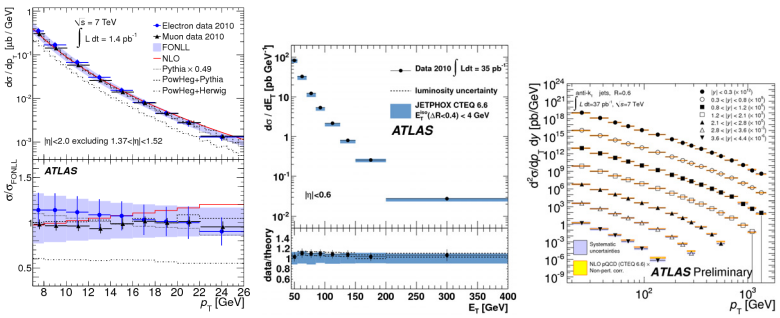


Fig. 1: (left) electron and muon differential cross-sections as a function of the charged lepton transverse momentum for $|\eta| < 2.0$. The ratio of the measured cross-section and the other predicted cross-sections to the FONLL calculation is given in the bottom of each plot. The Pythia (L0) cross-sections are normalised to the data in order to compare the shape of the spectra. (middle) measured (dots) and expected (shaded area) inclusive prompt photon production cross-sections, and their ratio, as a function of the photon $E_T$ and in the range $|\eta| < 0.6$. (right) inclusive jet double-differential cross section as a function of jet $p_T$ in different regions of $|y|$. For convenience, the cross sections are multiplied by the factors indicated in the legend. The data are compared to NLO pQCD calculations to which non-perturbative corrections have been applied

Photon production occurs at leading order via quark-gluon scattering, $qg \rightarrow q\gamma$, or quark-antiquark annihilation, $q\bar{q} \rightarrow g\gamma$. The measurement of photon production provides a clean test of the QCD, using a colorless probe which produces a well localized signal in the detector. The observed differential cross-section, as a function of $E_T$, is shown in Fig. 1 (middle) [9]. A good agreement is observed with the NLO computation from Jetphox [10] using the CTEQ 6.6 PDFs [11], especially for $E_T > 50$ GeV. The lower region is more difficult to model, being affected by a larger contribution from fragmentation.

Inclusive single-jet double-differential cross sections are measured as a function of $p_T$ and $y$ in the region $p_T > 20$ GeV, $|y| < 4.4$, where the rapidity $y = \frac{1}{2} ln \frac{E+p_z}{E-p_z}$ is used instead of $\eta$ for jets and massive particles [12]. Fig. 1 (right) shows the inclusive jet cross section compared with the NLO pQCD prediction from NLOJET [13] to which non-perturbative corrections have been applied. Data and theory are in good agreement over several orders of magnitude although some differences are observed at high jet $p_T$ and $|y|$.

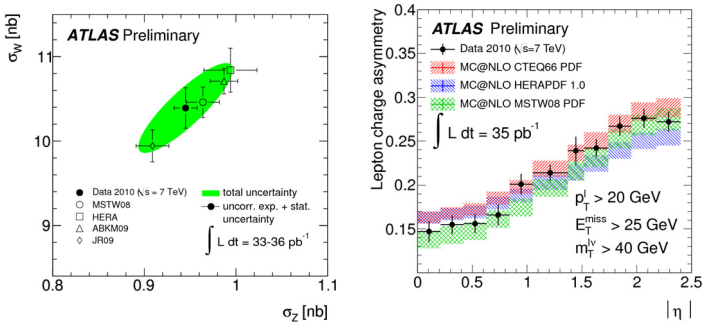


Fig. 2: (left) measured and predicted fiducial cross sections times leptonic branching ratios, $(\sigma W^+ + \sigma W)$ vs $\sigma Z/\gamma*$. The ellipses illustrate the 68% CL coverage for total uncertainties (full green) and excluding the luminosity uncertainty (open black). The uncertainties of the theoretical predictions correspond to the PDF uncertainties only. (right) measured $W$ charge asymmetry as a function of lepton pseudorapidity $|\eta_l|$ compared with theoretical predictions calculated to NNLO. The kinematic requirements are $p_T(l) > 20$ GeV, $p_T(\nu) > 25$ GeV and $m_T > 40$ GeV. Theoretical points are displaced for clarity within each bin

To select $W$ boson events in the electron channel, one isolated electron with tight identification is required with $E_T > 20$ GeV and $|\eta| < 2.47$ [14]. For the $W$ boson events selection in the muon channel, one isolated muon with $p_T > 20$ GeV and $|\eta| < 2.4$ is required. The missing transverse energy is required to be larger than 25 GeV while the transverse mass has to be larger than 40 GeV. The same selections are also used for the $Z$ events selection, but instead of one, two oppositely charged same flavour leptons are required with an invariant mass between 66 and 116 GeV. As shown in Fig. 2, the measured $W^{\pm}$ and $Z/\gamma^*$ cross sections are found to be described by Next-to-Next-to-Leading Order (NNLO) QCD calculations based on a number of different PDF sets. In p-p collisions the overall production rate of $W^+$ bosons is significantly larger than the corresponding $W$ rate, since the proton contains two $u$ and one $d$ valence quarks. The measurement of the lepton charge asymmetry:

$$A_l = \frac{d\sigma_{W_{l+}}/d\eta_l - d\sigma_{W_{l-}}/d\eta_l}{d\sigma_{W_{l+}}/d\eta_l + d\sigma_{W_{l-}}/d\eta_l} \tag{1}$$

can contribute significantly to the understanding of PDFs in the parton momentum fraction range $10^{-3} < x < 10^{-1}$. Systematic ef-

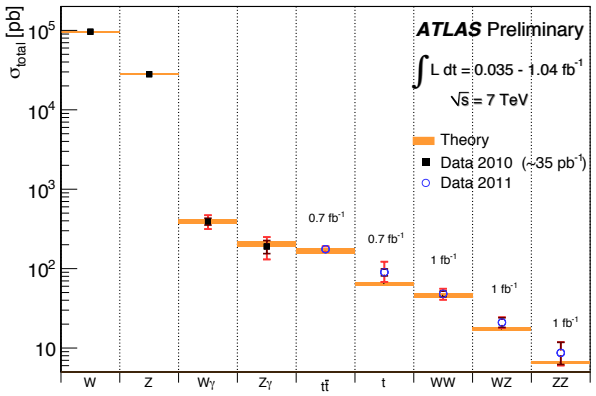


Fig. 3: Summary of several Standard Model total production cross section measurements compared to the corresponding theoretical expectations. The dark error bar represents the statistical uncertainly. The red error bar represents the full uncertainty, including systematics and luminosity uncertainties. All theoretical expectations were calculated at NLO or higher.

fects on the $W$ production cross section measurements are typically the same for positive and negative muons, mostly canceling in the asymmetry. Measurements in the electron and muon channels are presented in Fig. 2 with predictions obtained with MCNLO4 [15] and different PDF sets. The data are broadly compatible with all the predictions with different PDF sets, though some are slightly preferred to others.

The $WW$, $WZ$ and $ZZ$ production cross sections in p-p collisions were also measured using leptonic decay channels. Their production rates are sensitive to the triple gauge couplings of the $W$ and $Z$ bosons and their production are important backgrounds to many Standard Model searches. Based on 2011 data, with an integrated luminosity of 1 fb$^{-1}$, a total of 414 $WW$ candidates are selected with an estimated background 40% [16], 71 $WZ$ candidates with 15% background [17] and 12 $ZZ$ candidates with negligible background [18]. Fig. 3 summarizes several Standard Model total production cross section measurements, including the diboson ones. They are well compared to the corresponding theoretical predictions.

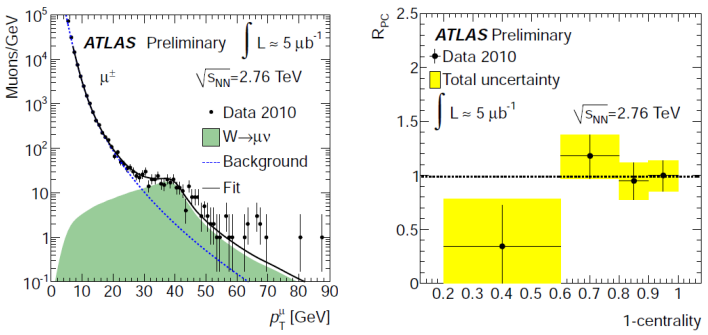


Fig. 4: (left) inclusive muon $p_T$ spectrum in Pb-Pb collisions fitted (solid line) by two components: signal $W \to \mu\nu$ in p-p collisions with Pythia at $\sqrt{s_{NN}} = 2.76$ TeV and a background parametrization (dashed line) obtained from studies of $c\bar{c}$ and $b\bar{b} \to \mu + X$ in p-p collisions. (right) $R_{PC}$ for $W$ bosons as a function of centrality, showing consistency with binary collision scaling.

## 3. Heavy Ions Results

Heavy ion collisions at the LHC can produce a hot and dense state of matter where the relevant degrees of freedom, quarks and gluons are thermalized. The higher LHC energies open the possibility to probe the primary binary (nucleus-nucleus) collisions via the $W$ and $Z$ bosons which, not interacting with the colour medium, can provide a direct measurement of the binary collisions. This can be used to normalize the production mechanisms of various other processes. In the analyses, Pb-Pb collision centrality is characterized by the total transverse energy, $\sum E_T$, measured in the ATLAS forward calorimeter. The full data sample is divided into four bins of collision centrality, 40-80%, 20-40%, 10-20% and 0-10%. For $Z$ bosons, events are selected containing two muons with a $p_T > 20$ GeV and opposite charges are required. For $W$ selection, Fig. 4 (right) shows the uncorrected inclusive muon spectrum for the entire sample. The spectrum shows a steep power law fall off up to 30 GeV where the presence of muons from the $W$ decays appears prominently. The yields are corrected by the reconstruction efficiency, derived in each centrality bin using Monte Carlo. Yields are estimated as a function of centrality, relative to the most peripheral centrality bin (40-80%), normalised

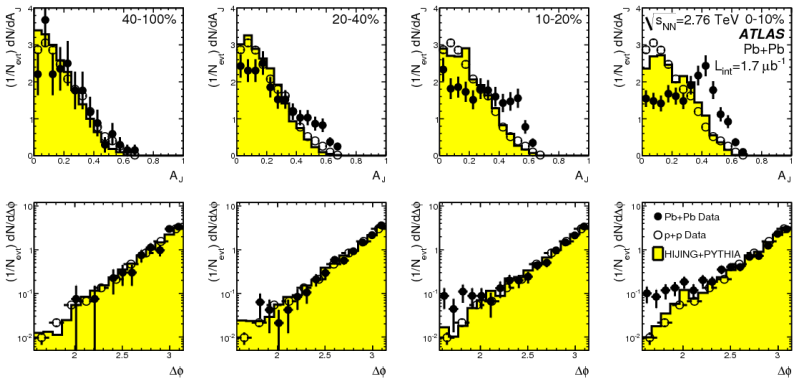


Fig. 5: (top) Dijet asymmetry distributions for data (points) and unquenched Hijing with superimposed Pythia dijets (solid yellow histograms), as a function of collision centrality (left to right from peripheral to central events). Proton-proton data from sqrt(s)=7 TeV, analyzed with the same jet selection, is shown as open circles. (bottom) Distribution of Delta-phi, the azimuthal angle between the two jets, for data and Hijing+Pythia, also as a function of centrality.

by the mean number of binary collisions relative to the most peripheral bin. Due to the large statistical errors on the normalised yield in the $Z$ sample, it is not possible to draw strong conclusions on any centrality dependency [19]. On the other hand, for $W$ bosons there is an indication that $W$ bosons are indeed produced at the initial phase of the collisions and do not interact with the medium [20].

ATLAS also studies the in-medium QCD energy loss ("jet quenching"), by looking at events with two imbalanced jets [21]. The jet energy imbalance is expressed in terms of the asymmetry $A_J = \frac{E_{T1}-E_{T2}}{E_{T1}+E_{T2}}$, where $E_{T1}$ is the transverse energy of the highest $E_T$ jet in the event and $E_{T2}$ is the transverse energy of the highest $E_T$ jet in the opposite hemisphere ($\Delta\phi > \pi/2$, with $\Delta\phi$ the azimuthal angle difference between the jets). Figure 5 shows dijet asymmetry and distributions for dijets in six centrality intervals obtained by requiring $E_{T1} > 100$ GeV and $E_{T2} > 25$ GeV. The measured distributions are compared to distributions obtained from the Pythia+Hijing Monte Carlo sample. Jets reconstructed with a smaller radius show the same modifications as seen in the original measurements while the $\Delta\phi$ distributions remain unmodified even in the most central colli-

sions. The consistency between these results strongly argues against the explanation that the modification results from fluctuations in the underlying event.

## 4. Conclusion

Production cross section measurements of various Standard Model processes have been performed by ATLAS in p-p collisions at the Large Hadron Collider, at $\sqrt{s} = 7$ TeV with 2010 and 2011 data. Theoretical predictions are in good agreement with all measurements within statistical and systematic uncertainties. In lead-lead collisions, the production of $W$ and $Z$ bosons has been observed. From the absence of suppression of the number of $W \to \mu\nu$ events as a function of collision centrality we can conclude that neither the $W$ bosons, nor the muons, interact with the medium. conversly, jets are found to be suppressed in central events by a factor two relative to peripheral events, with no significant dependence on the jet energy.

1. The ATLAS Collaboration, JINST **3**, S08003 (2008).
2. The ATLAS Collaboration, Eur. Phys. J. C **70**, 823 (2010).
3. The ATLAS Collaboration, subm to Phys. Lett. B [arXiv:1109.0525v1].
4. M. Cacciari, M. Greco, and P. Nason, JHEP 007, 9805 (1998).
5. M. Cacciari *et al.*, JHEP 033, 0407 (2004).
6. S. Frixione, P. Nason, C. Oleari, JHEP 070, 0711 (2007).
7. S. Alioli, P. Nason, C. Oleari and E. Re, JHEP 043, 1006 (2010).
8. T. Sjostrand, S. Mrenna and P. Z. Skands, JHEP 026, 0605 (2006).
9. The ATLAS Collaboration, subm to Phys. Lett. B [arXiv:1108.0253].
10. S. Catani *et al.*, JHEP 028, 05 (2002).
11. J. Pumplin *et al.*, JHEP 012, 07 (2002).
12. The ATLAS Collaboration, ATLAS-CONF-2011-047 http://cdsweb.cern.ch/record/1338578.
13. Z. Nagy, Phys. Rev. D **68**, 94002 (2003).
14. The ATLAS Collaboration, subm to Phys. Rev. D [arXiv:1109.5141v2].
15. S. Frixione and B. R. Webber, JHEP 029, 06 (2002).
16. The ATLAS Collaboration, ATLAS-CONF-2011-110 http://cdsweb.cern.ch/record/1373412.

17. The ATLAS Collaboration, ATLAS-CONF-2011-099
http://cdsweb.cern.ch/record/1369214

18. The ATLAS Collaboration, ATLAS-CONF-2011-107
http://cdsweb.cern.ch/record/1372920.

19. The ATLAS Collaboration, Phys Lett. B **697** 294-312 (2011).

20. The ATLAS Collaboration, ATLAS-CONF-2011-078
http://cdsweb.cern.ch/record/1353227.

21. The ATLAS Collaboration, Phys. Rev. Lett. **105**, 252303 (2010).

# CONTRIBUTION OF Ga EXPERIMENTS FOR UNDERSTANDING THE PHYSICS OF THE SUN AND THE PHYSICS OF NEUTRINO

V.N. Gavrin

*Institute for Nuclear Research RAS,*
*Moscow 117312 Russia*

**Abstract**

The Russian-American experiment SAGE began to measure the solar neutrino capture rate with a target of gallium metal in December 1989. Measurements have continued with only a few brief interruptions since that time. Assuming the solar neutrino production rate was constant during the period of data collection, combined analysis of 168 extractions through December 2007 gives a capture rate of solar neutrinos with energy more than 233 keV of $65.4^{+3.1}_{-3.0}(\text{stat.})^{+2.6}_{-2.8}(\text{syst.})$ SNU. The weighted average of the results of all Ga solar neutrino experiments, SAGE, Gallex, and GNO, is now $66.1 \pm 3.1$ SNU, where statistical and systematic uncertainties have been combined in quadrature. New test of SAGE was made with a reactor-produced $^{37}$Ar neutrino source. The ratio of observed to calculated rates in this experiment, combined with the measured rates in the three prior $^{51}$Cr neutrino-source experiments with Ga, is $0.87 \pm 0.05$. A probable explanation that this low result is overestimation of the cross section for neutrino capture by the two lowest-lying excited states in $^{71}$Ge has not been confirmed. Other explanations might be a statistical fluctuation or a real physical effect of unknown origin, such as a transition to sterile neutrinos. Possibilities of SAGE for investigation of transitions from active to sterile neutrinos with $\Delta m^2 > 0.5$ eV$^2$ with a sensitivity to disappearance of electron neutrinos of a few percent are discussed.

## 1. Introduction

The Ga experiments were built to measure the capture rate of solar neutrinos by the reaction $^{71}\mathrm{Ga} + \nu_e \rightarrow ^{71}\mathrm{Ge} + e^-$ and thus to provide information to understand the deficit of neutrinos observed in the $^{37}$Cl experiment [1] and in experiment Kamiokande [2]. The feature that distinguishes the Ga experiment from all other past or present solar neutrino detectors is its sensitivity to the proton-proton fusion reaction, $p + p \rightarrow d + e^+ + \nu_e$, which generates most of the Sun's energy. Ga experiments have provided the only direct measurement of the current rate of this reaction.

Initially there existed two Ga solar neutrino experiments. SAGE with a 50 tons Ga metal target started its operation in 1990 and it still continues running. Gallex' target contained 30 tons of gallium in a form of $GaCl_3$ solution and this experiment measured the solar neutrino capture rate from 1991 to 1997. In 1998 it was reconstituted under the name of GNO and it took data until 2003. This paper gives results of these experiments and combines them with SAGE data. The experiment SAGE is presented more detailed as it is still running.

## 2. SAGE

The SAGE experiment is in a dedicated deep-underground laboratory excavated into the side of Mt.Andyrchi in the Northern Caucasus mountains of Russia. The rock overburden is equivalent to 4700 m of water and the measured muon flux at the location of the experiment is $(3.03 \pm 0.10) \times 10^{-9}/(\mathrm{cm}^2\,\mathrm{s})$. The mass of gallium used in SAGE at the present time is 50 tons.

$^{71}$Ge has been extracted from the Ga target to measure the solar neutrino capture rate every month from January 1990 to the present time. The extraction procedures are described in Ref. [3–5]. Because only a few $^{71}$Ge counts are detected from each extraction, a single run result has a large statistical uncertainty and thus little significance. The combined result of each year of SAGE data since its beginning is shown in Fig. 1.

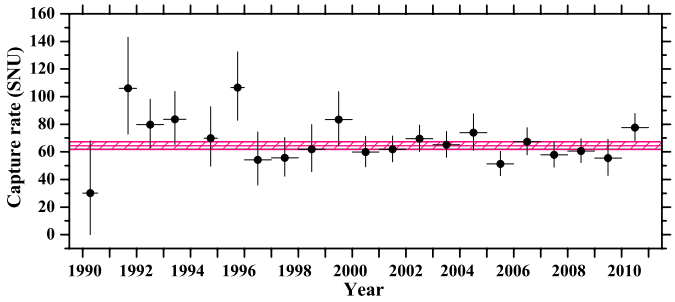


Fig. 1: Combined SAGE results for each year. Shaded band is the combined best fit and its uncertainty for all years. Vertical error bars with 68% confidence

The systematic uncertainties in the experiment have been considered in detail in Refs. [3,4,6].Total value of uncertainty is $^{+2.6}_{-2.8}$ SNU [1].

For all SAGE data from January 1990 through December 2007 (168 runs and 310 separate counting sets) the global best fit capture rate is $65.4^{+3.1}_{-3.0}$ SNU, where the uncertainty is statistical only. If one considers the L-peak and K-peak data separately, the results are $67.2^{+4.8}_{-4.6}$ SNU and $64.0^{+4.1}_{-4.0}$ SNU, respectively. The agreement between the two peaks serves as a strong check on the robustness of the event selection criteria. Including the systematic uncertainty, our overall result is $65.4^{+3.1}_{-3.0}$(stat.)$^{+2.6}_{-2.8}$(syst.) SNU.

## 3. Combined Ga Results

The waveform data from the Gallex experiment has recently been re-evaluated by Kaether using a new pulse-shape analysis method [7] and the result is $73.1^{+6.1+3.7}_{-6.0-4.1}$ SNU. The result of the GNO experiment was $62.9^{+5.5+2.5}_{-5.3-2.5}$ SNU [8]. If we combine the statistical and systematic uncertainties in quadrature, then the weighted combination of all the Ga experiments, SAGE, Gallex and GNO is $66.1 \pm 3.1$ SNU. (Present Ga experiment result.)

[1] In radiochemical experiments the capture rate has been conventionally expressed in "SNU units", defined as one neutrino capture per second in a target that contains $10^{36}$ atoms of the neutrino-absorbing isotope, in our case $^{71}$Ga.

## 4. The *pp* Neutrino Flux from the Sun

The measured capture rate in Ga experiments is the sum of the rates from all the components of the solar neutrino flux, which can be expressed as following:

$$[pp + {}^{7}\mathrm{Be} + \mathrm{CNO} + pep + {}^{8}\mathrm{B} \mid \mathrm{Ga}] = 66.1(1 \pm 0.047)\ \mathrm{SNU}.$$

We have ignored here the tiny hep-neutrino contribution and have combined the neutrino fluxes from $^{13}$N, $^{15}$O, and $^{17}$F decay into a single component of the solar neutrino flux, called here "CNO".

Using results of measurements of neutrino fluxes in Borexino [9] and SNO [10] and capture rates obtained in the chlorine experiment [1] we have calculated the contribution of each component of solar neutrino flux into the capture rate measured on Ga [6]:

$$[{}^{7}\mathrm{Be} \mid \mathrm{Ga}] = 19.1(1 \pm 0.12)\ \mathrm{SNU},$$
$$[{}^{8}\mathrm{B} \mid \mathrm{Ga}] = 3.6(1^{+0.32}_{-0.16})\ \mathrm{SNU},$$
$$[\mathrm{CNO} + pep \mid \mathrm{Ga}] = 3.68(1 \pm 1.0)\ \mathrm{SNU},$$
$$[pp \mid \mathrm{Ga}] = 39.7(1 \pm 0.14)\ \mathrm{SNU}.$$

## 5. Contribution to the Physics of the Sun

The neutrino capture rate on Ga $39.7(1 \pm 0.14)$ SNU corresponds to the value of *pp*-neutrino flux arriving on the Earth without changing its flavor $\Phi^{e}_{pp} = 3.38(1 \pm 0.14) \times 10^{10}/(\mathrm{cm}^2\mathrm{s})$. If use the value of survival factor $P_{ee} = 0.561(1^{+0.030}_{-0.042})$ then the value of total *pp* flux produced in the Sun arriving on the Earth with mixing flavors is $\Phi^{\mathrm{total}}_{pp} = 6.0(1 \pm 0.14) \times 10^{10}/(c\mathrm{m}^2\mathrm{s})$. There is a good numerical agreement between this result and the flux values of *pp* neutrino predicted from the two recent solar models with different composition $\Phi^{\mathrm{total}}_{pp} = 5.97 \pm 0.04$ and $6.04 \pm 0.03$, both in units of $10^{10}\nu_e/(\mathrm{cm}^2\mathrm{s})$.

Ga experiments: (I) have shown deficit of solar neutrino in the entire energy range; (II) presented direct experimental evidence of proton-proton chain in reactions of thermonuclear synthesis in the Sun; (III) have shown the correctness of SSM and LMA solution for neutrino oscillations. There is thus excellent agreement between theory and experiment for the Ga experiments.

**Table 1: Results of all neutrino source experiments with Ga**

| experiment | source | ratio | reference |
|---|---|---|---|
| GALLEX | $^{51}$Cr-1 | $0.95 \pm 0.11$ | [7, 11] |
| GALLEX | $^{51}$Cr-2 | $0.81 \pm 0.11$ | [7, 11] |
| SAGE | $^{51}$Cr | $0.95 \pm 0.12$ | [12] |
| SAGE | $^{37}$Ar | $0.79 \pm 0.10$ | [13] |
| Average | $^{37}$Ar, $^{51}$Cr | $0.87 \pm 0.05$ | [6, 14] |

## 6. Source Experiments

The experimental procedures of the SAGE and Gallex experiments, including the chemical extraction, counting, and analysis techniques, have been checked by exposing the gallium target to reactor-produced neutrino sources whose activity was close to 1MCi.

The results, expressed as the ratio $R$ of the measured $^{71}$Ge production rate to that expected due to the source is $R = 0.87 \pm 0.05$, more than two standard deviations less than unity (see Table 1). The quality of fit to the average value is quite high ($\chi^2$/DOF $= 1.9/3$, GOF $= 59\%$).

All possible explanations for this unexpectedly low result are discussed in detail in Ref. [6]. Foremost among these was overestimation of the cross section for neutrino capture to the lowest two excited states in $^{71}$Ge, which could yield a value of $R$ as small as 0.95. Other explanations might be a statistical fluctuation or a real physical effect of unknown origin, such as a transition to sterile neutrinos or quantum decoherence in neutrino oscillations [15]. The interpretation of the Ga source experiments in terms of oscillations to a sterile neutrino with $\Delta m^2 \approx 1$ eV$^2$, as well as the agreement of these results with the reactor experiments Bugey, Chooz, and Gösgen and the accelerator experiments LSND and MiniBooNE is considered in detail in Ref. [16]. If transitions to a sterile neutrino are occurring, the region of allowed oscillation parameters inferred from the four Ga source experiments is shown in Fig. 2.

## 7. The New Source Experiment

We believe that new experiments are necessary to understand the low result of the Ga source measurements. One such experiment at

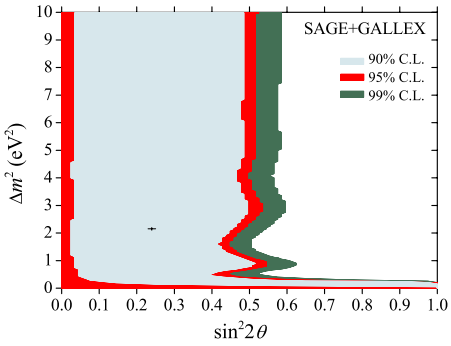


Fig. 2: Region of allowed mixing parameters inferred from gallium source experiments assuming oscillations to a sterile neutrino. Plus sign at $\Delta m^2 = 2.15$ eV$^2$ and $\sin^2(2\theta) = 0.24$ indicates the best-fit point

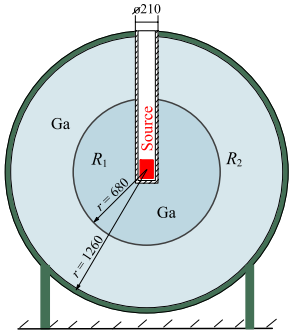


Fig. 3: Schematic drawing of proposed neutrino source experiment. $R1$ and $R2$ are the ratios of measured capture rate to predicted rate in the inner and outer zones, respectively. Outer radii r of the two zones and diameter of source reentrant tube are indicated in mm

the Research Center of Nuclear Physics (RCNP), Osaka that should provide information to better determine the cross section for neutrino capture at low energy is completed [17]. The result is the measured cross section which gave a slightly larger value than was roughly estimated by Bahcall and therefore it slightly amplifies the discrepancy observed in calibration measurements. Another experiment, which we intend to pursue, is an improved version of the Ga source measurements. Our plan, as schematically pictured in Fig. 3, is to place a $^{51}$Cr source with initial activity of 3 MCi at the center of a 50-tonne

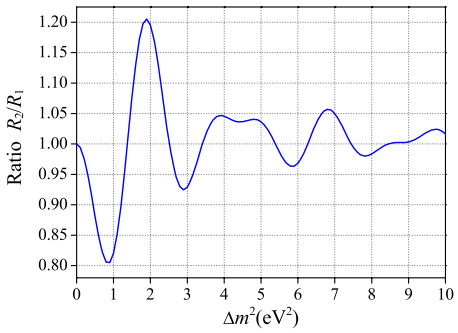


Fig. 4: Ratio of rates in the outer and inner zones versus $\Delta m^2$ for the $\sin^2(2\theta) = 0.3$

target of liquid Ga metal that is divided into two concentric spherical zones, an inner 8-tonne zone and an outer 42-tonne zone. If the neutrino capture cross section is that calculated by Bahcall [18] and oscillations to sterile neutrinos do not occur, then at the beginning of irradiation there is a mean of 65 atoms of $^{71}$Ge produced by the source per day in each zone. After an exposure period of a few days, the Ga in each zone is transferred to reaction vessels and the $^{71}$Ge atoms produced by neutrino capture are extracted.

If oscillations to a sterile neutrino are occurring with mass squared difference of $\Delta m^2$ and mixing parameter $\sin^2(2\theta)$ then the rates in the outer and inner zones of gallium will be different and their ratio, for the specific case of $\sin^2(2\theta) = 0.3$, will be as shown in Fig. 4.

In contrast, experiments with reactor and accelerator neutrinos suffer from several disadvantages. The neutrino energy $E$ is distributed over a wide spectrum and the dimensions $L$ of the sources and detectors are on the scale of several meters. Other disadvantages of a reactor or accelerator experiment are that the knowledge of the neutrino flux incident on the target is usually significantly worse than with a neutrino source and that, with some targets, there are appreciable uncertainties in the cross section for neutrino interaction.

If in new experiment in which a very-intense $^{51}$Cr source irradiates a target of Ga metal that is divided into two zones there is either a significant difference between the capture rates in the two zones, or the average rate in both zones is considerably below the expected rate, then there is evidence of nonstandard neutrino prop-

erties. The proposed experiment has the potential to test neutrino oscillation transitions with mass-squared difference $\Delta m^2 > 0.5$ eV$^2$. This capability exists because the experiment uses a compact nearly monochromatic neutrino source with well-known activity, the dense target of Ga metal provides a high interaction rate, and the special target geometry makes it possible to study the dependence of the rate on the distance to the source.

## Acknowledgments

We appreciate great hospitality of the Organizing Committee of the Conference. We are grateful to the Russian Foundation of Basic Research for support under grants 05-02-17199, 08-02-00146. The research was supported by Grants of President of Russian Federation NS-1782.2003.2 and NS-3517.2010.

1. B.T. Cleveland *et al.*, Astrophys. J. **496**, 505 (1998).
2. Y. Fukuda, Phys. Rev. Lett. **77**, 1683 1996.
3. J.N. Abdurashitov *et al.* [SAGE coll.], Phys. Rev. C **60**, 055801 (1999); [arXiv:astro-ph/9907113].
4. J.N. Abdurashitov *et al.* [SAGE coll.], J. Exp. Theor. Phys. **95**, 181 (2002); Zh. Eksp. Teor. Fiz. **122**, 211 (2002);[arXiv:astro-ph/0204245].
5. B.T. Cleveland, Nucl. Instr. Methods Phys. Res. **214**, 451 (1983).
6. J.N. Abdurashitov *et al.* [SAGE coll.], Phys. Rev. **C80**, 015807 (2009); [arXiv:nucl-ex/0901.2200v3].
7. F. Kaether, Ph.D. thesis, Datenanalyse der Sonnen neutrino experiments Gallex, Heidelberg, 2007, http://www.ub.uniheidelberg.de/archiv/7501/.
8. M. Altmann *et al.*, Phys. Lett. B **616**, 174 (2005).
9. C. Arpesella *et al.*(Borexino Collaboration), Phys. Rev. Lett. **101**, 091302 (2008).
10. B. Aharmim *et al.* (SNO Collaboration), Phys. Rev. Lett. **101** 111301 (2008).
11. F. Kaether, W. Hampel, G. Heusser, J. Kiko, and T. Kirsten, Phys. Lett. B **685**, 47 (2010).
12. J.N. Abdurashitov *et al.* [SAGE coll.],Phys. Rev. C **59**, 2246 (1999).
13. J.N. Abdurashitov *et al.* [SAGE coll.], Phys. Rev. C **73**, 045805 (2006).
14. V.N. Gavrin, V.V. Gorbachev, E.P. Veretenkin, and B.T. Cleveland, [arXive:nucl-ex/1006.2103v2] (2011).
15. Y. Farzan, T. Schwetz, and A.Yu. Smirnov, JHEP **07**, 067 (2008); [arxiv.org/abs/0805.2098v1].

16. C. Giunti and M. Laveder, Mod. Phys. Lett. A **22**, 2499 (2007); [arXiv/hep-ph/0610352v2]; M. A. Acero, C. Giunti, and M. Laveder, Phys. Rev. D **78**, 073009 (2008); [arXiv.org/0711.4222v3]; C. Giunti and M. Laveder [arxiv.org/0902.1992v2]; C. Giunti and M. Laveder [arxiv.org/1005.4599v2].

17. D. Frekers, H. Ejiri *et al.* will be published in Phys. Rev. Let. (2011).

18. J.N. Bahcall, Phys. Rev. C **56**, 3391 (1997); [arXiv/hep-ph/9710491].

# FINAL STATE INTERACTION OF PIONS IN $K^{\pm} \to \pi^{\pm}\pi^0\pi^0$ DECAY AND $\pi\pi$ SCATTERING LENGTHS

S.R. Gevorkyan

*Joint Institute for Nuclear Research, Dubna, Russia*

In 2003-2004 the collaboration NA48/2 at the CERN SPS collected a large amount of data ($\sim 6 \times 10^7$) on the decay $K^{\pm} \to \pi^{\pm}\pi^0\pi^0$. The dependence of the distribution on the invariant mass of two neutral pions $M_{00}$ (Fig. 1) shows a cusp-like anomaly in the vicinity of charged pions threshold $M_{00} = 2m_c$ [1,2].

As was pointed out by N.Cabibbo [3] this anomaly is a result of charge exchange process $\pi^+\pi^- \to \pi^0\pi^0$ in the decay $K^{\pm} \to \pi^{\pm}\pi^+\pi^-$. The amplitude of the decay $K^+ \to \pi^+\pi^0\pi^0$ reads:

$$T = T_0 + 2ia_x kT_+; \quad a_x(\pi^+\pi^- \to \pi^0\pi^0) = \frac{a_2 - a_0}{3}; \tag{1}$$

$T_0(K^+ \to \pi^+\pi^0\pi^0)$; $T_+(K^+ \to \pi^+\pi^-\pi^+)$ – unperturbed (without final state interaction) amplitudes; $a_0, a_2$ – s-wave $\pi\pi$ scattering lengths in the isospin $I = 0$ and $I = 2$ states; $k = \frac{1}{2}\sqrt{M_{00}^2 - 4m_c^2}$ - the relative momentum of charged pion in the reaction $\pi^+ + \pi^- \to \pi^0 + \pi^0$.

Under charged pions threshold this momentum becomes imaginary $k = i\kappa$ thus

$$|T|^2 = T_0^2 + 4\frac{(a_0 - a_2)^2 k^2}{9}T_+^2; M_{00}^2 > 4m_c^2,$$
$$|T|^2 = T_0^2 + 4\frac{(a_0 - a_2)^2 \kappa^2}{9}T_+^2 - 4\frac{(a_0 - a_2)\kappa}{3}T_0T_+; M_{00}^2 < 4m_c^2. \tag{2}$$

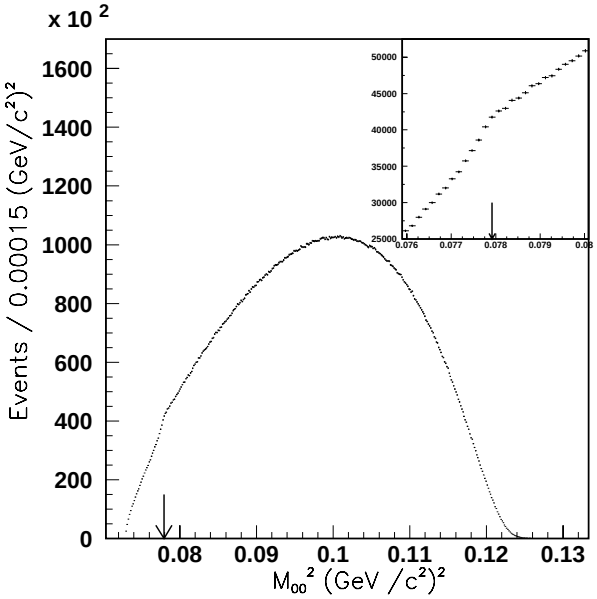


Fig. 1: Decay rate vs $M_{00}^2$

Above the threshold $M_{00}^2 > 4m_c^2$ the decay rate is proportional to the square of scattering lengths difference $(a_0 - a_2)^2$, the fact known for many years [4] while under threshold $M_{00}^2 < 4m_c^2$ the decay rate acquires interference term linear in $(a_0 - a_2)$. Such irregular behavior of the decay rate at threshold allows one to extract the value of the difference $(a_0 - a_2)$ fitting the experimental data [1,2] on the rate of $K^\pm \to \pi^\pm\pi^0\pi^0$ decay.

For many years the semileptonic decay $K^\pm \to \pi^+\pi^- e^\pm \nu$ ($K_{e4}$ decay) was seen as a cleanest method for measurement of $\pi\pi$ scattering lengths due to only two pions in the final state and well known connection between the pions phases difference in s and p- wave states with scattering lengths [5]. In addition it is desirable to know scattering lengths values with highest possible accuracy as at present the Chiral Perturbation Theory (ChPT) predicts their values with unusual for strong interaction precision ($\sim 2\%$).

The discovery of cusp effect by NA48/2 collaboration open a new challenges for precise determination of scattering lengths. The fit

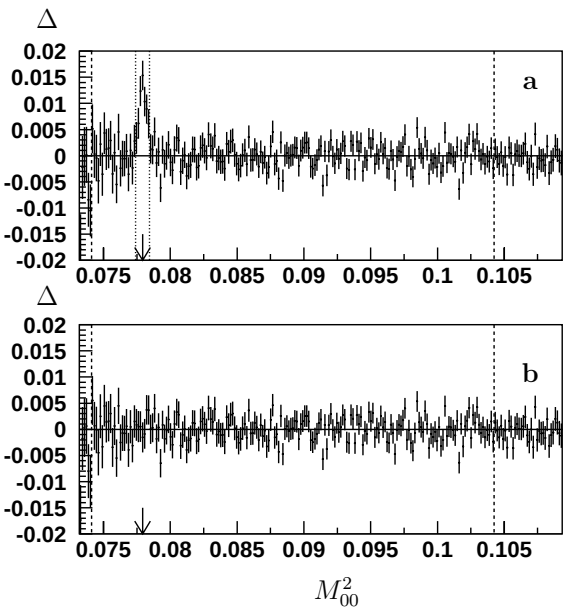


Fig. 2: $\Delta$=(data-fit)/data versus $M_{00}^2$: a – fit without pionium formation; b – fit including the electromagnetic effects

of the experimental distribution making use of two theoretical models [6, 7] being the extension of Cabibbo approach to higher order in scattering lengths ($\sim a^2$) allows to determine the them with accuracy comparable to theoretical predictions [1, 2].

Nevertheless there are two issues unsolved in the above models. At charged pions threshold one has to account for electromagnetic interaction of pions, leading to bound states (pionium atoms) just under threshold. In Fig. 2(a) the result of the fit without electromagnetic effects is shown [1]. The discrepancy at charged pions threshold is a result of neglect of this effect in the theoretical approaches. The better fit can be obtained (Fig. 2(b)), when the authors add a free parameter relevant to a term describing the expected formation of pionium atoms decaying to $\pi^0\pi^0$ at threshold. However the extracted in such a way probability of pionium atom creation $K^\pm \to \pi^\pm + A_{\pi^+\pi^-}$ normalized to the $K^\pm \to \pi^\pm\pi^+\pi^-$ decay rate turn out to be twice larger than the theoretical prediction [8].

The second problem closely connected to the bound state formation is the absence of a reliable way in upgraded approaches [6, 7] to estimate the contribution of higher order terms in strong interaction. To account for electromagnetic interaction leading to unstable bound states one needs expressions for decay amplitudes including the strong interaction between pions in all orders,the task which can't be obtained in the framework of two mentioned above [6, 7] theoretical models.

To resolve these challenges, we make use the well known methods of non-relativistic quantum mechanics. The amplitudes of kaon decay to two pions can be presented as the convolution of the unperturbed amplitude $M_0(r)$ with the two pions wave functions describing strong interactions in the $\pi^+\pi^-$; $\pi^0\pi^0$ states and appear to be a solution of couple Shrödinger equations [9]:

$$M_c(K \to \pi^+\pi^-) = \int \Psi_c^+(r) M_0(r) d^3r;$$
$$M_n(K \to \pi^0\pi^0) = \int \Psi_n^+(r) M_0(r) d^3r; \qquad (3)$$

$$-\Delta\Psi_c(r) + U_{cc}\Psi_c(r) + U_{cn}\Psi_n(r) = k_c^2\Psi_c(r);$$
$$-\Delta\Psi_n(r) + U_{nn}\Psi_n(r) + U_{nc}\Psi_c(r) = k_n^2\Psi_n(r). \qquad (4)$$

Here $k_c, k_n$ are pions relative momenta in charge $\pi^+\pi^-$ and neutral $\pi^0\pi^0$ pairs, while $U_{ik}$ are relative potentials in $\pi\pi$ elastic and charge exchange interaction. Assuming that only s-wave scattering $\pi\pi$ scattering take place and strong potentials with sharp boundary $U_{ik} \gg k_{c(n)}^2$, making use the known asymptotic behavior of wave functions and unitarity constrains we obtain a set of relations expressing the decay amplitudes through unperturbed one $M_{0c}, M_{0n}$ and $\pi\pi$ scattering amplitudes $f_x(\pi^+\pi^- \to \pi^0\pi^0)$, $f_c(\pi^+\pi^- \to \pi^+\pi^-)$, $f_n(\pi^0\pi^0 \to \pi^0\pi^0)$

$$M_c = M_{0c}(1 + ik_c f_{cc}) + ik_n M_{0n} f_x; \quad f_{cc} = \frac{a_{cc}(1 - ik_n a_{nn}) + ik_n a_x^2}{D};$$
$$M_n = M_{0n}(1 + ik_n f_{nn}) + ik_c M_{0c} f_x; \quad f_{nn} = \frac{a_{nn}(1 - ik_c a_{cc}) + ik_c a_x^2}{D};$$
$$f_x = \frac{a_x}{D}; \quad D = (1 - ik_c a_{cc})(1 - ik_n a_{nn}) + k_n k_c a_x^2. \qquad (5)$$

In the case of exact isospin symmetry in the vicinity of threshold these amplitudes manifest itself through the scattering lengths:

$$a_x = \frac{a_2 - a_0}{3}; \quad a_{nn} = \frac{a_0 + 2a_2}{3}; \quad a_{cc} = \frac{2a_0 + a_2}{6}. \tag{6}$$

To account for electromagnetic interaction among the pions we took advantage of well known receipt [11]. It turn out that to include the electromagnetic interaction in the considered approach it is sufficient to do a substitution: $ik_c \to \tau = \frac{d\log[G_0(kr)+iF_0(kr)]}{dr}\Big|_{r=r_0}$ where $F_0, G_0$ are the regular and irregular solutions of the Coulomb problem (Hypergeometric functions). In relevant region $kr_0 \ll 1$ ($r_0$ – strong potential radius):

$$\tau = ik - \alpha m\left[\log(-2ikr_0) + 2\gamma + \psi(1 - i\xi)\right];$$

$$\mathrm{Re}\ \tau = -\alpha m\left[\log(2kr_0) + 2\gamma + \mathrm{Re}\,\psi(1 - i\xi)\right], \xi = \frac{\alpha m}{2k};$$

$$\mathrm{Im}\ \tau = kA^2, \quad A = \exp\left(\frac{\pi\xi}{2}\right)|\Gamma(1 + i\xi)|. \tag{7}$$

Here $\gamma = 0.5772$ is the Euler constant while $\psi(\xi) = \frac{d\log\Gamma(\xi)}{d\xi}$-digamma function.

Inclusion of the electromagnetic interactions in a such way leads to the bound state in the very narrow region under charged pions threshold and correctly accounts for the electromagnetic interaction in all kinematical region [10]. It seems that the difference between predicted rate for creation of pionium atoms and fit result at threshold is due to the fact that in the vicinity of threshold besides the bound states there are contribution from unbound pairs, whose electromagnetic interaction gives almost the same size contribution as the pionium decay [12].

Another place where the developed approach can be applied is the $K_{e4}$ decay. As was mentioned above it is ideally suited for determination of $\pi\pi$ scattering lengths. From experimental data on $K_{e4}$ decay the phases difference between s and p pions states $\delta = \delta_s - \delta_p$, can be extracted.

The preliminary analysis of the experimental data obtained by NA48/2 collaboration leads to large discrepancy between the prediction for the value of scattering length $a_0$ from ChPT and its value obtained from experimental data [13] on $K_{e4}$ decay.

As was shown in works [14, 15] this discrepancy is due to the neglect of isospin breaking effects in the experimental data processing. Account [14] for the electromagnetic interaction between the pions in the decay $K^{\pm} \to \pi^+\pi^- e\nu$ and isospin breaking effects due to the possibility of charge exchange reaction among the pions in the final state [15] allows to adjust the data for scattering lengths from NA48/2 and theoretical predictions.

The considered approach can be applied to the wide class of the decays with two or more hadrons in the final state, leading to better understanding of strong interaction and giving the unique possibility to check different theoretical models predictions for meson-meson interactions at low energies.

1. J. Batley *et al.*, Phys. Lett. B **633**, 173 (2006).
2. J. Batley *et al.*, Eur. Phys. J. C **64**, 589 (2009).
3. N. Cabibbo, Phys. Rev. Lett. **93**, 121801 (2004).
4. V. Gribov, Nucl. Phys. **5**, 653 (1958).
5. B.Ananthanarayan *et al.*, Phys. Rept. **353**, 207 (2001).
6. N. Cabibbo, G. Isidori, JHEP **0503**, 021 (2005).
7. G. Colangelo, J. Gasser, B. Kubis, A. Rusetsky, Phys. Lett. B **638**, 187 (2006).
8. Z. Silagadze, JETP Lett. **60**, 689 (1994).
9. S. Gevorkyan, A. Tarasov, O. Voskresenskaya, Eur. Phys. J. C **67**, 143 (2010).
10. S. Gevorkyan, A. Tarasov, O. Voskresenskaya, Phys. Lett. B **649**, 159 (2007).
11. E. Wigner, Phys. Rev. **73**, 1002 (1948).
12. S. Gevorkyan, D. Madigozhin, A. Tarasov, O. Voskresenskaya, Phys. Part. Nucl. Lett. **5**, 85 (2008).
13. B. Bloch-Devaux, *Proceedings of the Kaon International Conference, Frascati, May* (2007).
14. S. Gevorkyan, A. Sissakian, A. Tarasov, H. Torosyan, O. Voskresenskaya, Phys. Atom. Nucl. **73**, 937 (2010).
15. S. Gevorkyan, A. Sissakian, A. Tarasov, H. Torosyan, O. Voskresenskaya, Phys. Atom. Nucl. **73**, 961 (2010).

# THE CUORE EXPERIMENT: A SEARCH FOR NEUTRINOLESS DOUBLE BETA DECAY

L. Gironi[1,2] on behalf of the CUORE collaboration

[1] *INFN - Milano Bicocca, Italy*
[2] *Università di Milano Bicocca, Italy*

**Abstract**

The observation of neutrinoless Double Beta Decay would reveal the Majorana nature of the neutrino and could give information about the absolute mass scale and mass hierarchy of the neutrino. Moreover, if this process were observed, it would imply the non-conservation of lepton number and would be a further confirmation of new physics beyond the Standard Model. It is then clear why many experiments are trying to observe this extremely rare process. Among the various experiments, interesting perspectives are related to the bolometric technique. Cuoricino, a tower of 62 $TeO_2$ crystals operated as bolometers for the study of neutrinoless Double Beta Decay of $^{130}Te$, obtained the best limit in the study of this process. Based on these results CUORE, an array of 988 bolometric detectors with a total mass of 741 kg, has been designed.

## 1. The Neutrinoless Double Beta Decay

Since the first evidence in the 1960's, many experiments have provided compelling evidence for neutrino oscillations from one flavor to another [1]. Neutrino oscillations imply that neutrinos have mass, and prompted by this discovery, the question of whether neutrinos are Dirac or Majorana particles has become one of the issues at the forefront of particle and nuclear physics. Unfortunately, up to now, oscillation experiments haven't given information about the absolute mass scale and mass hierarchy of the neutrino. Also for this reason,

great interest has been aimed in experiments able to determine the absolute neutrino masses.

Direct neutrino mass measurements are based on the analysis of the kinematics of charged particles emitted together with neutrinos in weak decays. The most sensitive measurements, involving electron neutrinos, are based on the study of the shape of the $\beta$ spectrum end-point. $\beta$-decay experiments are sensitive to an incoherent combination of the mass eigenvalues, called effective electron neutrino mass $m_\beta$ and defined as

$$\langle m_\beta \rangle = \Big( \sum_{i=1}^{3} m_i^2 |U_{ei}|^2 \Big)^{1/2}, \tag{1}$$

where $U_{ei}$ are the elements of the first row of the PMNS matrix [2]. The best limits on $m_\beta$ come from the Mainz and Troitsk [3] tritium $\beta$-decay experiments: $m_\beta < 2.3$ eV.

Cosmological constraints on neutrino masses come from the observation of the Cosmic Microwave Background (CMB) anisotropies and from the study of large scale structures. These observations are sensitive to the sum of the three neutrino masses

$$\Sigma = \sum_{i=1}^{3} m_i. \tag{2}$$

The CMB data of the WMAP experiment, combined with supernovae data and data on galaxy clustering can be used to obtain an upper limit on $\Sigma < 1.7$ eV [4].

Neutrinoless Double Beta Decay ($0\nu$DBD) experiments are sensitive to a coherent sum of the mass eigenvalues called effective Majorana mass and defined as

$$\langle m_{\beta\beta} \rangle = \Big( \sum_{i=1}^{3} m_i^2 |U_{ei}|^2 e^{i\alpha_i} \Big)^{1/2}, \tag{3}$$

where $\alpha_i$ are parameters containing the two Majorana phases. The $0\nu$DBD plays a primary role since it can also give important information on the nature of the neutrino (Dirac or Majorana) and on the Standard Model. Indeed the $0\nu$DBD would imply a lepton number

violation ($\Delta L = 2$) resulting in a further confirmation of new physics beyond the Standard Model.

From the experimental point of view, what is measured to evaluate the effective Majorana mass is the decay half life $T^{0\nu}_{1/2}$ of the process

$$\frac{1}{T^{0\nu}_{1/2}} = \frac{|m_{\beta\beta}|^2}{m_e^2} G^{0\nu} |M^{0\nu}|^2, \tag{4}$$

where $m_e$ is the electron mass, $G^{0\nu}$ is the two-body phase-space factor and $M^{0\nu}$ is the Nuclear Matrix Element (NME). While $G^{0\nu}$ can be calculated with reasonable accuracy, the NME value is strongly dependent on the nuclear model used for its evaluation.

$0\nu$DBD searches rely on the measurement of the two electron signal. Since the energy of the recoiling nucleus is negligible, the sum of kinetic energy of the two electrons is equal to the Q-value of the transition. This monochromatic signal is the main signature used by all the experiments. On the other hand, given the rarity of the process, the gathering of the $0\nu$DBD counts is complicated by the presence of background events in the energy region under investigation which can hinder the searched signal. The performance of the different $0\nu$DBD experiments is then usually expressed in terms of an experimental sensitivity $S^{0\nu}$, defined as the process half-life corresponding to the maximum signal that could be mimicked by the background fluctuations at a given statistical significance level

$$S^{0\nu} \propto \frac{N_A\, a\, \eta\, \epsilon}{W} \sqrt{\frac{M\, T}{B\, \Delta}}, \tag{5}$$

where $\eta$ is stoichiometric coefficient, $W$ is the molecular weight of the active mass, $a$ is the isotopic abundance (i.a.), $\epsilon$ is the detection efficiency, $T$ is the measurement live time [y], $M$ is the detector mass [kg], $B$ is the background level [counts/keV/kg/y] and finally $\Delta$ is the energy resolution [keV]. Despite its simplicity, this equation has the unique advantage of emphasizing the role of the essential experimental parameters.

## 2. Experimental Approaches

Many $0\nu$DBD experiments have been proposed in the last years. This multiplicity is a good strategy since different nuclei are studied and several experimental techniques, with different impact of backgrounds and systematic errors, are used. One of the most promising is the calorimetric approach where the detector is made of the $0\nu$DBD material since it allows the study of large quantities of isotope with an excellent energy resolution.

The most used techniques with a calorimetric approach are solid state detectors, phonon detectors and scintillators. Solid state detectors and phonon detectors allow to achieve excellent energy resolutions (less than 1% in the region of interest) and also give the possibility to build massive experiments (up to 1 ton). The bolometric technique has also the advantage that a wide choice of different materials can be used as absorber. This last feature is very important since in the case of $0\nu$DBD searches it could allows to cross check a possible evidence on different isotopes.

Bolometers can be essentially sketched as a two-component object: an energy absorber in which the energy deposited by a particle is converted into phonons and a sensor that converts thermal excitations into a readable signal. The absorber must be coupled to a constant temperature bath so the accumulated heat flows to the heat sink and the absorber returns to the base temperature with a time constant that, in first approximation, is $\tau = \mathrm{C/G}$, where C is the heat capacity of the bolometer and G is the thermal conductance of the link. The temperature variation induced by an energy release E in the absorber can be then written as

$$\Delta T\,(t) = \frac{E}{C} e^{-\frac{t}{\tau}}. \tag{6}$$

In order to obtain a measurable temperature rise the heat capacity of the absorber must be very small: this is the reason why bolometers need to be operated at cryogenic temperatures (of the order of 10-100 mK).

As mentioned above, the bolometric technique allows to study a wide variety of $0\nu$DBD candidates. The choice of the $^{130}$Te (Q-value $2527.5 \pm 0.013$ keV [5]) comes from a good compromise between differ-

ent requirements that characterize a $0\nu$DBD experiment. First of all the high natural abundance that allows to reach an high sensitivity even without enrichment which is expensive and difficult.

Once decided the isotope, the tellurium dioxide ($TeO_2$) was chosen as absorber. This choice is motivated by the favorable characteristics of these crystals if compared with Te ones (higher Debye temperature, better mechanical properties and good intrinsic radiopurity).

## 3. Cuoricino

The Cuoricino experiment, operated at the Laboratori Nazionali del Gran Sasso (LNGS) from early 2003 to June 2008, was a $^{130}$Te-based search for $0\nu$DBD. It consisted of an array of 62 $TeO_2$ bolometers with a total mass of 40.7 kg.

Cuoricino, thanks to its very low background level of $0.169 \pm 0.006$ counts/keV/kg/y in the Region Of Interest (ROI), allowed to reach the best sensitivity on $0\nu$DBD of $^{130}$Te ever obtained [6] and it was an important benchmark for CUORE. In addition to providing important information on the underground operation of a large array of bolometers, Cuoricino allowed to study in detail the different sources of spurious counts that limit the sensitivity of bolometric experiments. In particular Cuoricino has given strong indications of the existence of an important contribution to the background in the $0\nu$DBD region due to surface contamination of the setup materials.

In Figure 1 the Cuoricino single-hit (anticoincidence between crystals) background spectrum is reported. For the sake of clarity in the figure the two regions in which the background is predominantly caused by gamma particles or alpha particles are shown. Above 2615 keV, a flat continuum with several $\alpha$ peaks is clearly visible. The origin of the flat continuum is still a delicate issue. The most likely guess is that the flat continuum between 3-4 MeV can be ascribed to interactions of degraded $\alpha$ coming from the surfaces of the copper frames or of the crystals. Extending to lower energies, the flat continuum can give significant contributions to the background counting rate in the ROI.

No evidence of a $0\nu$DBD signal is found in the analyzed data. By applying a maximum likelihood procedure we obtain a 90% lower

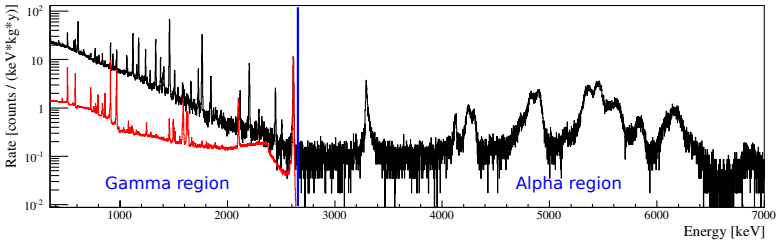


Fig. 1: Cuoricino single-hit (anticoincidence between crystals) background spectrum (black). The total energy spectrum of all Cuoricino detectors during calibration measurements is also shown (red). For convenience it is normalized to have the same intensity of the 2615 keV line of $^{208}$Tl as measured in the background spectrum. In the figure the two regions in which the background is predominantly caused by gamma particles or alpha particles are shown

limit for the lifetime set to:

$$T^{0\nu}_{1/2}(^{130}\mathrm{Te}) \geq 2.8 \times 10^{24} \quad \text{years} \quad (90\%\text{C.L.})$$

The evaluation of an upper limit for the effective Majorana mass is strictly related to the Nuclear Matrix Elements. Using the latest calculations by different authors [6] the lower limit on the effective Majorana mass fixed by Cuoricino is in the range:

$$\langle m_{\beta\beta} \rangle < 300\text{-}710 \quad \text{meV}$$

## 4. CUORE-0

CUORE-0 will consist of 52 CUORE-type crystals, selected from the already available CUORE crystals. The bolometers will be stacked in 13 planes into a single CUORE-like tower operated in the refurbished Cuoricino cryostat. The total mass of $^{130}$Te will be about 11 kg. CUORE-0 main purpose is to test the assembly procedure, the gluing and the wiring for CUORE but it will be also a sensitive $0\nu$DBD experiment in its own right. With an expected energy resolution in the ROI of 5 keV, CUORE-0 may improve the current Cuoricino limit on $0\nu$DBD by a factor of two within 1.5 y of live time. Preparations for CUORE-0 are on schedule and data taking will start within 2011.

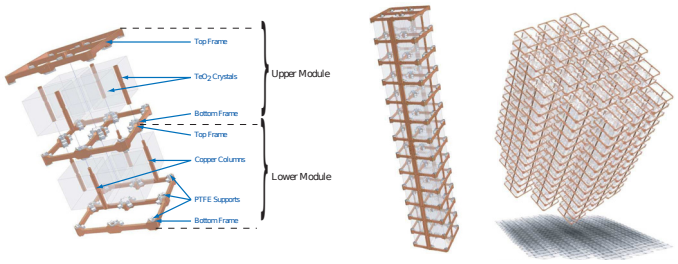


Fig. 2: The CUORE modular structure. On the left: two contiguous floors composed by four $5 \times 5 \times 5$ cm$^3$ crystals each. At the center: a CUORE tower in which 13 single modules are held together. On the right: the entire CUORE detector built of 19 towers

## 5. CUORE

The CUORE (Cryogenic Underground Observatory for Rare Events) experiment [7] is the natural evolution of Cuoricino. It aims at searching for $0\nu$DBD of $TeO_2$ with an effective Majorana mass sensitivity of a few tens of meV. It is presently under construction in the Hall A of the Gran Sasso Underground Laboratory.

The CUORE detector is an array of 988 cryogenic bolometers arranged in 19 vertical towers for a total mass of 741 kg, corresponding to 206 kg of $^{130}$Te. In Figure 2 the single module (i.e. one floor of one CUORE tower), the single tower and the entire CUORE detector are reported.

The experiment will take great advantage from the tightly packed structure thanks to the high background rejection capability that can be obtained by operating the detectors in anti-coincidence mode.

Assuming to reach the CUORE background goal of $< 10^{-2}$ counts/keV/kg/year, after 5 years of live time, CUORE has a $1\sigma$ sensitivity to the $0\nu$DBD half-life of $T^{0\nu}_{1/2} = 1.6 \times 10^{26}$ y and thus a potential to probe the effective Majorana neutrino mass down to 41-95 meV [8].

In 2009 the production of CUORE crystals started at SICCAS Jiading with a production capacity of about 30 crystals/month [9]. The production of crystals is systematically controlled and each production phase is certified. Very strict certification conditions were

applied for the dimensions of the crystals and for the quality of surface processing. Moreover, a dedicated cryogenic setup, the CUORE Crystals Validation Runs (CCVR), mounted and operated in Hall C of LNGS is used to test $TeO_2$ crystals. The tests are performed on crystals randomly chosen from each production batch and is aimed at checking the radioactive contamination level of crystals and their bolometric performance. Limits on crystals bulk contaminations obtained with these bolometric tests are well below the concentration limits requested for $TeO_2$ crystals to be used in CUORE experiment [9].

The CUORE cryostat is made of six nested vessels and its base temperature is expected to be as low as 6 mK. Three lead shields are used to protect the detector from environmental radioactivity and from contaminations in the building materials. A 25 cm thick octagonal lead layer outside the cryostat shields the detector from radiations coming from the bottom and from the sides. An equivalent shielding against radiation coming from the top is placed inside the cryostat, just above the detector. This is a 30 cm thick lead disk with a diameter of about 90 cm. Just below it, copper disks totaling an additional 8 cm shields are placed. An additional shielding of detector's sides and bottom is provided by a 6 cm lead layer. Outside the external lead shield a 18 cm thick polyethylene layer will be added in order to thermalize environmental neutrons that will then be absorbed by a 2 cm layer of $H_3BO_3$ powder contained in the hollow space between the lead and the polyethylene itself.

1. A. Strumia and F. Vissani, hep-ph/0606054.
2. Z. Maki, M. Nakagawa, and S. Sakata, Prog. Theor. Phys. **28**, 870 (1962).
3. Ch. Kraus, Eur. Phys. J. C **40**, 447 (2005);
   V.M. Lobachev, Nucl. Phys. B (Proc Suppl.) **91**, 280 (2001).
4. M. Fukugita *et al.*, Phys. Rev. D **74**, 027302 (2006).
5. M. Redshaw *et al.* Phys. Rev. Lett. **102**, (2009) 212502;
   N.D. Scielzo *et al.*, Phys. Rev. C **80**, 025501 (2009).
6. E. Andreotti *et al.*, Astropart. Phys. **34**, 822 (2011).
7. C. Arnaboldi *et al.*, NIM A **518**, 775 (2004).
8. F. Alessandria *et al.*, Submitted to Astropart. Phys., arXiv:1109.0494.
9. C. Arnaboldi *et al.*, Journal of Crystal Growth **312**, 2999 (2010).

# NEUTRINO OSCILLATIONS IN THE MINOS EXPERIMENT

Katarzyna Grzelak[1]
(for the MINOS Collaboration)

[1] *University of Warsaw, Faculty of Physics,*
*ul. Hoża 69, 00-681 Warsaw, Poland,*
*e-mail: Katarzyna.Grzelak@fuw.edu.pl*

**Abstract**

This contribution to the proceedings summarizes the latest results from the MINOS experiment. The experiment uses an intense neutrino beam optimized for $\nu_\mu$ or $\overline{\nu}_\mu$ production and two detectors: one located at Fermilab, and one situated 735 km away from Fermilab at the Soudan underground laboratory in Minnesota, to study the phenomenon of neutrino oscillations. By observing disappearance of $\nu_\mu$ ( $\overline{\nu}_\mu$) from the beam, MINOS can measure the oscillation parameters: atmospheric neutrino mass splitting $\Delta m^2$ ($\Delta \overline{m}^2$) and $\sin^2(2\theta_{23})$ ($\sin^2(2\overline{\theta}_{23})$). The result of a search for $\nu_e$ appearance in the $\nu_\mu$ beam is also reported.

## 1. Introduction

The MINOS experiment uses an intense accelerator beam of neutrinos to make the precise measurement of neutrino oscillation parameters that were first determined in interactions of atmospheric neutrinos [1]. In this region, the neutrino oscillations are dominated by the channel $\nu_\mu \to \nu_\tau$, but it is possible that a small fraction of muon neutrinos oscillates into electron neutrinos. The experiment studies the phenomenon of disappearance of muon neutrinos or muon antineutrinos from the beam. It also searches for the appearance of electron neutrinos due to the sub-dominant $\nu_\mu \to \nu_e$ oscillation mode.

The neutrino beam is produced at Fermilab and directed into two MINOS detectors [2]: Near (ND) situated 1km down the beamline

and Far (FD) situated 735 km away from Fermilab at the Soudan underground laboratory in Minnesota. Both MINOS detectors are tracking, sampling calorimeters composed of 2.54cm thick planes of iron and 1cm thick planes of plastic scintillator. The reported results are based on an exposure of $7.25 \times 10^{20}$ ($2.95 \times 10^{20}$) protons on target for the $\nu_\mu$ ($\overline{\nu}_\mu$) disappearance analysis and $8.2 \times 10^{20}$ protons on target for $\nu_e$ appearance analysis. All measurements were performed according to the rules of blind analysis.

## 2. Disappearance of Muon Neutrinos and Antineutrinos

The probability of disappearance of muon neutrinos from the beam, in the model of neutrino oscillations can be described by the approximated formula:

$$P(\nu_\mu \to \nu_\mu) \simeq 1 - \sin^2(2\theta_{23}) \sin^2 \frac{1.27 \Delta m^2 L}{E_\nu},$$

where $E_\nu$[GeV] is the neutrino energy and $L$[km] is the distance from the target. Thus, from the $\nu_\mu$ disappearance analysis the two parameters of the neutrino oscillation model: $\Delta m^2$ and $\sin^2(2\theta_{23})$ can be derived. Similarly, the $\overline{\nu}_\mu$ disappearance analysis gives access to parameters $\Delta \overline{m}^2$ and $\sin^2(2\overline{\theta}_{23})$.

Muon neutrinos (antineutrinos) can be detected by looking for the products of the interactions $\nu_\mu(\overline{\nu}_\mu) + Fe \to \mu^-(\mu^+) + X$. The characteristic feature of such interactions is the presence of a long, muon track emerging from the hadronic shower $X$. The neutrino energy is reconstructed as the sum of the muon energy and energy of the hadronic shower. The reconstructed neutrino energy distribution in the Far Detector and the ratio of the FD data and the expected spectrum for an exposure of $7.25 \times 10^{20}$ protons on target are shown in Figure 1. The energy spectrum is compared to the Monte Carlo predictions with and without oscillations. The shaded area shows the predicted background. The resulting best fit of the oscillation model gives $|\Delta m^2| = (2.32^{+0.12}_{-0.08}) \times 10^{-3}\text{eV}^2$ and $\sin^2(2\theta_{23}) > 0.90$ (90% confidence level) [3].

MINOS has previously made the first direct measurement of oscillation parameters for muon antineutrinos [4]. The data has been

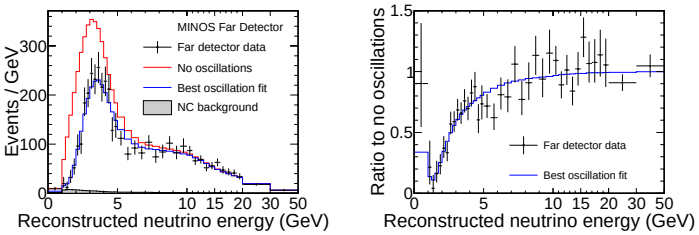


Fig. 1: Left: Comparison of the reconstructed neutrino energy spectrum in the Far Detector with the predictions for the $\nu_\mu$-CC energy distributions with and without oscillations. The shaded area shows the predicted background. Right: Ratio of the FD data and the expected $\nu_\mu$ energy spectrum in the absence of oscillations. Line represents the best oscillation fit curve

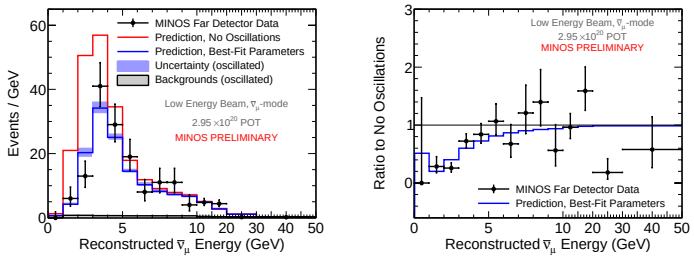


Fig. 2: Left: Comparison of the reconstructed neutrino energy spectrum in the Far Detector with the predictions for the $\overline{\nu}_\mu$-CC energy distributions with and without oscillations. The band around the oscillated prediction represents the total systematic uncertainty. Right: Ratio of the FD data and the expected $\overline{\nu}_\mu$ energy spectrum in the absence of oscillations. Line represents the best oscillation fit curve

taken with the beam optimized for $\overline{\nu}_\mu$ production. Assuming identical $\nu_\mu$ and $\overline{\nu}_\mu$ oscillation parameters, the MINOS measurements for muon neutrinos and muon antineutrinos were consistent at the 2.0% confidence level. Presented results are for an increased exposure from $1.71 \times 10^{20}$ to $2.95 \times 10^{20}$ protons on target. The reconstructed neutrino energy distribution in the Far Detector and the ratio of the FD data and the expected spectrum for an exposure of $2.95 \times 10^{20}$ protons on target are shown in Figure 2. The energy spectrum is compared to the Monte Carlo predictions with and without oscillations. The resulting best fit of the oscillation model gives $|\Delta m^2| = (2.62^{+0.31}_{-0.28}(\text{stat}) \pm 0.09(\text{syst})) \times 10^{-3}\text{eV}^2$ and

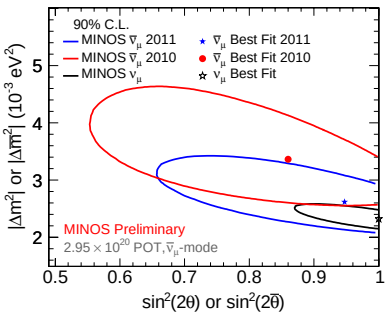


Fig. 3: Comparison of the allowed regions and best fits for the $\overline{\nu}_\mu$ parameters from the 2010 and 2011 analyses. The MINOS allowed region for $\nu_\mu$ oscillation is also shown

$\sin^2(2\overline{\theta}_{23}) = 0.95^{+0.10}_{-0.11}(\text{stat}) \pm 0.01(\text{syst})$ Figure 3 shows the allowed regions for the antineutrino oscillations parameters for the old and new antineutrino results, compared to the MINOS allowed region for neutrino oscillations. MINOS measurements for muon neutrinos and muon antineutrinos are now consistent at the 42% confidence level.

## 3. Appearance of Electron Neutrinos

Observation of electron neutrino appearance in the beam of muon neutrinos, in the atmospheric oscillation domain, would imply a non-zero value of the mixing angle $\theta_{13}$. The probability of $\nu_e$ appearance, $P(\nu_\mu \to \nu_e)$, is expressed by the formula that depends not only on $\theta_{13}$, but also on the unknown CP-violation phase $\delta_{CP}$, on the neutrino mass hierarchy and other parameters of the neutrino oscillation model.

Electron neutrinos can be detected by looking for the products of the interactions $\nu_e + Fe \to e^- + X$. In MINOS, electrons are expected to produce compact showers, spanning only a few planes and strips. The reconstructed energy distribution in the Far Detector for an exposure of $8.2 \times 10^{20}$ protons on target is shown in Figure 4. The black points represent the data. The histogram shows the expected background (unfilled area) and the contribution of $\nu_\mu \to \nu_e$ signal (filled area) for the best-fit value of $\sin^2(2\theta_{13}) = 0.041$. The largest background to the search originate from the neutral current

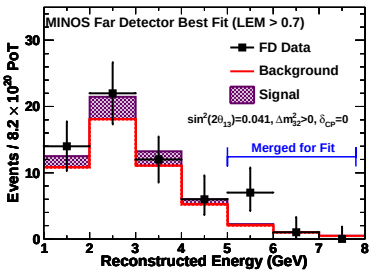


Fig. 4: Reconstructed neutrino energy spectrum for the $\nu_e$-CC candidate events in the Far Detector. The black points represent the data. The histogram shows the expected background (unfilled area) and the contribution of $\nu_\mu \to \nu_e$ signal (filled area) for the best-fit value of $\sin^2(2\theta_{13}) = 0.041$

interactions. Smaller background is related to the intrinsic electron neutrino component of the beam and charged current $\nu_\mu$ interactions where most of the energy is transferred into hadronic state. Additional background component in the Far Detector is due to the charged current interactions of tau neutrinos from the $\nu_\mu \to \nu_\tau$ oscillations. Figure 5 shows the allowed ranges and best fits as a function of CP-violation phase $\delta$ for normal and inverted neutrino mass hierarchy. The dashed line indicates the CHOOZ 90% C.L. upper limit [6]. The results of a search for $\nu_e$ appearance in the $\nu_\mu$ beam give the upper limit of $2\sin^2(\theta_{23})\sin^2(2\theta_{13}) < 0.12(0.20)$ at 90% confidence level for $\delta_{CP} = 0$ and the normal (inverted) neutrino mass hierarchy.

## 4. Conclusions

The MINOS experiment performed the measurement of atmospheric parameters of the neutrino oscillation model, independently for muon neutrinos and muon antineutrinos. The resulting mass-squared differences are the most precise measurements to date. MINOS has also made the attempt to measure the mixing angle $\theta_{13}$. This study found that $2\sin^2(\theta_{23})\sin^2(2\theta_{13}) < 0.12(0.20)$ at 90% confidence level for $\delta_{CP} = 0$ and the normal (inverted) neutrino mass hierarchy. This result significantly constrains the $\theta_{13}$ range allowed by other experiments.

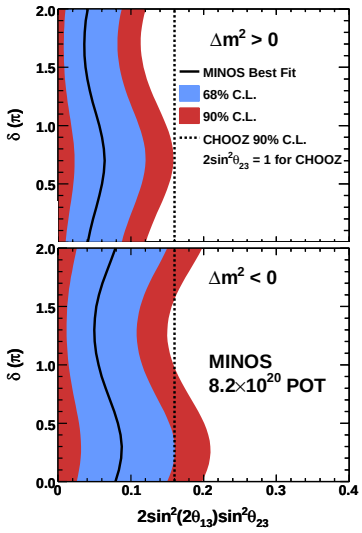


Fig. 5: Allowed regions and best fits for the $2\sin^2(\theta_{23})\sin^2(2\theta_{13})$ as a function of CP-violation phase $\delta$ for normal and inverted neutrino mass hierarchy. The dashed line indicates the CHOOZ 90% C.L. upper limit [6]

## Acknowledgements

This work was supported by the US DOE; the UK STFC; the US NSF; the State and University of Minnesota; the University of Athens, Greece, Brazil's FAPESP and CNPq and the Polish National Science Centre. We are grateful to the Minnesota Department of Natural Resources; the crew of the Soudan Underground Laboratory; and the staff of Fermilab for their contributions to this effort.

1. Y. Fukuda *et al.*, Phys. Rev. Lett. **81**, 1562 (1998).
2. D.G. Michael *et al.*, Nucl. Inst. Meth. A **596** (2008).
3. P. Adamson *et al.*, Phys. Rev. Lett. **106**, 181801 (2011).
4. P. Adamson *et al.*, Phys. Rev. Lett. **107**, 021801 (2011).
5. P. Adamson *et al.*, Phys. Rev. Lett. **106**, 181802 (2011).
6. M. Apollonio *et al.*, Eur. Phys. J. C **27**, 331 (2003).

# STATUS OF THE OPERA EXPERIMENT

Kaname Hamada
on behalf of the OPERA collaboration

*F-lab., Department of Physics, Nagoya University,*
*Furo-cho, Chikusa-ku, Nagoya-shi, Aichi-ken, 464-8602, Japan,*
*e-mail: khamada@flab.phys.nagoya-u.ac.jp*

**Abstract**

The OPERA experiment in the underground Gran Sasso Laboratory (LNGS) was designed to perform the first detection of neutrino oscillations in appearance mode through the $\nu_\mu \to \nu_\tau$ channel. The $\nu_\tau$ signature is provided by the identification of the $\tau$-lepton created in its charged current interaction. The OPERA hybrid apparatus consists of a large mass emulsion film/lead target complemented by electronic detectors. It is placed in the high energy long-baseline CERN to LNGS neutrino beam (CNGS) 730 km away from the neutrino source. The OPERA experiment is currently in data taking and analysis, and the first $\nu_\tau$ candidate event was observed in 2010. In this report, the status of the OPERA experiment and statistical significance of the first candidate observed so far are presented.

## 1. Introduction

In 1962, Maki, Nakagawa and Sakata proposed that oscillation may exist between massive neutrinos of different flavours [1]. In 1998, the Super-Kamiokande experiment established the deficit in atmospheric $\nu_\mu$ due to their disappearance through the oscillation mechanism [2].

The goal of OPERA is to detect $\nu_\mu \to \nu_\tau$ oscillation in the appearance mode in the CERN CNGS beam by detecting the decay topology of the $\tau$ induced in the $\nu_\tau$ charged current interactions [3].

OPERA is exposed to the long-baseline CNGS $\nu_\mu$ beam [4], 730 km away from the source. The beam is optimized for the observation

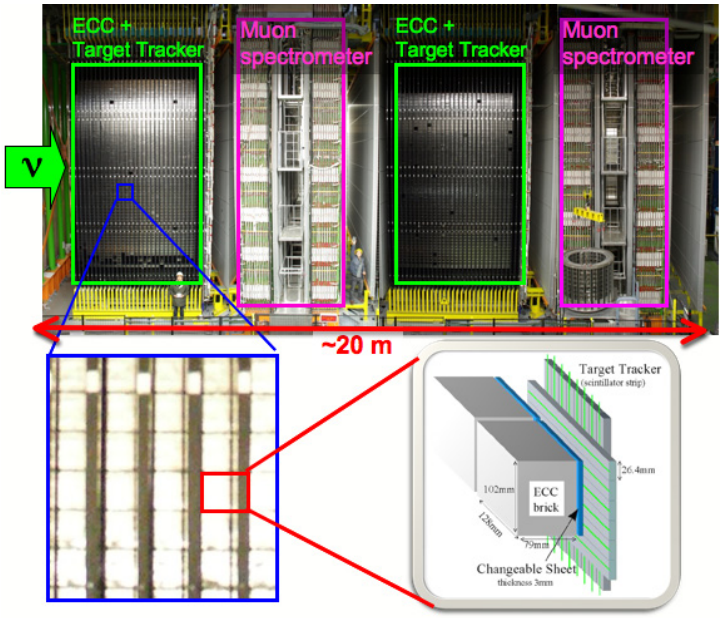


Fig. 1: The OPERA detector

of $\nu_\tau$CC interactions. The average neutrino energy is ∼17 GeV. The $\bar{\nu}_\mu$ contamination is 2.1% in terms of interactions, the $\nu_e$ and $\bar{\nu}_e$ contaminations are together lower than 1%, while the number of prompt $\nu_\tau$ is negligible.

## 2. The OPERA Detector

The challenge of the OPERA experiment is to achieve the very high spatial accuracy required for the detection of $\tau$ leptons (whose decay length is of the order of 1 mm in this experiment) inside a large-mass active target. The hybrid detector [5] is composed of two identical Super Modules (SM), each consisting of an instrumented target section of a mass of about 625 tons followed by a magnetic muon spectrometer (Fig. 1). A target section is a succession of walls filled with elements called bricks, interleaved with planes of scintillator strips, the Target Tracker (TT). The TT allows the initial localiza-

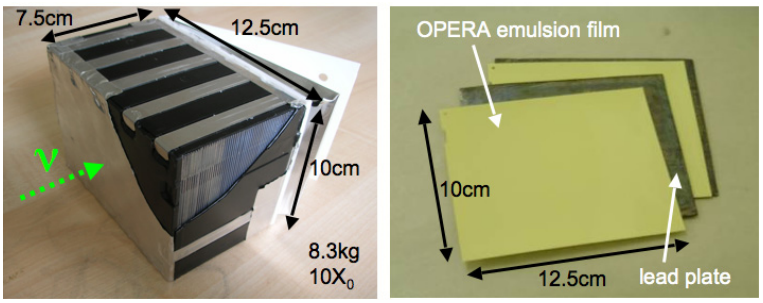


Fig. 2: An ECC brick, OPERA emulsion films and lead plates

tion of neutrino interaction by providing also its time stamp. A brick is an Emulsion Cloud Chamber (ECC) module consisting of 56 1 mm thick lead plates interleaved with 57 nuclear emulsion films (see Fig. 2). It weights 8.3 kg and its thickness corresponds to 10 radiation lengths along the beam direction. Tightly packed removable doublets of emulsion films called Changeable Sheets (CS) are glued to the downstream face of each brick. They serve as interfaces between the TT planes and the bricks to facilitate the location of neutrino interactions. Complex brick handling ancillary facilities are used to bring emulsion films from the target up to the automatic scanning microscopes [6].

An emulsion film is made of two layers of nuclear emulsion gel 44 $\mu$m thick deposited on each side of a 205 $\mu$m thick plastic base of $12.5 \times 9.9$ cm$^2$ [7]. A track of a minimum ionizing particle is shown in Fig. 3. Emulsion records charged particles as 3D tracks with submicron resolution. ECC technique is adequate to recognize $\tau$ decay topologies as proven by the DONuT experiment [8].

## 3. Location of Neutrino Interactons

The experiment is currently in the phase of its fourth year of data taking and of data analysis. The CNGS neutrino beam status shown in Table 1. The total number of protons on target was $12.65 \times 10^{19}$ as of 20 Aug. 2011. The results presented in this report are based on the decay search analysis of 2738 events from 2008 and 2009 samples.

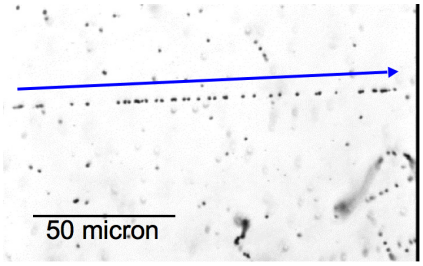


Fig. 3: The microscopic image of a Minimum Ionising Particle (M.I.P.) track in a developed emulsion film

In order to analyse the primary vertex a volume scan is performed over a 1 $cm^2$ area in at least 2 films upstream and 6 films downstream of the vertex lead plate. When a secondary vertex is found the kinematical analysis of the whole event is performed. This analysis makes use of the angles measured in the emulsion films, the momenta determined by multiple Coulomb scattering as measured in the brick, the momenta measured by the magnetic spectrometers, and the total energy deposited in the instrumented target acting as a calorimeter [9–11].

By applying this procedure, the first $\nu_\tau$ candidate event was observed in 2010, as reported in detail in [9].

## 4. Signal Detection Efficiencies and Physics Background

Charged charmed particles own lifetimes similar to that of the $\tau$ lepton and share analogous decay topologies. The finding efficiency of the decay vertices is therefore also similar for both types of particles. Comparing the observed charm event sample in size, decay topologies and kinematics with expectations from simulations constitutes a

**Table 1: Status of CNGS neutrino beam as of 20 Aug. 2011**

| Year | Beam days | Protons on target | Events in the bricks |
|---|---|---|---|
| 2008 | 123 | $1.78 \times 10^{19}$ | 1698 |
| 2009 | 155 | $3.52 \times 10^{19}$ | 3693 |
| 2010 | 187 | $4.04 \times 10^{19}$ | 4248 |
| 2011 | Ongoing | $3.31 \times 10^{19}$ | 3304 |

direct way to verify that prompt-decay selection criteria and their corresponding efficiencies as well as backgrounds evaluations. Recently published cross-sections by the CHORUS experiment [12] have been used in the simulation. The results of this comparison are shown in Table 2.

The expected numbers of events in the various $\tau$ channels for the nominal number of $22.5 \times 10^{19}$ p.o.t. and for the fraction of the 2008 and 2009 runs analysed so far are shown in Table 3. Full mixing and $\Delta m^2_{23} = 2.5 \times 10^{-3}$ eV$^2$ are assumed. The total number of signal events expected to be eventually detected has decreased from 10 as quoted in the experiment proposal [3] to 8. This reduction was essentially due to the lower efficiency in location of the interaction vertex resulting from a more reliable knowledge of the detector and of the analysis procedures.

The main source of background to all $\tau$ decay channels is constituted by charged charmed particles that decay into similar channels and are produced in $\nu_\mu$CC interactions where the primary muon is not identified.

The second main source of background in the $\tau \to h$ decay channel comes from one-prong inelastic interactions of primary hadrons pro-

**T a b l e 2: Comparison between charm event topologies observed and expected from simulations including background**

| Topology | Observed events | Expected events | | |
|---|---|---|---|---|
| | | Charm | Background | Total |
| Charged 1-prong | 13 | 15.9 | 1.9 | 17.8 |
| Neutral 2-prong | 18 | 15.7 | 0.8 | 16.5 |
| Charged 3-prong | 5 | 5.5 | 0.3 | 5.8 |
| Neutral 4-prong | 3 | 2.0 | $<0.1$ | 2.1 |
| Total | 39 | $39.1 \pm 7.5$ | $3.0 \pm 0.9$ | $42.2 \pm 8.3$ |

**T a b l e 3: Expected numbers of observed signal events for $22.5 \times 10^{19}$ p.o.t. and for the analysed sample of the data accumulated in the 2008 and 2009 runs**

| Decay channel | Number of signal events expected for | |
|---|---|---|
| | $22.5 \times 10^{19}$ p.o.t. | Analysed sample |
| $\tau \to \mu$ | 1.79 | 0.39 |
| $\tau \to e$ | 2.89 | 0.63 |
| $\tau \to h$ | 2.25 | 0.49 |
| $\tau \to 3h$ | 0.71 | 0.15 |
| Total | 7.63 | 1.65 |

duced in NC interactions, or in CC interactions where the primary lepton is not identified and in which no nuclear fragments can be associated with the secondary interaction. This has been evaluated with Monte Carlo Simulation and cross-checked with measurements (Fig. 4).

All background sources are summarized in Table 4. Systematic errors of 25% on charm background and of 50% on hadron and muon backgrounds are assumed. Errors arising from the same source are combined linearly, otherwise in quadrature.

## 5. Signal Statistical Significance

One $\nu_\tau$ candidate event is observed in the $\tau \to h$ decay channel that passes all the selection cuts; assuming full mixing and $\Delta m^2_{23} = 2.5 \times 10^{-3}$ eV$^2$ $0.49 \pm 12$ events are expected for this decay mode in the currently analysed sample . The background in this channel is estimated to be $0.05 \pm 0.01$(syst.) event. The probability of the event not to be due to a background fluctuations and thus the statistical significance of the observation is 95%. Considering all decay channels, the numbers of expected signal and background events are respectively $1.65 \pm 0.41$ and $0.16 \pm 0.03$(syst.), the probability for the event to be background being 15%.

**T a b l e 4: Expected numbers of observed background events from different sources for the nominal number of $22.5 \times 10^{19}$ p.o.t. and for the analysed sample of the data accumulated in the 2008 and 2009 runs. The quoted errors are systematic ones**

| Decay channel | Number of background events expected for | | | | | | | |
|---|---|---|---|---|---|---|---|---|
| | $22.5 \times 10^{19}$ p.o.t. | | | | Analysed sample | | | |
| | Charm | Hadron | Muon | Total | Charm | Hadron | Muon | Total |
| $\tau \to \mu$ | 0.025 | 0.00 | 0.07 | $0.09 \pm 0.04$ | 0.00 | 0.00 | 0.02 | $0.02 \pm 0.01$ |
| $\tau \to e$ | 0.22 | 0.00 | 0.00 | $0.22 \pm 0.05$ | 0.05 | 0.00 | 0.00 | $0.05 \pm 0.01$ |
| $\tau \to h$ | 0.14 | 0.11 | 0.00 | $0.24 \pm 0.06$ | 0.03 | 0.02 | 0.00 | $0.05 \pm 0.01$ |
| $\tau \to 3h$ | 0.18 | 0.00 | 0.00 | $0.18 \pm 0.04$ | 0.04 | 0.00 | 0.00 | $0.04 \pm 0.01$ |
| Total | 0.55 | 0.11 | 0.07 | $0.73 \pm 0.15$ | 0.12 | 0.02 | 0.02 | $0.16 \pm 0.03$ |

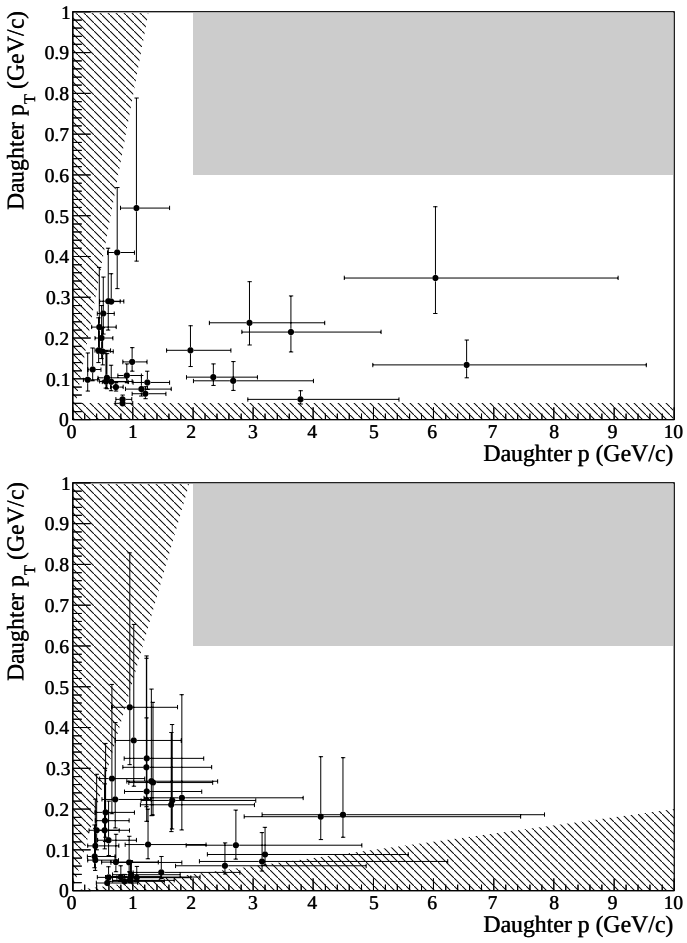


Fig. 4: Top: Scatter plot of $p_T$ vs. p of the daughter particle of single prong re-interactions of hadrons far from the neutrino interaction vertices where they are produced. Bottom: Scatter plot of $p_T$ vs. p of the daughter particle of single prong interactions of 4 GeV/c $\pi^-$. On both figures the dark area defines the domain in which $\tau$ decay candidates are selected and the hatched area defines the non-physical region $p < p_T$ together with the domain rejected by the selection cuts

## 6. Conclusions

The OPERA experiment is aiming at the first detection of neutrino oscillations in direct appearance mode where the oscillated neutrino is identified. The experiment is currently in the phase of its fourth year of data taking and of data analysis, and one $\nu_\tau$ candidate event was observed.

The results presented in this report are based on the decay search analysis of 2738 events from 2008 and 2009 samples. The observation of a $\nu_\tau$ candidate event is compatible with the expectation of 1.65 signal events. The significance of the observation of one decay in the $\tau \to h$ channel is 95%.


1. Z. Maki, M. Nakagawa and S. Sakata, Prog. Theor. Phys. **28**, 870 (1962).
2. Super-Kamiokande Collaboration, Y. Fukuda *et al.*, Phys. Rev. Lett. **81**, 1562 (1998).
3. OPERA Collaboration, M. Guler *et al.*, CERN-SPSC-2000-028, LNGS P25/2000.
4. Ed. K. Elsener, The CERN Neutrino beam to Gran Sasso (Conceptual Technical Design), CERN 98-02, INFN/AE-98/05;
   R. Bailey *et al.*, The CERN Neutrino beam to Gran Sasso (NGS) (Addendum to report CERN 98-02, INFN/AE-98/05), CERN-SL/99-034(DI), INFN/AE-99/05.
5. OPERA Collaboration, R. Acquafredda *et al.*, JINST **4**, P04018 (2009).
6. K. Morishima and T. Nakano, JINST **5**, P04011 (2010);
   N. Armenise *et al.*, Nucl. Instrum. Meth. A **551**, 261 (2005);
   M. De Serio *et al.*, Nucl. Instrum. Meth. A **554**, 247 (2005);
   L. Arrabito *et al.*, Nucl. Instrum. Meth. A **568**, 578 (2006).
7. T. Nakamura *et al.*, Nucl. Instrum. Meth. A **556**, 80 (2006).
8. DONuT Collaboration, K. Kodama *et al.*, Phys. Lett. B **504**, 218 (2011).
9. OPERA Collaboration, N. Agafonova *et al.*, Phys. Lett. B **691**, 138 (2010).
10. OPERA Collaboration, N. Agafanova *et al.*, New J. Phys. **13**, 053051 (2011).
11. OPERA Collaboration, N. Agafanova *et al.*, arXiv:1106.6211 [physics.ins-det], submitted to New J. Phys.
12. CHORUS Collaboration, A. Kayis-Topaksu *et al.*, CERN-PH-EP-2011-109, arXiv:1107.0613 [hep-ex], submitted to New J. Phys.

# A SEARCH FOR A TIME-REVERSAL VIOLATING TRANSVERSE MUON POLARIZATION USING STOPPED $K^+ \to \pi^0 \mu^+ \nu$ DECAY AT J-PARC

Michael D. Hasinoff
for the TREK (E06) collaboration

*University of British Columbia,*
*Vancouver, BC, V6T 1Z1, Canada*
*e-mail: hasinoff@physics.ubc.ca*

**Abstract**

We are preparing a new experiment to search for time-reversal violation by measuring the transverse muon polarization ($P_T$) in $K^+ \to \pi^0 \mu^+ \nu$ decay at J-PARC. The physics potential in terms of the discovery of new physics is competitive with other experiments currently being prepared. The detector system will be an upgraded version of our previous KEK-PS E246 experiment which should produce $\delta P_T \sim 10^{-4}$.

## 1. Introduction

The Standard Model (SM) of subatomic physics provides an incredibly successful description of all the existing experimental data. Nevertheless it is not thought to be the complete theory; it contains 26 free parameters including the non-zero neutrino masses and the CP-violating phase in the Cabbibo-Kobayashi-Maskawa (CKM) matrix. Numerous extensions to the SM have been proposed; most contain additional imaginary phases since it is well known that the CKM CP-violation is not large enough to explain the Baryonic Asymmetry

of the Universe [1]. Since any Lorentz invariant field theory is expected to conserve CPT, a non-zero measurement of Time-Reversal Violation (TRV) implies a corresponding CP-violation; therfore TRV searches can also reveal new sources of CPV [2].

The transverse muon polarization $P_T = \hat{s}_\mu \cdot (\hat{p}_{\mu^+} \times \hat{p}_{\pi^o})$ in $K^+ \to \pi^0 \mu^+ \nu$ ($K_{\mu 3}$) decay is a T-odd triple product correlation. This was first suggested by Sakurai [3] as a clear signature of TRV since the final state interactions (FSI), which arise from higher order loops in the electromagnetic interaction, are small ($\sim 10^{-5}$). Even more important is the fact that the SM contribution to $P_T$ is considerably smaller ($\sim 10^{-7}$). Therefore, a $P_T$ search is a search for physics beyond the SM. Various extensions to the SM such as multi-Higgs doublets, leptoquarks, R-parity violating-SUSY or squark-family mixing-SUSY allow $P_T$ values as large as $\sim 10^{-3}$, just below the current experimental limit from our previous E246 experiment [4] at KEK. In the (V-A) theory of the SM the $K^+_{\mu 3}$ hadronic decay matrix element can be written in terms of two form factors, $\mathrm{f}_\pm(q^2)$. Since the strong interaction conserves CP both these form factors must be real. Hence, if the ratio $\xi(q^2) = \mathrm{f}_-(q^2)/\mathrm{f}_+(q^2)$ has a non-zero imaginary component this TRV effect will imply the presence of a new scalar(S) or tensor(T) interaction. $P_T$ is related to $\mathrm{Im}(\xi)$ by a kinematic factor which has been carefully optimized for our experiment.

## 2. Time-Reversal Violation Experiment with Kaons (TREK) at J-PARC

Our new T-violation experiment at J-PARC [5] is based on an upgrade of our previous E246 detector [6]. TREK will have about ten times more acceptance, twenty times more integrated beam flux and a substantially improved analyzing power compared to E246. This will produce a factor of $\sim$20 improvement in sensitivity ($\delta P_T \sim 10^{-4}$), which will put the experiment well into the region where new physics effects might appear.

In order to optimize the performance of the experimental system, several improvements to the detector system are now underway. The principal concept of the experiment, namely the use of a stopped $K^+$ beam with the application of the muon field in the azimuthal direction

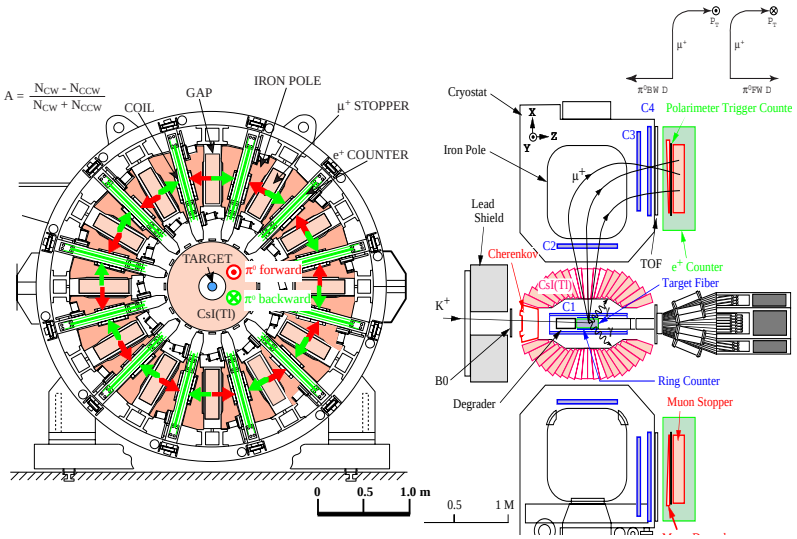


Fig. 1: End (and side) views of the superconducting toroidal spectrometer (STS) used in E246

parallel to the $P_T$ component is being retained. The following modifications (in relative order of importance) are being implemented: 1) an active muon polarimeter with a more uniform magnetic field for muon spin preservation, 2) two new central region GEM chambers for improved charged particle tracking, 3) a new $K^+$ scintillating fibre target with finer segentation, 4) an avananche photo-diode (APD) and faster amplifier for the CsI(Tl). Our detailed simulations indicate that a one year run at J-PARC with the new detector should provide a statistical and systematic accuracy of $\sim 10^{-4}$.

The most important upgrade item is the adoption of an active polarimeter and a new muon holding field magnet. This will allow a determination of the muon stopping position for each event which renders the experiment free from the background and systematic error associated with the ambiguities in the muon stopping distribution. This large acceptance ($\sim 3\pi$) polarimeter will measure both the positron energy and the emission angle and it will greatly increase the analyzing power. A uniform 0.03 T magnetic field will be applied at the muon stopping position in order to ensure the preservation of the

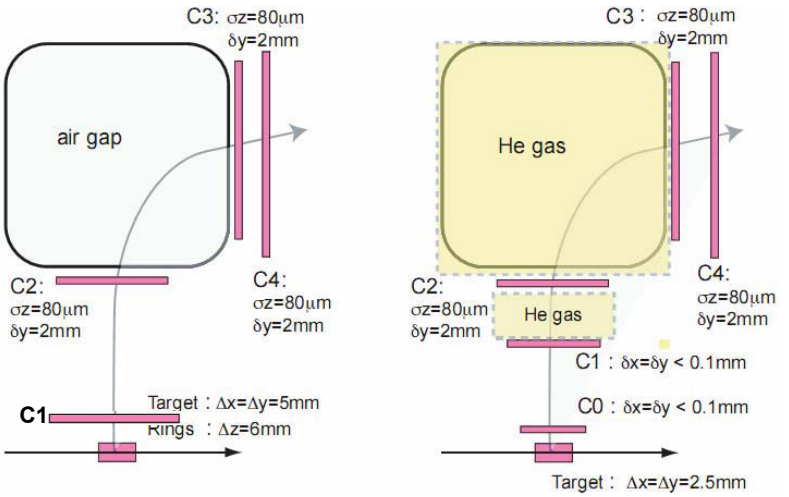


Fig. 2: Comparison of the tracking elements in E246 and TREK. By adding the new GEM chambers C0 & C1 we will be able to improve the track resolution and reduce the kaon decay-in-flight ($K_{\pi 2}$-*dif*) background

muon spin polarization by decoupling it from any ambient stray magnetic fields. Two drift chamber designs (with parallel plates or muon tubes) have been tested using full scale prototypes and a one sector prototype magnet has also been constructed. The data analysis for the muon tube polarimeter is now underway.

For the new TREK experiment at J-PARC one of the most serious systematic errors will be the background contamination from kaon decay-in-flight ($K_{\pi 2}$-*dif*) events. In order to improve the tracking resolution we will add a new high-rate cylindrical GEM tracking chamber with a spatial resolution better than 0.1 mm around the target system plus 12 new GEM planar tracking chambers with $< 0.1$ mm resolution at the outer surface of the CsI calorimeter as shown in Fig. 2. Detailed simulations indicate that the kaon decay-in-flight ($K_{\pi 2}$-*dif*) fraction in the $K_{\mu 3}$ data should be $\sim 0.2\%$, which is small enough to reduce the resulting systematic error below $\delta P_T = 10^{-4}$.

The new scintillating fibre target ($\phi = 7.5$ cm) will consist of 492 square fibres (3.0 mm). Each fibre will be read out using a new Hamamatsu MPPC. These small solid state PMTs offer the advantage

of compactness and low cost compared to either conventional single or multi-anode PMTs.

Given the higher beam rate at J-PARC, we will need to employ avalanche photo-diodes (APD) with a faster current preamplifier for the upgraded CsI(Tl) readout. The output from the amplifier system will be digitized by FADCs, which will provide a powerful method to resolve pulse pileup.

With these detector upgrades the total systematic error will be suppressed to below $10^{-4}$. In E246, one of the largest contributions to the systematic error was the muon field alignment. The rotation ($\delta_z$) around the z ($K^+$-beam) axis is the most troublesome introducing $\delta P_T \sim 5\times10^{-4}$ because its effect cannot be cancelled using the normal fwd $-$ bwd subtraction scheme. Since the precision of the magnetic field measurement ($\sim$1 mr) with a Hall probe is not sufficient to reduce the systematic uncertainty to the desired value, we plan to determine the $\delta_z$ misalignment using experimental data.

In order to reduce this systematic uncertainty, we will utilize a new analysis method using the arbitrary initial muon spin phases at the polarimeter ($\theta_0$). The time integrated asymmetry due to any possible detector misalignments is a simple function of $\theta_0$ namely, $A(\theta_0) = \delta_r \cos\theta_0 - \delta_z \sin\theta_0$ where $\delta_r$ is the effect from a field rotation around the radial direction. We can then calculate two asymmetries $A_{\rm sum}$ and $A_{\rm diff}$ as the sum and difference of $A_{\rm fwd}$ and $A_{\rm bwd}$ using the measured asymmetries for forward and backward pions, respectively. This leads to

$$A_{\rm sum}(\theta_0) = [A_{\rm fwd}(\theta_0) + A_{\rm bwd}(\theta_0)]/2 = \delta_r \cos\theta_0 - \delta_z \sin\theta_0, \quad (1)$$

$$A_{\rm diff}(\theta_0) = [A_{\rm fwd}(\theta_0) - A_{\rm bwd}(\theta_0)]/2 = F(P_T, \theta_0), \quad (2)$$

where $F(P_T, \theta_0)$ is the $A_T$ asymmetry arising from a non-zero $P_T$. We obtain no effects of $P_T$ in $A_{\rm sum}$ and no effects of misalignments in $A_{\rm diff}$, thereby enabling a very clean extraction of a small $P_T$ signal even with finite magnetic field misalignments.

## 3. Progress Report

We have cut and polished the ends of the 500 scintillator bars in the TRIUMF scintillator shop. We then milled a 1 mm groove along one side of each bar into which was glued a 1.4 m long Kuraray Y-11

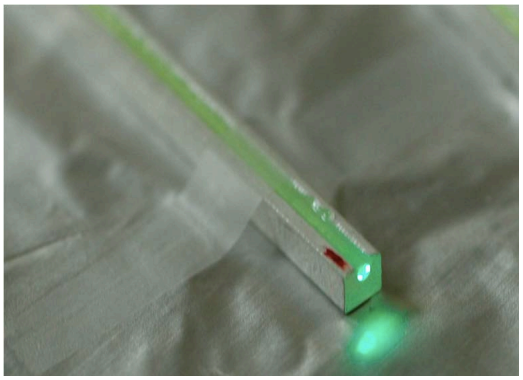

Fig. 3: Green WLS fibre glued into a 3mm scintillating bar

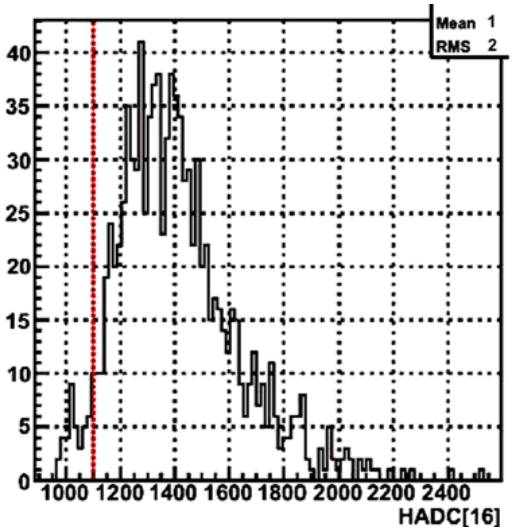


Fig. 4: Energy spectrum for penetrating cosmic rays passing through one 3mm square scintillator bar

WLS; the far end was then connected to a Hamamatsu MPPC using the same coupling system developed for the T2K FGD. Fig. 3 shows a picture of the green WLS fibre glued into the 3 mm scintillating bar and Fig. 4 shows the energy deposited in 1 bar by pass through

cosmic rays. The average energy deposited in 3 mm ($\sim 0.6$ MeV corresponds to $\sim 18$ photo electrons(pe)); hence we observe an overall light output of $\sim 30$ pe/MeV. The detection efficiency for minimum ionizing particles with a threshold cut of $\sim 5$ pe is 97%.

## 4. Summary

We are currently preparing a new experiment to search for Time-Reversal Violation at J-PARC by measuring the transverse muon polarization ($P_T$) in $K^+ \to \pi^0 \mu^+ \nu$ decays with a stopped $K^+$ beam. The detector system is an upgraded version of our previous KEK-PS E246 experiment. The improved detector will reduce both the statistical and the systematic errors by a factor of $\sim 20$, which will allow us to explore the region between the current upper limit $\sim 2 \times 10^{-3}$ down to the $10^{-4}$ level with a total experimental uncertainty of $10^{-4}$. This will either reveal new physics or, at the very least, provide more stringent constraints on the many various extentions to the current SM theory.

### Acknowledgements

This work is supported by the Natural Sciences and Engineering Research Council of Canada (NSERC).

1. A.D. Sakharov, Pisma Zh. Eksp. Teor. Fiz. **5**, 32 (1967) [JETP Lett. **5**, 24 (1967)].
2. I.I. Bigi and A.I. Sanda, *CP Violation* (Cambridge University Press, 2000).
3. J.J. Sakurai, Phys. Rev. **109**, 980 (1957).
4. M. Abe *et al.*, Phys. Rev. Lett. **93** 131601 (2004); Phys. Rev. D **73** 072005 (2006).
5. TREK proposal-http://j-parc.jp/NuclPart/pac_0606/pdf/p06-Imazato_2.pdf
6. M. Abe *et al.*, Nucl. Inst. & Meth A **506**, 60 (2003).

# MINIBOONE, A SHORT BASELINE NEUTRINO OSCILLATION EXPERIMENT AT FERMILAB

Teppei Katori for the MiniBooNE collaboration

*Massachusetts Institute of Technology, USA*

**Abstract**

The Mini-Booster Neutrino Experiment (MiniBooNE) is a short baseline $\nu_\mu \to \nu_e$ ($\bar{\nu}_\mu \to \bar{\nu}_e$) neutrino oscillation experiment at Fermilab, USA. The primary goal is to confirm or refute the oscillation signal observed at the LSND experiment at Los Alamos [1] under the two massive neutrino model. For the neutrino mode analysis, there is no excess of $\nu_e$ candidate event over background in the energy region where one expects signals with $\Delta m^2_{\rm LSND} \sim 1$ eV$^2$, but more than $3\sigma$ excess is observed in the low energy region [2]. This excess is not explained by known systematics. For the anti-neutrino mode, we again observe a $\bar{\nu}_e$ excess in the low energy region, and moreover, we also observe an excess in the energy region where we expect an excess from LSND-like neutrino mass splitting, $\Delta m^2_{\rm LSND}$ [3]. The latest update, in summer 2011 shows a lower significance with the two massive neutrino model over the null hypothesis, but the compatibility with the model is higher. however, a model-independent analysis shows the excess of $\bar{\nu}_e$ candidate events in the full energy region is incompatible with the null hypothesis at $2\sigma$ level.

## 1. MiniBooNE Experiment

The MiniBooNE experiment uses the Booster Neutrino Beam (BNB) to produce a mostly $\nu_\mu$ ($\bar{\nu}_\mu$) neutrino beam. The neutrinos are detected by the MiniBooNE detector, a spherical tank mineral oil-based Cherenkov detector. Figure 1 shows a schematic overview of the MiniBooNE experiment.

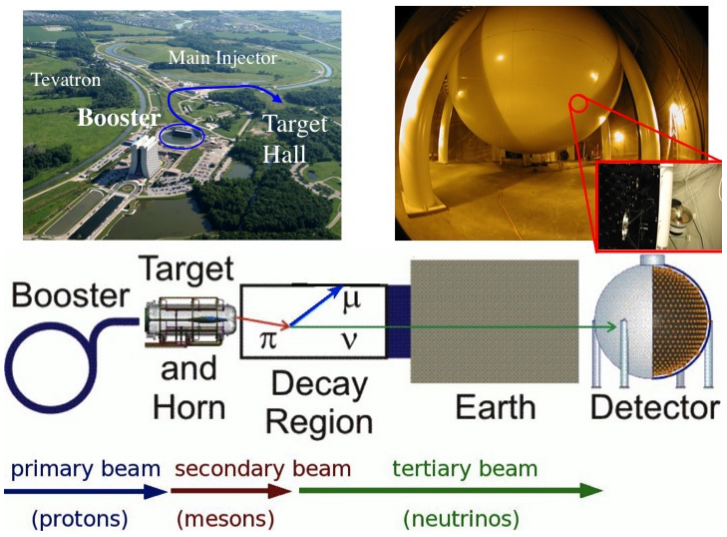


Fig. 1: The overview of the MiniBooNE experiment. The top left is a picture of the Fermilab, including the Booster and the target hall. The top right is a picture of MiniBooNE detector, inserted picture shows inside of the detector, black inner tank region and white outer tank region. The bottom sketch shows the Booster Neutrino Beamline (BNB)

### 1.1. Booster neutrino beam (BNB) [4]

The "primary" protons are extracted from the 8 GeV Fermilab Booster in a $\sim$1.6 $\mu$s pulse, typically at 2-5 Hz and $\sim 4 \times 10^{12}$ protons per pulse. Then these protons are sent to the beryllium target located inside of the magnetic horn. The collision of protons and the target creates a shower of "secondary" mesons, mainly pions. For the neutrino (anti-neutrino) mode running, $\pi^+(\pi^-)$ are focused by the toroidal magnetic field created by the horn, and the decay in flight of these pions creates a wide band "tertiary" neutrino (anti-neutrino) beam, with average energy $\sim$800 ($\sim$600) MeV. Since MiniBooNE is a $\nu_\mu \to \nu_e$ ($\bar{\nu}_\mu \to \bar{\nu}_e$) neutrino oscillation appearance experiment, beam produced $\nu_e$ ($\bar{\nu}_e$) are "intrinsic" background and we need precise predictions for their distributions. Although they provide only 0.6% of the flux prediction in both neutrino and anti-neutrino mode,

we further constrain their errors from control samples. For the anti-neutrino mode, the contamination of neutrino background is sizable. This is tuned from an *in situ* measurement of charged current (CC) pion production in anti-neutrino mode. This is possible because of $\pi^-$ absorption in the detector, and CC pion sample is dominated by CC$\pi^+$ from the $\nu_\mu$ contamination in the $\bar{\nu}_\mu$ beam [5].

### 1.2. MiniBooNE detector [6]

The MiniBooNE detector is a mineral oil-based Cherenkov detector, and it is located 541 m down stream from the target. The 610 cm radius spherical tank is separated into an inner region and an outer region by the optical barrier at 575 cm radius, as can be seen in Fig. 1, top right picture. In the inner region, 1,280 8-inch PMTs are equipped, and the outer region has 240 8-inch veto PMTs. These PMTs collect the light from Cherenkov radiation from charged particle tracks created by neutrino interactions. It can also see the small amount of scintillation light. The charged particle tracks are reconstructed by using both Cherenkov and scintillation information.

### 1.3. Track reconstruction [7]

The charge and time information from each PMT is used to construct charge and time likelihood functions, which are used to reconstruct particle tracks under assumption of particle type. Figure 2 shows how different topologies of Cherenkov ring patterns are related to each particle type. The particle track fitters are designed to find particle energy and direction.

### 1.4. Neutrino cross section models

Since a neutrino oscillation signal is the excess of data over prediction, we need to know the neutrino cross sections a *priori*. It is important to understand the $\nu_\mu$ CC quasi-elastic (CCQE) interaction model because it is related to $\nu_e$CCQE interactions (oscillation signal events) under the lepton universality. Since the lepton kinematics of $\nu_e$CCQE interactions are used to reconstruct the neutrino energy, $\nu_\mu$CCQE is the ideal place to understand neutrino interaction kinematics. The modified relativistic Fermi gas model successfully describes $\nu_\mu$CCQE

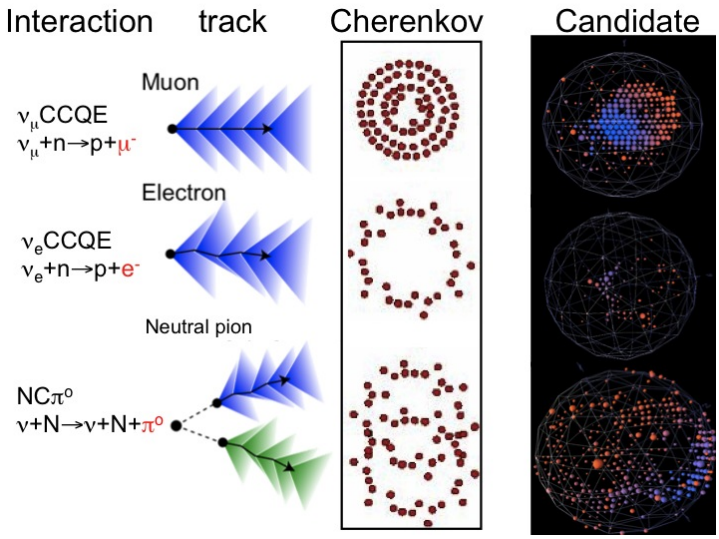


Fig. 2: Typical MiniBooNE interactions. From top to bottom, a $\nu_\mu$ charged current quasi-elastic (CCQE) event, a $\nu_e$ CCQE event, and a neutral current $\pi^\circ$ production event. The left column shows their interaction, next two columns shows features of tracks and Cherenkov rings from these particles. The right most column are event displays of candidate events. The each sphere represents a PMT hit, and size and color represent charge and timing

kinematics [8]. Then, we reconstruct neutrino energy from the measured energy and angle of the charged lepton.

For the oscillation analysis, the biggest misID is the $\pi^\circ$ from the neutral current (NC) interaction. Therefore, understanding of its kinematic distribution as a background is crucial. We modified the predicted NC$\pi^\circ$ distribution based on our measurement [9]. This not only corrects the distribution, but also constrains its error from 30% to 5%, because now the error of the prediction of this background is not from the interaction model, but from our measurement.

## 2. Neutrino Cross Section Measurements

Thanks to absolute flux prediction and fitters, we measured many absolute flux-averaged differential cross section, including CCQE, NC

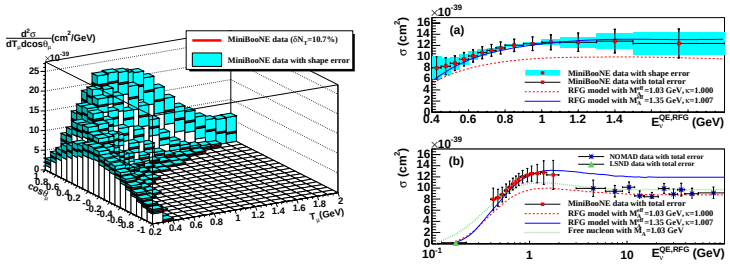


Fig. 3: The $\nu_\mu$ CCQE absolute cross section result. The left plot is the flux-averaged double differential cross section, as a function of muon kinetic energy and muon scattering angle. The 10.7% normalization error is not shown in the plot. The right plot is the flux-unfolded total cross section, as a function of neutrino energy. Notice left is described with measured variables and is nuclear model independent, while the detail of right plot (tails of the distributions) depends on the nuclear model because it is a function of model dependent reconstruction variables

elastic, NC $\pi^\circ$ production, CC$\pi^+$ production, and CC $\pi^\circ$ production interactions [10]. Indeed, MiniBooNE measured $\nu_\mu$ cross sections of 89% of all interaction types possibly measured in this energy range ($\sim$800 MeV). We focus on the measurement of the flux-averaged differential cross sections, where most of them are measured first time in history. They are a function of measured variables (*e.g.* muon energy, pion angle, etc) and thus nuclear model independent. Figure 3 left is an example of such a cross section. The cross section is traditionally shown as a function of the neutrino energy. Although neutrino energy is a model dependent parameter and the obtained cross section is hard to interpret, it is still useful to compare with other results (Fig. 3 right). Notice all neutrino cross sections measured by MiniBooNE, including CCQE, are higher than historically known values. This motivate a lot of theoretical work on neutrino cross sections, and upcoming MiniBooNE $\bar{\nu}_\mu$ cross section results [11] will be the best place to test theoretical models.

## 3. Neutrino Oscillation Analysis Results

MiniBooNE began data-taking in summer 2002, and it will finish in summer 2012. The signature of $\nu_\mu \to \nu_e$ ($\bar{\nu}_\mu \to \bar{\nu}_e$) is a single isolated

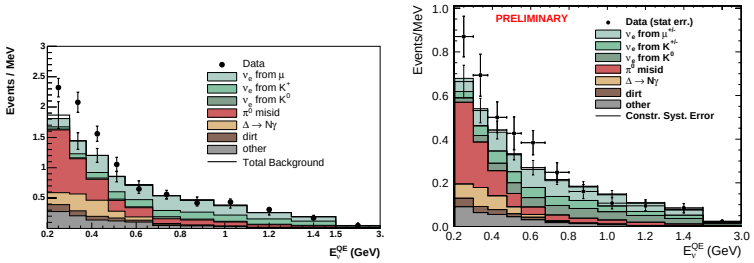


Fig. 4: MiniBooNE $\nu_\mu \rightarrow \nu_e$ and $\bar{\nu}_\mu \rightarrow \bar{\nu}_e$ oscillation results. Left is for neutrino mode, and right is for anti-neutrino mode. Data is shown with statistical error bar, and the systematic error bar is attached on the predicted background which also shows its composition

electron (positron). Since the detector is not magnetized, the analysis is almost identical for neutrino mode and anti-neutrino mode.

### 3.1. Other analyses

### 3.2. Neutrino mode oscillation analysis results

For the neutrino mode, MiniBooNE collected $6.46 \times 10^{20}$ protons on target (POT), corresponding to over $10^6$ neutrino interactions. Figure 4 left shows the $\nu_e$ candidate distribution, as a function of neutrino energy, together with the predicted background. Under the two massive neutrino model, we would expect a sizable excess at $> 475$ MeV if $\Delta m^2_{\rm LSND}$ is correct. Since this is not observed, we can reject possible $\Delta m^2_{\rm LSND}$ values from the parameter space with 90% C.L. However, we observed more than $3\sigma$ excess at $< 475$ MeV. This excess is not understood by known systematics.

### 3.3. Anti-neutrino oscillation analysis results

For the anti-neutrino mode, the last published result is based on $5.66 \times 10^{20}$ POT. Figure 4 right shows our summer 2011 update, where we include 50% more data. It also includes the constraint of the intrinsic $\nu_e$ from K-decay based on a SciBooNE measurement [12], where the SciBooNE detector is located upstream of the MiniBooNE detector. In our previous analysis, the excess in entire energy region was $43.2 \pm 22.5$. The summer 2011 update shows $57.7 \pm 28.5$,

thus the significance of excess over null hypothesis stays the same in a model independent way. However, as you see from Fig. 4 right, the excess below 475 MeV grew while the excess at higher energy shrank. The sizable excess at lower energies more closely resembles the neutrino mode distribution (Fig. 4, left) compared to the analysis with fewer statistics. This reduces the significance of two massive neutrino model over the null hypothesis, and now it is 91.1% C.L. whereas it was 99.4% favored before [3]. However, interestingly, the best fit point gives higher compatibility with LSND-like $\Delta m^2_{\rm LSND}$, and now it is 35.5% (it was 8.7% in [3]). After finishing data taking, we expect to have a further ∼30-40% more data.

Although the absence of the near detector makes it difficult, we can perform a shape-only disappearance analysis [13]. This is specifically the first $\bar{\nu}_\mu$ disappearance experiment targeting around $\Delta m^2$ ∼1-10 eV$^2$. The neutrino mode result is further refined by the joint analysis with SciBooNE [14].

Since MiniBooNE excesses are not understood by the Neutrino Standard Model, they may be the signal of new physics. In particular, Lorentz violation motivated models can qualitatively reproduce the MiniBooNE low energy excess [15]. We tested Lorentz and CPT violation, by fitting the sidereal time distribution of oscillation candidate events with a general function derived from the Standard Model Extension (SME) [16]. There was no statistically significant time variation, and limits are placed on several SME coefficients [17].

## 4. Conclusion

MiniBooNE is a short-baseline neutrino oscillation experiment at Fermilab. Updated anti-neutrino mode results show a slightly higher significance of the excess than the previous result in a model-independent test. The significance of the two massive neutrino oscillation hypothesis over the null hypothesis is reduced, but the compatibility with the massive neutrino oscillation hypothesis has increased. We expect a further ∼30-40% of data at the end of running, summer 2012.

**Acknowledgments**

I thank Joe Grange for a careful reading of this manuscript. I acknowledge to the organizer of "New Trends in High Energy Physics, Crimea 2011" for its hospitality during my stay at Alushta, Crimea, Ukraine.

1. A. Aguilar *et al.*, Phys. Rev. D **64**, 112007 (2001).
2. A.A. Aguilar-Arevalo *et al.*, Phys. Rev. Lett. **98**, 231801 (2007); Phys. Rev. Lett. **102**, 101802 (2009).
3. A.A. Aguilar-Arevalo *et al.*, Phys. Rev. Lett. **103**, 111801 (2009); Phys. Rev. Lett. **105**, 181801 (2010).
4. A.A. Aguilar-Arevalo *et al.*, Phys. Rev. D **79**, 072002 (2009).
5. A.A. Aguilar-Arevalo *et al.*, arXiv:1102.1964 [hep-ex].
6. A.A. Aguilar-Arevalo *et al.*, Nucl. Instrum. Meth. A **599**, 28 (2009).
7. R.B. Patterson *et al.*, Nucl. Instrum. Meth. A **608**, 206 (2009).
8. A.A. Aguilar-Arevalo *et al.*, Phys. Rev. Lett. **100**, 032301 (2008).
9. A.A. Aguilar-Arevalo *et al.*, Phys. Lett. B **664**, 41 (2008).
10. A.A. Aguilar-Arevalo *et al.*, Phys. Rev. D **81**, 092005 (2010); Phys. Rev. D **82**, 092005 (2010); Phys. Rev. D **81**, 013005 (2010); Phys. Rev. D **83**, 052007 (2011); Phys. Rev. D **83**, 052009 (2011).
11. J. Grange, arXiv:1107.5327 [hep-ex].
12. G. Cheng *et al.*, Phys. Rev. D **84**, 012009 (2011).
13. A.A. Aguilar-Arevalo *et al.*, Phys. Lev. Lett. **103**, 061802 (2009).
14. K.B. M. Mahn *et al.*, arXiv:1106.5685 [hep-ex].
15. T. Katori, V.A. Kostelecký, and R. Tayloe, Phys. Rev. D **74**, 105009 (2006); J.S. Díaz and V.A. Kostelecký, Phys. Lett. B **700**, 25 (2011); arXiv:1108.1799 [hep-ph].
16. V.A. Kostelecký and M. Mewes, Phys. Rev. D **69**, 016005 (2004); Phys. Rev. D **70**, 076002 (2004).
17. A.A. Aguilar-Arevalo *et al.*, arXiv:1109.3480 [hep-ex].

# SCIBOONE, A NEUTRINO CROSS SECTION MEASUREMENT EXPERIMENT AT FERMILAB

Teppei Katori for the SciBooNE collaboration

*Massachusetts Institute of Technology, USA*

**Abstract**

The SciBar Booster Neutrino Experiment (SciBooNE) is a $\nu_\mu$ ($\bar{\nu}_\mu$) neutrino cross section measurement experiment at Fermilab. The primary goal was to measure neutrino interaction cross sections of interest to the T2K experiment and to make neutrino oscillation measurements with MiniBooNE. The data was taken from summer 2007 to summer 2008.

## 1. SciBooNE Experiment

Figure 1 shows a schematic overview of the SciBooNE experiment. The Booster Neutrino Beamline (BNB) sends 8 GeV protons from the Booster to a beryllium target, which produces $\nu_\mu$ and $\bar{\nu}_\mu$ by the decay in flight of mesons (mainly pions). The SciBooNE detector is located 100 m downstream of the target, and 540 m downstream is the MiniBooNE detector. The BNB is the ideal beam to study neutrino interactions expected at T2K [1], because its flux average, $\sim$800 MeV, is close to JPARC neutrino beam (Fig. 1, top right). More detail on the BNB can be found elsewhere [2].

### 1.1. SciBooNE detector

Figure 2 left shows the SciBooNE detector. The SciBooNE detector consists of three parts, a vertex detector "SciBar", an electromagnetic calorimeter "electron cacher (EC)", and an iron-scintillator sandwich "muon range detector (MRD)".

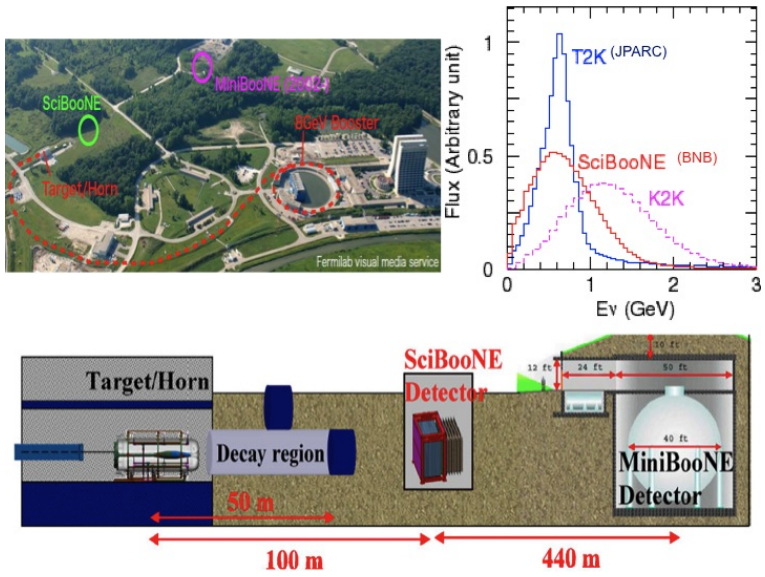


Fig. 1: Overview of the SciBooNE experiment. The top left is a picture of Fermilab, including SciBooNE and MiniBooNE detector locations, as well as the Booster and the target hall. The top right plot shows the neutrino flux comparison with arbitrary unit. The BNB has a similar average energy to JPARC, and this makes BNB the ideal place for the SciBooNE experiment

### *1.1.1. SciBar*

SciBar is an organic scintillation bar X-Y tracker, weighing roughly 15 tons ($3\times3\times1.7$ m$^3$), with a total of 14,366 channels. A scintillation bar has dimension $1.3\times2.5\times300$ cm$^3$, and it is made of extruded polystyrene, co-extruded with $TiO_2$ at the outer layer as a reflector. The doping is 1% PPO (fluor) and 0.03% POPOP (wave length shifter). Each has a hole in the middle to insert a green-to-blue wave length shifting fiber, which bring the signals to 64 ch multi-anode photo-multiplier tubes (MAPMTs). The scintillation bars were originally extruded at Fermilab for the K2K experiment at KEK (2003). After the experiment, it was dismantled, shipped back to Fermilab, and reassembled for the SciBooNE experiment (2007).

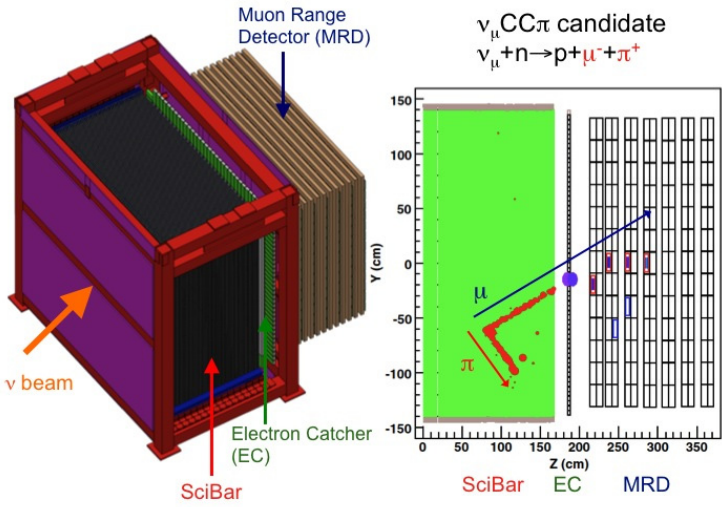


Fig. 2: (Left) The SciBooNE detector, from left to right, SciBar, EC, and MRD. (Right) event display of a typical muon-neutrino charged current charged pion production ($\nu_\mu$CC$\pi^+$) event [3]. The long muon track, which stops in the MRD after penetrating SciBar and EC, and short pion track, are identified. Low energy proton tracks are often missed

### *1.1.2. Electron Catcher, "EC"*

To enhance the particle ID of electrons, the EC is located right behind the SciBar. This 256 channel lead foil-scintillation fiber calorimeter has 11 radiation lengths to covert gamma rays efficiently. This was originally made for the Chorus experiment at CERN (1994), then used at the HARP experiment at CERN (2001), and finally transfered to Fermilab (2007).

### *1.1.3. Muon Range Detector, "MRD"*

This iron-scintillator sandwich detector can range out up to 0.9 GeV muons. The tracks are measured by 362 scintillator paddles connected to 2-inch PMTs.

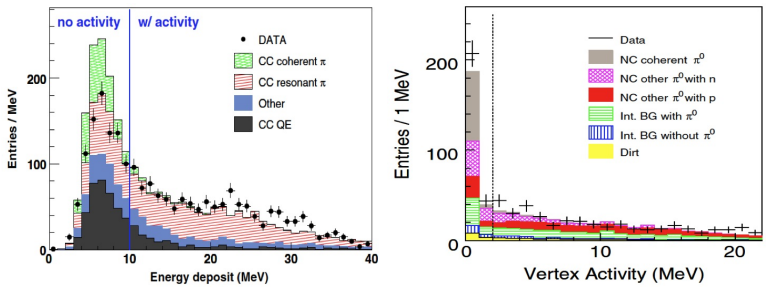


Fig. 3: Examples of vertex activity measurements. (Left) This is the distribution of maximum deposited energy in a scintillation bar around the vertex for the $\mu + \pi$ candidates in the CC$\pi^+$ sample [3]. We do not see any contribution from coherent $\pi^+$ production. (Right) This is the equivalent plot for NC$\pi^\circ$ sample [6], where we clearly see the contribution of coherent $\pi^\circ$ productions

## 2. SciBooNE Cross Section Measurements

SciBooNE collected $0.99 \times 10^{20}$ protons on target (POT) in neutrino mode, and $1.53 \times 10^{20}$ POT for anti-neutrino mode. The average neutrino energy for $\nu_\mu$ ($\bar{\nu}_\mu$) mode is $\sim$800 MeV ($\sim$600 MeV).

### 2.1. Coherent pion production measurement

The coherent pion production measurements have rather confusing results and they do not emerge to a single picture yet. The charged current charged pion production (CC$\pi^+$) measurement from K2K implies no coherent pion production [4], although MiniBooNE shows nonzero coherent contributions from its neutral current neutral pion production (NC$\pi^\circ$) measurement [5]. This clearly violates the naive expectation from isospin symmetry, where the CC coherent pion production rate is twice as high as that of NC coherent pion production. SciBooNE results support both [3, 6], non-existence of CC coherent pion and existence of NC coherent pion production. Since SciBar is a vertex detector, it can measure the nuclear break-up. We then utilize energy release near the vertex, called "vertex activity", because coherent interactions should not break up the nuclei and thus vertex activity should be small. Figure 3 shows the vertex activity plot for the CC$\pi^+$ and NC$\pi^\circ$ samples. The $\mu + \pi$ candidates in CC$\pi^+$

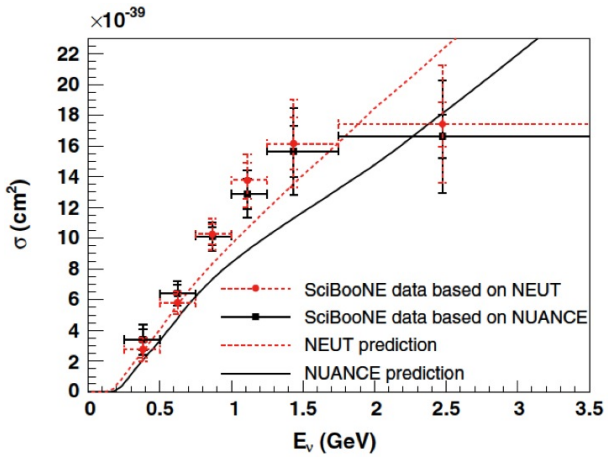


Fig. 4: $\nu_\mu$ CC inclusive cross section per nucleon on polystyrene ($C_8H_8$) target

sample show the absence of a coherent $\pi^+$ production contribution, but the NC$\pi^\circ$ sample clearly shows the contribution of coherent $\pi^\circ$ production. This new technique is more robust than estimating the coherent fraction with a kinematic template fit based on a specific cross section model (*e.g.* MiniBooNE [5]).

### 2.2. CC inclusive cross section measurement

The neutrino cross section measurement in the 1 GeV range is hindered by various nuclear effects (re-scattering, absorption, charge exchange, etc), so called final state interactions (FSIs). The CC inclusive measurement is insensitive to FSI compared with CC quasielastic (CCQE) measurements [7], where the number of tracks depends on FSI. The CC inclusive measurement is the sum of all channels with a single muon in final state, and all possible hadronic final states are integrated. Figure 4 right shows the result. Although the unfolding method is dependent upon the cross section model, two results based on different simulations agree. Notice the measured cross section around 1-2 GeV is higher than the historically known value, and is consistent with MiniBooNE [8] and MINOS [9], but not with NOMAD [10] and MINERvA $\bar{\nu}_\mu$CCQE preliminary [11]. There is

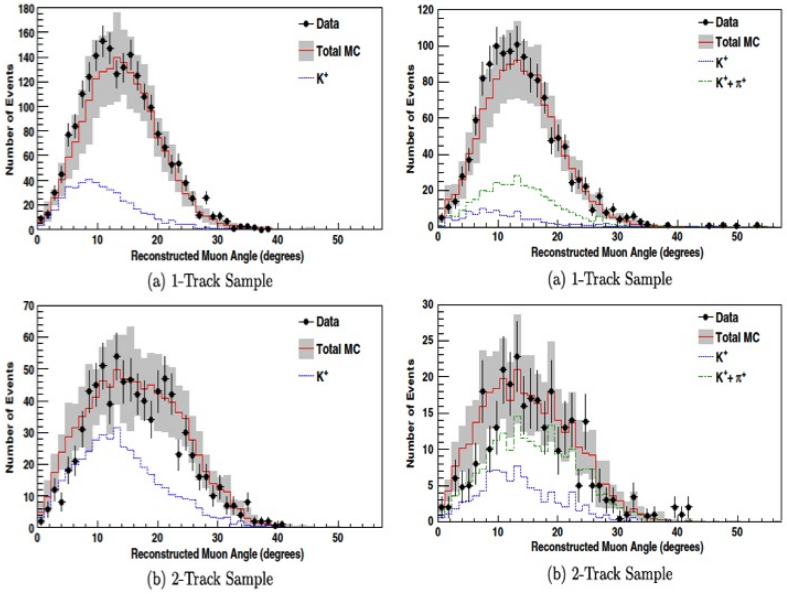


Fig. 5: The reconstructed muon angle distributions, for 1 track (top), 2 track (bottom), neutrino mode (left), and anti-neutrino mode (right). These plots are after the fit based on one of simulations we use. As you see, neutrinos from kaon decay are sensitive to 2 track samples (and also 3 track samples but with lower statistics), and the 1 track sample is dominated with pion decay neutrinos

a tremendous amount of work to be done in order to understand this [12].

## 3. SciBooNE for Neutrino Oscillation Physics

Because of its location (Fig. 1), the SciBooNE detector can serve as a near detector for the MiniBooNE neutrino oscillation experiment. Using the $\nu_\mu$ induced multi-track samples, we constrain the number of $\nu_e$ coming from kaon decay [13], which is one of the intrinsic background for MiniBooNE and has large uncertainty (40%). This analysis is possible because kaon decay originated muon neutrinos tend to be higher energy and tend to make multi-tracks in SciBooNE. As can be seen from Figure 5, this is true for both neutrino and anti-

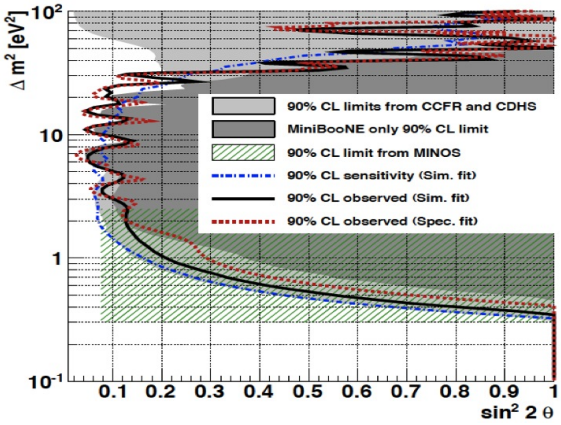


Fig. 6: An excluded region by SciBooNE-MiniBooNE joint analysis. Two independent fit methods (black solid and red dashed lines) extend the previously excluded region from the MiniBooNE only fit around $\Delta m^2$ ~5-40 MeV$^2$

neutrino mode. After the fit, we found the $K^+$ production rate to be $0.85\pm0.11$, $\sim 15\%$ lower rate than the prediction with $\sim$13% error.

Not only do SciBooNE and MiniBooNE share the same beamline, both have carbon as a target material (SciBar=$C_8H_8$, MiniBooNE=$CH_2$). Therefore simultaneous analysis can improve the MiniBooNE $\nu_\mu$ disappearance result [14]. Figure 6 is the result. Although the MiniBooNE systematic error is dominated by MiniBooNE detector error which doesn't cancel by simultaneous analysis, we can still extend the excluded region around $\Delta m^2$ ~5 to 40 eV$^2$ due to reductions in flux and cross section error by roughly a factor two.

## 4. Conclusion

SciBooNE is a 1 GeV range neutrino cross section experiment at Fermilab. The high resolution tracker "SciBar" is useful to measure complex event topologies, such as CC pion production. The vertex activity measurement provides a way to determine local energy deposits which cannot make a track and would otherwise be ignored. A synergy with the MiniBooNE experiment also produces interesting results.

**Acknowledgments**

I thank Ben Jones for a careful reading of this manuscript. I acknowledge to the organizer of "New Trends in High Energy Physics, Crimea 2011" for its hospitality during my stay at Alushta, Crimea, Ukraine.

1. K. Abe *et al.*, Phys. Rev. Lett. **107**, 041801 (2011); arXiv:1106.1238.
2. A.A. Aguilar-Arevalo *et al.*, Phys. Rev. D **79**, 072002 (2009).
3. K. Hiraide *et al.*, Phys. Rev. D **78**, 112004 (2008).
4. M. Hasegawa *et al.*, Phys. Rev. Lett. **95**, 252301 (2005).
5. A.A. Aguilar-Arevalo *et al.*, Phys. Lett. B **664**, 41 (2008); Phys. Rev. D **81**, 013005 (2010).
6. Y. Kurimoto *et al.*, Phys. Rev. D **81**, 033004 (2010); Phys. Rev. D **81**, 111102 (2010).
7. J. L. Alcaraz-Aunion and J. Walding, AIP Conf. Proc. **1189**, 145 (2009);
8. A.A. Aguilar-Arevalo *et al.*, Phys. Rev. D **81**, 013005 (2010); Phys. Rev. D **81**, 092005 (2010); Phys. Rev. D **82**, 092005 (2010); Phys. Rev. D **83**, 052007 (2011); Phys. Rev. D **83**, 052009 (2011).
9. M. Dorman, AIP Conf. Proc. **1189**, 133 (2009).
10. V. Lyubushkin *et al.*, Eur. Phys. J. C **63**, 355 (2009).
11. G. Perdue, arXiv:1105.1698 [hep-ex].
12. M. Martini *et al.*, Phys. Rev. C **80**, 065501 (2009); Phys. Rev. C **81**, 045502 (2010); ArXiv:1110.0221 [nucl-th]; J. Nieves *et al.*, Phys. Rev. C **83**, 045501 (2011); arXiv:1106.5374 [hep-ph]; J.E. Amaro *et al.*, Phys. Lett. B **696**, 151 (2011); Phys. Rev. C **82**, 044601 (2011); arXiv:1104.5446 [nucl-th]; O. Benhar *et al.*, Phys. Rev. Lett. **105**, 132301 (2010); Phys. Lett. B **702**, 433 (2011); A. Ankowski *et al.*, Phys. Rev. D **82**, 013002 (2010); Phys. Rev. C **83**, 054616 (2011); A.V. Butkevich *et al.*, Phys. Rev. C **84**, 015501 (2011); Phys. Rev. C **82**, 055501 (2010); J.T. Sobczyk, arXiv:1109.1081 [hep-ex]; C. Juszczak *et al.*, Phys. Rev. C **82**, 045502 (2010); A. Bodek *et al.*, Eur. Phys. J. C **71**, 1726 (2011). A. Meucci *et al.*, Phys. Rev. Lett. **107**, 172501 (2011); O. Buss *et al.*, arXiv:1106.1344 [hep-ph].
13. G. Cheng *et al.*, Phys. Rev. D **84**, 012009 (2011).
14. A.A. Aguilar-Arevalo *et al.*, Phys. Lev. Lett. **103**, 061802 (2009).
15. K.B.M. Mahn *et al.*, arXiv:1106.5685 [hep-ex].

# MICROBOONE, A LIQUID ARGON TIME PROJECTION CHAMBER NEUTRINO EXPERIMENT AT FERMILAB

Teppei Katori for the MicroBooNE collaboration

*Massachusetts Institute of Technology, USA*

**Abstract**

The Liquid Argon Time Projection Chamber (LArTPC) is a promising detector technology for future neutrino experiments. MicroBooNE is an upcoming LArTPC neutrino experiment which will be located on-axis of the Booster Neutrino Beam (BNB) at Fermilab, USA. Data taking will start from early 2014. The R&D efforts on this detection method and related neutrino interaction measurements are discussed.

## 1. Liquid Argon Time Projection Chamber (LArTPC)

Since the LArTPC was first proposed [1], the detection technique has mainly been developed by an Italian collaboration [2]. Its physics potential, especially in neutrino interaction measurements, has been demonstrated [3]. The notable features of this detector are its three-dimensional and calorimetric reconstruction capabilities for charged particle tracks (Figure 1, left).

The ArgoNeuT experiment was the first US LArTPC to take data in a neutrino beamline [4]. Although the fiducial volume is small, it can use the MINOS near detector [5], located behind of the ArgoNeuT detector, as muon range stack. Table 1 summarizes the ArgoNeuT detector parameters.

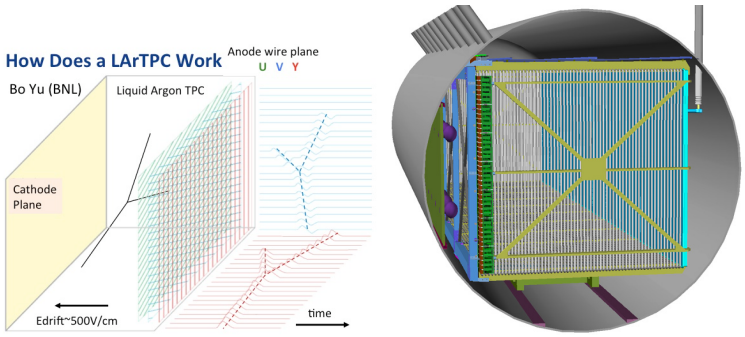


Fig. 1: (Left) The working principle of a LArTPC. A charged track in the TPC volume ionizes argon atoms and create ionization electrons. An imposed electric field (500 V/cm) causes electrons to drift toward readout anode wire planes and be collected. The signals from the wire planes provide 2 dimensional information about the event. The drift time of the ionization electrons gives the third coordinate. In other words, the time information is "projected" onto the third dimension. The combined wire and time information allows the tracks to be reconstructed in three dimensions. (Right) A drawing of the MicroBooNE cryostat with the TPC and PMT arrays on the left wall. The neutrino beam is perpendicular on the paper plane, and electrons are drifted toward the left where wire planes are located in front of the PMTs

## 2. MicroBooNE

Although ArgoNeuT mainly focuses on detector R&D, MicroBooNE (Figure 1, right) will focus on 50% R&D and 50% physics. In a LArTPC, single electron tracks can be distinguished from gamma rays that have converted to $e^+ - e^-$ pairs by utilizing the conversion length of the gamma ray and $\frac{dE}{dx}$ of the electron. Thus, MicroBooNE will have excellent particle identification for $\nu_e$ ($\bar{\nu}_e$) appearance oscillation experiments, where gamma rays are backgrounds. This discrimination power can be used to study the MiniBooNE low energy excess [6].

### 2.1. Detector R&D

MicroBooNE is one of the key steps on the path to a future large LArTPC detector, such as LAr20 (Tab. 1), which is a candidate detector for a long baseline neutrino experiment (LBNE) [7].

**T a b l e 1: Summary of 3 US LArTPCs**

| | ArgoNeuT | MicroBooNE | LAr20 |
|---|---|---|---|
| Cryostat volume | 0.7 ton | 150 ton | 25,000 ton |
| TPC volume | 0.25 ton | 89 ton | 16,700 ton |
| Max. drift length | 0.5 m | 2.5 m | 2.5 m |
| Electronics | JFET (293 K) | CMOS (87 K) | CMOS (87 K) |
| # of channel | 480 | 8,256 | $\sim$645,000 |
| Wire pitch | 4 mm | 3 mm | 3 mm |
| # of wire plane | 2 | 3 | 3 |
| Light collection | none | 30 of 8"PMT | TBD |

### *2.1.1. Fermilab materials test system (MTS)*

Table 1 summarizes the MicroBooNE parameters. The MicroBooNE detector has a bigger fiducial volume than the ArgoNeuT detector, and it requires a longer drift length of ionization electrons to see the charged particle tracks. As such, the liquid Argon is required to have a higher purity. For MicroBooNE, to preserve $> 50\%$ of electrons to be drifted without attaching to electro-negative impurities, we need to achieve $\sim$100 ppt level of oxygen-equivalent impurity concentration [8]. In order to achieve this goal, we have several test facilities. The Fermilab MTS cryostat "LUKE" (Figure 2, left) has a window at the airlock region. The test material is inserted and sample cage is lowered into the LUKE volume, which is filled with high purity liquid Argon. The impurity is monitored in the Argon gas and liquid regions. All materials used inside of the MicroBooNE cryostat are required to be tested by MTS.

### *2.1.2. Liquid Argon Purity Demonstrator (LAPD)*

Presumably, we cannot evacuate an ultra-large cryostat, such as LAr20 [7], before filling it with liquid Argon in order to remove impurities. LAPD (Figure 2, right) is a 30 ton vessel with 2 copper (Oxygen) and 2 Zeolite (water) filters [9]. We are testing a way to "push out" all impurities inside the vessel by flowing Argon gas through it, rather than evacuating the whole vessel. The purity and temperature are monitored at several places inside the tank. These provide important inputs for the design of a large LArTPC.

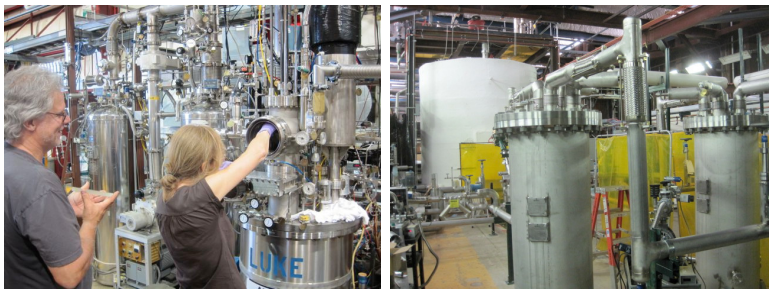


Fig. 2: (color online). (Left) The Fermilab MTS cryostat, "LUKE". In this picture, a scientist prepares a test sample in the sample cage. (Right) The Liquid Argon Purity Demonstrator (LAPD). Zeolite filters are seen in front and the 30 ton vessel is seen in back

### *2.1.3. Electronics*

For a large cryogenic detector, signal pre-amplifiers need to be located inside of the cryostat. We are currently studying such electronics. Although MOSFET itself works better with liquid Argon temperature (87K), careful design is required for the electronics to work in the cryogenic environment. A CMOS preamplifier test is an ongoing effort at BNL.

For the data taking, we are planning to use two different trigger modes, one for beam events and one for possible supernova events. The TPC wire read-out is performed by 12 bit 2 MHz ADCs. For beam events, lossless Huffman coding is enough to compress the data, but for supernova events, where at least 1 hr continuous buffering is required, further compression techniques are necessary. In order to avoid any loss, so called "dynamic decimation" is under study.

### *2.1.4. LArSoft*

LArSoft [10] is a general purpose framework used for all US LArTPC projects. It simulates from neutrino interactions through to a full detector simulation based on GEANT4 to generate TPC wire signals. Then fully automated reconstruction techniques are applied. LArSoft is developed and maintained by All US LArTPC collaborators. The data analysis of ArgoNeuT is also based on LArSoft. Figure 3 shows

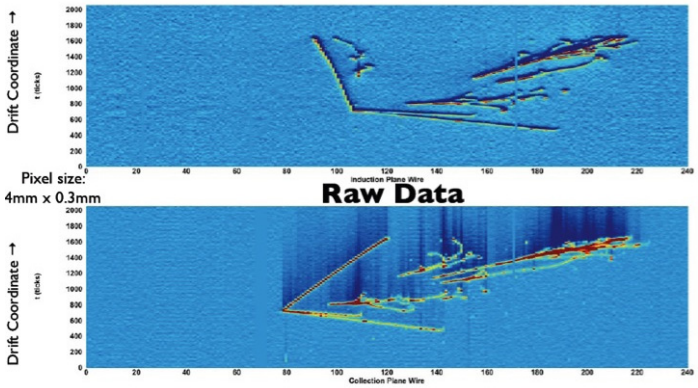


Fig. 3: A typical neutrino interaction event display from ArgoNeuT. Top figure shows the induction plane, and the bottom figure shows the collection plane of the TPC. The color represents the heights of the pulses on the wires. These are raw data, before Fourier deconvolution to remove electronics noise. Here, 4 gamma rays from the decay of 2 $\pi^{\circ}$ can be seen

a typical neutrino interaction event display in ArgoNeuT. Here, we can see the production of 2 $\pi^{\circ}$ which decay to 4 gamma rays, as well as other tracks.

### *2.1.5. Cryogenic large PMT system*

MicroBooNE will employ 30 8-inch cryogenic PMTs. Figure 4 (left) shows the PMT unit mechanical model. Since the prompt component of scintillation light is much faster (6 ns) than the electron drift velocity of the TPC (1.6 m/ms), scintillation light can be used as a trigger for the TPC detector. These PMTs have platinum coating under the photo-cathode that works below 150 K. The PMT base is custom designed in order to function in the cold environment. The vacuum UV (VUV) scintillation light from the liquid Argon is shifted to the blue region by wave length shifting plates. Figure 4 (right) shows a picture of our set up of the PMT test stand at the Fermilab proton assembly building (PAB).

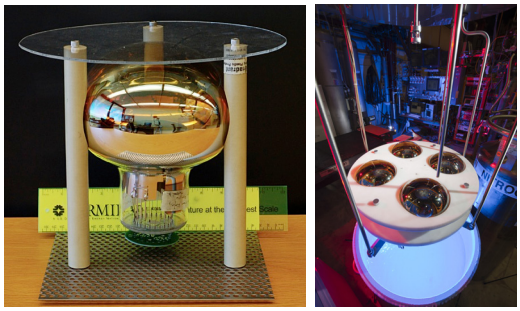

Fig. 4: (Left) A mechanical model of a PMT unit of MicroBooNE. A 8-inch cryogenic PMT is supported by 3 PEEK (Polyether ether ketone) posts with a wave length shifting plate on top. The wave length shifting plate is an acrylic plate, coated with a mixture of Tetra-Phenyl butadiene (TPB) and polystyrene as a wave length shifter. TPB shifts 128nm VUV scintillation light into the blue region, where the bi-alkali photo-cathode is the most sensitive. (Right) The PMT test stand at Fermilab PAB. We immerse 4 PMTs simultaneously in liquid nitrogen for testing to save the cooling time

### 2.2. Physics

On the order of 10,000 interactions are expected in many channels. On top of this, we expect on the order of 40,000 $\nu_\mu$CC and 7,700 $\bar{\nu}_\mu$CC interactions per year from the upgraded 700 kW NuMI beam ($\sim$6E20 POT/year) for the NOvA experiment [15],

Neutral current elastic (NCE) scattering is uniquely sensitive to the iso-scalar part of the axial current form factor, which is generally related with $\Delta s$, the strange quark spin component of the nucleon. $\Delta s$ relates the elastic scattering form factor and the parton distribution function (PDF),

$$G_A^s(Q^2 = 0) = \Delta s = \int_0^1 \Delta s(x) dx \ ,$$

which is measured through semi-inclusive DIS experiments [11]. However, the obtained values disagree with $\Delta s$ from a neutrino NCE measurement [12]. To determine $\Delta s$, measurements of low energy protons are crucial. MicroBooNE will be able to resolve very short proton tracks (a design goal is to measure $\sim$1.5 cm, equivalent to $\sim$40 MeV

kinetic energy). Such tracks are unmeasurable with Cherenkov [13] and fine-grained tracking detectors [14]. Obviously, how to handle the final state interaction (FSI) of such low energy protons is an issue.

Among the possible interaction measurements, MicroBooNE may be the first to observe two nucleon short range correlations in an unambiguous way with neutrinos ($\nu$2NSRC). The nucleon correlation is a recent hot topic in nuclear physics. Key points from a series of recent electron scattering experiments, mainly from JLab, are; (1) for a heavy nuclei, $\sim$20% of nucleons are in a 2NSRC state [16], (2) 90% are proton-neutron pair [17], and (3) 2 ejected nucleons' initial states are kinematically correlated [18]. In a $\nu_\mu$CC interaction, this interaction signature is a triple coincidence; a muon with 2 correlated protons,

$$\nu_\mu + X(n-p) \rightarrow \mu^- + p + p + X' \ .$$

There is wide-spread speculation that $\nu$2NSRC may contribute to recent large neutrino cross section results from MiniBooNE [19], SciBooNE [20], and MINOS [21]. All modern neutrino experiments measured higher cross sections than have been predicted, except NOMAD [22] and MINERvA preliminary results [23]. From the theoretical point of view [24], 2NSRC, together with meson exchange currents, enhance generally hard to identify multi-nucleon emission channels. However, high resolution LArTPC technology has the ability to track low energy protons, and it has the potential to identify $\nu$2NSRC for the first time in history. This process may shed light on neutrino cross section measurements around 1 GeV.

## 3. Long baseline Neutrino Experiment (LBNE)

An ultra-large LArTPC, LAr20 (Tab. 1) is a candidate far detector for LBNE [7]. The size of the detector as well as the number of channels required will be very large. However, due to an alternating anode and cathode plane structure, the drift length of electrons will be the same as in MicroBooNE. An array of wave-guides could be used as an event trigger, and the R&D of such a new detector is ongoing [25]. The low misidentification rate of gamma rays resembling single electrons makes LAr20 an ideal detector to search for $\nu_e$ ($\bar{\nu}_e$) appearance in order to study $\theta_{13}$ and the CP violation phase [7].

## 4. Conclusion

LArTPC is a promising detection technology for a future large neutrino detector. The MicroBooNE experiment will serve as a place for R&D of this future experiment. For the primary physics goal, it is the ideal experiment to investigate the MiniBooNE low energy excess thanks to its ability to separate an electron from electron-positron pair from a single gamma ray. Furthermore, MicroBooNE is both a high resolution and high statistics neutrino cross section experiment. Data taking is expected to start from early 2014.

### Acknowledgments

I thank Kinga Partyka for a careful reading of this manuscript. I acknowledge the organizer of "New Trends in High Energy Physics, Crimea 2011" for its hospitality during my stay at Alushta, Crimea, Ukraine.

1. C. Rubbia, CERN Report No. CERN-EP77-08, (1997).
2. S. Amerio *et al.*, Nucl. Instrum. Meth. A **527**, 329 (2004).
3. F. Arneodo *et al.*, Phys. Rev. D **74**, 112001 (2006).
4. J. Spitz, arXiv:1009.2515 [hep-ex].
5. P. Adamson *et al.*, Phys. Rev. D **81**, 072002 (2010).
6. A.A. Aguilar-Arevalo *et al.*, Phys. Rev. Lett. **98**, 231801 (2007); Phys. Rev. Lett. **102**, 101802 (2009).
7. M.C. Sanchez, AIP Conf. Proc. **1222**, 479-481 (2010).
8. A. Curioni *et al.*, Nucl. Instrum. Meth. A **605**, 306 (2009).
9. B. Rebel *et al.*, J. Phys. Conf. Ser. **308**, 012023 (2011).
10. `https://plone4.fnal.gov/P1/Main/wiki/LArSoft/LArSoft`
11. A. Airapetian *et al.*, Phys. Rev. Lett. **92**, 012005 (2004); Phys. Lett. B **666**, 446 (2008).
12. L.A. Ahrens *et al.*, Phys. Rev. D **35**, 785 (1987).
13. A.A. Aguilar-Arevalo *et al.*, Phys. Rev. D **82**, 092005 (2010).
14. H. Takei, AIP Conf. Proc. **1189**, 181 (2009).
15. A. Sousa, PoS **ICHEP2010**, 332 (2010).
16. K.S. Egiyan *et al.*, Phys. Rev. Lett. **96**, 082501 (2006).
17. E. Piasetzky *et al.*, Phys. Rev. Lett. **97**, 162504 (2006).

18. R. Shneor *et al.*, Phys. Rev. Lett. **99**, 072501 (2007).

19. A.A. Aguilar-Arevalo *et al.*, Phys. Rev. D **81**, 013005 (2010); Phys. Rev. D **81**, 092005 (2010); Phys. Rev. D **82**, 092005 (2010); Phys. Rev. D **83**, 052007 (2011); Phys. Rev. D **83**, 052009 (2011).

20. J.L. Alcaraz-Aunion and J. Walding, AIP Conf. Proc. **1189**, 145 (2009); Y. Nakajima *et al.*, Phys. Rev. D **83**, 012005 (2011).

21. M. Dorman, AIP Conf. Proc. **1189**, 133 (2009).

22. V. Lyubushkin *et al.*, Eur. Phys. J. C **63**, 355 (2009).

23. G. Perdue, arXiv:1105.1698 [hep-ex],

24. M. Martini *et al.*, Phys. Rev. C **80**, 065501 (2009); Phys. Rev. C **81**, 045502 (2010); ArXiv:1110.0221 [nucl-th]; J. Nieves *et al.*, Phys. Rev. C **83**, 045501 (2011); arXiv:1106.5374 [hep-ph]; J.E. Amaro *et al.*, arXiv:1104.5446 [nucl-th].

25. L. Bugel *et al.*, Nucl. Instrum. Meth. A **640**, 69 (2011).

# THE $\overline{P}ANDA$ DETECTOR AT FAIR

Tibor Keri
*on behalf of the $\overline{P}ANDA$ collaboration*

*DESY*

**Abstract**

The $\overline{P}ANDA$ collaboration propose a general purpose detector running with $\bar{p}$-beam for the upcoming FAIR project. A programmable apparatus with a $\bar{p}$-beam was designed to target a wide range of investigations on hadron physics while being flexible for new upcoming physical phenomena in this field. The design requirements and the setup will be described. Furthermore the technical infrastructure and expected performance will be discussed.

## 1. Introduction

The aim of the $\overline{P}ANDA$ experiment is to investigate many aspects of hadron physics, exotic particles, charmonium spectroscopy, hypernuclei and new forms of matter with a $\bar{p}$-beam having variable momenta at high precision. This is described and presented in detail separately during this conference [1] and elsewhere [2]. The technical environment and the high energy storage ring are discussed there as well. The major key points nevertheless will be summarized here for the design requirements. The $\overline{P}ANDA$ detector (Fig. 1) is designed as a programmable spectrometer to target the physics of strong interaction in a variety of experiments.

## 2. Detector Design Requirements

For these investigations a $\bar{p}$-beam will be used have full access to all quantum numbers. A variable beam momentum between 1.5 GeV/c and 15 GeV/c is foreseen. This corresponds to a center of mass

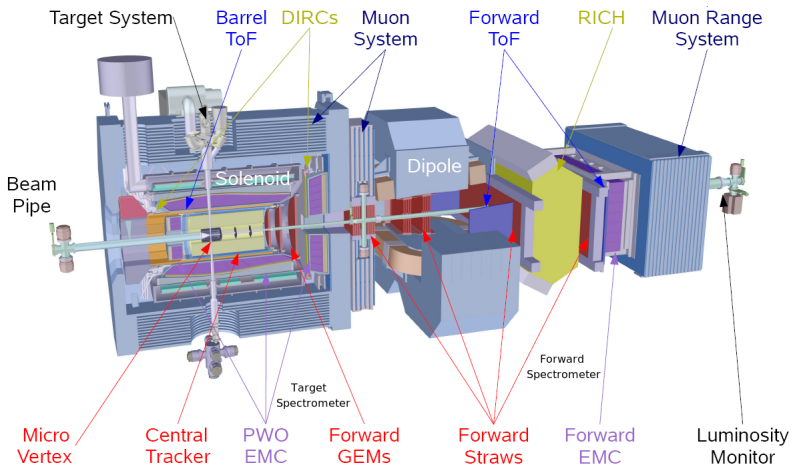


Fig. 1: The $\overline{P}ANDA$ detector consists of a target spectrometer on the left side and a forward spectrometer on the right side. The total length is about 12 m. The diameter of the target spectrometer is about 3.5 m

energy between ∼2.25 GeV and ∼5.46 GeV. The beam can be tuned to various conditions. A high precision setup with a high resolution $dp/p < 4 \times 10^{-5}$ at a luminosity of $10^{31}$ cm$^{-2}$s$^{-1}$ will be available. This will be achieved by electron cooling. With a stochastic cooling a high luminosity setup at $2 \times 10^{32}$ cm$^{-2}$s$^{-1}$ with a resolution $dp/p < 10^{-4}$ can be used. The duty cycle of the $\bar{p}$-beam will be with 2000 ns beam on (with sub-structure) and 400 ns beam off which is near to continous beam.

The planned luminosity versus time $L(t)$ (Fig. 2(a)) is partitioned in two stages which generally run in cycles ($t_{\mathrm{cycle}} = t_{\mathrm{prep}} + t_{\mathrm{exp}}$). During the preparation stage the beam is tuned for the experiment and lasts for the time $t_{\mathrm{prep}}$. The luminosity is increased to the desired value $L_{\mathrm{start}}$ before the experiment is started. In the experiment stage the luminosity decreases due to interaction with the target. Reaching the lower value of the luminosity $L_{\mathrm{low}}$ the experiment will be suspended and the $\bar{p}$-beam regenerated. The various time intervals depends on the experimental setup. The preparation time $t_{\mathrm{prep}}$ is in the range of ∼120 s — ∼290 s. Due to the wide variability of the $\bar{p}$-beam momenta the cycle time $t_{\mathrm{cycle}}$ varies widely in the range of

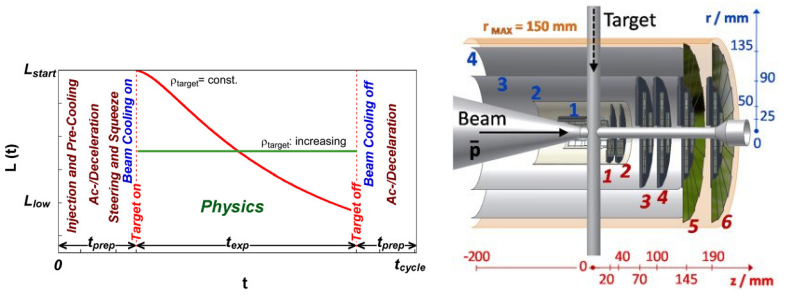


(a) (b)

Fig. 2: (a) Beam luminosity versus time (b) Setup of the micro vertex detector

$\sim$1280 s — $\sim$4820 s. For a constant target density (red line) the interaction rate is higher at the beginning of the experiment than at the end, yielding in lower efficiency of data taking. Depending on the variability of the target density the interaction rate can be tuned to best performance over the whole experiment time (green line). The $1/e$-beam lifetime is in the range of $\sim$1540 s — $\sim$35500 s.

The design requirements are various. To cover partial wave analysis for exotic particles a full $4\pi$-acceptance is needed. Investigations of charmonium decays require high vertexing resolution. The programmability of a physics engine makes high tracking resolution and good particle identification necessary. Rare interactions require high trigger rates and precise event selection. A modular system of subdetectors and variable targets support investigations of full final state reconstruction.

## 3. $\overline{P}ANDA$ Detector

These detector design requirements can be targeted by developing various novel detector techniques and modular readout design. Therefore the $\overline{P}ANDA$ detector (Fig. 1) consists of two parts. The target spectrometer (left side) is built around the interaction point while the forward spectrometer (right side) covers the forward acceptance.

**T a b l e 1: Parameters for Pellet and Cluster Jet target**

| target | Pellet | Cluster Jet |
|---|---|---|
| density | $< 4 \times 10^{15}$ atoms/cm$^2$ | $< 8 \times 10^{14}$ atoms/cm$^2$ |
| interactions | $\sim$100 per pellet | adjustable |
| structure | $\sim$0.5 cm | no time structure |
| size | diameter 20–30 $\mu$m | 1k–100k atoms |
| flow rate | $\sim$10k pellets/s | continous |
| feature | usable for vertexing | variable density |

### 3.1. Targets

For the fixed target setup various target sources are possible [3]. The two major techniques are pellet and cluster jet targets. Both techniques use usual materials like $H_2$, $D_2$, $N_2$, Ne, Ar and others. The parameters of these target are summarized in Table. 1. At a luminosity of $2 \times 10^{32}$ cm$^{-2}$s$^{-1}$ with $10^{11}$ stored $\bar{p}$-atoms the resulting average interaction rate is estimated to be $\sim$20 MHz.

For the future solid fiber targets of $C$, $CH_2$ and other materials are foreseen.

### 3.2. Target Spectrometer

The target spectrometer has a compact shell structure. From the interaction region to the outside a vertex detector, tracker detector, particle identifying detector, calorimeter, magnet and muon detectors are stacked.

The micro vertex detector (Fig. 2(b)) [4] consists of two inner barrels of Si-hybrid detectors and two outer Si-strip detectors. In the forward direction four Si-hybrid detectors and two mixed detectors are combined. The cell size of the Si-hybrids are 100$\times$100 $\mu$m while the Si-strips have a pitch size of 130 $\mu$m in the barrels and a pitch size of 70 $\mu$m in the discs. A continous readout is designed. The ToPiX (CMOS 130 nm) readout chip is used for $\sim$11M pixels. For the $\sim$200k strips n-XYTER or APV25-S1 will be used. The main challenge to measure the displacements is a low material budget ($< 10\% X_0$) for polar angles below 140°.

The goal for the central tracker is to have momentum resolution below 1% with low material budget. It supports particle identification by a measurement of energy deposition. Optimized gas-electron-

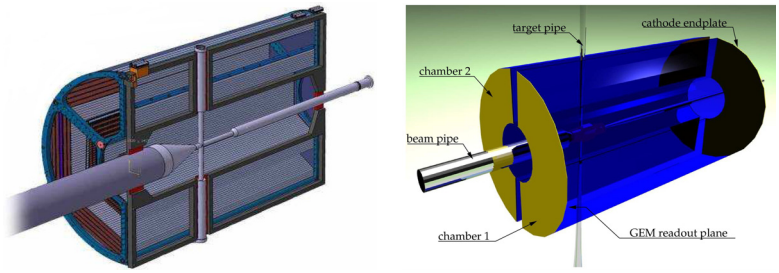


(a) (b)

Fig. 3: Setup of the central tracker options (a) Straw Tube Tracker (b) Time Proportional Chamber

multipler disc detectors cover the forward region. The innermost disc has a 90 cm diameter while the outermost has 148 cm diameter. The polar angle acceptance reaches from 3° to 20° and has space resolution below 100 $\mu$m. For the barrel part of the central tracker two concepts are under investigation. The first solution – straw tube tracker – (Fig. 3(a)) [5] uses ∼4.5k pressure stabilized tubes with 1 bar overpressure. The gas mixture consists of $Ar/CO_2$ with a ratio 90:10. As tube material W/Re-wires and 27 $\mu$m Mylar surfaced with 30 nm aluminium were selected. The second solution – time proportional chamber – (Fig. 3(b)) [6] has the same two half cylinder shape with a length of 150 cm, an inner radius of 15 cm and a outer radius of 42 cm. This gas detector has 700 l volume and has a $Ne/CO_2(+CH_4/CF_4)$ mixture. Continous readout with sampling is used.

For the particle identification detectors based on DIRC (detection of interally reflected Cherenkov radiation) are used (Fig. 4(a)) [7]. The barrel DIRC – improved BaBar DIRC – consists of 96 fused silica bars with the dimensions 17×33×2500 $mm^3$. Micro-channelplates (∼10k channels) are used as readout in a local 1 T magnetic field. Dispersion correction will be done with time propagation measurements. For polar angles in the range 22°–140° pions and kaons in the momentum range 0.5–4.0 GeV/c will be separated better than $3\sigma$. Around the barrel DIRC scintillating tiles are used to separate pions and kaons in the momentum range 0.4–0.7 GeV/c better than $3\sigma$ and for polar angles range 22°–90°. The scintillating tiles

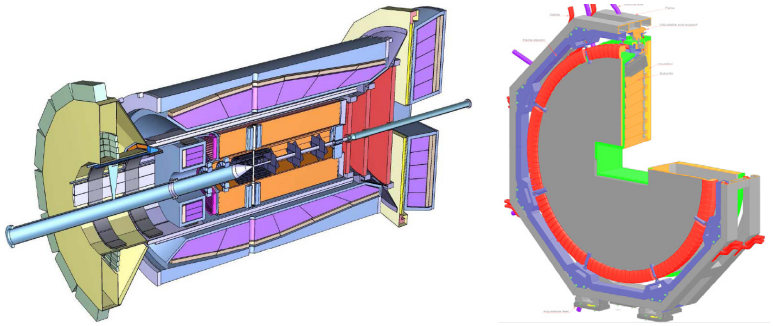

(a) (b)

Fig. 4: (a) Setup of the particle identification detectors and electromagnetic calorimeter of the target spectrometer (b) Setup of the novel disc DIRC

have a granular structure by using $3\times3$ cm$^2$ pads and readout based on Si-based photon detection. With timing resolution below 100 ps event timing and pattern recognition of the barrel DIRC can be improved. In the forward direction a disc DIRC (Fig. 4(b)) is foreseen. It uses several novel techniques in this field to separate pions and kaons in the momentum range 0.5–4.5 GeV/c and for polar angles range 5°–22°. A thin fused silica disc is used as radiator. Bars based on lithium-fluoride are attached to correct passively for dispersion. As an alternative dichroic mirrors can be used to select the measured wavelength. A Parallel-to-point optic element maps propagation photon angles to spatial positions on position sensitive photon detectors. These photon detectors are based on micro-channel-plates or Si-photon detectors as the magnetic field of 1 T cancels other photon detector solutions. Moderate timing resolution below 300 ps will be used to separate different signatures.

The next shell consists of an improved PWO-II based electromagnetic calorimeter (Fig. 4(a)) [8]. It operates at $-25$ °C with a temperature variation below 0.1 K. The crystals are built in such a way that in any direction the same material budget for homogenity is available. As readout vacuum-photo-triodes and Apfel ASIC [8] are designed for the barrel part. For the other parts large area avalance photo diodes with high quantum efficiency and sampling ADC are foreseen. With in total ∼16k PWO-crystals and a thickness of 22 radiation lengths almost $4\pi$ coverage can be achieved. Detection of

$\gamma$ in the range from a few MeV to 10 GeV can be obtained. The relative energy resolution is targeted to be below $1.5\%/\sqrt{E}+0.3\%$ ($[E]$ = GeV).

A superconducting solenoid magnet with 2 T magnetic field, 1.8 m coil diameter and 2.6 m coil length surrounds the calorimeter [9]. Outside an instrumented yoke with a muon system based on micro drift tubes is used to detect muons below 15 GeV/c.

### 3.3. Forward Spectrometer

The forward spectrometer combines a dipole magnet, forward tracker, forward particle identification detectors, forward calorimeter, muon range sytem and a luminosity monitor.

The normal conducting dipole magnet has a magnetic field integral of 1 Tm, 1.3 m opening width and 0.6 m opening height [9]. As forward tracker adjusted straw tubes in several layers are used. The forward tracking system has a planar shape with each two times 16 straw tubes each for a polar angle coverage below 10° horizontal and below 5° vertical.

The particle identification system consists of three parts. The first part is a ring imaging Cherenkov detector. It will be similar to the HERMES RICH detector with improvements [10]. Before and behind it forward time-of-flight detectors based on fast scintillator BC408 are placed. In total 46 slabs ($140 \times 10 \times 2.5$ cm$^3$) and 20 slabs ($140 \times 5 \times 2.5$ cm$^3$) achieve a timing resolution below 50 ps and $3\sigma$ pion-kaon-separation in the momentum range 2.8–4.7 GeV/c. As an alternative resistive plate chambers are under investigation. The third part is an electromagnetic and hadronic Shashlyk calorimeter. A module consists of 380 layers of 0.3 mm lead and 1.5 mm scintillator. The total length is 680 mm with a transverse size of $55 \times 55$ mm$^2$. Each module has 36 BCF-91A wavelength-shift-fibers (Ø 1 mm) for light collection and has 20 radiation lengths material budget. Conventional photo-multipliers are used as readout. A monitor for gain and aging effects is based on LEDs. The active area comprises $3 \times 1.5$ m$^2$. In total 374 super modules of four modules achieve a relative energy resolution of $5.6\%/E + 2.4\%/\sqrt{E} + 1.3\%$ ($[E]$ = GeV).

The rear end of the spectrometer is equipped with a muon range system. In total 37 layers of micro drift tubes contain ~4k tubes,

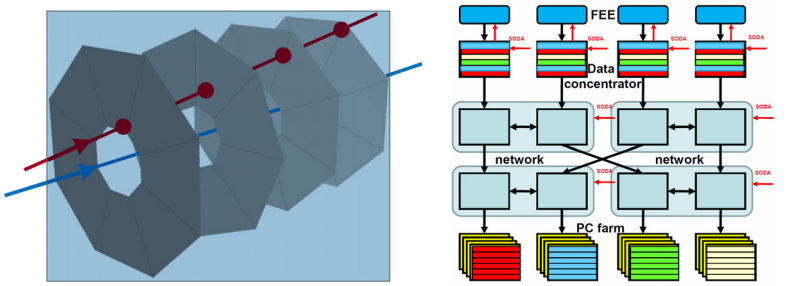


(a) (b)

Fig. 5: (a) Setup of the luminosity monitor. The blue line imitates $\bar{p}$ propagation while the red line shows particle propagation and interaction (dot) with four double sided Si-based detectors (gray rings). (b) Virtual event building with SODA (Synchronisation of data acquisition) by timestamping, data concentration and PC farming

$\sim$30k wires and $\sim$75k stripes. Finally a luminosity monitor (Fig. 5(a)) is used for luminosity normalisation based on low t elastic scattering. It consists of four double sided planes with a distance of 10 cm at 11 m behind the interaction point. Each plane has 8 trapezoidal Si-strip detectors, rotated by 22.5° to each other. The acceptance ranges from $\sim$0.115° to $\sim$0.458°.

### 3.4. Infrastructure

Due to similar signal and background signatures a central trigger is not available. Therefore the readout of each detector is running continuously or self triggered. Each single hit information will be tagged with a timestamp distributed over SODA (synchronisation of data acquisition) (Fig. 5(b)) [11]. The timing resolution achievable at the FEE (front end electronics) is below 20 ps and will distribute system informations to the FEE as well. A first hit information collection for each detector is done in the data concentrators (mixed color box). Over a high meshed network (cyan color box) the data for a burst are collected in computer nodes (single color box). For data reduction of several orders of magnitude the network and computer nodes reconstruct events and suppress coarse background [12].

For the detector control system a locally and remotely accessible system is foreseen [13]. It is based on AFECS, EPICS and MonaLisa

**T a b l e 2: Reconstructed events per year for various particles**

| events | particle |
|---|---|
| $\sim 2 \times 10^9$ | $J/\Psi$ |
| $\sim 2 \times 10^7$ | $\chi_2$ |
| $\sim 2 \times 10^7$ | $D\bar{D}$ |
| $\sim 2 \times 10^8$ | $\Xi\bar{\Xi}$ |

which are used successfully in large-scale experiments and infrastructures such as CERN, JLAB and others. For offline analysis a grid system based on AliEn and MonaLisa is used. This grid system was already successfully used to perform all the simulation and reconstruction for the $\overline{P}ANDA$ physics book [2].

### 3.5. Performance

The achievable performance of the $\overline{P}ANDA$ detector, with assumed 50% event reconstruction efficiency, results in an integrated luminosity of $\sim$8 pb$^{-1}$ per day or $\sim$3 fb$^{-1}$ per year for a luminosity of $2\times10^{32}$ cm$^{-2}$ s$^{-1}$. Fine scans to measure mass differences below 100 keV at a mass resolution of 10% are expected to be available. A wide range of hadronic and electro-magnetic decay modes are ready for investigations. The amount of reconstructed events per year for some selected particles are summarized in Table 2.

## 4. Summary

The $\overline{P}ANDA$ experiment at FAIR targets a wide range of questions on nucleon structure. For this a general purpose detector is foreseen to run with high luminosity and precise beam momenta. A variable $\bar{p}$-beam in combination with various targets is used. For precise measurements and monitoring rare interactions many new techniques were developed. Existing technologies were optimized to fit requirements in space and performance. With this programmable appartus new physics phenomena can be addressed as well.

**Acknowledgement**

We acknowledge financial support from the Bundesministerium für Bildung und Forschung (bmbf), the Deutsche Forschungsgemeinschaft (DFG), the Swedish Research Council, the Polish Ministry of Science and Higher Education, the University of Groningen, Netherlands, the Forschungszentrum Jülich GmbH, the Gesellschaft für Schwerionenforschung mbH (GSI), the Schweizerischer Nationalfonds zur Förderung der wissenschaftlichen Forschung (SNF), the Helmholtz-Gemeinschaft Deutscher Forschungszentren (HGF), the Russian funding agency "State Corporation for Atomic Energy Rosatom", the CNRS/IN2P3 and the Université Paris-sud, the British funding agency "Science and Technology Facilities Council" (STFC), the "Scottish University Physics Alliance" (SUPA), the Instituto Nazionale di Fisica Nucleare (INFN), the European Community FP6 FAIR Design Study: DIRAC secondary-Beams, contract number 515873, the European Community FP6 Integrated Infrastructure Initiative: HadronPhysics, contract number RII3-CT-2004-506078, the European Community FP7 Integrated Infrastructure Initiative: HadronPhysics II and the Deutscher Akademischer Austauschdienst (DAAD).

1. E. Strokovsky, Quest of $\overline{P}ANDA$ experiment, these proceeding.
2. arXiv:**0903.3905v1**[hep-ex] (2009).
3. doi:10.1016/j.nima.2011.09.024 & doi: 10.1142/S0218301309012562.
4. R. Arora *et al.,* TIPP conference 2011, ID 100.
5. NIM A617 (2010) 148-150.
6. arXiv:**0911.0759v1**[physics.ins-det] (2011).
7. J. Schwiening *et al.,* TIPP conference 2011, ID 124.
8. arXiv:**0810.1216v1**[hep] (2010).
9. arXiv:**0907.0169v1** [physics.ins-det] (2009).
10. NIM A553 (2005) 205-209.
11. I. Konorov *et al.,* IEEE NSS 2009, N25-249.
12. H. XU *et al.*, TIPP conference 2011, ID 12.
13. K. Schwarz *et al.,* CHEP conference 2011, ID 471.

# LATEST OSCILLATION RESULTS FROM T2K

Marat Khabibullin

*Institute for Nuclear Research*
*of the Russian Academy of Sciences*
*(On behalf of the T2K Collaboration)*

**Abstract**

The latest oscillation results obtained in the off-axis accelerator neutrino experiment T2K are presented. In the data sample, corresponding to $1.43\times10^{20}$ protons on target, $6\nu_e$ candidate events pass the selection criteria, while the expected number of background events for $\sin^2 2\theta_{13} = 0$ is $1.5 \pm 0.3$ (syst.). The probability to observe six or more candidate events due to background is 0.7%, equivalent to $2.5\sigma$ significance.

In the $\nu_\mu$-disappearance analysis the obtained atmospheric oscillation parameters are consistent with results from the Super-Kamiokande and MINOS experiments.

## 1. Introduction

T2K is a second generation long baseline (LBL) accelerator neutrino experiment: in contrast to the first generation experiments, like K2K, MINOS and OPERA, T2K has neutrino detectors located slightly offset with respect to the initial proton beam (off-axis angle is 2.5°).

Experiment T2K (Tokai-to-Kamioka) is an International Collaboration of about 500 members from 58 institutes of 12 countries. The source of muon neutrinos and near detectors are located at the Japan Proton Accelerator Research Complex (J-PARC, Tokai Village, Ibaraki Prefecture, Japan), while as a far detector the well-known Super-Kamiokande (SK) detector located at 295 km is used (Kamioka, Gifu Prefecture, Japan).

A primary goal of the T2K is a measurement of the only unknown mixing angle $\theta_{13}$ by detecting the electron neutrinos at the far detector in the initially almost pure muon neutrino beam ("$\nu_e$-appearance").

A secondary goal is a precision measurement of so-called atmospheric oscillation parameters $(\theta_{23}, \Delta m^2_{23})$ by detecting a deficit of muon neutrinos at the far detector ("$\nu_\mu$-disappearance").

## 2. Physics Motivation: Neutrino Oscillations

At present it is known that neutrinos are produced and detected in weak interactions as leptons of three flavours: electron $\nu_e$, muon $\nu_\mu$ and tau $\nu_\tau$ (for a detailed review of neutrino parameters see [1]). Neutrino flavour eigenstates $|\nu_\alpha\rangle$ $(\alpha = e, \mu, \tau)$ are not equal to the neutrino mass eigenstates $|\nu_i\rangle$ with mass eigenvalues $m_i$ $(i = 1, 2, 3)$. A conversion from the mass basis to the flavour basis is governed by the $3\times3$ unitary matrix $U_{\mathrm{PMNS}}$ (Pontecorvo-Maki-Nakagawa-Sakata) [2, 3], which can be parametrized in such a way, that it only depends on 3 mixing angles and one CP-violating phase: $\theta_{12}, \theta_{23}, \theta_{13}$ and $\delta_{\mathrm{CP}}$.

Two of these four parameters are measured in solar/reactor and atmospheric/accelerator experiments, respectively: $\theta_{12} \approx 34^\circ$ and $\theta_{23} \approx 45^\circ$. The corresponding mass squared differences, defined as $\Delta m^2_{ij} \equiv m^2_j - m^2_i$, have the following values: $\Delta m^2_{12} \approx 7.6 \times 10^{-5}$ $\mathrm{eV}^2/\mathrm{c}^4$ and $|\Delta m^2_{23}| \approx 2.4 \times 10^{-3}$ $\mathrm{eV}^2/\mathrm{c}^4$. The sign of the $\Delta m^2_{23}$ is remained undetermined ("mass hierarchy problem").

The best upper limit for $\theta_{13}$ was obtained in 1999 by the reactor experiment CHOOZ and slightly corrected in 2010 by the LBL experiment MINOS: $\theta_{13} < 11^\circ$ $(\sin^2 2\theta_{13} < 0.15)$ [4, 5]. If $\theta_{13}$ has non-zero value, then one can study a potential CP-violation in the lepton sector.

The "appearance" probability $P(\nu_\mu \to \nu_e)$ to observe an electron neutrino at the distance $L$ from the source of the muon neutrinos with an inital energy $E$ depends on the mixing angles, mass squared differences and $L/E$ ratio:

$$P(\nu_\mu \to \nu_e) \approx \sin^2(2\theta_{13}) \sin^2(\theta_{23}) \sin^2\left(\frac{\Delta m^2_{23} L}{4E_\nu}\right). \qquad (1)$$

The "disappearance" probability $P(\nu_\mu \to \nu_\mu)$ in two-flavour oscillation scenario has the following form:

$$P(\nu_\mu \to \nu_\mu) \approx 1 - \sin^2(2\theta_{23}) \sin^2 \left( \frac{\Delta m^2_{23} L}{4E_\nu} \right). \quad (2)$$

Using the equations (1)–(2) and other inputs one can compute the expected number of events $N^{\rm exp}_{\rm SK}$ and the neutrino energy spectra at the far detector and compare them with observed number of events $N^{\rm obs}_{\rm SK}$ and the measured energy spectrum. Fitting these two numbers and/or energy spectra it is possible to get the parameters in question ($\theta$, $\Delta m^2$).

## 3. T2K Experimental Method

Muon neutrinos in the accelerator experiments are produced as tertiary particles of proton interactions in a special target. In the T2K [6] protons are accelerated at J-PARC in three stages: 1) at LINAC – up to 400 MeV (currently 181 MeV); 2) at Rapid Cycling Synchrotron (RCS) – up to 3 GeV; 3) at Main Ring (MR) – up to 30 GeV, after which the protons are extracted into the neutrino beamline in 8 bunches per spill (6 before November 2010).

Neutrino beamline consists of two main parts: primary section, which transports the protons from the MR to a target, and secondary section, where the secondary particles (pions, kaons *etc.*) are produced and decayed. The positive pions produced in a graphite target are collected and focused into the decay volume by three horns. Muon neutrinos are mainly produced in the $\pi^+$-decays: $\pi^+ \to \mu^+ \nu_\mu$. Undecayed hadrons and low energy muons ($p_\mu < 5$ GeV/c) are absorbed by the beam dump, which is followed by the muon monitors (MUMON) providing the information on the intensity and profile of the high energy muons. In order to check the intensity, direction, profile and losses of the proton beam the primary section is equipped with many beam monitors.

The near detector complex ND280 is located in a specially excavated pit at about 280 meters from the target. It consists of two independent detectors (Fig. 1): the INGRID at 0° with respect to the proton beam axis (on-axis), and the ND280 at 2.5° (off-axis). The

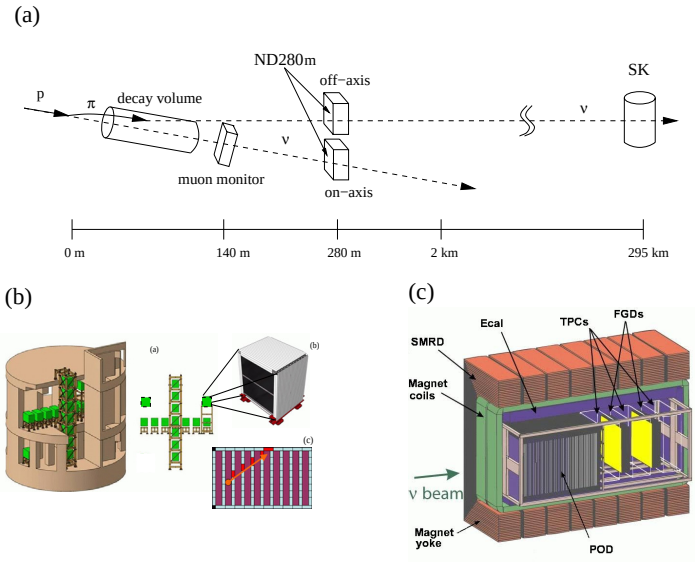


Fig. 1: T2K experimental setup: a) a schematic view; b) near detectors: INGRID (left) and the off-axis ND280 (right)

on-axis near detector INGRID (Interactive Neutrino GRID) is used to monitor the neutrino beam profile, direction and interaction rates on the day-by-day basis. The off-axis near detector ND280 consists of a $\pi$0-detector (P0D), a tracker with two fine-grained detectors (FGD) sandwiched by three time projection chambers (TPC).The tracker and P0D are surrounded by the components of the electromagnetic calorimeter (ECAL), and all of them are installed inside an UA1/NOMAD magnet which provides a magnetic field of 0.2 T in the direction perpendicular to the off-axis beam (X-direction). The yoke of the magnet is instrumented as a side muon range detector. The main function of the off-axis ND280 complex is to measure the neutrino flux, energy spectrum, interaction rates and cross-sections *before* the oscillation.

The far detector SK is a 50-kton water Cherenkov detector (22.5 kt in the fiducial volume, FV) located at 295 km also at 2.5°. SK detector consists of two main parts: the inner detector (ID) with about

11,100 photomultipliers (20" Hamamatsu PMT) and the outer detector (OD) with about 1900 PMTs (8"). The main feature of SK detector is an excellent particle identification of muons and electrons with about 99% efficiency.

The main advantages of the off-axis conception are as follows: 1) at $0^\circ$ the neutrino energy is propotional to the parent pion momentum $E_\nu \sim p_\pi$, while at $2.5^\circ$ the neutrinos have almost monochromatic spectrum with a high beam intensity; 2) the neutrino energy peak corresponds to the first oscillation maximum; 3) the beam $\nu_e$-contamination at SK is low ($\sim 1\%$); 4) the background from the neutral current (NC) $\nu_\mu$-interactions at the high energy tail is considerably suppressed.

## 4. T2K Experimental Data and Selection Criteria

T2K beam data taking was started in January 2010 and paused because of the Great East Japan Earthquake in March 2011. An analysis of $\nu_e$-appearance [7] and $\nu_\mu$-disappearance events was carried out for $1.43\times10^{20}$ protons on target (p.o.t.) collected in the first two runs Run I (Jan–Jun 2010) and Run II (Nov 2010–Mar 2011). The beam power reached 145 kW in March 2011 with $9\times10^{13}$ protons per pulse.

A direction of the off-axis beam during the Runs I and II had being checked by means of the MUMON and INGRID which demonstrated, that the beam direction was stable well within $\pm1$ mrad (1 mrad shift corresponds to about 2% shift of the $E_\nu$ peak energy at 295 km). INGRID also showed a very stable neutrino interaction rate of about 1.5 events per $10^{14}$ p.o.t.

The signature of the neutrino interaction in the SK detector is a single electron- or muon-like Cherenkov ring caused by a lepton from a charged-current quasi-elastic (CCQE) process in the water: $\nu_l + n \rightarrow l^- + p$, where $l = e, \mu$. The main backgrounds in case of the $\nu_e$-appearance are the intrinsic $\nu_e$ from the beam and NC-interactions with $\pi^0 \rightarrow \gamma\gamma$ in the final states: $\nu_X + n \rightarrow n + \pi^0$ when one photon is missed and another one mimics the electron. In case of the $\nu_\mu$-disappearance the main background comes from the charged-current processes with one charged pion in the final state (CC1$\pi$): $\nu_\mu + n \rightarrow \mu^- + n + \pi^+$ or $\nu_\mu + p \rightarrow \mu^- + p + \pi^+$.

In order to reject these background events the selection criteria were fixed from Monte Carlo (MC) studies before the data were collected. The observed number of events $N_{SK}^{obs}$ obtained after applying these selection criteria is compared to the expected number of events $N_{SK}^{exp}$, computed taking into account a neutrino flux, cross-section predictions and using a normalization factor from the analysis of events in the off-axis near detector. For the neutrino flux prediction at SK many inputs were used: the beam monitor data; the hadron production calculations based on the results of the NA61/SHINE CERN experiment [8] and FLUKA MC simulations, also the GEANT3 with GCALOR simulations and cross-sections based on models and external measurements.

To satisfy the general selection criteria related to the $\nu_e$-appearance and $\nu_\mu$-disappearance analyses the event at SK should have the following parameters: its timing is within the range from $-2$ to 10 $\mu$s around the beam trigger time; it's a fully-contained (FC) event which means that the vertex and the ring are within the ID, and there is no activity in the OD. 121 events survived these criteria. This number was reduced to 88 after demanding the energy deposited in the ID to be at least 30 MeV (visible energy $E_{vis}$) and the vertex to be in the fiducial volume (FCFV) constrained by an inward 2 meter distance from each ID wall. 41 events have a single Cherenkov ring: 8 $e$-like and 33 $\mu$-like.

## 5. $\nu_e$-appearance Results

Six out of 8 $e$-like events have $E_{vis} > 100$ MeV and no delayed-electron signal. To suppress misidentified $\pi^0$ mesons, the reconstruction of two rings is forced, and a cut on the two-ring invariant mass $M_{inv} < 105$ MeV/$c^2$ is imposed. To suppress the background from the intrinsic $\nu_e$ component, the reconstructed neutrino energy required to be $E_\nu^{rec} < 1250$ MeV. No events were rejected after the last two cuts, so, the number of the candidate $\nu_e$-events is $N_{SK}^{obs} = 6$. The expected number of events computed for $\sin^2 2\theta_{13} = 0$ is $N_{SK}^{exp} = 1.5 \pm 0.3$, where the total systematic uncertainty $^{+22.8}_{-22.7}\%$ is taken into account. The probability to observe 6 or more events for $\sin^2 2\theta_{13} = 0$ is 0.7% (2.5$\sigma$ significance). 90% confidence inter-

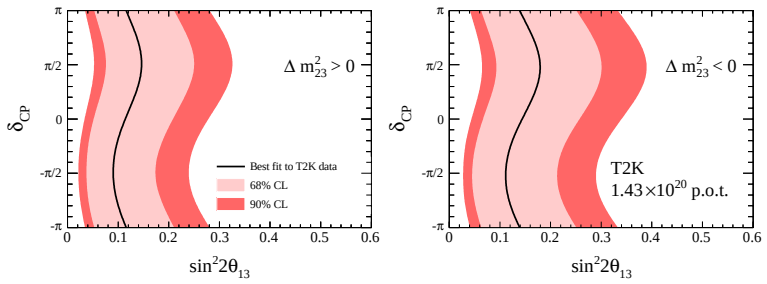


Fig. 2: Contours for $\nu_e$-appearance parameters: the 68% and 90% C.L. regions for $\sin^2 2\theta_{13}$ for each value of $\delta_{\rm CP}$ for normal (left) and inverted (right) mass hierarchy

vals for $\theta_{13}$ calculated by the Feldman and Cousins method [9] are as follows (Fig. 2): $0.03 < \sin^2 2\theta_{13} < 0.28$ for a normal mass hierarchy ($\Delta m^2_{23} > 0$) and $0.04 < \sin^2 2\theta_{13} < 0.34$ for an inverted mass hierarchy ($\Delta m^2_{23} < 0$).

## 6. $\nu_\mu$-disappearance Results

The 33 events with a single $\mu$-like ring are further checked to reject CC1$\pi$ background events by requiring one or zero delayed electrons (from the muon decay) and the reconstructed muon momentum $p_\mu > 200$ MeV/c: 31 events survived. Under a null oscillation hypothesis the expected number of $\nu_\mu$ is 104 with a systematic uncertainty $^{+13.2}_{-12.7}$%, which corresponds to a 4.5$\sigma$-significance exclusion of this hypothesis. The reconstructed neutrino energy spectrum at SK demonstrates a clear oscillation pattern (Fig. 3).

The atmospheric oscillation parameters were extracted using two independent fitting methods: A) finding a maximum of a likelihood function with varying systematic errors, and B) minimizing a special $\chi^2$ with fixed systematic errors. Both methods gave very close best fit results consistent with the previous measurements by MINOS and SK: $\sin^2 2\theta_{23} \approx 0.99$ in the method A (0.98 in method B), $\Delta m^2_{23} = 2.6 \times 10^{-3}$ eV$^2$/c$^4$.

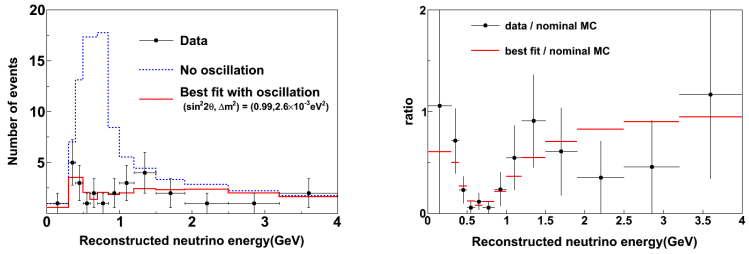


Fig. 3: Reconstructed neutrino energy spectrum at SK (left) and data/MC ratio (right) for $\nu_\mu$-disappearance events

## 7. Conclusions

The latest oscillation results obtained in the first off-axis accelerator neutrino experiment T2K are presented. In the data sample, corresponding to $1.43\times10^{20}$ p.o.t. (2% of the final T2K goal), $6\nu_e$ candidate events pass the selection criteria, while the expected number of background events for $\sin^2 2\theta_{13} = 0$ is $1.5 \pm 0.3$ (syst.). The probability to observe six or more candidate events due to background is 0.7%, equivalent to $2.5\sigma$ significance. At 90% C.L., the data are consistent with $0.03(0.04) < \sin^2 2\theta_{13} < 0.28(0.34)$ for $\delta_{\rm CP} = 0$ and normal (inverted) hierarchy.

In the $\nu_\mu$-disappearance analysis the obtained atmospheric oscillation parameters are consistent with results from the SK and MINOS experiments.

J-PARC plans to restart the work of the accelerator complex in December 2011, and T2K is going to resume the data taking as soon as possible.

This work was supported in part by the "Neutrino Physics" Program of the Russian Academy of Sciences, by the RFBR (Russia)/JSPS (Japan) grant № 11-02-92106 and by the Science School grant № 65038.-2010.2.

1. K. Nakamura *et al.* (Particle Data Group), J. Phys. G **37**, 075021, 164 (2010).
2. B. Pontecorvo, Sov. Phys. JETP **26**, 984 (1968).
3. Z. Maki, M. Nakagawa, S. Sakata, Prog. Theor. Phys. **28**, 870 (1962).
4. M. Apollonio *et al.* (Chooz Collab.), Phys. Lett. B **466**, 415 (1999).

5. P. Adamson *et al.* (MINOS Collab.), Phys. Rev. D **82**, 051102 (2010).
6. K. Abe *et al.* (T2K Collaboration), Nucl. Instrum. Methods (2011), in press, doi: 10.1016/j.nima.2011.06.067; arXiv:1106.1238 [physics.ins-det].
7. K. Abe *et al.* (T2K Collaboration), Phys. Rev. Lett. **107**, 041801 (2011).
8. N. Abgrall *et al.* (NA61/SHINE Collab.), Phys. Rev. C **84**, 034604 (2011).
9. G.J. Feldman and R.C. Cousins, Phys. Rev. D **57**, 3873 (1998).

# RECENT HIGHLIGHTS IN PHENIX AT RHIC

E. Kistenev (for the PHENIX Collaboration)

*Physics Department, Brookhaven National Laboratory,*
*Upton, NY 11973-5000, USA*
*e-mail: kistenev@bnl.gov*

**Abstract**

By 2011 PHENIX experiment at Relativistic Heavy Ion Collider of the Brookhaven National Laboratory completed 10 year of data taking in p+p, d+Au, Cu+Cu and Au+Au collisions at different energies. Accumulated data revealed increasingly detailed picture of the hot and dense matter created in heavy ion collisions. RHIC's unique feature – ability to accelerate polarized protons helped to further expand physics reaches of RHIC experiments. This paper highlights recent PHENIX results for direct photons produced in p+pand nucleus-nucleus collisions together with first observation of W-boson production in polarized p+pcollisions which directly demonstrates the parity violating coupling of the W to light quarks.

## 1. Direct Photon Measurements in PHENIX

The data presented in this paper are from p+p , d+Au , Cu+Cu and Au+Au data sets at $\sqrt{s_{NN}} = 200$ GeV taken with the PHENIX detector [1] in 2004-2008. The PHENIX central arms, each covering $\pm 0.35$ units of pseudorapidity around midrapidity and $90^\circ$ in azimuth, contain charged-particle tracking chambers and two kinds of electromagnetic calorimeters. The BBC and Zero-Degree Calorimeters (ZDC) are used for minimum bias event selection and centrality determination (when appropriate).

Among the observables used to probe the high temperature and high density phase of heavy nucleus collisions direct photons are considered of particular interest. Nuclear modifications to the yield of

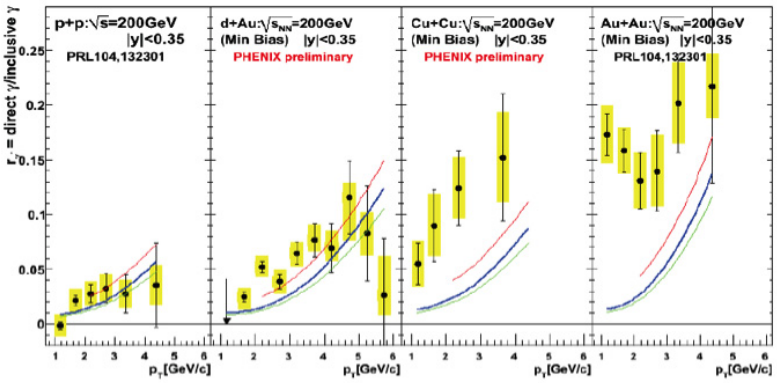


Fig. 1: (color online) The fraction $r_\gamma$ of direct photons in the inclusive photon yield as a function of $p_{\mathrm{T}}$ in p+p , d+Au , Cu+Cu and Au+Au (min. bias) collisions [2]. The error bars and the boxes represent statistical and systematic uncertainties, respectively. The curves are from an NLO pQCD calculation

direct photons reflects medium effects on contributing production mechanisms. Hard scattered photons produced early in collision history are not expected to flow. The rate and azimuthal asymmetries of photons produced at low to medium $p_{\mathrm{T}}$ (1-5GeV/c) [2, 9] will be influenced by the emission from expanding medium and reflect initial anisotropy of the collision region.

Direct photons yields, their flow and gamma-jet correlations are measured by statistical subtraction of the estimated meson (mainly $\pi^0$) decay photon contribution from the inclusive photon and $\gamma$-$h$ samples. An alternative method for measuring direct photons is provided by the low-mass $e^+e^-$ pairs produced by a higher order QED correction to the real photon emission process. Any source of real photons must also emit virtual photons and their yield is related to that of real photons. In the low mass region, where the $p_{\mathrm{T}}$ of the $e^+e^-$ pair is much greater than its mass ($m_{ee} \ll p_{\mathrm{T}}$), the yield of the intermediate virtual photons is approximately the same as that of real photons. Therefore, in this quasi-real virtual photon region, the production of real direct photons can be deduced from measurements of $e^+e^-$ pairs.

Figure 1 shows the fraction $r_\gamma = \frac{\text{direct } \gamma}{\text{inclusive } \gamma}$ of the direct photon component in p+p , d+Au , Cu+Cu and Au+Au collisions, respec-

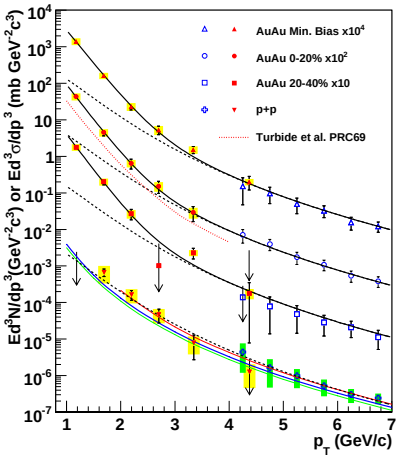


Fig. 2: (color online) Invariant cross section p+p and invariant yield Au+Au of direct photons as a function of $p_{\mathrm{T}}$ [2, 4, 5]. The solid curves on the p+p data represent NLO pQCD direct photon calculations [3]. The dashed curves on the Au+Au data show the p+p fit scaled by $T_{\mathrm{AA}}$. The solid curves on the Au+Au data are an exponential fit plus the $T_{\mathrm{AA}}$ scaled p+p fit

tively. The curves represent the expectations from a NLO pQCD calculation [3]. The three curves correspond (from top to bottom) to the theoretical scales set to $\mu = 0.5\ p_{\mathrm{T}}$, $p_{\mathrm{T}}$, and $2\ p_{\mathrm{T}}$, respectively. While the fraction $r_\gamma$ is consistent with the NLO pQCD calculation in p+p and d+Au, it is larger than the calculation in both Cu+Cu and Au+Au for $p_{\mathrm{T}} < 5$ GeV/$c$.

In Figure 2 the direct photon yield in Au+Au computed using the relation $dN_\gamma^{\mathrm{dir}}(p_{\mathrm{T}}) = r_\gamma \times dN_\gamma^{\mathrm{incl}}(p_{\mathrm{T}})$ is compared in to the direct photon data from [4, 5] and NLO pQCD calculations. In central collisions it shows excess over collision scaled p+p data, and the shape of the excess is well described by the exponential with inverse slope $T \simeq 220$ MeV. If the direct photons in Au+Au collisions are of thermal origin, the inverse slope $T$ is related to the initial temperature $T_{\mathrm{init}}$ of the dense matter. In hydrodynamical models, $T_{\mathrm{init}}$ is 1.5 to 3 times $T$ due to the space-time evolution [6].

If photons are radiated inside an expanding matter having azimuthally anisotropic momentum distribution, their momenta add or subtract for radiation along or opposite to the motion. Neglecting

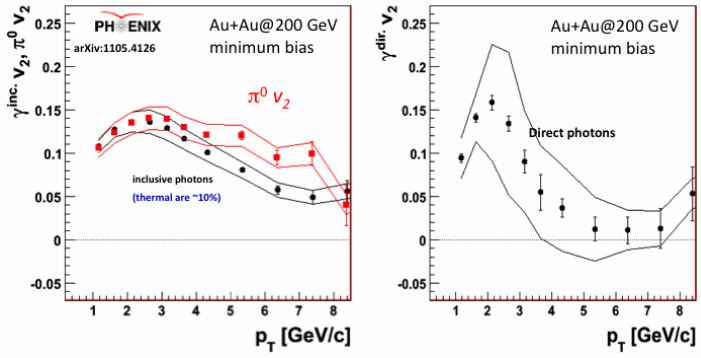


Fig. 3: (color online) Left panel: Comparison between elliptic flow ($v_2$) of $\pi^0$ and inclusive photons in minimum bias Au+Au collisions. Right panel: Direct photon flow in the most central Au+Au collision computed using a subtraction procedure

pion mass, thermal photons must have the same or greater elliptic flow ($v_2$) as pions [7].

An earlier low $p_{\rm T}$ measurements of photon flow for $\pi^0$ and inclusive photons has been published in [8]. Using recent (2007) high statistics p+p and Au+Au data PHENIX extended $p_{\rm T}$ range for $v_2$ measurements to 15 GeV/c and dramatically improved $v_2$ precision in the low to medium $p_{\rm T}$ range.

To correct for a large contribution from hadron decays, predominantly from $\pi^0$ (~80%) and $\eta$ (~15%), and for cluster merging for high $p_{\rm T}$ $\pi^0$'s the $v_2$ flow of the direct photons was calculated as $v_2^{\gamma,{\rm dir}} = \frac{R_\gamma(p_{\rm T})\times v_2^{\gamma,{\rm inc}} - v_2^{\gamma,{\rm bg}}}{R_\gamma(p_{\rm T})-1}$, where $R_\gamma(p_{\rm T}) = N^{\rm inc}(p_{\rm T})/N^{bg}(p_{\rm T})$ is the direct photon excess ratio, and $N^{\rm inc} = N^{\rm meas} - N^{\rm hadr}$ is for inclusive photons. The $v_2$ values for $\pi^0$ in minimum bias Au+Au events are compared to similar data for inclusive photons in Figure 3 left panel [9]. The $v_2$ data for direct photons in the most central Au+Au events are shown in the right panel in the same Figure.

The two sets of points (inclusive photons and $\pi^0$) are barely different in the thermal $p_{\rm T}$ range indicating the dominance of the photons with flow values close to that of hadrons. Qualitative conclusions of the left panel are confirmed quantitatively in the right panel displaying subtraction data for direct photons in the most central Au+Au

collisions. Below $p_{\mathrm{T}} \sim 5$ GeV/c $v_2$ of direct photons has value comparable to that of hadrons. At higher $p_{\mathrm{T}}$ it drops to zero as expected if photons produced in hard scattering (reverse compton scattering and quark-antiquark annihilation) dominate in that $p_{\mathrm{T}}$ range.

## 2. Cross Section and Parity Violating Spin Asymmetries of $W^{\pm}$ Boson Production in Polarized p+p Collisions at $\sqrt{s} = 500$ GeV

The role and interplay of the constituent and sea quarks in the proton spin is one of the key questions in the particle physics. Theoretical predictions vary between nearly equal contributions from all flavors of sea quarks to the preponderance of $\overline{d}$ over $\overline{u}$ in the proton sea. The W production at RHIC provides sensitivity to $(\Delta\overline{u} - \Delta\overline{d})$ missing in SIDIS measurements due to fragmentation function uncertainties. In polarized proton-proton collisions the longitudinally polarized $\overline{u}$ and $\overline{d}$ are accessed through a measured single spin asymmetry of the decay leptons $A_l = \frac{\sigma_+ - \sigma_-}{\sigma_+ + \sigma_-}$ where $\sigma_{+(-)}$ is the cross section for a positively(negatively) charged leptons from W bosons produced in the scattering of a longitudinally polarized proton with positive(negative) helicity on an unpolarized proton. For leptons detected in forward (backward) directions this asymmetry is nearly equal to $\Delta q/q(\Delta\overline{q}/\overline{q})$, the asymmetry measured in the central region is a linear combination of polarized parton distribution functions which must be combined with other measurements for a flavor separation.

In the 2009 Run at RHIC there were polarized p+p collisions at $\sqrt{s}$= 500 GeV for physics for the first time. The data accumulated at PHENIX over a four week period (integrated luminosity of 8.6 pb$^{-1}$), allowed a first look at $W$ production as a tool for studying the proton spin. The average polarization of the beams was $0.39 \pm 0.04$. During that Run, only the central arms of PHENIX which cover $|\eta| < 0.35$ in rapidity were ready to record the high $p_{\mathrm{T}}$ leptons that arise from $W$ decay. PHENIX employed a combination of electromagnetic calorimeters, drift chambers and pad chambers in the PHENIX central magnet to measure and identify particles. A variety of cuts (positions, timing, and an E/p) reduced the backgrounds from QCD processes (mostly pion production) to a level where a Jacobian signal

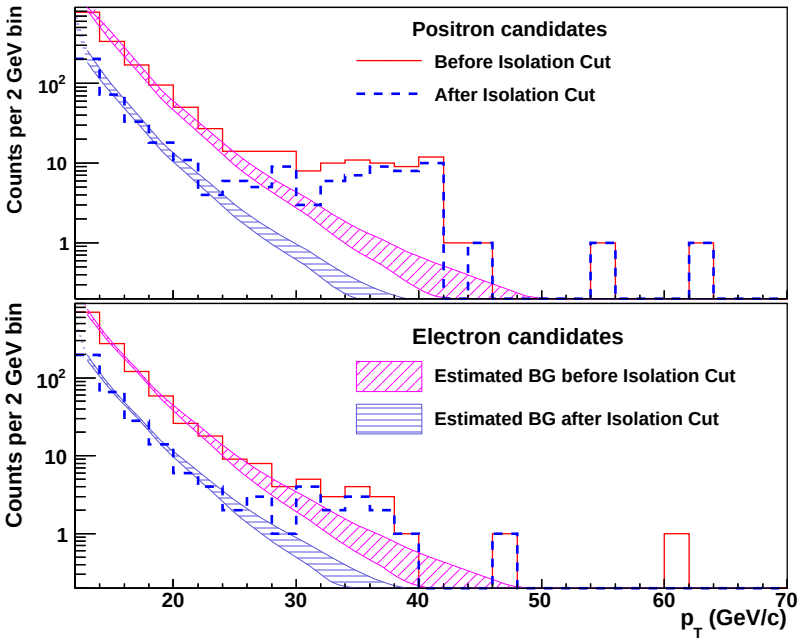


Fig. 4: (color online) Background subtracted spectra of positron (upper panel) and electron (lower panel) candidates before the isolation cut compared to the spectrum of $W$ and $Z$ decays from an NLO calculation [14, 15]. The gray bands reflect the uncertainty of the background

in the electron and positron $p_{\mathrm{T}}$ spectra could be seen; see solid red histogram in Figure 4. For the purposes of determining the longitudinal single-spin asymmetry, an additional isolation cut was made: we required that total amount of additional energy and momenta in a cone of radius 0.5 in $\eta$ and $\phi$ around the identified cluster was less than 2 GeV. This last cut reduces the background in the signal region ($30 < p_{\mathrm{T}} < 50$ GeV/c ) by a factor of about 4 (see dashed blue histogram in Figure 4). We are not able to exclude events due to $Z$ production and decay from our data sample; the number of $Z$ events expected is small, about 7% of the $W^+$ sample and about 30% of the $W^-$ sample.

To compute the $W^{\pm}$ production cross sections, we used the NLO and NNLO calculations to subtract the $Z$ contribution in our sample

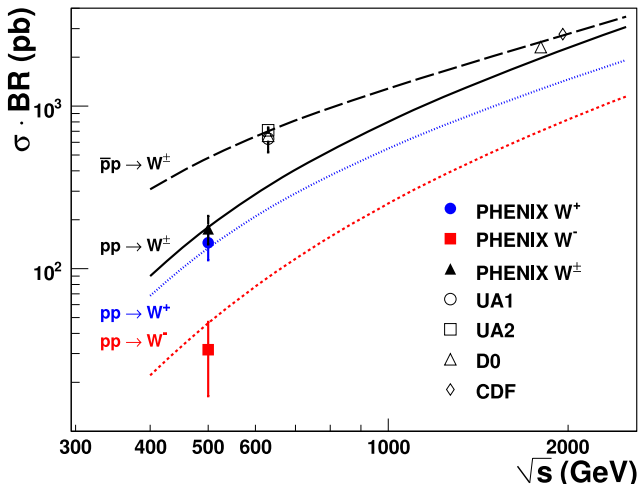


Fig. 5: (color online) Inclusive cross sections for $W$ leptonic decay channel of this measurement and $\bar{p}p$ measurements [12,13,16,17]. Statistical and systematic uncertainties were added here in quadrature. The curves are theory calculations [18]

and to correct for $W$ decays that were outside of the detector acceptance. The contribution from $Z$ decays is 6.9% for $W^+$ and 30.6% for $W^-$. The fraction of the total cross section within $|y| < 0.35$ in rapidity, $p_{\mathrm{T}} > 30$ GeV/$c$, and $|\Delta\phi| < \pi$ is estimated to be 11.3% of positrons from $W^+$ and 7.4% of electrons from $W^-$. The theoretical uncertainties from NLO and NNLO calculations and varied parton-distribution functions (PDFs) [10,11] are small compared to other sources of systematic uncertainty. With these corrections, $\sigma(pp \to W^+X) \times BR(W^+ \to e^+\nu_e) = 144.1 \pm 21.2(\mathrm{stat})^{+3.4}_{-10.3}(\mathrm{syst}) \pm 21.6(\mathrm{norm})$ pb, and $\sigma(pp \to W^-X) \times BR(W^- \to e^-\bar{\nu}_e) = 31.7 \pm 12.1(\mathrm{stat})^{+10.1}_{-8.2}(\mathrm{syst}) \pm 4.8(\mathrm{norm})$ pb, where $BR$ is the branching ratio. These are shown in Fig. 5 and compared to published Tevatron and S$p\bar{p}$S data [12,13,16,17].

To calculate the spin asymmetry, the sample with the isolation cut was used to minimize the background contamination. To reduce the ambiguity of charge misidentification to a negligible level, a further cut was applied to the bend angle ($\alpha$) to be $|\alpha| < 1$ mr. When a polarized beam collides with a unpolarized beam, the raw parity

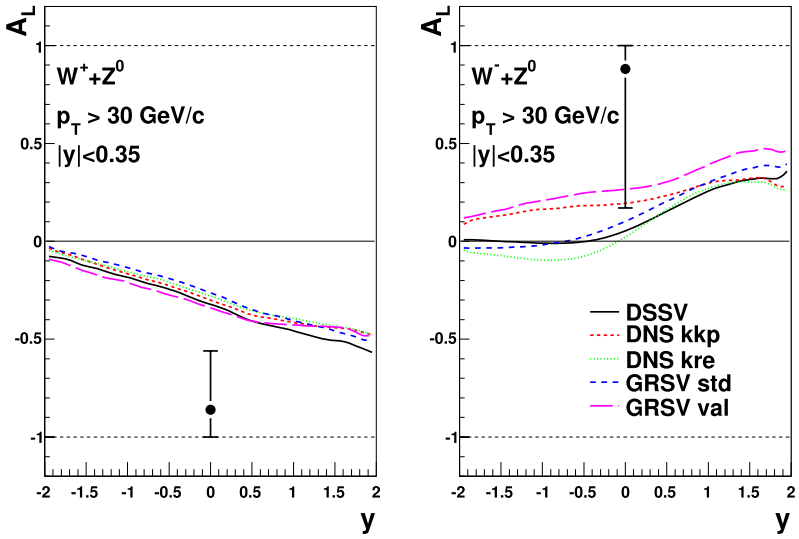


Fig. 6: (color online) Longitudinal single-spin asymmetries for electrons and positrons from $W$ and $Z$ decays. The error bars represent 68% CL. The theoretical curves are calculated using NLO with different polarized PDFs [14]

violating single spin asymmetry is defined by

$$\epsilon_L = \frac{N^+ - R \cdot N^-}{N^+ + R \cdot N^-}, \tag{1}$$

where $N^+$ is the number of events from a beam of positive helicity and $N^-$ is the number of events from a beam of negative helicity, and $R$ is the ratio of the luminosity for the positive and the negative helicity beams. The longitudinal spin asymmetry is then calculated from the measured asymmetry according to

$$A_L = \frac{\epsilon_L \cdot D}{P}, \tag{2}$$

where $P$ is the beam polarization and $D$ is a dilution correction to account for the remaining background in the signal region.

Figure 6 compares measured longitudinal single-spin asymmetries to estimates based on a sample of polarized PDFs extracted from fits of DIS and semi-inclusive DIS data [14]. The experimental results

are consistent with the theoretical calculations at 6-15% confidence level for $A_L^{e^+}$ and at 20-37% for $A_L^{e^-}$. The observed asymmetries are sensitive to the polarized quark densities at $x \sim M_W/\sqrt{s} \simeq 0.16$, and directly demonstrate the parity violating coupling between $W$ bosons and light quarks.

## 3. Summary

The direct photon production data accumulated by PHENIX confirm the unique role of direct photons in probing the sQGP evolution and its properties. Consistency between high $p_{\mathrm{T}}$ yields of direct photons in heavy ion collisions and collision scaled p+p yield confirms collision scaling. The low $p_{\mathrm{T}}$ behavior of direct photons in central Au+Au collisions is dramatically different from all other particles exhibiting an order of magnitude exponential enhancement as $p_{\mathrm{T}} \to 0$ suggestive of thermal emission from the sQGP. The assumed thermal nature of low to medium $p_{\mathrm{T}}$ photons is further confirmed by the presense of a large flow of direct photons in $p_{\mathrm{T}}$ range below 5 GeV/c.

We also present here the first measurements of production cross section and nonzero parity violating asymmetry in $W$ and $Z$ production in polarized $p+p$ collisions at $\sqrt{s} = 500$ GeV. The results are found to be consistent with theoretical expectations and similar measurements of $A_L^{e^\pm}$ [19]. RHIC luminosity and PHENIX detector upgrades in progress will make it possible in the future to significantly reduce the uncertainties for $A_L$ and to extend the measurement to forward rapidity, which will improve our knowledge of flavor separated quark and antiquark helicity distributions.

1. K. Adcox *et al.* (PHENIX), Nucl. Instrum. Meth.A **499**, 469 (2003).
2. A. Adare *et al.*, Phys. Rev. C **81**, 034911 (2010).
3. L.E. Gordon and W. Vogelsang, Phys. Rev. D **48**, 3136 (1993) and W. Vogelsang, private communication (2008).
4. S.S. Adler *et al.*, Phys. Rev. Lett. **94**, 232301 (2005).
5. S.S. Adler *et al.*, Phys. Rev. Lett. **98**, 012002 (2007).
6. D. d'Enterria and D. Peressounko, Eur. Phy. J. **C46**, 451 (2006).
7. B. Kopeliovich, Private communicaion (May 2011).
8. S. Adler *et al.*, Phys. Rev. Lett. **96**, 032302 (2006).

9. arXiv:1105.4126v1 [nucl-ex] 20 May 2011.
10. A.D. Martin, W.J. Stirling, R.S. Thorne, and G. Watt, Eur. Phys. J. C **63**, 189 (2009).
11. A.D. Martin, R.G. Roberts, W.J. Stirling, and R.S. Thorne, Eur. Phys. J. C **28**, 455 (2003).
12. D.E. Acosta *et al.*, Phys. Rev. Lett. **94**, 091803 (2005).
13. C. Albajar *et al.*, Z. Phys. C **44**, 15 (1989).
14. D. de Florian and W. Vogelsang, Phys. Rev. D **81**, 094020 (2010).
15. P.M. Nadolsky and C.P. Yuan, Nucl. Phys. B **666**, 31 (2003).
16. B. Abbott *et al.*, Phys. Rev. D **61**, 072001 (2000).
17. J. Alitti *et al.*, Z. Phys. C **47**, 11 (1990).
18. K. Melnikov and F. Petriello, Phys. Rev. D **74**, 114017 (2006).
19. M. M. Aggarwal *et al.*, arXiv:1009.0326 [hep-ex].

# THE LHEC AT CERN AND ITS DETECTOR

Peter Kostka[1]
on behalf of the LHeC Study Group

[1]*DESY*

**Abstract**

Some aspects of a design concept [1] for a high luminosity $e^{\pm}$-nucleon collider of 1.3 TeV centre of mass energy are presented[1]. It could be realized at CERN's existing LHC beam facility with the addition of a 60 GeV electron ring or linear accelerator, extendable up to $\approx$140 GeV. The detector under design has to meet the high precision requirements of the physics program along with challenging constraints from the interaction region design.

## Introduction

The new electron-hadron collider, the **L**arge **H**adron **e**lectron **C**ollider (LHeC), exceeds the integrated luminosity collected at HERA by two orders of magnitude and the kinematic range by a factor of twenty in the four-momentum squared, $Q^2$, and in the inverse Bjorken $x$. Electrons of 60 GeV up to 140 GeV collide with LHC protons of 7000 GeV with an $ep$ design luminosity of about $10^{33}\,\mathrm{cm}^{-2}\mathrm{s}^{-1}$. The physics program is devoted to an exploration of the TeV energy frontier, complementing the LHC and its discovery potential for physics beyond the Standard Model with high precision deep inelastic scattering (DIS) measurements. These are projected to solve a variety of fundamental questions in strong and electroweak interactions continuing and extending the unique analysis of DIS lepton-hadron scattering into unknown areas of physics and kinematics. A huge physics potential

[1]The list of authors can be found in [1].

is opened also by the $(Q^2,\ 1/x)$ region accessible in electron-ion (eA) scatterings at the LHeC which is by four orders of magnitude larger compared to previous lepton-nucleus DIS experiments. Half of the LHeC is already built – the LHC.

For the new electron accelerator two design configurations are being discussed: the electron beam circulates in the existing LHC tunnel – Ring-Ring design (RR) – and the alternative, less invasive with respect to the existing LHC infrastructure, the construction of a new linear accelerator complex, with options for energy recovery – Linac-Ring option (LR). Prior to the technical design phase, which starts 2012, the electron accelerator design decision will be taken initiating the schedules for the TDR, prototyping, industrial production and installation of the accelerator and detector components. The current goal is the inauguration of the LHeC in time with the maximum luminosity phase of the LHC, tentatively planed for 2023. Its design is for synchronous $pp$ and $ep$ operation collecting as much as possible integrated luminosity with the LHeC detector, required for the analysis of rare and new physics processes, preferentially occurring at high $Q^2$ and large Bjorken $x$.

The physics program let to some selected requirements for the detector design.

- The detector should be modular and flexible to accommodate the high acceptance as well as the high luminosity running foreseen for the two main physics programs.
- The detector design will be based on recent detector developments in order to meet the ambitious physics requirements, using settled technology, avoiding extended R&D programs and being of comparatively reasonable cost.
- Good vertex resolution for decay particle secondary vertex tagging is required, which implies a small radius and thin beam pipe optimized in view of synchrotron radiation and background production.
- The tracking and calorimetry in the forward and backward direction have to be set up such that the extreme asymmetry of the production kinematics is taken into account by layout and choice of technology for the detector design and to ensure high efficiency measurements.

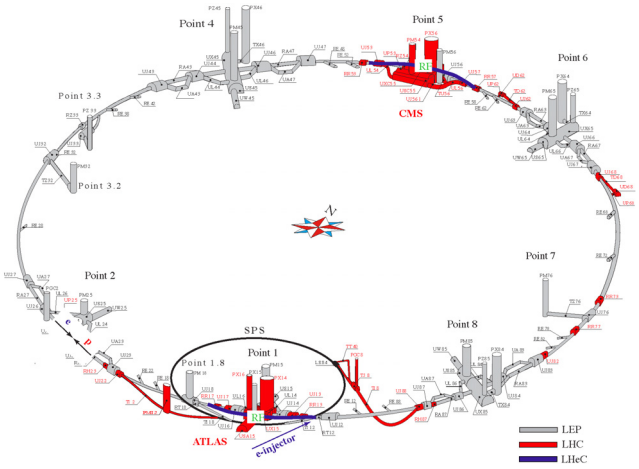


Fig. 1: Schematic Layout of the LHC (grey/red) with the bypasses of CMS and ATLAS for the ring electron beam (blue) in the RR version. The $e$ injector is a 10 GeV superconducting linac in triple racetrack configuration which is considered to reach the ring via the bypass around ATLAS

## Accelerator Complex

The default electron beam energy is chosen to be 60 GeV. For the design study it has been assumed that $ep$ collisions take place at point 2 which currently houses the ALICE experiment. The electron ring (Fig. 1) bypasses CMS and ATLAS towards the outside of the ring in separate tunnels of about 1.3 km length each, which also host the electron rf and cryogenics equipment. A similar bypass may be foreseen for the LHCb experiment. The maximum energy one may achieve with the ring arrangement could reach about 120 GeV requiring, however, many parameters to be extreme as the rf power and synchrotron radiation effects increase $\propto E_e^4$. The linac layout (Fig. 2) is similarly optimised for luminosity and cost. This results in two s.c. linacs of 1 km length each, which are traversed three times to achieve the 60 GeV energy while the luminosity is enhanced, by likely more than an order of magnitude, using energy recovery by decelerating the spent beam. Energies significantly higher than 60 GeV can be achieved with a straight linac arrangement for which a principle design, choosing 140 GeV, is included in the design re-

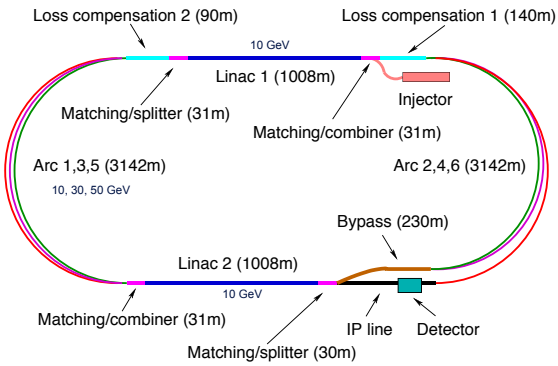


Fig. 2: Schematic layout of the 60 GeV linac in racetrack configuration. The circumference matches 1/3 of the LHC

port [1], possibly complemented with 10 GeV stages for energy recovery.

Many parameters of the $ep$ collider are determined by the LHC hadron beams. A selection of parameters is given in Tab. 1 for $E_e = 60$ GeV. For the RR configuration, the $\beta_{x,y}$ functions and luminosity values correspond to the 1° optics, in which the first $e$ beam magnet is placed 6.2 m apart from the IP. In a further, the high luminosity option the $\beta$ functions are smaller and the luminosity is enhanced by a factor of 2. This is achieved by placing the first magnet at 1.2 m distance from the IP which restricts the polar angle acceptance to 8-172°. The $e^+$ intensity value in the LR configuration reflects current expectations and may be surpassed with dedicated R&D.

Special attention is devoted to the interaction region design, which comprises beam bending, direct and secondary synchrotron radiation, vacuum and beam pipe demands. First considerations have been made for the civil engineering. The ring requires for each bypass a new tunnel of about 1.3 km length. The ring injector has a length of about 150 m and may be placed at the Prevessin site on surface, which would require a transfer tunnel to reach the ATLAS bypass, or possibly in a new cavern underground. The 60 GeV racetrack arrangement for the linac requires a new tunnel of about 9 km length. It is envisaged to place it inside the LHC, at the depth of the LHC, in order to minimize the interference with land surrounding

**T a b l e 1: Parameters of the RR and RL configurations**

| | | Ring | Linac |
|---|---|---|---|
| *electron beam* | | | |
| beam energy $E_e$ | [GeV] | 60 | |
| $e^-$ ($e^+$) per bunch | $N_e{\cdot}[10^9]$ | 20 (20) | 1 (0.1) |
| $e^-$ ($e^+$) polarisation | [%] | 40 (40) | 90 (0) |
| bunch length | [mm] | 10 | 0.6 |
| tr. emittance at IP $\gamma\epsilon^e_{x,y}$ | [mm] | 0.58, 0.29 | 0.05 |
| IP $\beta$ function $\beta^*_{x,y}$ | [m] | 0.4, 0.2 | 0.12 |
| beam current | [mA] | 131 | 6.6 |
| energy recovery intensity gain | | – | 17 |
| total wall plug power | [MW] | 100 | |
| syn rad power | [kW] | 51 | 49 |
| critical energy | [keV] | 163 | 718 |
| *proton beam* | | | |
| beam energy $E_p$ | [GeV] | 7000 | |
| protons per bunch | $N_p{\cdot}[10^{11}]$ | 1.7 | |
| transverse emittance $\gamma\epsilon^p_{x,y}$ | [$\mu$m] | 3.75 | |
| *collider* | | | |
| Lumin. $e^-p$ ($e^+p$) | [$10^{32}\mathrm{cm}^{-2}\mathrm{s}^{-1}$] | 9 (9) | 10 (1) |
| bunch spacing | [ns] | 25 | |
| rms beam spot size $\sigma_{x,y}$ | [$\mu$m] | 30,16 | 7 |
| crossing angle $\theta$ | [mrad] | 1 | 0 |
| $L_{eN} = AL_{eA}$ | [$10^{32}\mathrm{cm}^{-2}\mathrm{s}^{-1}$] | 0.3 | 1 |

the CERN site and to avoid a clash with the proton injection line TI2.

## Detector Design

The physics program depends on a high level of precision, as for the measurement of $\alpha_s$, and on the reconstruction of complex final states, like the charged current single top production and decay or the precision measurement of the $b$-quark density. The detector acceptance has to extend as close as possible to the beam axis because of the interest in the physics at low and at large Bjorken $x$.

The detector for the LR or the RR options can be nearly identical apart from two notable differences. For the RR case the high luminosity ($\mathcal{L} \sim 10^{33}$ $\mathrm{cm}^{-2}\mathrm{s}^{-1}$) may be reached by inserting focussing quadrupoles near to the interaction point. This requires the inner

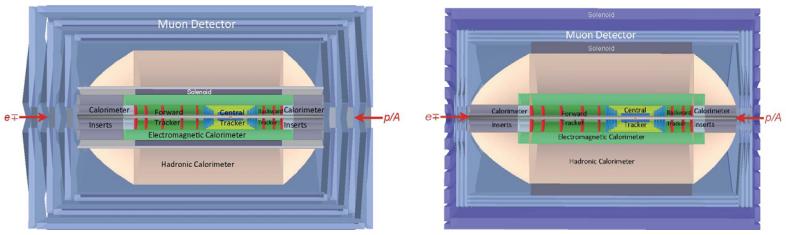


Fig. 3: **Left** The LR detector in the r-z plane with its components and the characteristic dipole and solenoid placement between the electromagnetic and the hadronic calorimeters. The proton beam, from the right, collides with the electron beam, from the left, at the IP which is surrounded by a central tracker system complemented by large forward and backward tracker telescopes followed by sets of calorimeters. The detector dimensions are $\approx$ 14 m in $z$ and a diameter of $\approx$ 9 m. **Right**: The option B of the detector (RR option only). The larger solenoid surrounds the hadronic calorimetry. The volume outside the solenoid is filled with an approximately uniform magnetic field of 1.5 T and is instrumented with 3 multilayers of muon chambers. The overall dimensions of this detector configuration are about 11 m length and 8 m diameter

detector to be modular allowing for a transition between the phase of maximum luminosity and of maximum polar angle acceptance (1° and 179°), respectively. In the LR case an extra dipole field throughout the entire interaction region is required to separate the $e$ and the $p/N$ beams along with a larger beam pipe due to the wider synchrotron radiation fan (inner beam pipe wall: elliptical $\approx$10 cm in -x-direction, circular inner radius of 2.2 cm x-direction). In order to ensure optimal polar angle acceptance, the innermost subdetector dimensions have to be adapted to the beam pipe shape. A further general demand is a high modularity enabling much of the detector construction to be performed above ground for keeping the installation time at a minimum, and to be able to access inner detector parts within reasonable shut down times.

The LHeC detector is asymmetric in design, reflecting the beam energy asymmetry, consisting of an inner silicon tracker, with extended forward and backward parts, surrounded by an electromagnetic calorimeter. In the baseline detector configuration (Fig. 3-left) it is separated from the hadronic calorimeter by a solenoid with 3.5 T field which incorporates a dipole, in the LR case. The hadron calorimeter is enclosed in a muon tracker system. The dimensions of

the detector are constrained by the radial extension of the beam pipe in combination with maximum polar angle coverage (1° and 179°) for forward going final state particles and backward scattered electrons at low $Q^2$, respectively. The outer radial size is mainly determined by the requirement of full energy containment of hadronic showers in the calorimeter. The dipoles for the LR cannot be of a too large radius to act on the beam. For the physics performance it can be advantageous to place the solenoid outside the hadronic calorimeter. This option, termed B, has also been studied for the RR case and is shown in Fig. 3-right. In any case the main detector is complemented by hadron tagging detectors in the forward direction and a polarimeter and luminosity measurement system backwards, see [1].

As shown in Fig. 4-left the baseline detector has the solenoid in between the two calorimeters, combined with a dipole field in the LR case. The main detector is subdivided into a central barrel and asymmetric forward and backward end-cap regions, which differ in their design. The RR configuration may require separate data taking phases with maximum polar angle acceptance, for physics at low and high $x$, and with ultimate luminosity, for electroweak physics and the search for rare phenomena. Correspondingly, the LHeC inner detector is designed here with a modular structure. Figs. 4-right shows the detector with the low $\beta$ quadrupoles inserted to reach the highest luminosity. It is under discussion that the maximum luminosity option is not pursued as tentatively it promises only a factor of two enhanced luminosity.

### Tracking

The constraints given by the magnet system (dipole/solenoid) force the tracking detectors kept small in radius. The design of the tracking detectors (Fig. 4-right) inside the electromagnetic calorimeter adopted here is an all-Silicon detector, with very high resolution. All of the components need power and cooling, influencing the material budget of the tracker system which should be kept as low as possible. The technology used must be advanced at the industrial level, radiation hard and relatively cheap. A good candidate are n_in_p single sided sensors [2]. The total area of Si is $34\,\mathrm{m}^2$ to be compared e.g. with the $220\,\mathrm{m}^2$ of Si of the CMS tracker.

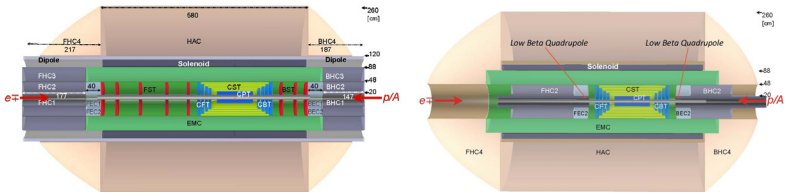


Fig. 4: **Left**: The baseline configuration (LR case). In the central barrel, the following components are considered: a central silicon pixel detector (CPT); silicon tracking detectors (CST,CFT/CBT) of different technology; an electromagnetic calorimeter (EMC) surrounded by the magnets and followed by a hadronic calorimeter (HAC). An electron at low $(Q^2, x)$ is scattered into the backward silicon tracker (BST) and its energy measured in the BEC and BHC calorimeters. In the forward region similar components are placed for tracking (FST) and calorimetry (FEC, FHC) of TeV energy final states. **Right**: The $rz$ cross section of the main detector for the RR detector version in which the luminosity is maximised by replacing the forward and backward tracker telescopes by low $\beta$ quadrupole magnets. The polar angle acceptance is thus reduced to about $8 - 172^\circ$. As compared to the high acceptance detector the forward/backward tracking has been removed and the outer calorimeter inserts have been moved nearer to the interaction point

The sensors, integrated electronics, readout/trigger circuitry, mechanics, cooling, etc. available today have to be used in order to meet the goal of installation in the early 2020's. Conventional wire bonded or bump bonded solutions may be cost efficient and rely on components available today. An example is the 2_in_1 strip sensor design with $p_t$-trigger functionality discussed by the CMS upgrade design group [3]. The 2_in_1 sensor design is an elegant way of saving resources when designing a tracker.

### Calorimetry

The baseline design foresees a modular structure of independent electromagnetic (EMC) and hadronic (HAC) calorimeter components. The design of the EMC modules vary for the very forward region, where energies up to $\approx 5\,\text{TeV}$ are expected. In the barrel and the backward region a precise measurement of the scattered electron with energy $\mathcal{O}(60\,\text{GeV})$ is paramount. Based on experience with H1 and ATLAS the EMC the default choice is a Liquid Argon (LAr) Calorimeter. The superconducting dipoles (light grey in Fig. 4-left)

are placed in a common cryostat with the detector solenoid (dark grey) and the LAr EMC (green) (see details in [1]). The HAC is an iron-scintillator tile calorimeter [5] providing the required mechanical stability for the inner LAr and Magnet cryostat and guiding the return flux of the magnetic field, as in ATLAS [6]. The restrictive geometry of the forward/backward insert calorimeters (Fig. 4-left) requires a non-conventional and challenging design based on previous developments e.g. [8] and is using tungsten as the absorber material, in particular for the forward inserts.[2] For the hadronic absorber, also copper might be considered as an alternative. The choice of the sampling calorimetry for all calorimeter parts is motivated by the good experience from past experiments along with considerations on the available technologies, and cost, although other approaches (Dual Readout Calorimetry [9], *etc.*) could be considered.

### Muon Detector

The two LHC general purpose detectors, ATLAS and CMS, combine Drift Tubes and Cathode Strip Chambers for precision measurements along with Resistive Plates Chambers and Thin Gap Chambers for Trigger and second coordinate measurements e.g. [11]. A similar approach (e.g. [12]) can also be considered for the LHeC. Three muon double detector layers (Fig. 3-left $r$-$z$ view of the baseline detector A) are mechanically attached to an iron structure which provide the return flux of residual magnetic field from the inner solenoid. Of particular interest is the design for option B (Fig. 3-right), where by means of a second larger active return shielding solenoid surrounding the muon detector, an iron free area with almost constant field (1.5 T) would provide precise muon tracking as was first proposed by the 4th concept detector collaboration for the ILC [10].

## Status and Next Steps

The draft design report is being reviewed in 2011 by referees appointed by the CERN directorate, dealing with the physics, accel-

[2] About 26 cm of tungsten will absorb electromagnetic showers completely and will contain the hadronic shower to a large extent ($\approx 30\mathrm{X}_0 + \approx 10\lambda_I$) and over a large range of energy.

erator, detector and special aspects of the project, including a cost estimate. The updated report is being prepared for publication. The LHeC has to run while the LHC is still operational. This defines 2023 (the long shutdown LS3) as the natural and mandatory timeline of its realization. Preliminary studies and simulations indicate the validity of the proposed design concepts. More studies and results are being collected and presented in the Conceptual Design Report [1].


1. LHeC Study Group, *"A Large Hadron Electron Collider at CERN"*, Draft Design Report, LHeC-Note-2011-003 GEN, to be published (2011).
2. P. Allport, *Conventional Silicon Pixel/Strip Tracker*, talk at 3rd CERN-ECFA-NuPECC Workshop on LHeC, 12. November 2010.
3. R. Horisberger, *Tracking at Phase II, Pixel, Strixel & Strips*, CMS Tracker Week, La Biodola, Isola d'Elba, 27. May 2010.
4. H. van der Graaf, *Gossip and GridPix at LHeC*, talk at 3rd CERN-ECFA-NuPECC Workshop on LHeC, 12. November 2010.
5. O. Gildemeister, F. Nessi-Tedaldi, M. Nessi, *An economic concept for a barrel hadron calorimeter with iron scintillator sampling and WLS-fiber readout*, 1991.
6. P. Adragna and others, Nucl. Instrum. Meth. A **615**, 158 (2010).
7. A. Airapetian and others, *ATLAS calorimeter performance Technical Design Report*, ATLAS, 1996.
8. J.H. Adams, G.L. Bashindzhagian, V.I. Zatsepin, M.M. Merkin, M.I. Panasyuk and *et al.*, Instrum. Exp. Tech. **44**, 455 (2001).
9. R. Wigmans, J. Phys. Conf. Ser. **160**, 012018 (2009).
10. J. Hauptman, *Particle physics experiments at high energy colliders* (WILEY-VCH Verlag GmbH&Co. KGaA, Weinheim, 2011).
11. G. Mikenberg, Mod. Phys. Lett. A **25**, 649 (2010).
12. J. Burnens, R. Oliveira, G. Glonti, O. Pizzirusso, V. Polychronakos and *et al.*, *A spark-resistant bulk-micromegas chamber for high-rate applications*, 2010, 1011.5370, arXiv, physics.ins-det

# OPERATION AND PERFORMANCE OF THE CMS SILICON TRACKER

Manfred Krammer[1]
on behalf of the CMS Tracker Collaboration

[1]*Institute of High Energy Physics, Austrian Academy of Sciences, Vienna, Austria, e-mail: manfred.krammer@oeaw.ac.at*

**Abstract**

The CMS silicon tracker is the largest silicon detector ever built. It consists of a pixel detector with 66 million channels and a 200 $m^2$ area silicon strip detector with 10 million read out channels. The presentation describes the operation of this detector in 2010 and 2011 at the LHC during proton-proton as well as heavy ion collisions. Reconstructed photon conversions and nuclear interactions are used to evaluate the material description of the tracker. The resolution and efficiency of the track and vertex reconstruction are measured with data and compared to the results from simulation. Finally, an outlook is given to the considerations towards an upgrade of the CMS silicon strip tracker for the operation at the high luminosity upgrade of the LHC. Beside the challenges to develop sensors withstanding the high radiation field, CMS is exploring options and developing solutions that would allow to include tracking information into the Level-1 trigger of CMS.

## 1. Layout of the CMS Silicon Tracker

At CERN, the European Laboratory for Particle Physics in Switzerland, the Large Hadron Collider LHC started operation in 2009. In the first years, the LHC produces proton-proton collisions at a centre of mass energy of 7 TeV with an envisaged luminosity of up to $10^{34}$ $cm^{-2}s^{-1}$. A running period colliding lead ions took place at the end of 2010 and is also foreseen for the end of 2011. To exploit this machine several experiments went into operation to analyze the collisions, among them the multi-purpose experiment CMS.

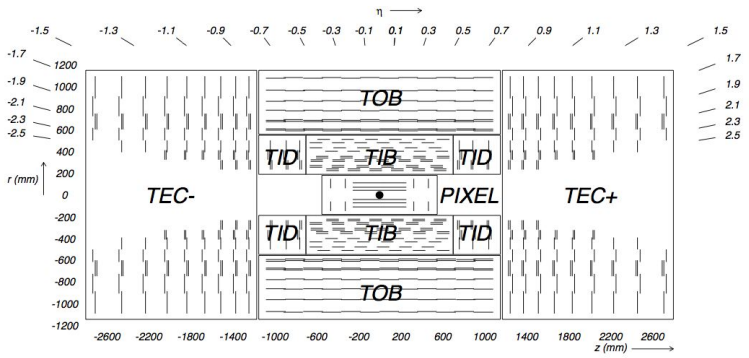


Fig. 1: Schematic cross section through the CMS tracker. Each line represents a detector module. Double lines indicate back-to-back modules which deliver stereo hits

The CMS detector [1] consists of several shells of different detector elements. Particles created in the collisions in the very centre of the detector will first traverse the 'Tracker', a system of silicon sensors designed to provide a precise and efficient measurement of the trajectories of charged particles.

This Tracker is geometrically divided into several substructures (see figure 1): the pixel detector very close to the interaction point and the Silicon Strip Tracker (SST) consisting of the inner barrel detector (TIB), the inner discs (TID), the outer barrel (TOB) and the two end cap detector systems (TEC). The overall length of the Tracker is 5.4 m with an outer diameter of 2.4 m.

The pixel detector consists of three cylindrical layers of hybrid pixel modules surrounding the interaction point at radii of 4.4, 7.3 and 10.2 cm. Two discs of pixel modules on each side complement the pixel detector. Figure 2 shows a graphical view of the pixel detector and a cut through the central part.

The pixel detector modules are built as hybrid pixel assemblies containing the components described in the following. The active silicon sensors are realized on high-resistance n-substrate, with an implanted pn-junction and a pixel cell size of $100\times150$ $\mu$m$^2$. Indium bumps are deposited onto the sensors for subsequent connection to the readout electronics. The readout electronics consists of custom

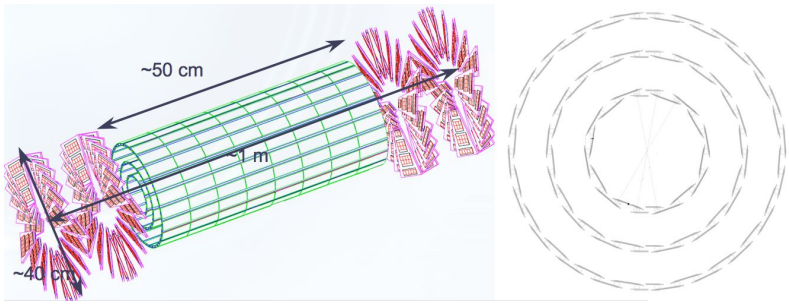


Fig. 2: View of the pixel detector (left) and cut through the central part (right)

ASICs fabricated in a commercial 0.25 $\mu$m process. Each chip processes the signals from 4160 pixels. Up to 16 chips are bump bonded onto one sensor wafer. On top of the sensor and chip assembly is a low mass multilayer printed circuit board holding an additional control chip and other components. Further details of the technology used for the pixel detector can be found in [2].

The SST surrounds the pixel detector and adds 10 layers of strip detectors in the central region (4 TIB, 6 TOB). In addition, 3 small and 9 large detector discs (TID and TEC) are located on either side [3]. The basic construction element of the silicon strip tracker is a module. The supporting frame of a module is made of carbon fibre or graphite. Glued onto the frame is a Kapton layer to electrically isolate the frame from the silicon and to provide the electrical connection to the silicon backplane. Depending on the module type, silicon strip sensors with different strip pitches, sensor thicknesses (320 $\mu$m and 500 $\mu$m) and material resistivities are used [4]. A ceramic multilayer circuit holds the readout chips and the auxiliary chips. A glass pitch adapter is mounted between the hybrid and the first silicon sensor to match the different pitches of the sensor strips to the chips' input pads. Wire bond connections between the individual channels of the readout chips and the pitch adapter, between the pitch adapter and the first sensor, and where applicable, between the two sensors provide the electrical connections. The modules of the TIB, the TID and the four inner rings of TEC consist of only one silicon sensor, whereas the modules of the TOB and the three outer

**T a b l e 1: Some key parameters of the SST construction**

| | |
|---|---|
| Area of active silicon | $\approx$ 200 m$^2$ |
| Number of silicon sensors | 24,244 |
| Different sensor designs | 15 |
| Number of modules | 15,148 |
| Mechanically different module designs | 27 |
| Number of strips | $\approx$ 9,300,000 |
| Number of electronics channels | $\approx$ 9,300,000 |
| Number of readout chips | $\approx$ 73,000 |
| Number of wire bonds | $\approx$ 25,000,000 |

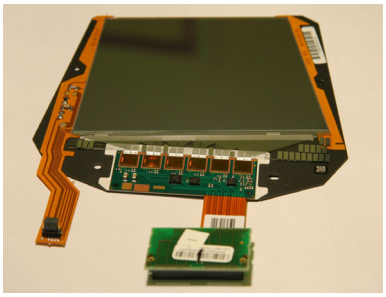

Fig. 3: A module for the TEC subdetector of the CMS silicon tracker

rings of TEC hold two sensors. All barrel modules are of rectangular shape. The modules of the discs have a wedge shape in order to form rings. Figure 3 shows a production module of the second ring of the TEC. The first two layers in TIB and TOB, the first two rings in TID and the rings 1, 2, and 5 in TEC are instrumented with double-sided modules. These are made of two independent single-sided modules, mounted back to back and rotated by 100 mrad with respect to each other. Table 1 lists some numbers illustrating the overall dimensions of the SST.

The SST was completed at CERN using the tracker integration facility – a clean room with facilities to assemble, connect and operate parts of the tracker in turn. The sealed SST was finally transported to the experimental area and lifted down into the cavern. On December 15, 2007 the tracker was inserted into its final place inside the experiment CMS. The pixel detector was completed independently and, after the installation of the LHC beam pipe in CMS, the pixel detector was inserted into the tracker in April 2008.

## 2. Detector Operation 2010 and 2011

### 2.1. Pixel Detector Operation

The pixel detector was operated in 2010 and 2011 with a coolant temperature of +7.4 °C. With increasing irradiation of the sensors the temperature will have to be decreased for future runs. In the winter stop of 2010, a test with a coolant temperature of –10 °C was performed and the calibration of the temperature dependent digital-to-analog converters was demonstrated successfully.

The pixel detector has to withstand the highest particle rate densities and is therefore also exposed to the heaviest radiation damage of all CMS subdetector systems. During p-p collision, on average 3000 pixels are hit per bunch crossing and read out with a Level-1 trigger rate close to 100 kHz. During the Pb-Pb run of the LHC in 2010, the trigger rate was only about 150 Hz whereas the number of pixels hit per event was up to 30,000 for central collisions. These condition changes made it necessary to update the firmware of the pixel Front End Driver (FED) several times to cope for example with the different event sizes.

During the 2010 and 2011 operation, 96.9% of the Read Out Chips (ROCs) were fully functional. Some problems, e.g. with slow analogue outputs, could also be fixed by firmware updates. Other problems, such as bad modules, were repaired during the winter shutdown end of 2010. The fact that the pixel system can be accessed for maintenance independently from the SST has paid off in this respect.

The CMS data-taking efficiency was about 92% with the pixel detector contributing only about 6% to the inefficiency.

The pixel hit efficiency was calculated as the ratio of found pixel hits to the number of expected hits. The expected hits were determined from the extrapolation of charged tracks to the pixel modules and from a search for a hit within a defined area around the impact point. Excluding known defect pixels, the hit efficiency in both the barrel and the end caps is above 99%. The spatial resolution of the pixel modules is shown in figure 4 for both the transverse and the longitudinal coordinate. The result as a function of the cluster size is in very good agreement with Monte Carlo simulations as can be seen in the figure.

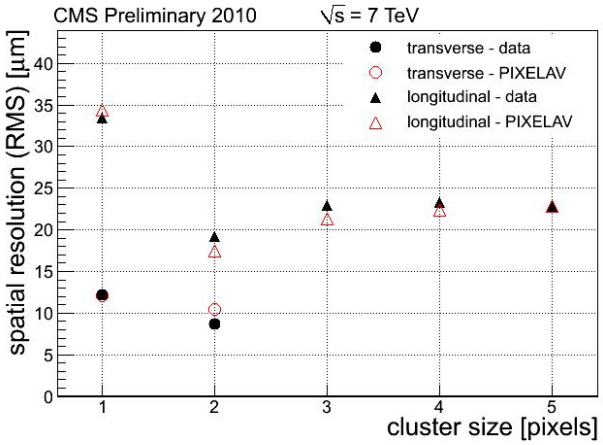


Fig. 4: Transverse and longitudinal pixel spatial resolution as a function of the cluster size. Full dots and triangles are measurements, open symbols are simulations

### 2.2. Strip Detector Operation

The SST is a very large system and hence the operation is very complex. The cooling of the SST uses $C_6F_{14}$ which is forced by two cooling plants through 180 lines. The temperature in 2010 and 2011 was set to 4 °C which is sufficiently low taking into account the low radiation load accumulated so far. During the 2010 operation, two lines were leaky and had to be closed. Nevertheless, the leakage rate increased over time reaching unacceptable levels. In the 2010 winter stop, an intervention took place resulting in the closure of three additional lines. The present low leak rate of 0.7 kg/day is acceptable and stable over months. The modules connected to the closed cooling loops show slightly higher temperatures but can be operated safely.

The power supply system for the SST has to provide up to 60 kW electrical power. 2000 power supply units provide the low and high voltages needed by the detector modules. The location of the power supplies is within the LHC cavern and, as a consequence, the access is limited to periods when the LHC machine is stopped. The failure rate in 2010 was about 1% and is decreasing during 2011.

The status of the functionality of the SST channels at the end of August 2011 shows 97.7% of fully working channels, stable over time.

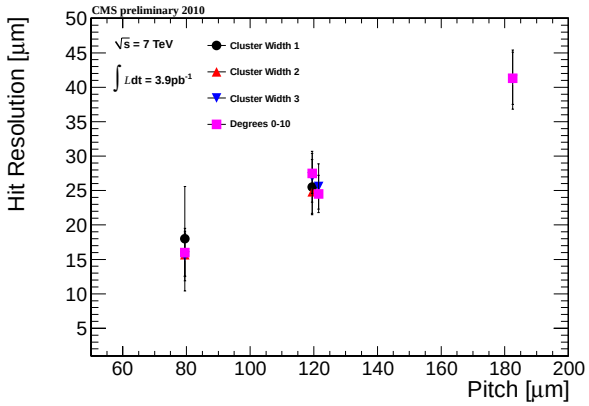


Fig. 5: Measured spatial resolution for strip sensors of TIB (strip pitches 80 $\mu$m and 120 $\mu$m) and TOB (strip pitches 122 $\mu$m and 183 $\mu$m)

The SST has been designed with high redundancy, and therefore the low number of malfunctioning channels has no influence on the physics performance of the detector.

The data aquisition of the SST has been running very stably and it has collected high-quality physics data with an uptime of greater than 98.5% during the p-p runs in 2010 and 2011.

The signal-to-noise ratio of the different strip modules depends on the strip geometry, the thickness of the sensors, and on the module design (single- or two-sensor modules). The signal-to-noise values for tracks perpendicular to the silicon plane (most probable value of the distributions) have been measured to be 18.5, 19.4, 23.9, 18.4 and 22.4 for TID, TEC (thin sensors), TEC (thick sensors), TIB and TOB modules, respectively. The hit efficiency of the SST was measured to be 99.9% in an analysis excluding known defect modules. The strip sensor hit resolutions were measured using tracks passing through regions with sensor overlaps. The results are shown in figure 5 for tracks perpendicular to the sensor surface as a function of the strip pitch for various sensor types. All measured spatial resolutions are well below the binary resolution given by the strip pitch.

More details on the operational performance of the pixel detector and of the SST can be found in references [5] and [6].

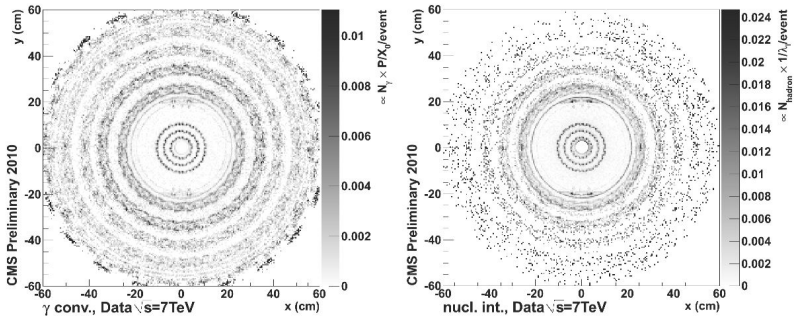


Fig. 6: Maps of the x-y cross section of the reconstructed material distribution for photon conversions (left) and for nuclear interactions (right) in data (x-y bin size $0.5 \times 0.5$ cm$^2$)

## 3. Tracker Performance

The overall tracker performance is largely affected by the material of the tracker itself. The tracker material modifies the trajectories of charged tracks through bremsstrahlung, photon conversion, nuclear interactions, multiple scattering, and energy loss. It is therefore of utmost importance to have a precise description of the material distribution in order to correctly treat all these effects in the detector simulation. To check the consistency of the tracker simulation with the material distribution of the real detector the vertices of photon conversions and nuclear interactions are reconstructed using data (see figure 6) [7]. A quantitative comparison of data and simulation is shown in figure 7 for several radial bins corresponding to specific substructures. Overall, the observed relative agreement is about 10%, except for a localized larger discrepancy in one area.

As an example for the tracker performance the measured impact parameter resolution is shown in figure 8 as a function of the track $p_T$ [8]. The resolution is better for higher track momenta as expected, as these particles are less deflected by multiple scattering while traversing the material of the beam pipe. The comparison with the simulation proves the excellent understanding of the detector.

An important figure of merit of the CMS tracker is the resolution of the muon transverse momentum. This parameter depends on

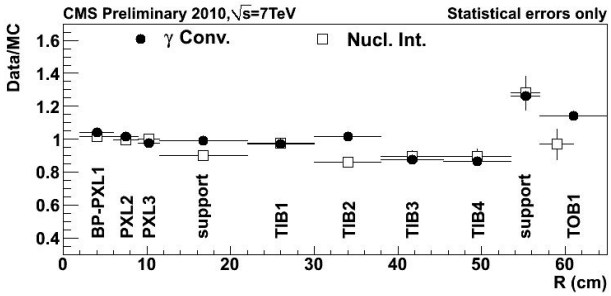


Fig. 7: Ratio of the number of candidates in data and in simulation for photon conversion reconstruction (black circles) and for nuclear interaction reconstruction (open squares) for radius bins embracing the major Pixel barrel or Tracker substructures, only statistical errors are shown

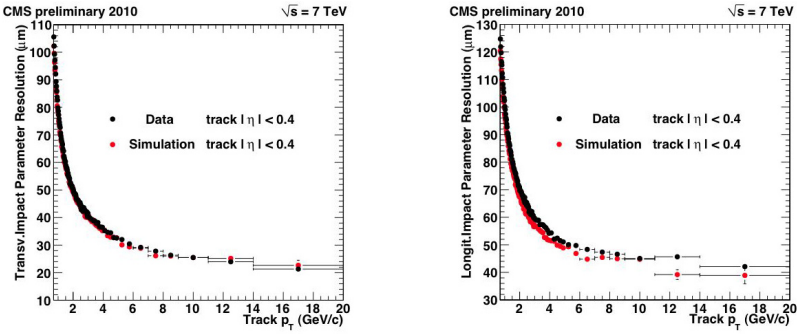


Fig. 8: Measured resolution of the track transverse (left) and longitudinal (right) impact parameter as a function of the track $p_T$. Only central tracks with $|\eta| < 0.4$ are considered. Black and red symbols correspond to results from data and simulation, respectively

the precise knowledge of the material distribution, the tracker alignment, the knowledge of the magnetic field, and on the reconstruction algorithm. Figure 9 shows the measured transverse momentum resolution for muons originating from the decay of $J/\psi$ mesons from early collision data. These muons have on average a momentum of a few GeV/c. At this energy the reconstruction of the muons in CMS is dominated by the Tracker data and is therefore an excellent tool to study the performance of the Tracker. The muon resolution is found to be in quite good agreement with simulation, except for the

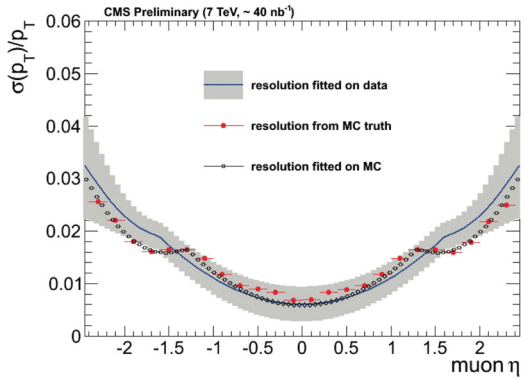


Fig. 9: Resolution of the muon transverse momentum as measured with about 40 $nb^{-1}$ of integrated luminosity (black line) compared to the Monte Carlo resolution computed from Monte Carlo truth (red points) and from a fit (black squares). The gray band represents the error on the fitted function for data computed from the errors on the parameters

transition region from the barrel to the end caps where a difference of about 5% is observed. More details on this study can be found in reference [9].

## 4. Future Upgrade of the SST

The present CMS strip tracker is designed to be operated for a lifetime of 10 years at the LHC design luminosity of $10^{34}$ $cm^{-2}s^{-1}$. The lifetime of the silicon detector is limited by the radiation induced change of the doping concentration in the substrate and by the subsequent need for an increase of the operating voltage. The planning of the CERN management foresees to upgrade the LHC machine in steps towards a possible luminosity of about $5\times10^{34}$ $cm^{-2}s^{-1}$ at around 2020. At this luminosity the particle flux emerging from the interaction point exceeds the capabilities of the present CMS tracker and of the present CMS trigger system. As a consequence of both the predicted end of the tracker lifetime and of the need for a more performant tracker at the increased luminosity, CMS is planning to construct a new tracker [10].

The challenges for the construction of this new tracker are manifold:

- The upgraded tracker has to perform up to an integrated luminosity of about 3000 $fb^{-1}$. To withstand the enormous radiation doses the development of new sensor materials is required, especially for the innermost regions.
- The particle fluxes are expected to be an order of magnitude larger compared to the present tracker. In order to keep the channel occupancy low, smaller cell sizes are needed what leads to an increase in channel numbers.
- The new Tracker has to provide data for the Level-1 trigger decision logic. This is mandatory for CMS to maintain the overall Level-1 trigger rate within 100 kHz.
- Despite the higher number of channels the power dissipation must not be increased compared to the present tracker.
- The amount of material in the tracker volume, e.g. in the support and cooling structures, has to be significantly reduced.

On all these listed aspects research and development is ongoing within the CMS collaboration. To cope with the expected data rate and with the requirement to provide trigger Level-1 input, a hierarchical baseline strategy is followed [11]. Detector modules are being developed which are able to discriminate the particles' $p_T$ by two closely spaced ($\approx$1 mm) silicon modules. The strong CMS magnetic field bends the trajectories of charged particles and the angle of the through going particle is therefore a function of $p_T$ (see the sketch in figure 10 for explanation). Rejecting particles below a $p_T$ of 1-2 GeV/c locally reduces the amount of data to be processed significantly. Two layers of such modules ("double stacks") may then be mounted spaced by about 1-2 cm. The combined information from both layers is then used to find track elements, named "tracklets". Tracklets from several double stacks are then combined to form Level-1 tracks. The performance of various tracker geometries with different numbers of double-stack layers and of simple tracking layers is under study using simulation tools developed for this purpose.

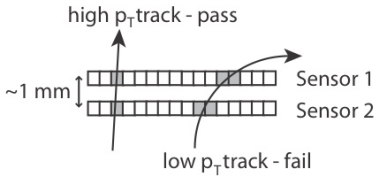


Fig. 10: Concept of a double sensor module capable to reject low $p_T$ tracks

## 5. Summary

CMS has commissioned the worlds largest silicon detector. The LHC collision data collected with the CMS tracker have demonstrated the excellent performance of this scientific device. The measured performance parameters are in good agreement with simulation, proving that the detector is well understood. The reliable reconstruction of tracks and vertices provides an excellent input for the CMS physics analysis. Despite the fact that this detector has only started its operation, the development of its replacement has already started. The challenges ahead for the new tracker are huge and hence a long development time is foreseen to construct the new device in time for the LHC high-luminosity operation phase.

1. CMS Collaboration, JINST **0803**, S08004 (2008); doi:10.1088/1748-0221/3/08/S08004.
2. A. Dominguez, Nucl. Instr. and Meth. A **581**, 343 (2007).
3. G.H. Dirkes, Nucl. Instr. and Meth. A **581**, 299 (2007).
4. M. Krammer, Nucl. Instr. and Meth. A **531**, 238 (2004).
5. A. Starodumov, Proceedings of Science, Proceedings of the 20th Workshop on Vertex Detectors, Rust, Austria, June 19-24, 2011, CMS CR-2011/187.
6. L. Demaria, Proceedings of Science, Proceedings of the 20th Workshop on Vertex Detectors, Rust, Austria, June 19-24, 2011; CMS CR-2011/181.
7. Studies of Tracker Material, CMS PAS TRK-10-003, 2010.
8. Tracking and Primary Vertex Results in First 7 TeV Collisions, CMS PAS TRK-10-005, 2010.
9. Measurement of Momentum Scale and Resolution using Low-mass Resonances and Cosmic Ray Muons, CMS PAS TRK-10-004, 2010.
10. CMS Expression of Interest in the SLHC, CERN/LHCC 2007-014 , LHCC-G-131, March 15, 2007.
11. D. Abbaneo, Proceedings of Science, Proceedings of the 20th Workshop on Vertex Detectors, Rust, Austria, June 19-24, 2011.

# TOP QUARK PAIR CROSS-SECTION MEASUREMENT USING CMS DATA AT A 7 TeV CENTRE-OF-MASS ENERGY

Jérémie Lellouch[1] for the CMS collaboration

[1] *Universiteit Gent, Belgium*

**Abstract**

We present several measurements of the top quark pair production in data collected by the CMS detector at the LHC at a centre-of-mass energy of 7 TeV. We use data collected during the years 2010 and 2011. We give an overview of the top pair cross-section measurement analyses at CMS, presenting all the exploited channels. We use dilepton, lepton + jets and fully hadronic topologies. In the dilepton channel we look for a final state containing two electrons or muons and high missing transverse energy and at least two jets. In the lepton + jets and hadronic channels one or two W bosons originating from the top quark is allowed to decay hadronically; we therefore require repectively at least 4 or 6 jets. b-jet identification is used in order to enhance signal purity in the final selection. We also present advanced analysis techniques such as data-driven background estimation. The results of the measurements, including systematic uncertainties, are presented and discussed. They are then compared with the theoretical predictions and with the current results of the CDF and D0 collaborations at the Tevatron, and an outlook of expected progress of the CMS experiment is given.

## 1. Introduction

Top quark physics is essential to the understanding of the electroweak sector of the Standard Model as it allows for many types of precision measurements to be performed As the heaviest of quarks the top also couples maximally to the Higgs field. Those measurements are crucially important to better constrain the mass of the

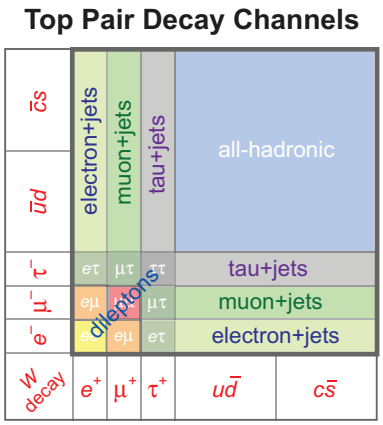


Fig. 1: Graphical summary of top pair decay channels

Higgs boson and to test the robustness of the Standard Model. Top topologies are also a good window to physics beyond the Standard Model.

Top topologies provide an excellent benchmarking tool to a wide array of ingredients used in physics analyses at the LHC. Lepton identification and excellent resolution on missing transverse energy ($\not\!\!E_T$) is essential in di-lepton and lepton+jets topologies, while performant jet reconstruction algorithms and energy scale and efficient b-jet identification (b-tagging) are useful in all the channels. Top physics is therefore a laboratory for analysis techniques.

At the LHC at a centre-of-mass energy of 7 TeV top pairs are dominantly produced via gluon fusion. An approximate NNLO calculation of the top pair production cross-section at 7 TeV is given to be $\sigma_{t\bar{t}} = 163^{+11}_{-10}$ pb by Kidonakis *et al.* Figure 1 summarises the top pair decay modes. All those channels are exploited by the CMS collaboration.

## 2. The CMS Detector

CMS [1] is a general-purpose particle detector located at the LHC proton-proton collider at CERN. The detector features a super-conducting solenoid with an internal diameter of 6 m and an axial mag-

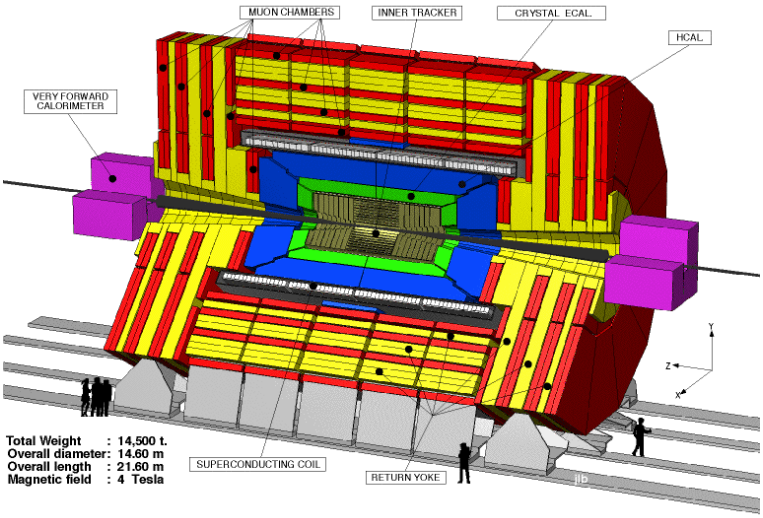


Fig. 2: The CMS detector

netic field of 3.8 T. The solenoid encloses the pixel detector, the silicon tracker, the crystal electromagnetic calorimeter and the brass and scintillator hadron calorimeter. A steel flux return yoke stands outside the solenoid and is instrumented with gas ionisation detectors, which constitute the CMS muon system. A view of the CMS detector can be seen on figure 2.

The presence of excellent all-silicon tracking enables CMS to use particle-flow algorithms to reconstruct physics objects. Such algorithms make use of information coming from all the sub-detectors to reconstruct each object. The presented results use up to 1.14 $fb^1$ of integrated luminosity.

## 3. Top Pair Production Cros-section Extraction

The lepton+jets channel [2] features a relatively clean signature where the multi-jet background can be kept under control. Events are triggered using single-lepton terms and exactly one isolated lepton and central jets with high travserse momentum are required. A veto on

di-events is applied so as to reduce the Z+jets background. The main backgrounds are W+jets production and multi-jet production; the latter is estimated from data from a side-band sample of loosely isolated leptons. In order to measure the production cross-section a simultaneous kinematic fit of predicted template shapes to data is performed in both the electron and the muon channel, using a minimum-likelihood technique. In each channel both the exclusive 3-jet bin and the inclusive 4-jet bins are used; missing transverse energy is used in the 3-jet bin while the mass of the hadronically decaying top is used in the 4-jet bin as they are the most discriminating variables between signal and background. Such a simultaneous fit allows better shape constrains. This analysis, performed on 36 $\mathrm{pb}^{-1}$ of 2010 data, yields a production cross section of $\sigma_{t\bar{t}}^{\mathrm{lj}} = 173 \pm^{36}_{32} \pm 7$ (lumi.) pb.

The analysis can be improved upon by using flavour information [3]. A b-tagging working point with 55% b-tag efficiency and 1.5% mis-tag rate is chosen and either one or two b-tagged jets are required. The fit is then performed on the secondary vertex mass, which allows better discrimination against light-flavour backgrounds, in bins of $N_{\mathrm{jets}}$ and $N_{\mathrm{b\text{-}tags}}$. Since jet energy scale and b-tagging efficiency are correlated parameters which can induce large variations to the yield in each bin, they are treated as nuisance parameter in the fit procedure. This yields a production cross section of $\sigma_{t\bar{t}}^{\mathrm{lj\text{-}tag}} = 173 \pm 9$ (stat.) $\pm$ 17 (syst.) $\pm$ 7 (lumi.) pb; systematic uncertainties are dominated by jet energy scale. This is CMS' most precise single measurement.

The di-lepton channel [4] features a very clean signature but requires good lepton identification and good resolution on missing transverse energy. Events are triggered using di-lepton terms. Exactly one pair of oppositely charged, isolated leptons are required, along with one or two central jets. A cut on missing transverse energy (50GeV in the 1-jet bin, 30 GeV in the 2-jet bin) is applied in the ee and $\mu\mu$ channels. The main background is the Z/$\gamma$+jets production and is estimated from data by counting the number of Z+jets events in a Z mass window of $76 < M_{ll} < 106$ GeV and comparing the yields with simulation. A b-tagging working point featuring 80% signal efficiency for a 10% mis-tag rate is chosen. The cross-section is extracted by performing a counting experiment on the distribution of jet multiplicity for the ee, e$\mu$ and $\mu\mu$ channels combined. This result has been obtained with 1.14 $\mathrm{fb}^{-1}$ of 2011 data. This yields a production cross

section of $\sigma_{t\bar{t}}^{\mathrm{ll}} = 169.9 \pm 3.9$ (stat.) $\pm 16.3$ (syst.) $\pm 7.6$ (lumi.) pb, the dominant systematic uncertainties being b-tagging and lepton identification. This channel has been extended by adding the $\mu\tau$ decay mode [5], using 1.09 fb$^{-1}$ of 2011 data. Events are triggered using single-muon terms, and one muon and one oppositely-signed tau are required each with $p_T > 20$ GeV. At least two jets with $p_T > 20$ GeV, one of which being b-tagged, are also required, along with a missing transverse energy cut of 40 GeV. The main background comes from jets faking taus. The probability for a jet to fake a tau is estimated on data selected with high-$p_T$ jet triggers, in which the trigger-matched jet is not considered so as to avoid trigger bias; real tau contribution is subtracted using simulation. The cross-section is extracted from the reconstruction of the top quark mass using a kinematic fit. This yields $\sigma_{t\bar{t}}^{\mu\tau} = 148.7 \pm 23.6$ (stat.) $\pm 26$ (syst.) $\pm 8.9$ (lumi.) pb. The uncertainty is dominated by the fake tau background estimation, tau identification and b-tagging.

The last mode investigated by CMS is the all-hadronic decay channel [6]. This measurement has been performed with 1.09 fb$^{-1}$ of 2011 data. It is very challenging as the multi-jet background coming from QCD interactions is very large. Events are required to contain 6 jets, the four leading having $p_T > 60$ GeV, the fifth $p_T > 50$ GeV and the sixth $p_T > 40$ GeV. Events with more jets are kept provided the additional jets satisfy $p_T > 30$ GeV. At least two jets are required to be b-tagged with a working point giving a 38% b-tag efficiency and a mis-tag rate of 0.12%. The two W bosons are reconstructed using the non b-tagged jets, assuming a mass of 80.4GeV; the top quarks are then reconstructed with the two W and the b-tagged jets, assuming $m_t = m_{\bar{t}}$. The combinations are then fitted, and the events with $P(\chi^2) > 1\%$ are kept. The multi-jet background is estimated from a side-band data sample in which 6 non b-tagged jets are required. The events are then reweighted so that the jets' kinematics match that of the b-tagged jet sample. The kinematic fit is then performed on the reweighted sample. The shape of the multi-jet background is then given by the reweighted data. The cross-section is extracted via a minimum likelihood fit of the signal and background shapes to the observed distribution of the top mass. This yields $\sigma_{t\bar{t}}^{\mathrm{hadro}} = 136 \pm 20$ (stat.) $\pm 40$ (syst.) $\pm 8$ (lumi.) pb. The uncertainty is dominated by jet energy scale, b-tagging and the multi-jet background model.

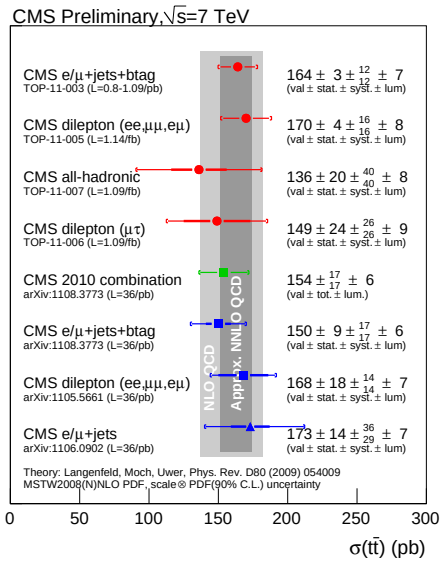


Fig. 3: CMS results from 2010 and 2011 and combination of 2010 results. The shaded bands represent the NLO and NNLO calculations

This difficult measurement has been achieved thanks a very good understanding of the CMS detector.

## 4. Combination of the CMS Results and Comparison with Theory

The CMS results obtained with 2010 data are combined [7] so as to reduce the systematic uncertainty on the total cross-section measurement. The combination is done using the so-called BLUE method [8], which assumes uncorrelated systematics between the considered channels. The combination yields a top pair production cross-section of $\sigma_{t\bar{t}}^{\mathrm{CMS}} = 154 \pm 17 \pm 6$ (lumi.) pb. This is to be compared with the MCFM NLO calculations, which give $\sigma_{t\bar{t}}^{\mathrm{NLO}} = 158 \pm^{23}_{24}$ pb. All the CMS results presented here are summarised, along with with combination, on figure 3, while a superimposition of the Tevatron and CMS results with theoretical calculations can be seen on figure 4.

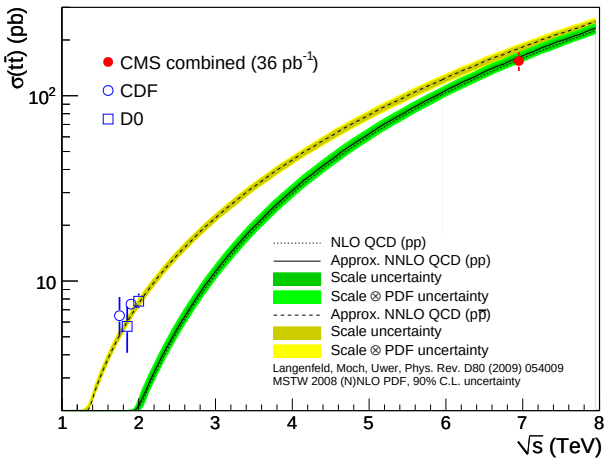


Fig. 4: Top pair production cross-section as a function of centre-of-mass energy. Blue crosses represent Tevatron results while the red cross represent the CMS 2010 combined result. The measurements agree with theoretical predictions

Those plots show that the CMS results are now starting to constrain NLO calculations.

## 5. Conclusion

The full set of top pair production cross-section measurement made with the CMS detector has been presented. Results have been obtained with 2010 and 2011 data and include up to 1.14 $\mathrm{fb}^{-1}$; they have been obtained in the di-lepton, semi-leptonic and all hadronic decay channels. When combined using the BLUE method, the 2010 results yield a total production cross-section of $\sigma_{t\bar{t}} = 154 \pm 17 \pm 6$ (lumi.) pb. This value agrees with theoretical calculations. Including more recent results in the combination will further decrease the systematic uncertainty and further constrain the NLO and NNLO calculations.

### Acknowledgements

We wish to congratulate our colleagues in the CERN accelerator departments for the excellent performance of the LHC machine. We

thank the technical and administrative staff at CERN and other CMS institutes, and acknowledge support from: FMSR (Austria); FNRS and FWO (Belgium); CNPq, CAPES, FAPERJ, and FAPESP (Brazil); MES (Bulgaria); CERN; CAS, MoST, and NSFC(China); COLCIENCIAS (Colombia); MSES (Croatia); RPF (Cyprus); Academy of Sciences and NICPB (Estonia); Academy of Finland, MEC, and HIP (Finland); CEA and CNRS/IN2P3 (France); BMBF, DFG, and HGF (Germany); GSRT (Greece); OTKA and NKTH (Hungary); DAE and DST (India); IPM (Iran); SFI (Ireland); INFN (Italy); NRF and WCU (Korea); LAS (Lithuania); CINVESTAV, CONACYT, SEP, and UASLP-FAI (Mexico); MSI (New Zealand); PAEC (Pakistan); SCSR (Poland); FCT (Portugal); JINR (Armenia, Belarus, Georgia, Ukraine, Uzbekistan); MST,MAE and RFBR (Russia); MSTD (Serbia); MICINN and CPAN (Spain); Swiss Funding Agencies (Switzerland); NSC (Taipei); TUBITAK and TAEK (Turkey); STFC (United Kingdom); DOE and NSF (USA).

1. The CMS collaboration, *The CMS experiment at the CERN LHC*, JINST 3:S08004,2008
2. The CMS collaboration, arXiv:1106.0902v1 [hep-ex]
3. The CMS collaboration, arXiv:1108.3773v1 [hep-ex]
4. CMS-TOP-PAS-11-005, http://cdsweb.cern.ch/record/1377323?ln=en
5. CMS-TOP-PAS-11-006, http://cdsweb.cern.ch/record/1371010?ln=en
6. CMS-TOP-PAS-11-007, http://cdsweb.cern.ch/record/1371755?ln=en
7. CMS-TOP-PAS-11-001, http://cdsweb.cern.ch/record/1336491?ln=en
8. L. Lyons, D. Gibaut, NIMA **A270** 110-117, (1998).

# OVERVIEW OF RECENT HERMES RESULTS

H. Marukyan
(on behalf of the HERMES Collaboration)

*A.I. Alikhanian Nationl Science Laboratory*
*(Yerevan Physics Institute)*

**Abstract**

The main topic of the HERMES experiment at DESY was to investigate the spin structure of the nucleon, namely the decomposition of nucleon spin into contributions from quark and gluon spins and their orbital angular momenta. Many exciting, unexpected results have been obtained at HERMES by measuring inclusive, semi-inclusive as well as exclusive processes in deep-inelastic lepton scattering. An overview of most recent results of the analysis of HERMES experimental data is presented.

## 1. Introduction

The HERMES experiment was designed to study/resolve the so called "Proton Spin Puzzle" originating from the measurement of European Muon Collaboration in 1988 indicating that only a small fraction of the proton spin is carried by quarks [1]. Conceptually, the nucleon spin can be decomposed from the contribution of the spin of its constituents (the quarks and gluons) and their total orbital angular momenta. The HERMES experiment aims to obtain information on all these contributions by measuring cross section asymmetries from the inclusive, semi-inclusive and exclusive processes in deep-inelastic scattering (DIS), respectively. Particularly, the possible role of the quark orbital angular momentum is addressed by studying hard exclusive processes such as deeply virtual Compton scattering (DVCS) which are interpreted in terms of generalized parton distributions (GPDs).

Another field of investigations which could provide insights into the yet unmeasured quark orbital angular momenta is the study of transverse momentum dependent (TMD) parton distribution functions in semi-inclusive DIS. They are needed for a complete understanding of the nucleon structure and describe the correlation between the quark or the nucleon spin with the quark transverse momentum, which leads to a three-dimensional description of the nucleon structure in the momentum space. This paper presents a selection of interesting new results obtained by the HERMES Collaboration over the past year.

HERMES used the longitudinally polarized ($P_{B,\max} \approx 0.6$) electron or positron beam of 27.6 GeV scattered off longitudinally or transversely polarized hydrogen and longitudinally polarized deuterium targets ($P_T^{H,D} \approx 0.85$) [2] or unpolarized gaseous targets internal to the HERA storage ring. The scattered leptons and produced particles like hadrons of different type or photons were detected by the HERMES spectrometer [3]. The particle identification capability of the experiment were significantly enhanced in 1998 when the threshold Cerenkov detector was upgraded to a dual ring imaging system (RICH). The average lepton identification efficiency was at least 98% with hadron contamination of less than 1%. In the end of 2005, a recoil detector (RD) was installed in the target region of HERMES, the main purpose of which was the detection of the recoil target protons in order to enhance access to hard exclusive processes.

## 2. Inclusive DIS: Structure Function $F_2$

The statistics collected at HERMES with unpolarized hydrogen and deuterium targets is highly competitive with respect to other fixed target experiments. This motivates the new extraction of the structure functions $F_2^p$ and $F_2^d$ [4] determined using a parametrization of existing data for the longitudinal-to-transverse virtual-photon absorption cross section ratio. The HERMES results provide data in the range $0.006 < x < 0.9$ and $0.1\ \mathrm{GeV}^2 < Q^2 < 20\ \mathrm{GeV}^2$, covering the perturbative to non-perturbative transition region of QCD in a so-far largely unexplored kinematic region, while they are in agreement with existing world data in the region of overlap.The measured cross sections are used in combination with data from other exper-

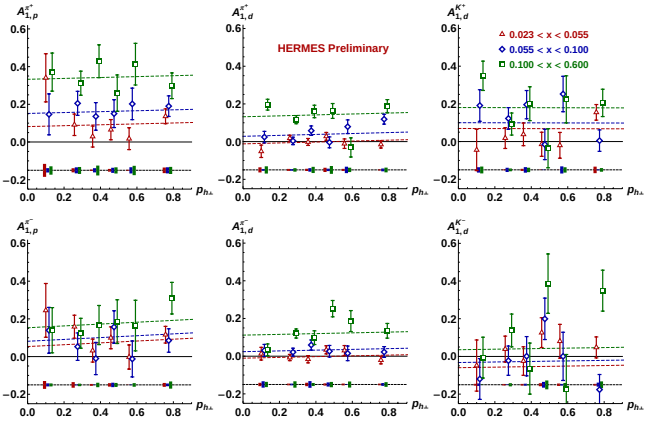


Fig. 1: Semi-inclusive DSAs binned in $P_{h\perp}$ in $x$-slices. The plots are overlaid with polynomial fits to measure possible $P_{h\perp}$ dependences

iments, to perform fits to the photon-nucleon cross section, using the functional form from the Abramowicz-Levin-Levy-Maor (ALLM) model [5]. The deuteron-to-proton cross section ratio is also reported by HERMES.

## 3. Semi-Inclusive DIS: Double-Spin Asymmetries

Longitudinal double-spin asymmetries (DSAs) in DIS have been an valuable source of information about the spin-structure of the nucleon [6]. Recent interest in unintegrated structure functions has encouraged a re-analysis of the HERMES dataset in order to provide semi-inclusive longitudinally-polarized double-spin asymmetry data with multi-dimensional kinematic dependences. Presenting the measured DSAs in two dimensions, e.g. in $z$ and $p_{h\perp}$ (respectively denoting the hadron's energy fraction and the transverse momentum with respect to the momentum of the virtual photon), can provide additional information on the character of quark fragmentation. It can also help to unravel both the parton distribution and fragmentation function product as well as the flavor structure tangled in the sums.

Figure 1 shows the results for the asymmetry $A_1^h$ as a function of $p_{h\perp}$ for three different values of $x$ for charged pions from the proton

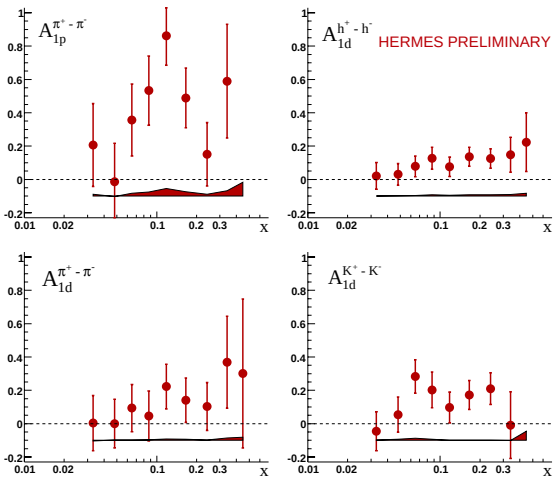


Fig. 2: Hadron charge-difference asymmetries for pions from the proton and pions kaons and undifferentiated hadrons from the deuteron target

target and charged pions and kaons from the deuteron target. These data were fit with a series of low-order polynomials in $x$ and $p_{h\perp}$. Within the measured uncertainties no $p_{h\perp}$ dependence is seen.

Another goal of the re-analysis of HERMES double-longitudinally-polarized dataset is to examine the hadron charge-difference asymmetries $A_1^{h^+ - h^-}$, shown in Fig. 2 for pions from the proton and pions, kaons and combined hadrons for deuterium target. The latter result has been compared with similar measurement from COMPASS [7], and they are found to be consistent despite considerably different $Q^2$ values.

A variety of new parton distribution functions (PDFs) describing the (spin-orbit) correlations between the quark or nucleon spin with the quark transverse momentum arise in the case when the cross section is not integrated over the transverse momentum $p_T$ of the quarks. At leading-twist, eight TMDs enter the semi-inclusive DIS cross section in conjunction with the fragmentation functions (see e.g. [8]).

The amplitudes of three DSAs related to so called 'worm-gear' TMD $g_{1T}^{\perp}$ are extracted together with six previously measured amplitudes of single-spin asymmetries (SSAs) [9, 10] using HERMES data

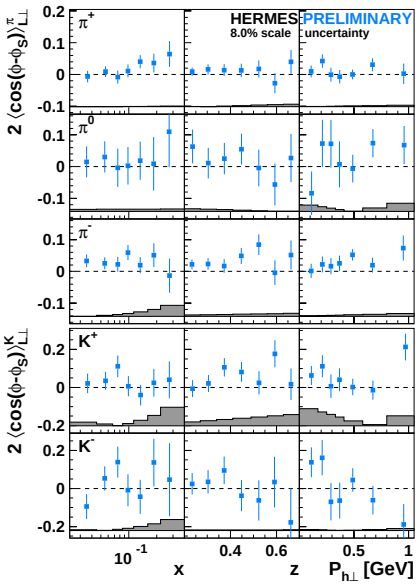


Fig. 3: Results for the $2\langle\cos(\phi-\phi_S)\rangle^h_{L\perp}$ DSA amplitudes for pions and charged kaons as a function of $x$, $z$ or $p_{h\perp}$. The shaded bands represent the systematic uncertainty. A common 8% scale uncertainty arises from the precision of the beam and target polarization measurement

recorded during the 2003-2005 running period with a longitudinally polarized electron/positron beam scattered off a transversely polarized hydrogen gas target. Fig. 3 shows the results for the $2\langle cos(\phi-\phi_S)\rangle^h_{L\perp}$ asymmetry amplitudes for pions and charged kaons as a function of $x$, $z$ or $p_{h\perp}$. The results show a positive amplitude for $\pi^-$ and possibly also for $\pi^+$ and $K^+$. For $\pi^0$ and $K^-$ they are found to be consistent with zero. The amplitudes for the sub-leading twist DSAs, not shown here, are both consistent with zero for all measured mesons.

## 4. Exclusive Processes

The measurements of hard exclusive productions of mesons and real photons (DVCS) opens an exciting new field in understanding the

nucleon structure in terms of GPDs, accessible in these processes. Depending on the type of the produced particle in the final state, the measurements are sensitive to different combinations of GPDs. The interest in this field was significantly increased when it was shown that certain GPDs are related to the total angular momentum carried by partons in the nucleon [13].

### 4.1. SDMS In Exclusive $\rho^0$ Production

Hermes previously published results on spin density matrix elements (SDMEs) in exclusive $\rho^0$ production [11]. In order to determine SDMEs from experimental data, they were considered as being independent free parameters in the fit of the production and decay angular distribution of the vector meson. This is referred to as the "SDME method".

SDMEs are dimensionless quantities and therefore depend on ratios of amplitudes rather than on amplitudes themselves. SDMEs can be rewritten in terms of amplitude ratios. In an alternative method of fitting the angular distribution, these ratios are considered as being independent free parameters. This method is referred to as the "amplitude method". In order to extract the helicity amplitudes themselves, experimental data on the differential cross section with respect to the Mandelstam $t$ variable, $ds/dt$ (which is proportional to the sum of squared moduli of all the amplitudes) are required in addition to the experimentally determined amplitude ratios. An analysis of these combined data would allow the extraction of the moduli of all amplitudes and of the phase differences between them with the common phase remaining undetermined.

The re-derived results on SDMEs obtained from the amplitude method [12] are found to be consistent with those determined from the SDME method [11]. On the other hand the new method enhanced the sensitivity for polarized SDMEs.

### 4.2. Double-Spin Asymmetries In DVCS

DVCS is the one of the cleanest process that can be used to constraint GPDs via Compton form factors (CFFs). HERMES has previously published results on various asymmetries measured in hard

exclusive leptoproduction of real photons from a nucleon or nuclear targets [14–21]. The asymmetries arise from the DVCS process and its interference with the Bethe-Heitler process.

A new results on DSAs in exclusive electroproduction of real photons from a transversely polarized hydrogen target measured with respect to the product of target polarization with beam helicity and beam charge, and with respect to the product of target polarization with beam helicity alone was published [22]. They are related to the real part of the same combination of Compton form factors as that determining the previously published transverse target single-spin asymmetries through the imaginary part [16]. The results for the double-spin asymmetries are found to be compatible with zero within the uncertainties of the measurement, and are not incompatible with the predictions of the only available GPD-based calculation.

Due to different kinematic prefactors, the amplitudes of DSA related to the real part of the interference term are suppressed compared to those extracted from transverse target single-spin asymmetry. Therefore, in contrary to the latter case they do not have significant sensitivity to the CFF $\mathcal{E}$ regarding the measured uncertainties. Nevertheless, they may serve as additional constraints in global fits to extract GPDs from measurements.

### 4.3. DVCS With Recoil Detector Information

In previously published HERMES results mentioned in section 4.2 the exclusive events were selected using the missing-mass technique without detection of recoiling particles. The signal in this case contains also the contribution from associated $\Delta$ resonance production. In order to ensure exclusivity and to reduce the background from the associated BH process, a RD was installed at HERMES at the end of 2005. It was in operation using unpolarized hydrogen and deuterium targets from 2006 to 2007.

In Fig. 4 the amplitudes of the single-charge beam-helicity asymmetry are given for exclusive samples including those extracted from $ep \to ep\gamma$ events with detection of the recoiling target proton. For comparison, the unresolved events were selected by standard missing-mass technique, the unresolved-reference events from this unresolved sample by requiring the missing 4-momentum to be within the ac-

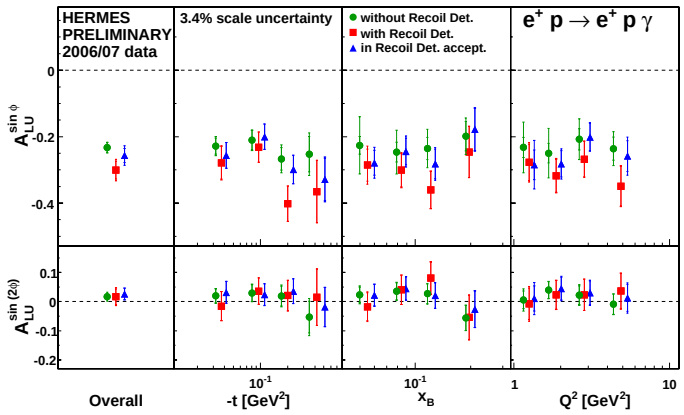


Fig. 4: Amplitudes of the single-charge beam-helicity asymmetry for each of the exclusive sample (see text)

ceptance of the RD, and the pure events were selected using the kinematic event fitting.

## 5. Outlook

In spite of many years of experiments, a detailed decomposition of the spin of the nucleon remains elusive. With the recent HERMES results some new information have been obtained. More precise results from HERMES data analysis of semi-inclusive and exclusive DIS are expected in future.

1. J. Ashman *et al.*, (EMC), Phys. Lett. B **206**, 364 (1988).
2. A. Airapetian *et al.*, (HERMES), Nucl. Instr. Meth. A **540**, 68 (2005).
3. A. Ackerstaff *et al.*, (HERMES), Nucl. Instr. Meth. A **417**, 230 (1998).
4. A. Airapetian *et al.*, (HERMES), JHEP **05**, 126 (2011).
5. H. Abramowicz, E. M. Levin, A. Levy, and U. Maor, Nucl. Phys. B **470**, 3 (1996).
6. A. Airapetian *et al.*, (HERMES), Phys. Rev. D **71**, 012003 (2005)
7. M. Alekseev, *et al.*, (COMPASS), Phys. Lett. B **660**, 458 (2008).
8. A. Baccheta *et al.*, JHEP **02**, 093 (2007).

9. A. Airapetian *et al.*, (HERMES), Phys. Rev. Lett. **103**, 152002 (2009).
10. A. Airapetian *et al.*, (HERMES), Phys. Lett. B **693**, 11 (2010).
11. A. Airapetian *et al.*, (HERMES), Eur. Phys. J. C **62**, 659 (2009).
12. A. Airapetian *et al.*, (HERMES), Eur. Phys. J. C **71**, 1609 (2011).
13. X. Ji, Phys. Rev. Lett. **78**, 610 (1997).
14. A. Airapetian *et al.*, (HERMES), Phys. Rev. Lett. **87**, 182001 (2001).
15. A. Airapetian *et al.*, (HERMES), Phys. Rev. D **75**, 011103 (2007).
16. A. Airapetian *et al.*, (HERMES), JHEP **06**, 066 (2008).
17. A. Airapetian *et al.*, (HERMES), JHEP **11**, 083 (2009).
18. A. Airapetian *et al.*, (HERMES), Nucl. Phys. B **829**, 1 (2010).
19. A. Airapetian *et al.*, (HERMES), Phys. Rev. C **81**, 035202 (2010).
20. A. Airapetian *et al.*, (HERMES), JHEP **06**, 019 (2010).
21. A. Airapetian *et al.*, (HERMES), Nucl. Phys. B **842**, 265 (2011).
22. A. Airapetian *et al.*, (HERMES), Phys. Lett. B **704**, 15 (2011).

# HEAVY-FLAVOR PHYSICS WITH THE CMS EXPERIMENT

Nicola Pozzobon[1]
(on behalf of the CMS Collaboration)

[1]*Dipartimento di Fisica "G. Galilei",*
*Università degli Studi di Padova,*
*and Istituto Nazionale di Fisica Nucleare, Sezione di Padova*
*Padova, 35131, ITALY,*
*e-mail: nicola.pozzobon@pd.infn.it*

**Abstract**

A representative sample of CMS analyses in Heavy-Flavor Physics, based on proton-proton collision data collected in 2010 and 2011 at a center-of-mass energy of 7 TeV, are reviewed, including measurements of heavy quarkonia as well as open $b$-quark production. The status and prospects of the searches for rare $B$ decays and measurements of CP violation in the $B$ sector are presented.

## 1. Introduction

The importance of Heavy-Flavor Physics in the latest years is mainly due to the need of testing Quantum Chromo-Dynamics and the way it reproduces measured production cross section and polarization of *beauty* and *charm* quarks in hadronic interactions. Moreover, Heavy-Flavor final states can be used as a test-bench for physics beyond the Standard Model, including CP violation, for example through the study of new resonances and rare decays. The CMS Experiment at the CERN Large Hadron Collider has a rich Heavy-Flavor Physics program thanks to the excellent performance of the wide-coverage muon system and the tracking system consisting of silicon

pixels and strips. Some representative studies with proton-proton collision data at $\sqrt{s} = 7$ TeV, collected mainly in 2010, are described in these proceedings in order to give a taste of the quality of the ongoing effort focussing on common points shared by different analyses.

The CMS muon system is interlayered in the return yoke of the 3.8 T solenoid and surrounds the tracking system and the calorimeters of CMS up to a pseudorapidity of $|\eta| = 2.4$. Three different technologies are exploited as muon detectors: drift tubes in the barrel region, cathode strip chambers in the end-caps and resistive plate chambers for fast triggering purposes. Tracking of charged particles at CMS is performed with silicon strip tracker complemented by a silicon pixel detector for precise vertexing and to improve track quality. The resolution on primary vertex measurement has been determined in early 7 TeV proton-proton collisions to be $\simeq 25$ ($\simeq 20$) $\mu$m in the transverse (longitudinal) plane, when $\simeq 30$ tracks are used in the reconstruction. A detailed description of the CMS detector, as well as more details on its subsystems and their performance, can be found elsewhere [1–3].

## 2. Heavy Quarkonia Production

The double-differential production cross-sections of Heavy-Flavor resonances have been measured by CMS, including prompt and non-prompt fractions. The event selection technique is common to the studies looking for a $J/\psi$ in the final state. The measurement of $J/\psi$ and $\psi(2S)$ production cross section relies on the clear dimuon signature of one possible final state. Events are selected with either single or double muon trigger, each muon is requested to satisfy some quality constraints in terms of associated tracks and both tracks in the muon pair must point to the same primary vertex within the typical extrapolation resolution. The signal yield is extracted by fitting the signal and background shapes in a certain muon pair invariant mass window. The differential cross section is then calculated as

$$\frac{d^2\left(\sigma \times B\right)}{dp_T d\eta} = \frac{N_{\text{signal}}}{\text{Acceptance} \times \text{Efficiency} \times \text{Luminosity} \times \Delta p_T \Delta \eta}.$$

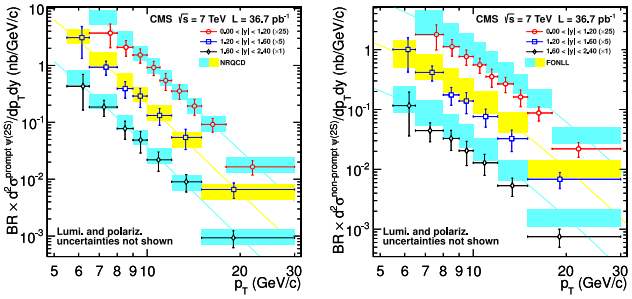


Fig. 1: Measured prompt (left) and non-prompt (right) $\psi(2S)$ production cross section as a function of both $\psi(2S)$ $p_T$ and rapidity

The prompt and non-prompt fractions are extracted via a two-dimensional fit to the dimuon invariant mass and to $L_{J/\psi}$, the most probable distance in the transverse plane between the primary vertex and the dimuon vertex. The main systematic uncertainties affecting the measurement of $J/\psi$ and $\psi(2S)$ prompt and non-prompt fractions include the tracker misalignment, the modeling of $b$ lifetime, the resolution on primary vertex, the background shape determination in mass sideband regions and the different efficiency in detection of muons from the prompt and non-prompt categories. These fractions have been found to be in a reasonable agreement with NRQCD predictions, with the only exception of non-prompt fractions at high $p_T$, as shown in Fig. 1.

The $\psi(2S)$ peak is used as a benchmark for the observation [4] of $X(3872)$. The final state chosen for the simultaneous observation of $\psi(2S)$ and $X(3872)$ is $J/\psi\ \pi^+\pi^- \to \mu^+\mu^-\pi^+\pi^-$. Pairs of tracks of opposite charge are selected as pion candidates, besides muon pair selection which is the same as the $J/\psi$ one, and all the four tracks are constrained to a common vertex. The measured ratio between $\sigma \times B$ for $X(3872)$ and $\psi(2S)$ is $0.087 \pm 0.017$ (stat.) $\pm\, 0.009$ (syst.). Also the production of $\Upsilon$ states has been measured by CMS at the LHC in $pp$ collisions in dimuon final states [5]. The results for the measurement of the production cross section times branching ratio can be summarized as: $7.37 \pm 0.13(\text{stat.})^{+0.61}_{-0.42}(\text{syst.}) \pm 0.81(\text{lumi.})$ nb for $\Upsilon(1S)$, $1.90 \pm 0.09(\text{stat.})\ ^{+0.20}_{-0.14}(\text{syst.}) \pm 0.24(\text{lumi.})$ nb for $\Upsilon(2S)$, $1.02 \pm 0.07(\text{stat.})^{+0.11}_{-0.08}(\text{syst.}) \pm 0.11(\text{lumi.})$ nb for $\Upsilon(3S)$.

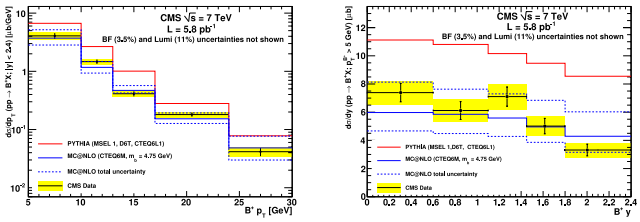


Fig. 2: $B^{\pm}$ production cross section as a function of $B$ $p_T$ (left) and rapidity (right)

## 3. Exclusive $B$-hadron Production

The production of $B$-hadrons is measured in exclusive channels in final states with $J/\psi$ in association with other tracks. Three studies were performed using similar techniques. The first measurement of the process $B^{\pm} \to J/\psi\ K^{\pm}$ at the LHC [6] employed a double muon trigger for the $J/\psi$ selection, requiring muons to have opposite charge, invariant mass within $(1.95, 3.25)$ GeV/$c^2$, and an additional track sharing the vertex and assumed to be the $K^{\pm}$ candidate. The measurement of $B^0 \to J/\psi\ K_S \to J/\psi\ \pi^+\pi^-$ [7], besides the $J/\psi$ selection, requires two additional tracks with opposite charge, assumed to be pions, with invariant mass close to the $K_S$ one. The third measurement [8] concerns the decay of $B_s^0$ into $J/\psi\phi$ in the final state $\mu^+\mu^- K^+ K^-$. Major backgrounds come from $J/\psi$ and misreconstructed $B \to J/\psi \to K^*(892)$. The signal yield of each channel is extracted for each bin in transverse momentum and rapidity with a maximum likelihood fit to the hadron mass $m_B$ and to the proper decay length $L_{xy} \times m_B/p_T^B$. The proper decay length is measured as a consistency check and found to be in agreement with the world-average value. All the measured double-differential cross sections are in reasonable agreement with the predictions of MC@NLO in terms of shape and absolute normalization, as shown in Fig. 2 for $B^{\pm}$ as an example.

## 4. Open $b$-quark Production

The measurement of open-beauty production relies on the identification and measurement of jets from $b$-quarks [9]. Data are selected

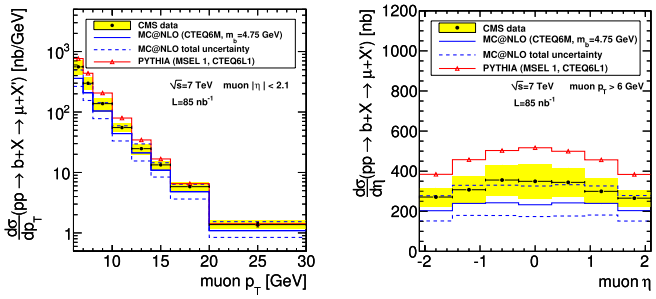


Fig. 3: Open $b$ production cross section as a function of muon $p_T$ (left) and pseudorapidity (right) in events witout requiring secondary vertices measured with fit to muon $p_T^{\mathrm{rel}}$ templates

with a single muon trigger. All tracks are clustered in jets with anti-$k_T$ algorithm. Jets from $b$-quarks are identified from muons in jets. The fraction of muon momentum orthogonal to jet, $p_T^{\mathrm{rel}}$, is used to discriminate different flavor fractions. Templates from Monte-Carlo (MC) simulated data ($b$- and $c$-jets) and data (light quark background) are built and their relative weight is fitted to data. Light flavor and $c$ are merged together as they are indistinguishable. The overall $b$-fraction is measured to be about 46%. The systematic uncertainties are dominated by the shape of $p_T^{\mathrm{rel}}$ templates: signal template is validated with a $b$-enriched sample selected from muons with large impact parameter, with a measured $b$-fraction of $\sim 86\%$. Other systematic uncertainties are due to the data-driven light flavor background template, MC generation and fragmentation models. The double-differential cross section is measured, as well as the total value, in the muon acceptance region $p_T > 6$ GeV/$c$ and $|\eta| < 2.1$: $\sigma = 1.32 \pm 0.01(\mathrm{stat.}) \pm 0.30(\mathrm{syst.}) \pm 0.15(\mathrm{lumi.})$ $\mu$b, to be compared to MC@NLO prediction of $0.95 \pm^{+0.41}_{-0.21}(\mathrm{scale}) \pm 0.09(m_b) \pm 0.05(\mathrm{pdf})$ $\mu$b. Differential cross sections are shown in Fig. 3. A complementary measurement [10] employs an event sample with muons and jets identified with secondary vertex $b$-tagging, allowing for an enriched sample with $b$-fraction around 86%. Secondary vertices from tracks with high impact parameter significance are usually associated to long-lived particles, as $b$-flavored hadrons are. At least three tracks with hits in the Pixel Detector are required to define a secondary vertex. The cross section is measured to be $108 \pm 1(\mathrm{stat.}) \pm 17(\mathrm{syst.}) \pm 4(\mathrm{lumi.})$ nb, to

be compared to MC@NLO prediction of $114 \pm^{+40}_{-23}$ (scale) $\pm 3(m_b) \pm$ 5(pdf) nb.

Inclusive $b$-jet production can be measured without muons for the determination of the $b$-fraction [11]. Secondary vertices are searched for in data which have been selected with a single jet trigger. The purity of the sample is measured in two complementary ways to be $\sim 75\%$. The first strategy fits the distribution of vertex invariant mass to templates from MC. The second one is based exclusively on MC flavor fractions and tagging efficiencies. The measured double-differential cross section is in agreement with MC@NLO predictions except for jet $p_T > 100$ GeV/$c$ and jet rapidity larger than 1.5, as shown in Fig. 5.

Correlated production of $b\bar{b}$ pairs is important as $b\bar{b}$ pairs represent a background for many rare processes. The production cross section has been measured in the final state with opposite-charge muon pairs [12]. Muon pairs are selected with a low $p_T$ threshold and resonant states such as $Z$, $\Upsilon$ and $J\psi$ are rejected using invariant mass information. The sample composition is defined with a fit to muon impact parameter templates from either MC (beauty, charm, in-flight decays) and data (prompt muon production). Templates for single muon are symmetrized to classify each muon pair. The $b\bar{b}$ fraction is measured to be $0.651 \pm 0.003$, as shown in Fig. 4, resulting into a measured cross section times branching ratio of $26.18 \pm 0.14$(stat.)$\pm$ 2.82(syst.) $\pm$ 1.05(lumi.) nb, to be compared to MC@NLO prediction of $19.95 \pm 0.46$(stat.)$^{+4.68}_{-4.33}$(syst.) nb.

Angular distributions of $b\bar{b}$ pairs are affected by the final state topology of the parton-parton elementary process and a precise measurement of them can give important hints to understand heavy flavor jet production mechanism. Data are collected with a single jet trigger at different energy thresholds [13], requiring the absolute value of the jet pseudorapidity to be lower than three and candidate $b$-hadrons to be within the tracking volume. Two secondary vertices, with more than three tracks each, identify the candidate $B\bar{B}$ pair. The vector joining the secondary and the primary vertex is used to define the flight direction of each $b$-hadron. The $b$-hadron momentum is calculated from the sum of the momenta of all the tracks associated to the secondary vertex. The strategy is validated from MC, where the

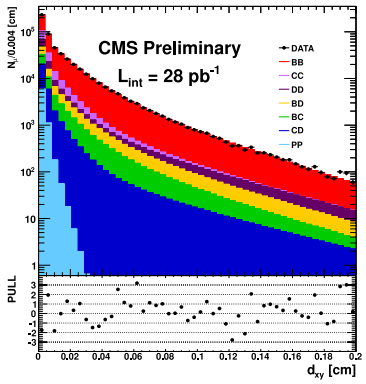


Fig. 4: The amount of events from $b\bar{b}$ decays in the data sample is obtained with a fit to the two dimensional template distributions of the impact parameters of the muons. The figure shows a 1D projection of the fitted 2D templates, superimposed to data

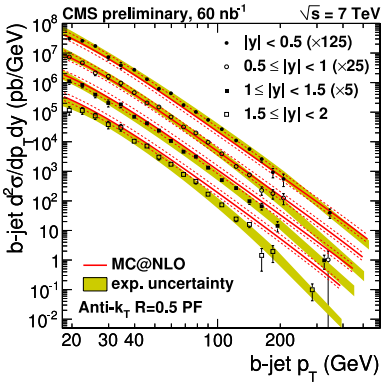


Fig. 5: Measured $b$-jet differential cross section compared to the MC@NLO calculation

measured flight directions are compared to the generated ones resulting in typical angular separations in the $\eta \times \phi$ space smaller than 0.05. Major backgrounds come from misreconstructed secondary vertices, $c\bar{c}$ processes with $D$-meson final states, sequential $B \to D$ with two secondary vertices and light flavor QCD. The measured angular correlations are shown in Fig. 6.

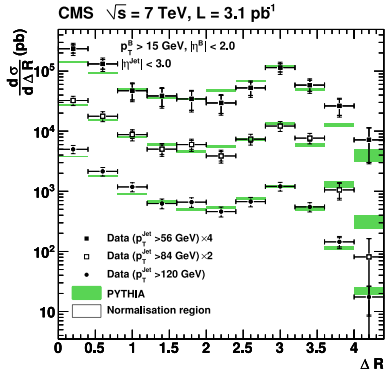


Fig. 6: Differential $B\bar{B}$ production cross sections as a function of $\Delta R$ for the three leading jet $p_T$ regions

## 5. Rare Decays and CP Violation

Besides all the heavy-flavor production studies, also CP violation studies and searches for rare decays have started at CMS. One of the most interesting searches is the search for rare decays $B^0 \to \mu\mu$ and $B_s^0 \to \mu\mu$ [14]. Data are selected from a low $p_T$ dimuon trigger sample. The dimuon invariant mass is required to be in the $(4.9, 5.9)$ GeV/$c^2$ interval. The selections are optimized using MC signal events and data sideband events with $m_{\mu\mu} < 5.2$ GeV/$c^2$ and $m_{\mu\mu} > 5.45$ GeV/$c^2$, to be blind and unbiased in the signal region. The selection criteria include muon $p_T > 4.5$ GeV/$c$ (4 GeV/$c$ for the second muon), $p_T$ of the candidate $B$ larger than 6.5 GeV/$c$, and track-based isolation criteria on candidate $B$. Main backgrounds come from semileptonic $B$ decays in association to a misidentified hadron, other rare decays such as $B_s \to K\ K$ and misreconstructed secondary vertices. The search is simultaneous for $B^0 \to \mu^+\mu^-$ and $B_s^0 \to \mu^+\mu^-$. $B^\pm \to J/\psi\ K^\pm$ is used for relative normalization:

$$\frac{B(B_s^0 \to \mu^+\mu^-)}{\mathrm{N}(B_s^0)} \times \mathrm{Acc}(B_s^0) \times \mathrm{Eff}(B_s^0 \to \mu^+\mu^-) \times f_s =$$

$$= \frac{B(B^\pm \to J/\psi[\mu^+\mu^-]K^\pm)}{\mathrm{N}(B^\pm \to J/\psi K^\pm)} \times \mathrm{Acc}(B^\pm) \times \mathrm{Eff}(B^\pm \to J/\psi[\mu^+\mu^-]K^\pm) \times f_u.$$

Event selection is validated with a $B^0 \to J/\psi[\mu^+\mu^-]\phi$ sample. The observed yields in the signal windows are consistent with the SM expectation for signal and background. The following upper limits for the branching fractions have been obtained: $1.9 \times 10^{-8}$ at 95% CL for $B_s^0 \to \mu^+\mu^-$ and $4.6 \times 10^{-9}$ at 95% CL for $B^0 \to \mu^+\mu^-$.

## 6. Summary

The CMS experiment is competitive in heavy-flavor physics measurements with *pp* collisions, finding its strength in the Silicon Tracker and in the Muon System, which can provide precise identification and measurements of muons, tracks and vertices. The event selection and data analysis techniques proved to be sound and effective and some of them are successfully shared among different search channels.

The CMS experiment could perform interesting heavy-flavor physics measurements also with heavy ion collisions, which are widely documented elsewhere, such as the suppression of excited $\Upsilon$(nS) states.


1. CMS Collaboration, JINST **03** (2008) S08004.
2. CMS Collaboration, CMS PAS **MUO-10-002**.
3. CMS Collaboration, CMS PAS **TRK-10-005**.
4. CMS Collaboration, CMS PAS **BPH-10-018**.
5. CMS Collaboration, Phys. Rev. D **83** (2011) 112004.
6. CMS Collaboration, Phys. Rev. Lett **106** (2011) 112001.
7. CMS Collaboration, Phys. Rev. Lett **106** (2011) 252001.
8. CMS Collaboration, Phys. Rev. D **84** (2011) 052008.
9. CMS Collaboration, CMS PAS **BPH-10-007**.
10. CMS Collaboration, CMS PAS **BPH-10-008**.
11. CMS Collaboration, CMS PAS **BPH-10-009**.
12. CMS Collaboration, CMS PAS **BPH-10-015**.
13. CMS Collaboration, JHEP **03** (2011) 136.
14. CMS Collaboration, Phys. Rev. Lett. **107** (2011) 191802.

# LATEST RESULTS FROM ALICE

Eugenio Scapparone
on behalf of the ALICE Collaboration

*Istituto Nazionale di Fisica Nucleare,*
*Sezione di Bologna, Italy*

**Abstract**

In this paper selected results obtained by the ALICE experiment at the LHC will be presented. Data collected during the pp runs taken at $\sqrt{s}$=0.9, 2.76 and 7 TeV and Pb-Pb runs at $\sqrt{s_{\rm NN}}$=2.76 TeV allowed interesting studies on the properties of the hadronic and nuclear matter: proton runs gave us the possibility to explore the ordinary matter at very high energy and up to very low $p_t$, while Pb-Pb runs provided spectacular events where several thousands of particles produced in the interaction revealed how a very dense medium behaves, providing a deeper picture on the quark gluon plasma(QGP) chemical composition and dynamics.

## 1. Detector Description

The most important requirements for a general purpose heavy ion experiment at the LHC are a powerful particle identification over a wide momentum interval, a robust tracking capability in a very high multiplicity environment and a very low cut in transverse momentum $p_{\rm t}$. The ALICE detector matches these needs using several detectors, and implementing almost all the known particle identification (PID) techniques. A robust tracking and the vertex finding are provided by the Internal Tracking System (ITS), made by three different silicon based detectors, followed by a large volume TPC [1]. As fas as the PID is concerned, each detector covers a different range of momentum: $\mathrm{d}E/\mathrm{d}x$ vs $p_{\rm t}$ is provided by ITS and by TPC, particle masses difference, reflecting in a different time of flight and Cherenkov angle,

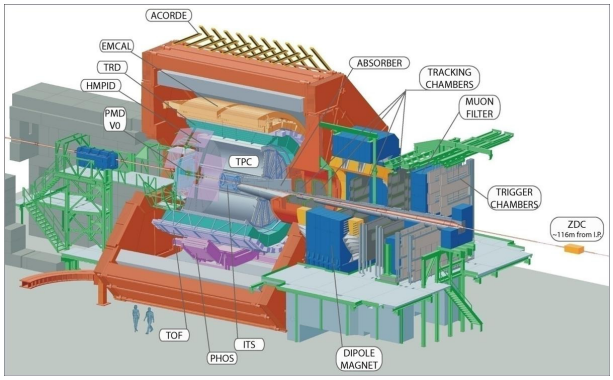


Fig. 1: Sketch of the ALICE experiment

is measured by the Time Of Flight (TOF) and by the High Momentum Particle Identification System (HMPID). Electrons are tagged by the Transition Radiation Detector (TRD), $\gamma$-rays by the Photon Spectrometer(PHOS), electromagnetic shower by the EMCAL, while muons from the forward muon arm. The barrel, immersed in a 0.5 T solenoidal magnetic field, is made of several detectors: the Silicon Pixel Detector (SPD), the closest to the interaction point (IP), is followed by the Silicon Drift Detector (SDD) and by the Silicon Strip Detector (SSD). These dominate the vertex resolution, ranging from 250 $\mu$m ($p_{\rm t}$=0.2 GeV/$c$) to 20 $\mu$m ($p_{\rm t}$=10 GeV/$c$).

Placed at a radius ranging from 0.85 to 2.5 m, the large TPC, consists of two 2.5 m long drift volume ($\simeq$88 m$^3$), separated by a central cathode. The large number of samples allows the TPC to measure the track d$E$/d$x$ with a 5% error. The TOF is a high segmentation MRPC detector ($\simeq$ 150,000 channels) with an excellent time resolution, better than 100 ps, placed over the full azimuthal angle and $|\eta|$<0.9. It provides a 3$\sigma$ discrimination for $\pi$/K and K/p up to 2.5 GeV/$c$ and 4 GeV/$c$ respectively. The goal of the TRD detector, made of a radiator and a drift chamber operated with Xe/$CO_2$ mixture (85%/15%), is the tagging of the electrons. The PHOS, the EMCAL and the HMPID are additional detectors with partial coverage of the central barrel. The largest detector in the forward region is the "muon arm", consisting of an hadron absorber, MWPC cham-

bers, a 0.7 T dipole followed by RPCs to tag muons and to and measure their $p_{\rm t}$. Several small and important detectors run in the forward and backward region and close to the beam pipe: T0, V0, Photon Multiplicity Detector (PMD) and the Forward Multiplicity Detector(FMD). Spectator protons and neutrons are detected by the Zero Degree Calorimeters (ZDC), consisting of two sets of calorimeters placed at $\pm \simeq$116 m from the IP. More information on detector design and performance can be found in [1].

## 2. Results from Proton-Proton Collisions

One of the initial ALICE goals in the pp run is the fine tuning of the detector Monte Carlo simulation. Although a first successful commissioning was performed with cosmic ray data, hadronic collisions offered the possibility to make a step forward in the detector understanding and Monte Carlo modelling. As an example photon tagging allowed a measurement of the material budget radial distribution. This gave the possibility to improve the detector knowledge and to obtain a much better detector simulation, where the $\gamma$ yield as a function of the distance from the IP nicely agree in the data and in the MC. Proton runs are a rich source of physics, where ALICE exploits its peculiarity, making use of the low momentum cut.

### Multiplicity studies

Multiplicity studies provide informations on the energy density of the interaction and is one of the primary information needed to test Monte Carlo simulation. Moreover this is a basic variable, so that a quick comparison between the four LHC experiment is made available. ALICE measured the charged particle multiplicity per pseudorapidity interval $\mathrm{d}N/\mathrm{d}\eta_{\rm ch}$ at $\sqrt{s}$=0.9, 2.36 and 7 TeV, with the average charged particle multiplicity per unit of rapidity ranging from ($3.81 \pm 0.01$ (stat) $\pm$ 0.07 (sys)) to ($6.01 \pm 0.01$ (stat) + 0.20,–0.12 (sys)). While data agree nicely with the other LHC detectors, none of the investigated models (Pythia, Phojet) and their tunes describe the average multiplicity and the multiplicity distribution well. At $\sqrt{s}$ = 0.9 and 2.36 TeV, the Pythia tunes Perugia-0 and D6T fail

in reproducing the average multiplicity, while Phojet does not reproduce data at $\sqrt{s}$=7 TeV and is far away from describing the increase in multiplicity from $\sqrt{s}$=0.9 TeV to $\sqrt{s}$=2.36 TeV and from $\sqrt{s}$=2.36 TeV $\sqrt{s}$=7 TeV. At 0.9 TeV, the high-multiplicity tail of the distributions is best described by the Phojet model, while at 2.36 TeV, Pythia tune ATLAS-CSC is the closest to the data.

The situation does not improve when considering the particle $p_{\mathrm{t}}$ prediction: the transverse momentum distribution at 900 GeV and the dependence of average $p_{\mathrm{t}}$ on $N_{\mathrm{ch}}$ is not reproduced by the ATLAS-CSC Pythia tune [10]. At present we do not have an event generator/tune that can reproduce the LHC data in a satisfactory way.

### Strange baryons

The yields and $p_{\mathrm{t}}$ spectra of identified charged particle ($\pi$, K, p) and neutral strange particles ($\mathrm{K}^0$, $\Phi$, $\Lambda$, $\Xi$) have been measured at $\sqrt{s}$=0.9 and 7 TeV. While the $\phi$ is properly reproduced by Pythia (especially by the D6T tune), the $\mathrm{K}^0$ transverse momentum spectrum is overestimated by the Pythia tune ATLAS-CSC and Phojet below 0.75 GeV/$c$ but is lower by a factor of $\simeq 2$ in the $p_{\mathrm{t}}$ range 1-3 GeV/$c$. As far as strange baryons is concerned, Phojet and Pythia tunes are well below the data by a factor ranging from 3 to 10, depending on the baryon and on the particle $p_{\mathrm{t}}$. Moreover data taken at $\sqrt{s}$=7 TeV shows the ratio $\Omega/\Xi$ is underestimated by Pythia of a factor up to 6. From an experimental point of view it's worth noting the ratio of $\Lambda/\mathrm{K}^0$ agrees very well with the STAR data taken at $\sqrt{s}$=200 GeV and the ratio $\Xi/\Lambda$ is within the error.

### J/$\psi$ study

J/$\psi$ study has been one of the most compelling evidence for quark gluon plasma formation more than two decades ago. The study of this vector meson suppression at higher energy allows a big step in the understanding of the color field mechanisms at work in this new state of the matter. Proton-proton runs offer the possibility to test the detector performance in J/$\psi$ detection and a reference data for Pb-Pb analysis. ALICE can detect the J/$\psi \rightarrow \mu^+\mu^-$ channel taking advantage of the forward muon arm detector ($2.5 < \mathrm{y} < 4$) and the

J/$\psi \to e^+e^-$ channel by using the barrel detectors ($|\eta| < 0.9$). ALICE measurement at central rapidity reaches $p_t$=0 and is therefore complementary to the CMS data, available at $|y| < 1.2$ for $p_t > 6.5$ GeV/$c$, and ATLAS, which covers the region $|y| < 0.75$ and $p_t > 7$ GeV/$c$. At $\sqrt{s} = 7$ TeV the ALICE measured cross section is [2]:

$$\sigma_{J/\psi}(|y| < 0.9) = 10.7 \pm 1.2(\text{sta.}) \pm 1.7(\text{sys.}) + \\ +1.6(\lambda = 1) - 2.3(\lambda = -1)\ \mu\text{b}, \quad (1)$$

$$\sigma_{J/\psi}(2.5 < y < 4) = 6.31 \pm 0.25(\text{sta.}) \pm 0.80(\text{sys.}) + \\ +0.95(\lambda = 1) - 1.96(\lambda = -1)\ \mu\text{b}, \quad (2)$$

where $\lambda$=1 is for fully transverse and $\lambda$=–1 for longitudinal polarization. The J/$\psi$ decaying into muons are compared to those detected by LHCb at $2.5 < y < 4$, finding a good agreement. In the barrel region the CMS data ($|y| < 2$) and ATLAS ($|y| < 0.9$) can be compared with those detected by ALICE only for $p_t > 7$ GeV. It is worth noting these results refer to inclusive production, therefore the measured yield is a superposition of a direct component and of J/$\psi$ coming from the radiative decay of higher-mass charmonium states.

## 3. Results from Pb-Pb Collisions

Data collected during the 2010 gave a first look at the hot and dense medium formed at $\sqrt{s_{NN}}$=2.76 TeV when Pb-Pb ions collide.

### Energy density

The energy density available in the Pb-Pb interactions is much larger with respect to the p-p one, resulting in a very high number of particle produced. At $\sqrt{s_{NN}}$=2.76 TeV and for central collisions, ALICE measured an average density of primary charged particles at midrapidity $\langle N_{ch} \rangle = (1584 \pm 4(\text{stat}) \pm 76(\text{sys}))$. Normalizing per participant pair, we obtain $dN_{ch}/d\eta/(0.5N_{part})$=(8.3 $\pm$0.4(sys)), about a factor 2 higher with respect to RHIC. This is larger than most of the predictions and about 50% more than expected from simple phenomenological extrapolations from RHIC energy: the logarithmic law that described the multiplicity dependence with energy, does not

hold anymore. Following the Bjorken approach the average energy density has been derived. The average amount of transverse energy produced per unit of pseudorapidity per participant pair in central collisions is about 9 GeV, a factor $\simeq$3 larger than at RHIC (the larger multiplicity at LHC being accompanied by an increase in the average transverse momentum of the produced particles), corresponding to an energy density of about 15 GeV/fm$^3$. The centrality dependence of the charged particle multiplicity is rather mild, favouring models incorporating some mechanism (such as parton saturation) moderating the increase with centrality of the average multiplicity per participant pair.

### Nuclear modification factor $R_{AA}$

The partons generated by a ion-ion collision at high energy, experience high energy loss collisions in the hot dense medium, showing a high opacity to their traveling inside. The depletion in the hadron yield is a powerful probe to investigate this effect. The nuclear modification factor $R_{AA}$ is defined as the ratio of the charged particle yield in Pb-Pb to that in pp, scaled by the number of binary nucleon-nucleon collisions $N_{\rm coll}$. ALICE measured the nuclear modification factor $R_{AA}$ of inclusive charged particle momentum distributions out to $p_{\rm t}$=20 GeV/$c$, where the spectra are dominated by leading jet fragments. ALICE performed a first analysis [3] where the prediction at $\sqrt{s}$=2.76 TeV was extrapolated from the data collected at $\sqrt{s}$=0.9 and 7 TeV. The analysis was improved after data at $\sqrt{s}$=2.76 TeV where taken. The two analysis agree quite well within the systematical error and show the $R_{AA}$ ratio has a minimum at around 6 GeV, where the suppression is stronger than at RHIC ($\sqrt{s_{\rm NN}}$= 0.2 TeV), and then rises smoothly towards higher momentum. This latter feature is not evident has not been seen in the published RHIC data. However, initial state effects (shadowing/saturation), which presumably are very strong at LHC and which might depend on both impact parameter and momentum transfer, can complicate a straight forward interpretation of the data and the comparison between different beam energies. The powerful ALICE PID allows the study of $R_{AA}$ for different hadrons separately. $R_{AA}$ looks almost universal for $p_{\rm t}$>6 GeV/$c$; at low $p_{\rm t}$ the $\Lambda$ baryon don't show any nuclear modifi-

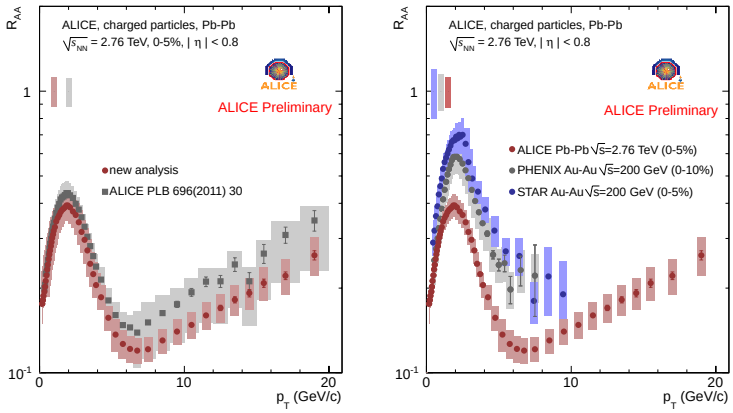


Fig. 2: ALICE $R_{AA}$ for the two different analysis(left) and compared to RHIC results(right)

cation factor ($R_{AA} \simeq 1$) while K behaves like all the other hadrons. It is worth noting D mesons are expected to show a smaller nuclear modification factor, since the main source of energy loss (gluon radiation) is depleted by the Casimir effect for heavy quark. This is found, although with a still high statistical error, in the data where a larger $R_{AA}$ is found for $D^0, D^+$ in the interval 4 GeV/$c \leq p_t \leq$5 GeV/$c$.

### Elliptic flow

The elliptic flow represents a powerful test to investigate the hydrodinamical properties of the quark gluon plasma. A perfect fluid shows a very small viscosity: this can be studied by looking at the efficiency in transferring the geometrical collision system anisotropy into momentum anisotropy. The distribution of the azimuthal angle, measured with respect to the reaction plane, is expanded into Fourier terms, where the second coefficient is the so called "elliptic flow", $v_2$. The large elliptic flow observed at RHIC, is described reasonably well by theoretical models based on relativistic hydrodynamics with a QGP equation of state and a ratio of the shear viscosity to the entropy density within a factor of $\simeq$5 by the supposed universal lower bound of $1/4\pi$. This indicates the QGP expands as a nearly perfect fluid. The first ALICE results [4] shows the elliptic flow at $\sqrt{s_{\rm NN}}$=2.76 TeV is

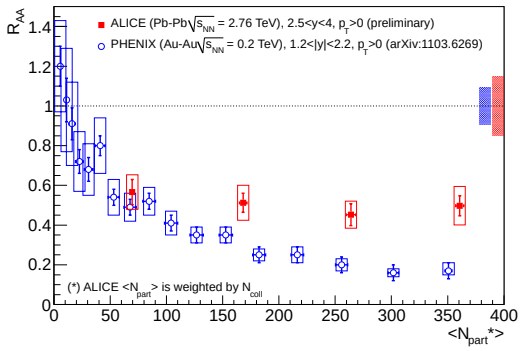


Fig. 3: ALICE J/$\psi$ measurement in the forward region compared with RHIC results

$\simeq$30% larger with respect to RHIC. Nevertheless the $v_2$ as a function of $p_t$ is close to the RHIC measurement, showing the system hydrodynamic properties at RHIC and LHC are similar. The increase of the elliptic flow observed at LHC therefore comes from the increase of the average $p_t$. An important difference with respect to RHIC results is the elliptic flow study for different hadrons separately. While at RHIC the $v_2/n_q$, where $n_q$ is the number of hadron valence quark, is similar for pion, kaons and protons, at LHC just pion and kaons $v_2/n_q$ is compatible; protons have a lower $v_2/n_q$, showing the quark scaling does not hold for $p_t < 0.5$ GeV/$c$.

### J/$\psi$ suppression

J/$\psi$ measurement is one of the key measurement for a high energy heavy ion experiment. For $p_t$>0 and 2.5<y<4, ALICE tags the J/$\psi$ through the J/$\psi \to \mu^+\mu^-$ channel. A rather small J/$\psi$ suppression of about 0.5 was observed, practically independent of centrality: this is a smaller suppression than that observed at RHIC. An interesting result is the comparison with ATLAS, where data are taken only at $p_t > 6.5$ GeV/$c$, shows a much stronger centrality dependence and suppression, hinting for a $p_t$ dependence of the J/$\psi$ suppression. The measurement of the J/$\psi$ in the J/$\psi \to e^+e^-$ channel is challenging with the present statistics and large hadronic background. However the signal has been extracted in the centrality class 0-40%

and the central to peripheral (40-80%) ratio ($R_{\rm CP}$) has been evaluated. Within the large systematic uncertainties, the dielectron $R_{\rm CP}$ is compatible with ATLAS and ALICE di-muon $R_{\rm CP}$ measurements.

The above results hint at J/$\psi$ regeneration in hot matter at LHC energies, but it is worth noting the J/$\psi$ production can be modified by the initial state effect which could modify the medium: ALICE needs a p-Pb run as reference to disentangle the contributions from cold nuclear matter.

1. Alice Coll., J. Phys. G: Nucl. Part. Phys. **30**, 1517 (2004).
2. Alice Coll., Phys. Lett. B **704**, 442 (2011).
3. Alice Coll., Phys. Lett. B **696**, 30-39 (2011).
4. Alice Coll., Phys. Rev. Lett. **105**, 252302 (2010).

# QUESTS FOR $\overline{\text{P}}$ANDA EXPERIMENT

E.A. Strokovsky[1]
for the $\overline{\text{P}}$ANDA Collaboration

[1] *Joint Institute for Nuclear Research*
*Dubna, Moscow region, 141980, Russia*
*e-mail: Eugene.Strokovsky@lhep.jinr.ru*

**Abstract**

The physics program of the $\overline{P}$ANDA experiment at FAIR, studying antiproton interaction with protons and nuclei at intermediate energies, is briefly outlined. Some selected points of the program are discussed in more details.

## 1. The FAIR complex (Facility for Antiproton and Ion Research)

The PANDA Experiment will be one of the key experiments at the Facility for Antiproton and Ion Research (FAIR) which is under construction and currently being built on the area of the GSI Helmholtzzentrum fur Schwerionenforschung in Darmstadt, Germany. This new generation facility will provide excellent instrumental basis for research in fundamental as well as applied physics. The present general scheme of the FAIR is shown in Fig. 1.

The central part of FAIR is a synchrotron complex providing intense pulsed ion beams (from p to U). Antiprotons produced by a primary proton beam will then be filled into the High Energy Storage Ring (HESR) and will collide with the fixed target inside the PANDA Detector (Fig. 2) described in the dedicated talk [3]. Start of operating of the SIS100 accelerator and the HESR ring is planned for 2017 year.

**T a b l e 1: Planned beam parameters from the SIS100/300 complex**

| Program | Max. kinetic energy | Intensity per spill | Average intensity |
|---|---|---|---|
| Beams of radio-active ions | 0.4 ÷ 1.5 GeV/u all elements up to U | $\mathbf{5 \cdot 10^{11}}$ for expts at storage ring | $\mathbf{3 \cdot 10^{11}}$/sec big duty cycle at fixed targs |
| **Antiprotons** | **14 GeV** | $\mathbf{5 \cdot 10^{10}}$ | ... |
| Dense nuclear matter | Up to 34 GeV/u Uranium **(with SIS-300)** | ... | $\mathbf{2 \cdot 10^{9}}$/sec big duty cycle |
| Plasma physics | Ions 0.4 – 1 GeV/u | $\mathbf{1 \cdot 10^{12}}$ | ... |
| Atomic physics | Ions 1 – 10 GeV/u | ... | $\mathbf{10^{9}}$/sec big duty cycle |

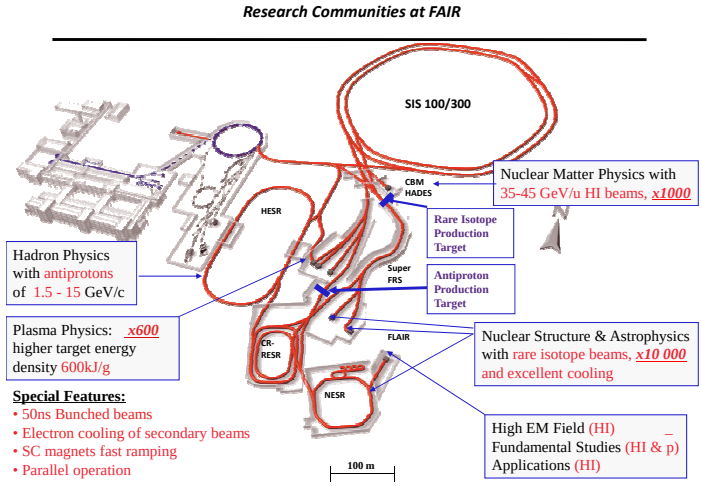


Fig. 1: The FAIR complex [1]. Existing GSI accelerators are shown at left in gray. Future elements (in colour) include the SIS100/300 heavy-ion synchrotron, the HESR ring, the CR and NESR rings, the superconductive separator Sup-FRS and the storage ring for nuclear fragments (NESR) as well as the main detectors PANDA and CBM. The UNILAC/SIS18 will serve as injector for SIS100/300

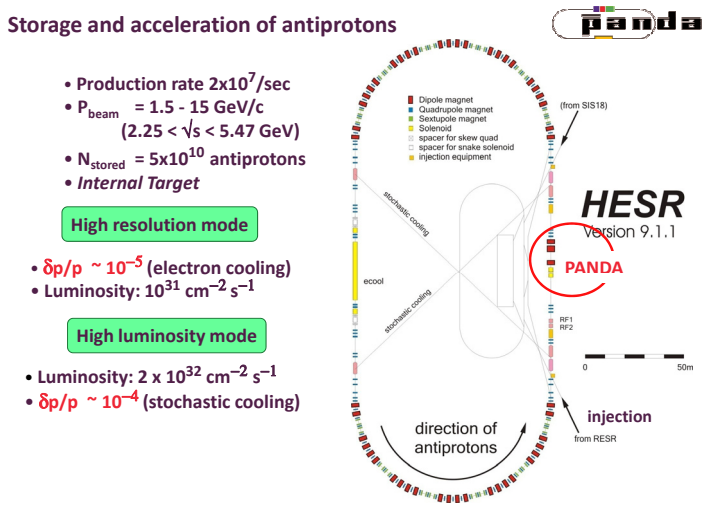


Fig. 2: Scheme of the HESR ring [2]. HESR will have systems of stochastic cooling of $\bar{p}$ up to $T_{kin} \approx 14$ GeV and $e^-$ cooling for $T_{kin} \leq 9$ GeV

## 2. $\overline{\text{P}}$ANDA for Physics of Strong Interactions

The $\overline{\text{P}}$ANDA Collaboration with more than 450 scientist from 17 countries intends to do basic research on various topics around the weak and strong forces, exotic states of matter and the structure of hadrons. The present $\overline{\text{P}}$ANDA physics program is presented in the "PANDA Physics Book" [4].

This program includes several directions, namely: **(1)** study of QCD bound states (i.e. charmonium spectroscopy, $D$-meson spectroscopy, gluonic excitations (hybrids, glueballs), (multi)strange and charmed baryons as shown in Fig. 3) what has fundamental importance for quantitative understanding of QCD; **(2)** non-perturbative QCD dynamics; **(3)** hadrons in the (finite) nuclear medium and, in particular, charmonia absorption in the nuclear matter and estimation of the charmonium-nucleon interaction; **(4)** physics of hypernuclei (including formation of hypernuclei containing two hyperons); **(5)** study of nucleon structure by detecting electromagnetic final states like $e^+e^-$ or $\mu^+\mu^-$ (what probes the electromagnetic form-

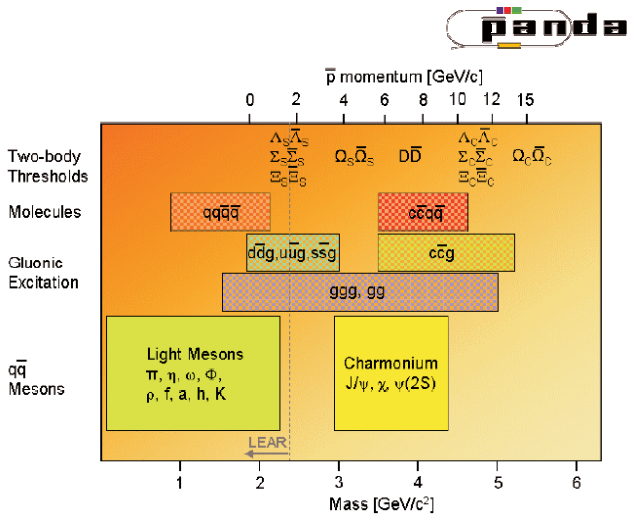


Fig. 3: QCD systems to be studied at $\overline{\mathrm{P}}$ANDA

factors in the time-like region) or the MMT-DY pairs (what gives an access to the structure functions) as well as probing of the "generalized distribution amplitudes" by detecting hard exclusive meson production (for example, the $\bar{p}+p \to \gamma\pi^0$ channel); **(6)** some aspects of the electroweak physics, including CP-violation processes.

There is a possibility to investigate productions of some of the listed QCD objects on short-range $NN$ correlations in nuclei either in subthreshold region or in the region forbidden for $\bar{p}$ interaction with free nucleon.

## 2.1. Charmonium

Open problems and questions concerning charmonium were discussed at this Conference by I.Denisenko in his talk about results from BES-III [5]; see also [6]. Therefore only two most important features of charmonium study with the $\overline{\mathrm{P}}$ANDA detector are outlined here.

**First,** in the $\bar{p}p$ annihilation all mesons, with any $J^{PC}$ quantum numbers can be formed, while in the $e^+e^-$ annihilation only $J^{\mathrm{PC}} = 1^{--}$ mesons can be produced from the virtual photon.

**Second,** the extraordinary beam monochromaticity (in the high resolution mode of the HESR) allows to perform scanning of the resonance line by the fine changing of the beam energy.

Indeed, let the cross section for the formation of a resonance with spin $J$ in the process $\bar{p}p \to \bar{c}c \to$ (final state) is given by the well known Breit-Wigner formula:

$$\sigma_{\rm BW} = \frac{2J+1}{4} \cdot \frac{\pi}{k^2} \cdot \frac{Br_{\rm in} Br_{\rm out} \Gamma_{\rm R}^2}{\left(E_{\rm cm} - M_{\rm R}\right)^2 + \Gamma_{\rm R}^2/4} \ , \qquad (1)$$

where $M_{\rm R}$ is the resonance mass, $\Gamma_{\rm R}$ is its total width, $Br_{\rm in}$ and $Br_{\rm out}$ are the branching ratios into the initial and final states and $E_{\rm cm}$ is the center-of-mass energy.

The number of detected final state events ($N_{\rm event}$) is a convolution of the cross section (2) and the beam energy spread function $f(E_{\rm cm}, \delta E_{\rm cm})$:

$$N_{\rm event} = \mathcal{L}_0 \left\{ \varepsilon \int dE_{\rm cm} \cdot f(E_{\rm cm}, \delta E_{\rm cm}) \cdot \sigma_{\rm BW}\left(E_{\rm cm}\right) + \sigma_{\rm bckg} \right\} \ , \quad (2)$$

where $\sigma_{\rm bckg}$ corresponds to background processes. It is obvious that parameters $M_{\rm R}$, $\Gamma_{\rm R}$ and the product $Br_{\rm in}Br_{\rm out}$ can be extracted by measuring the formation rate $N_{\rm event}$ for that resonance as a function of the c.m. energy $E_{\rm cm}$ provided the beam energy spread is much less than the $\Gamma_{\rm R}$. The fine scans of resonance lines allow to measure their masses with accuracy up to $\approx$ 100 KeV and widths up to $\approx$ 10 % because the beam monochromaticity $\Delta p/p \sim 10^{-5}$ corresponds to the mass uncertainty $\Delta M \sim 20$ KeV [7].

### 2.2. Non-perturbative QCD dynamics

Several physics problems are considered in the "PANDA Physics Book" [4] within this direction, in particlular the binary annihilation channel $\bar{p}p \to \bar{Y}Y$ into hyperon pairs. Some spin observables can be measured for this channel, including those for the $\bar{\Xi}\Xi$ case.

To the same direction belongs the old puzzle discovered at LEAR: strong violation of the OZI [8] rule in some channels of the $\bar{p}p$ annihilation at rest [9,10]. The strongest effect was observed in annihilation channels $\bar{p}p \to \phi\gamma$ and in the Pontecorvo reaction $\bar{p}d \to \phi n$

where the 4-momentum transfer to the meson squared is the biggest (in absolute value): the ratio of yields $R(\phi n/\omega n) = (156 \pm 29) \times 10^{-3}$. Similar observation exists for other Pontecorvo reactions with deuterons, namely $\bar{p}\,d \to K^+\Sigma^-$ and $\bar{p}\,d \to K^0\Lambda$, where the yield ratio $R(K^+\Sigma^-/K^0\Lambda) = 0.92 \pm 0.15$ while OZI-rule predicts for this ratio $\approx 0.012$. Another example concerns the $\bar{p}\,p \to \phi\phi$ channel: the measured cross section $\sigma(\phi\phi)_{\rm exp} \sim 4\ \mu$b while according the OZI rule it must be $\sigma\,(\phi\phi) = \sigma\,(\omega\omega)\tan^4\,(\theta - \theta_i) \approx 10\,$nb (here $\theta$, $\theta_i$ are the mixing angles). It is worthwhile to note that the $\sigma\,(\omega\omega)$ cross section was not measured yet and a theoretical estimate is used here.

To explain the observations, it was suggested the model of polarized strangeness sea in nucleons and some observable consequences were predicted [11]. But present data about the contribution to the nucleon spin from the strangeness sea show that, being negative, this contribution is rather small [12]: $(\Delta s + \Delta\bar{s})_{Q^2\to\infty} = (\hat{a}_0 - a_8)\,/3 = -0.08 \pm 0.01\,(\text{stat.}) \pm 0.02\,(\text{syst.})$.

$\overline{\rm P}$ANDA experiment can provide data to solve the puzzle by looking at $\bar{p}\,p \to (\phi\phi)\,,\ (\omega\omega)\,,\ (K^*K^*)\,,\ (\rho\rho)$ ... binary channels. In particlular, yield estimates for $\bar{p}\,p \to (\phi\phi)$ show that the best world statistics can be obtained within 1.5 hours of measurements (the expected rate is $\sim 2$ events/sec in high luminosity mode of the HESR) [13].

### 2.3. Hadrons in medium

The idea of modification of particle properties in nuclear medium is quite old. There are many well known examples for this (for example, neutron is stable in meduim while it is unstable in free space, the lifetime of hypernuclei differs from that of the free $\Lambda$ etc).

Studies of $\Delta$-excitations in nuclei and pion propagation in nuclear matter (as well as search for effects of poin condensate in nuclei) performed in 80's had shown existence of collective phenomena when pion propagates in nuclear medium [14] and stimulated ideas about possibility of partial restoration of the SU(4) symmetry in nuclear medium. One of important observations is that theoretical predictions made for infinite nuclear matter must be modified in application to the finite nuclear medium.

Annihilation of $\bar{p}$ in nuclei provides a way to study possible modification of $D\bar{D}$ spectra in nuclear medium. The reason for this is

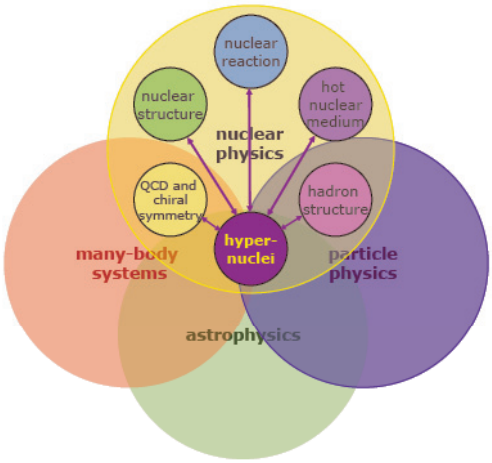


Fig. 4: Hypernuclear physics relations with other branches of physics

based on idea of partial restoration of chiral symmetry in nuclear medium as well as on present theoretical ideas that spectra of systems built from light quarks are sensitive to quark condensate (which may differ in nuclear matter from that in empty space) while spectra of $(\bar{c}\,c)$ systems are sensitive to gluon condensate [4], [15]. The "in-medium" mass can be reconstructed from di-leptons (in the $\bar{c}\,c$ case) or hadronic decays of the $D$-mesons.

In addition, the $\bar{p}A$ annihilation will be used as a tool for extracting experimental information about $J/\psi$-nucleon interaction.

### 2.4. Hypernuclei

Hypernuclei, i.e. systems where at least one nucleon is replaced by a hyperon ($Y$), allow access to a whole set of nuclear states with extra degree of freedom: the strangeness. There is a variety of consequences for different branches of physics (Fig. 4).

For example, as concerns nuclear physics: **(1)** probing of nuclear structure and its possible modifications due to the presence of a hyperon; **(2)** tests and experimental estimations of shell model parameters; **(3)** description of nuclear matter in terms of quantum field

theories and effective field theories (EFT). For particle physics the immediate output is for: **(1)** study of the $YN$ and $YY$ forces; **(2)** unified description of the baryon-baryon interaction in terms of potentials; **(3)** study of weak decays when $\Lambda \to \pi N$ is suppressed, but $\Lambda N \to NN$ and $\Lambda\Lambda \to NN$ are allowed (this gives access to study weak interaction between four baryons); **(4)** production of double hypernuclei with two $\Lambda$-hyperons; **(5)** production of hyperatoms (or multi-strange atoms); **(6)** use of hypernuclei as doorway to exotic quark states (like H-dibaryon).

## 3. Summary

The $\overline{\mathrm{P}}$ANDA experiment will use the antiproton beam from the HESR colliding with an internal proton (for a number of topics – nuclear) target and a general purpose spectrometer to carry out a rich and diversified hadron physics program.

The experiment is being designed to fully exploit the extraordinary physics potential arising from the availability of high-intensity, cooled antiproton beams. The aim of the rich experimental program is to improve our knowledge of the strong interaction and of hadron structure [4].

Significant progress beyond the present understanding of the field is expected due to drastic improvements in statistics and precision of the future data.

1. B. Sharkov, talk at the PANDA collaboration meeting (March 2010).
2. P. Montagna, talk at IFAE conference 2011, Perugia, Apr 11.
3. T. Keri for PANDA Collaboration: dedicated talk at this Conference.
4. PANDA Collaboration, "Physics Performance Report for PANDA: Strong Interaction Studies with Antiprotons" (PANDA Physics Book), arXiv:0903.3905v1 (2009); see also URL http://www-panda.gsi.de/framework/documents.php
5. I. Denisenko, talk at this Conference.
6. A. Gillitzer, in: Proceedings of the 11-th International Workshop on Meson Production, properties and Interactions (MESON 2010), ed. by A. Wronska, S. Kistryn, H. Machner, C. Guaraldo, Int. Jour. Mod. Phys. A **26**, 523 (2011).
7. A. Gillitzer, talk at the "QCD exotics" Conference, Bad Honnef, Jan. 17-21, 2005.

8. S. Okubo, Phys. Lett. B **5**, 165 (1963); G. Zweig, CERN Report No.8419/TH412 (1964); I. Iizuka, Prog. Theor. Phys. Suppl. 37, **38**, 21 (1966).

9. V.P. Nomokonov, M.G. Sapozhnikov, Physics of Elementary Particles and Atomic Nuclei **34**, 184 (2003); hep-ph/0204259, 2002.

10. C. Amsler, Rev. Mod. Phys. **70**, 1293 (1998); C. Amsler *et al.*, Phys. Lett. B **346**, 363 (1995); V.G. Ableev *et al.*, Nucl. Phys. A **594**, 375 (1995).

11. J. Ellis, M. Karliner, D. Kharzeev and M.G. Sapozhnikov, Phys. Lett. B **353**, 319 (1995); J. Ellis, M. Karliner, D. Kharzeev and M.G. Sapozhnikov, Nucl. Phys. A **673**, 256 (2000).

12. V.Yu. Alexakhin *et al.*, Phys. Lett. B **647**, 8 (2007).

13. M.G. Sapozhnikov, talk at ITEP seminar (Oct. 2008), unpublished.

14. V.G. Ableev *et al.*, **E1-83-486**, JINR, Dubna, 1983; C. Ellegaard *et al.*, Phys. Rev. Lett. **50**, 1745 (1983); see also reviews: V.G. Ableev *et al.*, in: Proc. of the Intern. Symposium on Modern Developm. in Nuclear Physics, June 27-July 1, 1987, Novosibirsk, ed. by O.P. Sushkov, World Sci. Singapore-New-Jers.-Hong-Kong, p. 690 (1988); E.A. Strokovsky *et al.*, Phys. Part. Nucl. **24**, 255 (1993) and references therein.

15. A. Hayashigaki *et al.*, Phys. Lett. B **487**, 96 (2000).

# JINR PARTICIPATION IN THE TUS AND NUCLEON SPACE EXPERIMENT PREPARATION

L. Tkachev, S. Biktemerova, V. Boreiko, N. Gorbunov, A. Grinyuk, V. Grebenyuk, A. Kalinin, D. Naumov, S. Porokhovoy, B. Sabirov, A. Sadovsky, A. Skrypnik, S. Slepnev, M. Slunecka, A. Tkachenko

*JINR, Dubna*

**Abstract**

The JINR team participates in a preparation of the two space experiments: TUS and NUCLEON, together with SINP MSU that is principal investigator and the other space organizations. The TUS space experiment is aimed to study energy spectrum, composition and angular distribution of the Ultra High Energy Cosmic Rays (UHECR) at $E \sim 10^{20}$ eV. The TUS mission is planned for operation at the end of 2011 at the dedicated "Mikhail Lomonosov" satellite. The main aim of the NUCLEON space experiment is the measurement of the cosmic rays flux, composition and a possible anisotropy in the energy range $10^{11}$–$5\times10^{14}$ eV. The NUCLEON mission is planned for operation at the end of 2013.

## 1. Introduction

The TUS space experiment is aimed to study energy spectrum, composition and angular distribution of the Ultra High Energy Cosmic Rays (UHECR) at $E \sim 10^{20}$ eV. The TUS mission is planned for operation at 2012 at the dedicated "Mikhail Lomonosov" satellite. The TUS detector will measure the fluorescence and Cherenkov light radiated by EAS of the UHECR using the optical system – Fresnel mirror-concentrator of 7 modules of $\approx 2$ m$^2$ area in total. A production of the flight model of the optical system is in progress. Status of

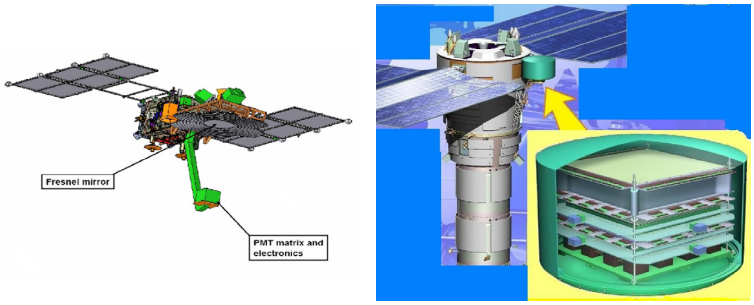


Fig. 1: Left: the TUS detector at the "Mikhail Lomonosov" satellite, right: scheme of NUCLEON detector at the RESURS type satellite

the Fresnel mirror production, the method and results of its optical parameters measurement are presented

The TUS project task is an experimental study of UHECR. The fluorescent and Cherenkov radiation of Extensive Air Showers (EAS) generated by UHECR particles will be detected at night side of the Earth atmosphere from the space platform at heights 400-500 km. It will make it possible to measure the CR spectrum, composition and arrival directions at $E > 7 \times 10^{19}$ eV beyond the GZK energy limit. There are two main parts of this detector: a modular Fresnel mirror and a matrix of PMTs with corresponding DAQ electronics. The SINP MSU (main investigator), JINR and Consortium "Space Regatta" together with several Korean and Mexican Universities are collaborating in the TUS detector preparation. The TUS mission is now planned for operation at the dedicated "Mikhail Lomonosov" satellite shown in Fig. 1.

Main TUS parameters are: mass $< 60$ kg, power consumption $\approx 65$ W, data rate 200 Mbytes/day (1 EAS event contains $\approx 80$ Kbytes), Field-of-View $\pm 4.5$ degree, number of pixels $16 \times 16$ (Hamamatsu type R1463 PMT: 13 mm tube diameter, multi-alcali cathode, UV glass window), pixel FOV $\approx 10$ mrad, Fresnel mirror area is 1.8 m$^2$, focal distance 1.5 m.

Photo detector and electronics consists of 256 PMT pixels with the time resolution 0.8 $\mu$s and the spatial resolution $5 \times 5$ km (for the orbit height of 500 km). The digital integrators allow us to use the same photo detector to study different phenomena in the atmosphere in

wide time interval: from $\sim 100$ $\mu$s (EAS) to 1 ms – 100 ms (transient luminous events, TLE) and up to 1 s (micrometeors). A prototype of such photo detector was tested during 2 years of "Universitetsky-Tatiana" mission [1].

In the TUS photo detector box the pinhole camera is added for study of TLE. The pinhole camera consists of multianode PMT and a hole at the focal distance from the PMT cathode. In design of the camera the multianode PMT of JEM-EUSO type is used [2]. The JEM-EUSO UV sensor will be tested in TLE data taking by the pinhole camera.

The main idea of this project is to develop a method and to design a scientific instrument being able to measure the Cosmic Ray (CR) flux, composition and a possible anisotropy in the energy range $10^{11}$–$5\times10^{14}$ eV with the high precision charge resolution. At the same time the principal condition is that this instrument should be relatively light (weight $< 200$ kg) and of small dimensions (size $<1.0$ m$^3$) to be of use on regular serial Russian satellites as an additional load. That makes possible long duration (5 years) regular flights and provides the rather low price of the project.

The NUCLEON charge range sensitivity is up to $Z \gg 30$. Such a measurement is motivated by the "knee" problem: change of the slope and composition in the cosmic ray energy spectrum from $E^{-2.7}$ to $E^{-3.0}$ at energies about $10^{15}$ eV and the CR anisotropy measurements in MILAGRO [3], ARGO YBJ [4], TIBET [5] and IceCube [6] at the 10–100 TeV energy intervals. The NUCLEON instrument is planned to be launched by the KOSMOS type satellite (Fig. 1) in 2013 with exposure time in orbit of about 5 years.

## 2. Status of the TUS Fresnel Mirror Production and Tests

The Fresnel mirror module prototypes were produced and tested in 2008-2009. The mirror module consists of the multilayer carbon plastic and aluminium honeycomb support to keep its properties stable in the day and night part of the space orbit cycle with the temperature difference of $\pm 80$ °C. In Fig. 2 the technological Fresnel mirror module and the fiducial net are shown inside of a thermo vacuum

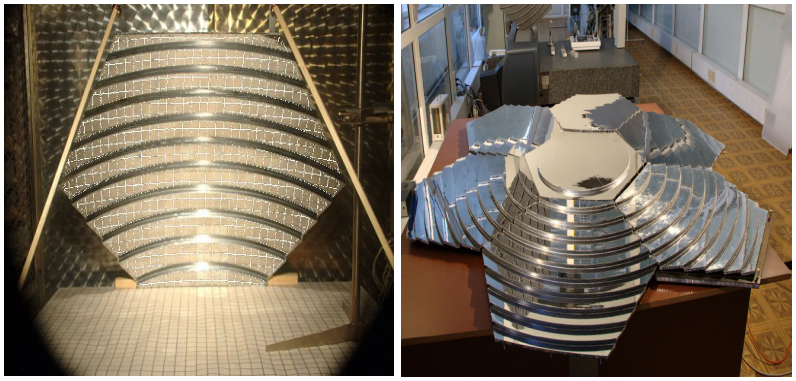

Fig. 2: Left: the mirror module test in thermo vacuum camera at temperature $\pm 80$ °C and pressure 0.02–1.0 atm. Right: the preassemble of the technological Fresnel mirror before tests

camera during tests at temperature $\pm 80$ °C and pressure 0.02–1.0 atm. The fiducial net reflection was used to check the mirror optical quality. The tests gave a positive result – no essential difference in the mirror properties was found. The image lines were obtained by the off-line reconstruction fit of reflected fiducial net lines to quantify deviations between expected and measured mirror surface.

The technological prototype of the segmented 7-module Fresnel mirror produced in 2010 is shown in Fig. 2. The mirror was successfully tested according to the space qualification requirements. Test devices with the mirror are presented in Fig. 3.

The main TUS collaboration task is production of flight model of the Fresnel mirror in 2011. The work is in progress: eight lateral and two central modules were fabricated and covered by reflective aluminium and protective $MgF_2$ layers. Various measurements of the optical parameters of the mirror modules were fulfilled. At the moment the flight TUS Fresnel mirror production is at the conclusive phase.

## 3. The Optical Parameter Measurements

The optical parameters measurement is the important part of the TUS preparation program. Results of this measurement are impor-

Fig. 3: The technological Fresnel mirror at space qualification tests

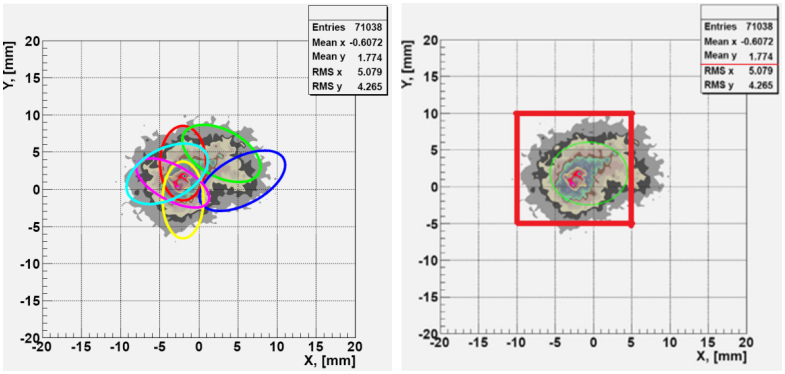


Fig. 4: The laser beam spot image distribution on the focal screen for the lateral Fresnel mirror modules (left panel) in comparison with the photo-receiver pixel size (right panel)

tant for future data analysis, especially for an evaluation of the systematic uncertainties. Also in this measurements the best mirror modules were selected among all produced ones.

The special procedure was elaborated to measure the mirror module optical parameters. The Eclipse 700/1000 coordinate measuring machine from Carl Zeiss, complimented by a laser head and a web camera, was used for the PSF (point spread function) measurements of the lateral and central TUS Fresnel mirror modules.

An example of the PSF measurement for the lateral Fresnel mirror modules is presented in the Fig. 4. The two-dimensional x, y-web

Fig. 5: Left: the PSF angular dependence of the lateral Fresnel mirror module. Right: the spot image distribution on the focal screen for the central mirror modules

camera coordinate plot of the laser beam images on the focal mirror plane is shown. The PSF parameters are by the definition RMSx and RMSy of this distribution which are RMSx = 5.1 mm and RMSy = 4.3 mm – both are reasonably inside of the photo receiver pixel size that is $15 \times 15$ mm$^2$.

The PSF dependence of angles between light source (parallel laser beams) direction and the mirror optical axis that is important for the EAS track image reconstruction on the PMT matrix was measured. An example of such dependence for the lateral mirror module is presented in the Fig. 5. The green and magenta ellipses correspond to PSF positions at $\varphi = 0^\circ$ and $\varphi = 45^\circ$ respectively and $\theta = 1^\circ$, $2^\circ$, $3^\circ$. $4^\circ$ those are angles between laser beam direction and optical axis, the blue ellipses correspond to PSF positions at $\varphi = 90^\circ$ and $\theta = 1.5^0$, $3.0^\circ$, $4.5^\circ$ etc. The PSF angular dependencies for the other lateral modules are similar.

## 4. The NUCLEON Space Experiment Preparation

The design, production and tests of the NUCLEON trigger system including the trigger electronics is the JINR responsibility including the FE and DAQ electronics to elaborate the 1-st and 2-nd level trigger signals. The trigger module consists of two X-, Y-planes of 16 scintillator strips and each plane is equipped by the pair of 1-channel PMTs and a 16-channel PMT.

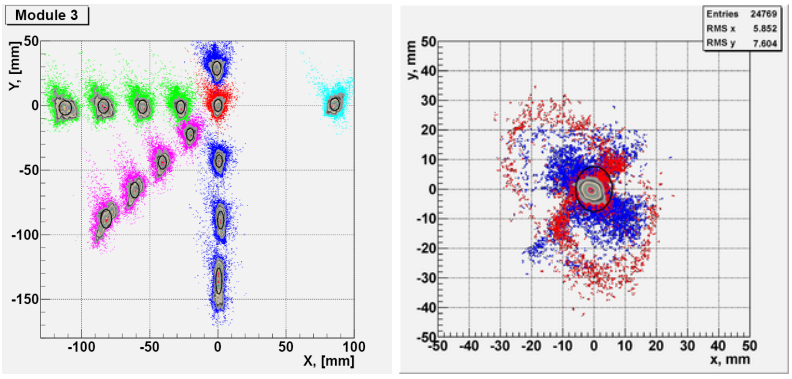


Fig. 6: Left: three modules of the NUCLEON flight trigger system prototype. Right: the technological NUCLEON detector at the design bureau "Arsenal" (St. Petersburg) test facility

The trigger system has a few levels of duplication to provide reliability during 5 years of the data taking in space. The prototype trigger system was produced and tested at the SPS CERN H2 test beams of the $\pi^-$ energy interval 200–350 GeV and of MIPs – halo muons. The conclusion is the trigger system technical parameters correspond to the initial requirements to the triggers of the 1-st and 2-nd levels: the tuning of the 1-channal PMT HV and the thresholds of the DAQ electronics give the possibility to suppress 350 GeV $\pi^-$-events down to $6\times10^{-5}$ as is needed for the NUCLEON experiment in space. The beam test result is shown in Fig. 7.

## 5. Conclusion

The technological TUS mirror was successfully tested in 2010 according to the space qualification requirements. The optical parameters of the flight mirror are in reasonable correspondence both with the Field-of-View of the TUS photo receiver as well as with the PMT pixel size. The TUS mission is planned for operation at the 2012 at the dedicated "Mikhail Lomonosov" satellite for 3 years of data taking [7].

The complex space qualification tests of the NUCLEON technological apparatus were fulfilled at the ARSENAL space center of

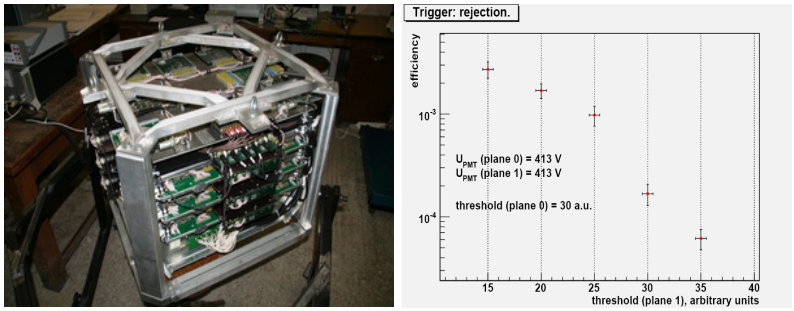


Fig. 7: Left: assembling of the technological NUCLEON detector prototype for the CERN SPS beam test. Right: result of the trigger efficiency system test at the 350 GeV $\pi^-$ beam

St. Petersburg in 2010 and at the SPS CERN H2 test beams afterwards which are presented in Fig. 6 and Fig. 7. The flight NUCLEON detector production is in progress including the micro calorimeter. The NUCLEON collaboration aim is to be ready for a launch and the data taking from orbit at the end of 2013.

1. V. Sadovnichi *et al.*, Cosmic Research **45**, 273 (2007).
2. Y. Takahashi and the JEM-EUSO Collaboration,New Journal of Physics, **11**, 065009 (2009).
3. MILAGRO collaboration, *32nd International Cosmic Ray Conference, Aug. 11-18, Beijing, China.*
4. ARGO_YBJ collaboration, *32nd International Cosmic Ray Conference, Aug. 11-18, Beijing, China. ID-0507.*
5. TIBET ASy collaboration, *32nd International Cosmic Ray Conference, Aug. 11-18, Beijing, China. ID-0379, ID-1167.*
6. IceCube collaboration, *32nd International Cosmic Ray Conference, Aug. 11-18, Beijing, China. ID-0305, 0306.*
7. M.I. Panasyuk *et al.*, *TUS Mission. Technological developments in Russia for JEM-EUSO collaboration*, this conference, ID 1261.

# PHYSICS AT HERA

Monica Turcato

*Universität Hamburg, Institut für Experimentalphysik*
*Luruper Chaussee 149, 22761 Hamburg, Germany*

**Abstract**

The H1 and ZEUS collaborations at the electron-proton collider HERA are publishing their final analyses based on the final statistics and on the combination of their data sets. These results are an important input to the determination of the proton structure to be used in the predictions for proton-proton processes at the LHC. The most recent results obtained at HERA on inclusive, jet and heavy flavour cross sections and their impact on the determination of the proton structure are discussed. The proton parton distribution functions (PDFs) determined using the HERA data as sole input are presented. Predictions for cross sections at the LHC based on these PDFs are shown.

## 1. Introduction

Since the end of data taking at the electron-proton collider HERA in June 2007, the two collaborations H1 and ZEUS are finalising their analyses using their full statistics. The main goal of the analyses is a deeper understanding of QCD and in particular of the proton parton distribution functions (PDFs). These are extremely important because of their large impact on the predictions of cross sections at the LHC. The HERA data cover a kinematic region in Bjorken $x$ corresponding to the rapidity plateau for the LHC processes. Therefore a precise measurement of the proton PDFs in the HERA region provides through DGLAP evolution accurate PDFs for the LHC regimes.

The cross sections of inclusive neutral- (NC) and charged-current (CC) deep inelastic $e^{\pm}p$ scattering (DIS) allow an accurate determination of the valence- and the sea-quark content of the proton, as well as of the gluon. A further improvement of the understanding of

the proton PDFs comes from other more exclusive QCD processes, like jet and heavy flavour production. The study of such exclusive processes allows on one hand the test of theoretical predictions based on fits using inclusive data only. On the other hand, the precision reached on these measurements is so high that they can be used as important input to QCD fits. The H1 and ZEUS collaborations are combining their results in order to achieve the best possible precision. In this paper, a selection of the most recent H1 and ZEUS combined results is presented.

## 2. Inclusive Measurements

Inclusive NC and CC DIS cross sections are measured at HERA to investigate the proton structure and to determine the proton PDFs. A combination of the H1 and ZEUS inclusive cross sections based on the data collected between 1994 and 2000 (HERA I running) has been published [2].

The combination of the data sets was done using a $\chi^2$ minimisation method [2]. The $\chi^2$ function takes into account the correlated systematic uncertainties for cross-section measurements, thus achieving a reduction of the systematic in addition to the statistical uncertainties. The combined cross sections are significantly more precise than the individual measurements over the whole kinematic range. The total uncertainty of the combined measurements is typically smaller than 2% for $3 < Q^2 < 500$ GeV$^2$ and reaches 1% for $20 < Q^2 < 100$ GeV$^2$, where $Q^2$ is the negative four-momentum squared of the intermediate boson. In Fig. 1 (left), the combined HERA I NC cross sections are shown separately for the $e^-p$ and the $e^+p$ data samples, and compared to theoretical predictions based on the HERAPDF1.0 PDF set (described below).

The HERA I combined H1 and ZEUS inclusive cross sections were used as the sole input to extract the HERAPDF1.0 PDF set [2]. The data at low $x$ determine the sea-quark and the gluon distributions while the large-$x$ data constrain the up and down valence quark distributions. Due to the accuracy of the input data, the HERAPDF1.0 PDFs have a precision of the order of a percent in the medium-$x$ region, which corresponds to the rapidity plateau region of the LHC

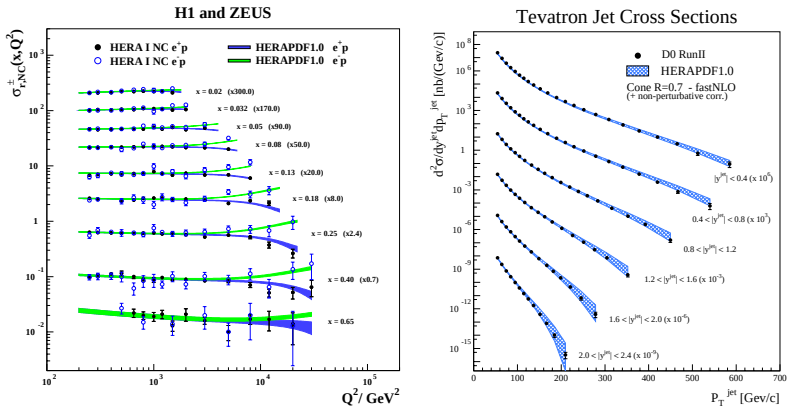


Fig. 1: Left: HERA I combined (H1 and ZEUS) NC cross sections for $e^-p$ and $e^+p$ interactions. Right: jet production at D0 compared with predictions obtained using HERAPDF1.0

measurements. To test the validity of the PDFs in a kinematic region not covered by the data used to extract them, predictions for jet production at the Tevatron were produced. The description of jet production at D0 [3] is good, as shown in Fig. 1 (right).

The statistical precision of the combined HERA I data is limited in the high-$x$ and high-$Q^2$ regions. The precision in this region can be significantly improved by adding the NC and CC cross sections measured using the data collected in the HERA II running period (2003–2007). This corresponds to a three-fold increase in the overall statistics and especially a 10-fold increase in the $e^-p$ data sample.

The combination of the HERA I and partial [4, 5] HERA II data samples has been recently released as a preliminary result [6]. The only missing data are the ZEUS NC $e^+p$ cross sections for HERA II [7] which were released after this combination was performed.

The improved precision of the HERA I+II combined data is clearly visible when Fig. 1 (left) is compared to Fig. 2 (left), where the HERA I and HERA I+II NC cross sections are shown. The uncertainties are visibly reduced in the high-$x$ and high-$Q^2$ regions. The data are compared with predictions based on the HERAPDF1.0, which describe the data well.

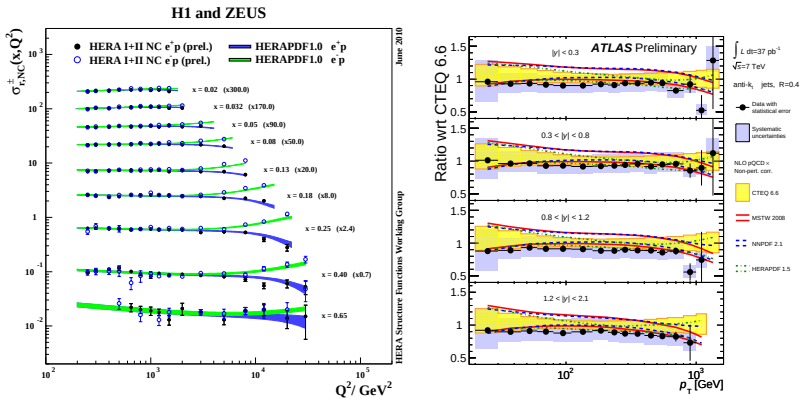


Fig. 2: Left: HERA I+II combined NC cross sections for $e^-p$ and $e^+p$ interactions. Right: ATLAS inclusive jet double-differential cross sections as a function of the jet $p_T$ in different central regions of rapidity $|y|$

The HERA I+II combined cross sections have been used as the sole input to extract the HERAPDF1.5 PDF set [8]. Predictions based on the HERAPDF1.5 are compared to jet cross sections measured at ATLAS [9] in Fig. 2 (right). The predictions based on the HERA data alone are able to well describe jet production at ATLAS.

## 3. Jet and Heavy Flavour Production

Although very precise proton PDFs can be obtained by using only inclusive NC and CC cross section measurements, the inclusion of jet and heavy flavour production can further improve the results. In this section, two recent results obtained using jet and charm data in the PDF fits are discussed.

### 3.1. Jet production and $\alpha_s$

The data sample used for the extraction of the HERAPDF1.5 PDF set was enlarged by including jet cross section measurements [10] to extract the PDF set HERAPDF1.6 [11]. The use of jet cross sections in the fit allows the simultaneous determination of the PDFs and the strong coupling constant, $\alpha_s$. This was not possible in the previous

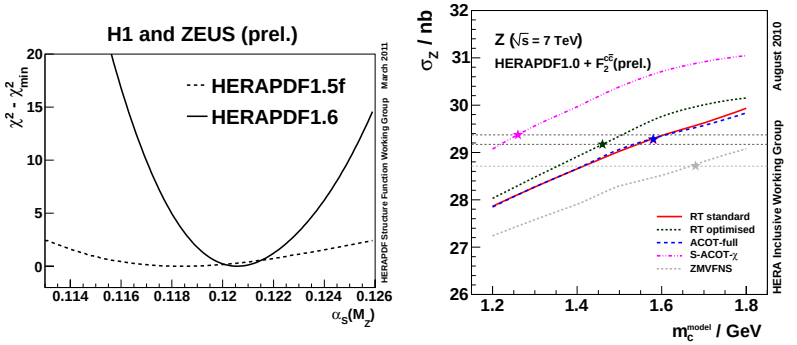


Fig. 3: Left: $\Delta\chi^2$ distribution as a function of $\alpha_s(M_Z)$ for the fit to the inclusive (HERAPDF1.5f) and inclusive+jet data samples (HERAPDF1.6). Right: $Z$ production cross section at the LHC for $\sqrt{s} = 7$ TeV as a function of $m_c^{\mathrm{model}}$

fits yielding HERAPDF1.0 and 1.5, as the correlation between the gluon PDF and $\alpha_s(M_Z)$ is too strong when inclusive data alone are used.

A new parameterisation of the PDFs was introduced in order to allow a greater flexibility in the gluon density. This helps to avoid a parameterisation bias when more data, which are sensitive to the gluon distribution, like jet production, are included. The fit to the NC and CC data as included in HERAPDF1.5, but using the new PDF parameterisation, is referred to as HERAPDF1.5f.

The power of the fits to determine $\alpha_s$ using inclusive or inclusive+jet data is well illustrated in Fig. 3 (left), where the $\chi^2$ of the HERAPDF1.5f and HERAPDF1.6 with free $\alpha_s$ is shown as a function of $\alpha_s(M_Z)$. The HERAPDF1.5f fit shows a shallow minimum, while the HERAPDF1.6 fit with the addition of the jet data provides a strong constraint on $\alpha_s$.

### 3.2. Charm production

The combined H1 and ZEUS measurement of the charm contribution to the proton structure function $F_2$, $F_2^{c\bar{c}}$ [12], was used to investigate the PDF fit formalism, in particular the role of the charm mass parameter in the different models [13] used by different groups of fitters. In all models, the threshold behaviour of heavy quarks is controlled

by the parameters $m_{c,b}^{\rm model}$. The charm data are sensitive to the value of $m_c^{\rm model}$ and to the scheme used for the treatment of heavy quarks in the PDF fits.

For each of the different heavy-flavour schemes, a fit to the combined $F_2^{c\bar{c}}$ data together with the published combined HERA I data was performed. In each implementation, an optimal value of $m_c^{\rm model}$ was determined corresponding to the best description of the data. The obtained values for $m_c^{\rm model}$ show a sizable spread, from 1.26 to 1.68 GeV. However, the description of the data is satisfactory in each of the schemes as long as the corresponding $m_c^{\rm model}$ is used.

Without the charm data, the available data could not be used to distinguish between different values of $m_c^{\rm model}$. Predictions for $W$ and $Z$ production at the LHC showed a sizable spread when $m_c^{\rm model}$ was varied between 1.2 and 1.8 GeV in order to estimate the prediction uncertainties due to the choice of this parameter, or when different schemes were considered at a fixed value of $m_c^{\rm model}$. The uncertainty on the prediction for $W$ and $Z$ can be significantly reduced when $m_c^{\rm model}$ is constrained by the HERA data and the optimal value of $m_c^{\rm model}$ is used in each model, as shown in Fig. 3 (right).

The inclusion of the $F_2^{c\bar{c}}$ measurements in the PDF fits can therefore help to reduce the uncertainties on the $W$ and $Z$ production cross sections at the LHC in a model-independent way.

### 3.3. HERAPDF1.7

Recently, a preliminary set of PDFs, HERAPDF1.7 [14], was released, extracted including inclusive, jet and charm data altogether. The quality of the fit confirms the consistency of the data between different measured processes. This is the first step towards a HERA fit including all possible precision information from inclusive and exclusive processes for the determination of the proton structure.

## 4. Conclusions

The H1 and ZEUS collaborations are combining their data in order to achieve the best possible precision in the measurement of inclusive neutral- and charged-current DIS cross sections, jets and heavy flavour processes. Precise sets of parton distribution functions have

already been published using the data collected during the HERA I data-taking period. Now, a better precision is provided by including the HERA II data and by including jets and heavy flavour measurements. The HERA proton PDFs provide reliable predictions for cross sections at the LHC.


1. Y. Stelmakh, A.N. Wall, Nucl. Phys. B **26**, 447 (1976).
2. H1 and ZEUS Coll., F.D. Aaron *et al.*, JHEP **1001**, 109 (2010).
3. D0 Coll., V.M. Abazov *et al.*, Phys. Rev. Lett., **101**, 062001 (2008).
4. H1 Coll., F.D. Aaron *et al.*, H1prelim-09-042;
   H1 Coll., F.D. Aaron *et al.*, H1prelim-09-043.
5. ZEUS Coll., S. Chekanov *et al.*, Eur. Phys. J. C **62**, 625 (2009);
   ZEUS Coll., S. Chekanov *et al.*, Eur. Phys. J. C **61**, 223 (2009);
   ZEUS Coll., H. Abramowicz *et al.*, Eur. Phys. J. C **70**, 945 (2010).
6. H1 and ZEUS Coll., F.D. Aaron *et al.*, H1prelim-10-141, ZEUS-prel-10-017.
7. ZEUS Coll., H. Abramowicz *et al.*, ZEUS-prel-11-003.
8. H1 and ZEUS Coll., F.D. Aaron *et al.*, H1prelim-10-142, ZEUS-prel-10-018.
9. ATLAS Coll., ATLAS-CONF-2001-047.
10. H1 Coll., F.D. Aaron *et al.*, Eur. Phys. J. C **65**, 363 (2010);
    H1 Coll., F.D. Aaron *et al.*, Eur. Phys. J. C **67**, 1 (2010);
    ZEUS Coll., S. Chekanov *et al.*, Phys. Lett. B **547**, 164 (2002);
    ZEUS Coll., S. Chekanov *et al.*, Nucl. Phys. B **765**, 1 (2007).
11. H1 and ZEUS Coll., F.D. Aaron *et al.*, H1prelim-11-034, ZEUS-prel-11-001.
12. H1 and ZEUS Coll., F.D. Aaron *et al.*, H1prelim-09-171, ZEUS-prel-09-015.
13. W.K. Tung, *et al.*, JHEP **02**, 053 (2007);
    M. Kramer, F.I. Olness, and D.E. Soper, Phys. Rev. D **62**, 096007 (2000);
    R.S. Thorne and R.G. Roberts, Phys. Rev. D **57**, 6871 (1998);
    R.D. Ball *et al.*, arXiv 1002:4407.
14. H1 and ZEUS Coll., F.D. Aaron *et al.*, H1prelim-11-143, ZEUS-prel-11-010.

# SEARCH FOR $\mu \to e\gamma$ DECAY MEG LATEST RESULT

Yusuke Uchiyama[1] for the MEG collaboration

[1]*ICEPP, the University of Tokyo*
*7-3-1 Hongo, Bunkyo-ku, Tokyo 113-0033, Japan*

**Abstract**

We present the new result of a search for the decay $\mu^+ \to e^+\gamma$ based on the data of muon decays collected by the MEG detector in 2009 and 2010. We performed a likelihood analysis on the combined data-set with a sensitivity of $1.6 \times 10^{-12}$ and set an upper limit on the branching ratio $\mathcal{B}(\mu^+ \to e^+\gamma) < 2.4 \times 10^{-12}$ at 90 % confidence level. This is five times stricter limit than the previous experimental limit.

## 1. Introduction

The conservation of lepton flavor in the standard model (SM) is considered to be accidental; it is just as a consequence of the absence of neutrino masses and there is no explicit gauge symmetry for it. Definitive observations of the neutrino oscillations now imply finite neutrino masses, hence a new physics where the lepton flavors are no longer conserved. Nevertheless, in the minimum extension of SM with finite but tiny neutrino masses, lepton-flavor violating processes in charged lepton sector (cLFV) are highly suppressed and out of experimental reach ($\mathcal{B} < 10^{-51}$). However, introduction of new physics such as supersymmetric grand-unified theories generally induces cLFV, possibly as large as the existing experimental limits [1,2]. Therefore, improving limits of cLFV would give stringent constrains on such models, while an observation of cLFV process can be a clear indication of new physics beyond the SM. The search for the decay $\mu^+ \to e^+\gamma$ gives one of the most stringent limits to such scenarios.

The existing limit is $\mathcal{B} < 1.2 \times 10^{-11}$ (90% CL) set by the MEGA experiment in 1999 [3]. The MEG experiment [4] at Paul Scherrer Institue (PSI) started physics data acquisition in 2008 aiming at the search for the decay down to the sensitivity of $O(10^{-13})$. The first result based on the initial three months data was reported in [5]. In this paper, we present a new result based on MEG data collected in 2009 and 2010.

The event signature of $\mu^+ \to e^+\gamma$ decay is characterized by kinematics of a simple two-body decay. The positron and photon are coincident in time, emitted back-to-back, and each of them has an energy of half of muon mass, 52.8 MeV. To use this kinematic signature, we experimentally use positive muons stopped in material. Using positive muons prevents nucleus in the material from forming muonic atoms. There are two kinds of backgrounds. One is a physics background from a radiative muon decay, $\mu^+ \to e^+\nu_e\overline{\nu}_\mu\gamma$ (RMD). It becomes a prompt background when the two neutrinos carry off little energy. However, the branching fraction to such phase space is highly suppressed, and it can be well under control with reasonable detector energy resolutions. The other is an accidental overlap of a high-energy positron from a normal muon decay, $\mu^+ \to e^+\nu_e\overline{\nu}_\mu$ (Michel decay) with an uncorrelated high-energy gamma ray from RMD, annihilation-in-flight of positron or bremsstrahlung. The rate of the accidental background can be written as $R_{acc} \propto (R_\mu)^2 \cdot f_e \cdot f_\gamma \cdot (\Delta\Theta_{e\gamma})^2 \cdot \Delta t_{e\gamma}$, where $R_\mu$ is an instantaneous rate of muon beam; $f_e$ and $f_\gamma$ are the positron and gamma ray background yield at the signal region shown in Fig. 1 and 2, respectively; $\Delta\Theta_{e\gamma}$ and $\Delta t_{e\gamma}$ are resolutions of angle and timing measurements, respectively. At our muon rate and with our detector resolutions, the accidental background becomes dominant. The keys of the experiment to suppress it are a continuous positive muon beam and precision detectors for positron and gamma ray with spatial, temporal, and energy resolutions.

## 2. Experimental Setup

We conduct the experiment at the $\pi$E5 beam-line in PSI accelerator facilities. The primary proton beam from the 590 MeV ring-cyclotron at a current of 2.2 mA has a time structure of 50 MHz.

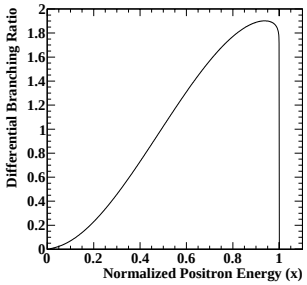


Fig. 1: Positron energy spectrum of Michel decay as a function of normalized positron energy $x = 2E_e/m_\mu$. Positron background yield around the signal energy ($x \approx 1$) is abundant

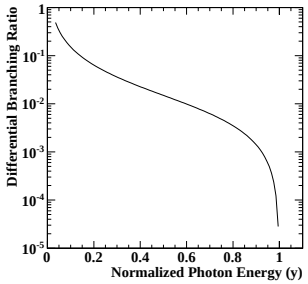


Fig. 2: Gamma ray energy spectrum from radiative muon decay as a function of normalized gamma-ray energy $y = 2E_\gamma/m_\mu$. The yield around the signal region ($y \approx 1$) is highly suppressed

It is fast enough compared to the muon lifetime, resulting in a constant decay rate of muon which is the best from the viewpoint of background suppression. The beam-line provides the world's most intense DC surface muons. The surface muons, which are fully polarized, are transported with being purified, focused, and degraded through the MEG beam transport system consisting of a Wien filter, triplet magnets, and beam transport solenoid, and finally stopped in a thin target composed of 205 $\mu$m polyethylene/polyester sheet. The remaining polarization of the decaying muon along the beam axis is measured to be $\langle P_\mu \rangle = -0.89 \pm 0.04$. The stopping rate is tuned in at $3 \times 10^7 \mu^+$/sec.

The MEG detector consists of a superconducting spectrometer and a liquid xenon (LXe) detector (Fig. 3). It covers about 10% of solid angle. Positrons are measured by the spectrometer, called COBRA (COnstant-Bending-RAdius), consisting of a superconducting magnets specially designed to form a highly graded magnetic field, a set of drift chamber system (DC) to measure the trajectory of positrons, and two sets of timing counters (TC) of plastic scintillators. The gradient field enables us to efficiently measure high-rate positrons by a preferential acceptance to high momentum as well as by quickly sweeping particles away from the tracking volume. The corresponding gamma rays emitted in the opposite side are detected by the LXe detector. Excellent properties of LXe such as high stop-

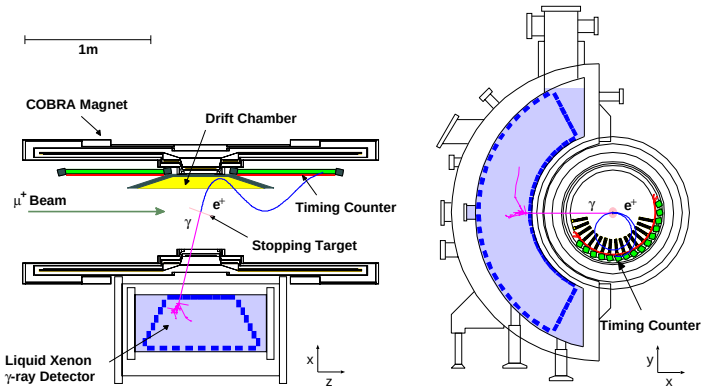


Fig. 3: Schematic of MEG detector

ping power, high light yield, fast response, and homogeneity fit our requirements. It measures the energy, timing, and position of incident gamma rays at the same time with 900-liter LXe as a scintillation medium and 846 photomultipliers directly immersed in LXe.

Measurement of Michel positrons gives us tools of calibration of the spectrometer; the precisely-known Michel spectrum, especially its kinematical edge, gives the energy scale and the momentum resolution; two-turn events are used to measure the angular resolution by comparing the angles at the matching point reconstructed independently with each turn. A part of each run was taken with negative pion beam and $LH_2$ target to produce neutral pions through the charge-exchange reaction. The decay $\pi^0 \to 2\gamma$ was measured to calibrate the LXe detector. Because of its kinematics, we can get almost monochromatic gamma rays at energies of 55 and 83 MeV by selecting events with the two gamma rays emitted back-to-back ($\theta_{\gamma\gamma} > 170^\circ$) with a tagging NaI detector placed at the opposite side of the LXe detector. They are used to measure the energy scale and the resolution. The relative time is calibrated with RMD which are time coincident events. The positions of intra-/inter-detectors are calibrated with cosmic rays as well as optical surveys of detector alignment. The performance of the detector is summarized in Table 1. An improvement of time resolution in 2010 was given by the upgrade of the electronics, while the worse tracking resolutions were due to an increase in noise in DC coming from the HV distributor.

**T a b l e 1: Summary of the performance**

| Dataset | $\sigma_{E_e}$ [a] (MeV) | $\sigma_{E_\gamma}$ [b] (%) | $\sigma_{t_{e\gamma}}$ (psec) | $\sigma_{\theta_{e\gamma}}/\sigma_{\phi_{e\gamma}}$ (mrad) | $\epsilon_e$ (%) | $\epsilon_\gamma$ (%) | $\mu^+$ [c] ($10^{13}$) |
|---|---|---|---|---|---|---|---|
| 2009 | 0.31 | 1.9/2.4 | 146 | 14.5/13.1 | 40 | 58 | 6.5 |
| 2010 | 0.32 | 1.9/2.4 | 122 | 17.1/14.0 | 34 | 59 | 11 |

[a] for the core component with fraction of 80(79)% for 2009(2010).
[b] for deep ($> 2$ cm) / shallow ($< 2$ cm) events from the detector surface.
[c] the total number of muons stopped on the target.

## 3. Analysis and Result

Observables used to discriminate signal from backgrounds are the following: gamma-ray energy ($E_\gamma$), positron energy ($E_e$), time difference of the two particles ($t_{e\gamma}$) and angle difference between gamma-ray direction and reverse direction of positron ($\theta_{e\gamma}$ and $\phi_{e\gamma}$ for polar and azimuthal angles, respectively). Events around the signal region in $(E_\gamma, t_{e\gamma})$-plane were hidden until the analysis was fixed. The detector calibration and performance evaluation were done using calibration samples and events outside the hidden box (sideband data). The backgrounds can also be estimated using sideband data: $t_{e\gamma}$-sideband for the accidental one and $E_\gamma$-sideband for the RMD one.

We estimate the number of $\mu^+ \to e^+\gamma$ signal ($N_{\rm sig}$), RMD ($N_{\rm RMD}$), and accidental background BG ($N_{\rm BG}$) in a pre-defined fit region with an unbinned maximum likelihood fit. The fit region is taken widely enough to estimate the background distributions. An extended maximum likelihood is build as,

$$\mathcal{L}(N_{\rm sig}, N_{\rm RMD}, N_{\rm BG}) = \frac{N^{N_{\rm obs}} e^{-N}}{N_{\rm obs}!} e^{-\frac{(N_{\rm RMD}-\langle N_{\rm RMD}\rangle)^2}{2\sigma^2_{\rm RMD}}} e^{-\frac{(N_{\rm BG}-\langle N_{\rm BG}\rangle)^2}{2\sigma^2_{\rm BG}}}$$
$$\times \prod_{i=1}^{N_{\rm obs}} \left( \frac{N_{\rm sig}}{N} \cdot S(\vec{x}_i) + \frac{N_{\rm RMD}}{N} \cdot R(\vec{x}_i) + \frac{N_{\rm BG}}{N} \cdot B(\vec{x}_i) \right), \qquad (1)$$

where $\vec{x}_i$ is a vector of the five observables for the $i$-th event, and $S$, $R$, and $B$ are probability density functions (PDFs) of signal, RMD, and BG, respectively. $N_{\rm obs}$ is the observed total number of events in the fit region, while $N = N_{\rm sig} + N_{\rm RMD} + N_{\rm BG}$ is the expected

one. $\langle N_{\rm RMD}\rangle (= 79.4)$ and $\langle N_{\rm BG}\rangle (= 881.7)$ are the numbers of RMD and BG events extrapolated from the sidebands together with their uncertainties $\sigma_{\rm RMD} (= 7.9)$ and $\sigma_{\rm BG} (= 15.1)$, respectively. The PDFs are obtained mostly from the experimental data on the event-by-event basis to incorporate the position-dependent LXe detector response and tracking quality for each positron as well as correlations among tracking variables. To compute a reduced one-dimensional confidence interval on $N_{\rm sig}$, a profile likelihood ratio [6] is formed as,

$$\lambda_{\rm p}(N_{\rm sig}) = \frac{\mathcal{L}(N_{\rm sig}, \hat{\hat{N}}_{\rm RMD}(N_{\rm sig}), \hat{\hat{N}}_{\rm BG}(N_{\rm sig}))}{\mathcal{L}(\hat{N}_{\rm sig}, \hat{N}_{\rm RMD}, \hat{N}_{\rm BG})} \ , \tag{2}$$

where $\hat{\hat{N}}_{\rm RMD(BG)}(N_{\rm sig})$ are given by the $N_{\rm RMD(BG)}$ that maximize the likelihood for fixed $N_{\rm sig}$ while single hat numbers are the best-fit values. This profile likelihood ratio is used as the ordering principle of the unified approach of confidence interval construction [7].

To convert $N_{\rm sig}$ to the branching ratio, we divide it by the effective total number of measured muon decays. To reduce the systematic uncertainty from the beam instability and the variation of detector condition, we use Michel decay and RMD acquired simultaneously with the physics data as the normalization channels. The results from the two channels, which have independent systematic uncertainties each other, are in good agreement and combined to give the normalization factor of the combined data-set (2009+2010), $\mathcal{B}(\mu^+ \to e^+\gamma) = N_{\rm sig}/(3.3 \pm 0.2) \times 10^{12}$.

The sensitivity of this search is defined as a median of upper-limit distribution over an ensemble of toy-MC experiments with null signal. The branching-ratio sensitivity at 90% CL is evaluated to be $1.6 \times 10^{-12}$. We confirmed this sensitivity with experimental data; we performed the likelihood analysis on several comparable analysis windows in $t_{e\gamma}$-sideband by shifting the reference of the time difference which give results of upper limits of $(1-3) \times 10^{-12}$.

We opened the hidden box when all the studies were completed. Figure 4 shows the event distributions inside the box for the combined data-set. Events with high signal likelihood in descending order of $S/(f_R R + f_B B)$, where $f_R = 0.1$ and $f_B = 0.9$ are the fractions of the RMD and BG events in the fit region, were carefully checked and no strange behavior of detectors was found for all those events.

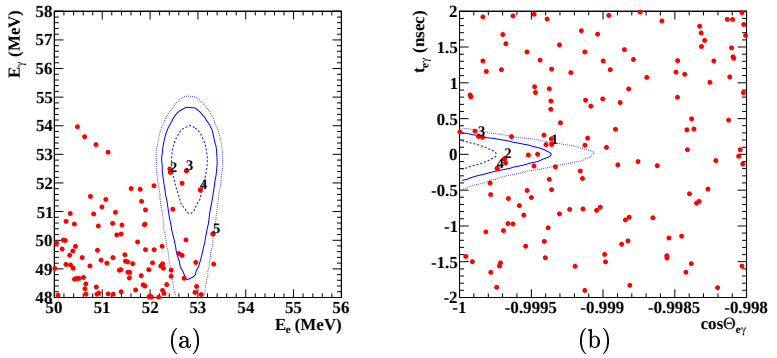


Fig. 4: Event distributions of combined data-set (a) in $(E_e, E_\gamma)$-plane after cuts on $\cos\Theta_{e\gamma}$ and $t_{e\gamma}$ with 90% efficiency for each are applied and (b) in $(\cos\Theta_{e\gamma}, t_{e\gamma})$-plane after cuts on $E_e$ and $E_\gamma$ with 90% and 73% efficiency respectively are applied, where $\Theta_{e\gamma}$ is opening angle between the two particle directions. The contours of signal PDF at 1-, 1.64-, and 2-$\sigma$ are superimposed. Events with the highest relative signal likelihood are numbered. Same events in the two plots are numbered correspondingly

The profile likelihood ratios of each data-set as well as the combined one are shown in Fig. 5. The 2009 data show some excess of events where the best-fit value is at $N_{\rm sig} = 3.4$ with the p-value for the null signal of 8%, whereas the 2010 data show the negative fluctuation of the background. The combined data are in good agreement with the background expectation. The confidence region is computed with taking into account possible systematic effects by fluctuating the PDFs and normalization factor for each toy-MC experiment in accordance with their uncertainty values. The impact on the shift of the branching ratio upper limit is about 2% in total: the largest contributions come from the uncertainties of the offsets of the relative angles, the correlations in the positron observables, and the normalization. The 90%-CL upper limit on the branching ratio is given as,

$$\mathcal{B}(\mu^+ \to e^+\gamma) < 2.4 \times 10^{-12} \quad (90\%\ \text{CL}). \tag{3}$$

This is a five times stricter constraint than that of previous experiment.

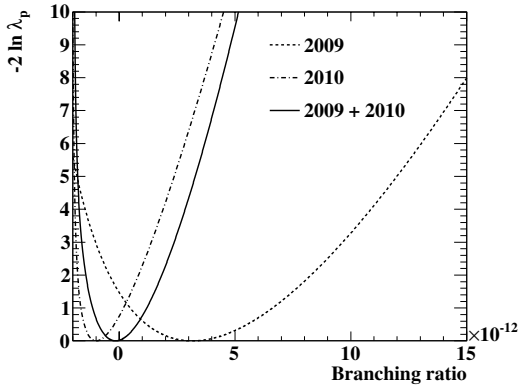


Fig. 5: Profile likelihood ratios as a function of $\mathcal{B}(\mu^+ \to e^+\gamma)$ for each data-set as well as the combined one

## 4. Conclusion

We searched for the unexplored region of the lepton-flavor violating decay $\mu^+ \to e^+\gamma$ with a sensitivity of $1.6 \times 10^{-12}$. The MEG 2009 and 2010 combined data are consistent with null signal hypothesis, and set a new constraint to the existence of the decay, $\mathcal{B}(\mu^+ \to e^+\gamma) < 2.4 \times 10^{-12}$ (90% CL). This is five times tighter than the previous limit.

MEG continues data acquisition at least until the end of 2012 and is expected to reach the sensitivity of a few times $10^{-13}$.

1. R. Barbieri, L. Hall and A. Strumia, Nucl. Phys. B **455**, 219 (1995).
2. J. Hisano *et al.*, Phys. Lett. B **391**, 341 (1997).
3. M.L. Brooks *et al.* [MEGA collaboration], Phys. Rev. Lett. **83**, 1521 (1999).
4. T. Mori *et al.*, Rerearch proposal to PSI, R-99-05 (1999), `http://meg.web.psi.ch/docs/`.
5. J. Adam *et al.* [MEG collaboration], Nucl. Phys. B **834**, 1 (2010).
6. K. Nakamura *et al.* (Particle Data Group), J. Phys. G **37**, 075021 (2010).
7. G.J. Feldman and R.D. Cousins, Phys. Rev. D **57**, 3873 (1998).

# BEYOND THE STANDARD MODEL SEARCHES AT THE TEVATRON

Sergey A. Uzunyan
on behalf of the DØ and CDF collaborations

*Department of Physics, Northern Illinois University, DeKalb, IL 60115, USA*

**Abstract**

We report on 2010-2011 searches for physics beyond the standard model from the DØ and CDF collaborations at the Tevatron. The analyzed data samples of $p\bar{p}$ collisions at a center-of-mass energy of 1.96 TeV correspond to an integrated luminosities of 4–9 fb$^{-1}$.

## 1. Introduction

Extensions of the standard model (SM) predict the appearance of new particles or of event excesses in final states rarely observed in the SM. New or improved limits were placed in searches conducted in 2010-2011 by the DØ and CDF collaborations for processes predicted by Extra Dimension theories, production of the fourth generation of quarks and neutrinos, and for processes resulting in final states with same sign leptons. We present also analyses that show deviations from the SM predictions: the observation of an unexpected peak in the dijet invariant mass distribution in the $W + 2jet$ final state, the measurement of the forward-backward asymmetry in $t\bar{t}$ production, and the measurement of the like-sign dimuon charge asymmetry.

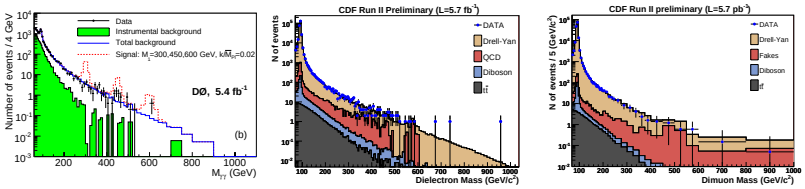


**(a)** **(b)** **(c)**

Fig. 1: The invariant mass distributions obtained in (a) D0 diphoton [1], (b) CDF dielectron [2], and (c) CDF dimuon [3] analyses.

## 2. Searches for Extra Dimensions

### 2.1. Randall-Sundrum gravitons in dilepton final states

The Randall Sundrum (RS) model proposes that gravity and the SM particle and fields are located in separate space branes and predicts spectra of the heavy graviton states. The graviton ($G$) production is parameterized by the $k/\overline{M}_{Pl}$ parameter, where $k$ is the curvature scale of the extra dimension and $\overline{M}_{Pl} = M_{Pl}/\sqrt{8\pi}$ is the reduced Plank scale. The RS-gravitons would preferably decay into photon or lepton pairs. The DØ and CDF collaborations study the $\gamma\gamma$, $ee$, or $\mu\mu$ invariant mass spectra in which RS-gravitons would appear as narrow resonances. These distributions obtained by the most recent analyses are shown in Figure 1. No resonances were observed and 95% C.L. limits on the mass of the lightest graviton were set for the spectra of $k/\overline{M}_{Pl}$ values (Figure 2). For $k/\overline{M}_{Pl} = 0.1$ RS-graviton masses are excluded up to 1050 GeV by the DØ analysis of diphoton and dielectron data samples [1], and up to 1111 GeV by the CDF searches in diphoton, dielectron and dimuon datasets [2, 3].

### 2.2. Randall-Sundrum gravitons in the diboson final states

RS-gravitons can also decay to boson pairs. Figure 3(a) shows the 95% C.L. limits on the graviton mass obtained by the DØ collaboration in the analysis of $G \to WW$ and $G \to WZ$ decays in the final states with two leptons, two jets and missing transverse energy $\not\!\!E_T$, or in the final state with three leptons and $\not\!\!E_T$ [4]. The RS-graviton mass is excluded in the 300–754 GeV region. The CDF collaboration analyzed the $G \to ZZ$ decay in the $ll + 2jet$, $ll + 2\nu$ and four

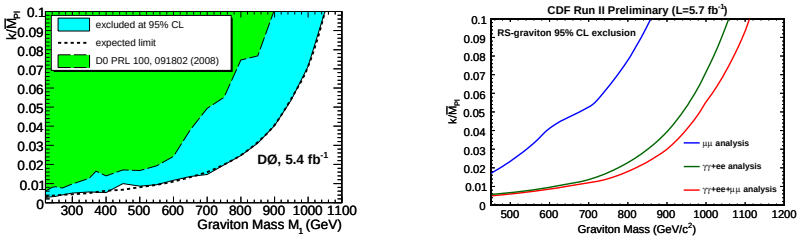


**(a)** **(b)**

Fig. 2: The two-dimensional exclusion regions in the $(k/\overline{M}_{Pl}, M_1)$ plane placed in: (a) combined $\gamma\gamma + ee$ analysis, D0 [1]; (b) combined $\gamma\gamma + ee + \mu\mu$ analysis, CDF [3].

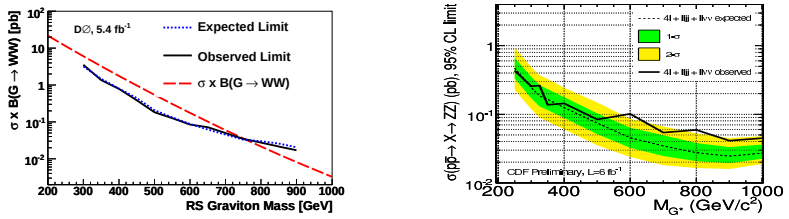


**(a)** **(b)**

Fig. 3: (a) The 95% C.L. limits on RS graviton production in $G \to WW$ channel as a function of the graviton mass, DØ [4]; (b) The 95% C.L. limits on $\sigma(p\bar{p} \to G \to ZZ)$, combined $4l$, $ll\nu\nu$, and $lljj$ final states, CDF [5].

lepton final states [5]. In the four-lepton mode four resonance-like events that correspond to the invariant mass of the $ZZ$ system near 325 GeV were found; analysis of the first two final states show agreement with the standard model predictions. Figure 3(b) shows the combined limits on the RS-graviton mass. The 95% C.L. observed and expected limits on the production cross section of RS-graviton with a mass of 325 GeV are 0.17 and 0.28 pb respectively.

### 2.3. Universal Extra Dimensions

Universal extra dimensions (UED) models assume that all SM fields can propagate to extra dimensions. The DØ collaboration studied the one extra dimension case that is compactified with radius $R_c$. In this model a pair of Kaluza-Klein photons can decay through gravitational

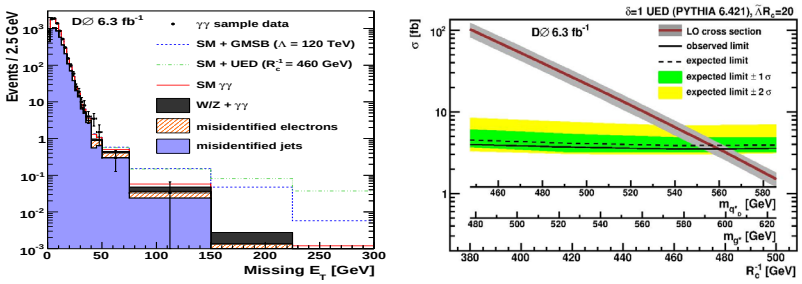


**(a)** **(b)**

Fig. 4: (a) The $\not\!\!E_T$ distributions for data, SM backgrounds and UED and GMSB signals, D0 [6] ; (b) The expected and observed 95% C.L. exclusion limits as function of the compactification radius $R_c^{-1}$ of the UED model.

interactions into photons and gravitons. Gravitons escape detection, resulting in $\gamma\gamma + \not\!\!E_T$ signature which was analyzed using 6.3 fb$^{-1}$ of DØ data [6]. The $\not\!\!E_T$ distribution of the $\gamma\gamma$ events is shown in Figure 4(a). The data are in agreement with the SM predictions and values of the compactification radius $R_c^{-1}$ were excluded below 477 GeV at 95% C.L, as shown in Figure 4(b). This analysis also places limits on the parameters of the gauge mediated supersymmetry breaking model (GMSB), in which the same signature appears as a result of processes with $\tilde{G}\gamma\tilde{G}\gamma$ final state if the gravitino is the lightest SUSY particle.

## 3. Searches for Fourth Generation Quarks and Neutrinos

There are a number of standard model extensions predicting fourth generation particles. For the fourth generation quarks it is assumed that they would have masses larger than the top quark mass and then, when decaying, produce event signatures similar to those from top quark decays. The fourth generation neutrino would be a mixture of unstable and stable mass eigenstates $N_2$ and $N_1$ (where the stable $N_1$ state may be the least massive fourth generation particle) that can be produced at the Tevatron via the $p\bar{p} \to Z/\gamma^* \to N_2N_2 \to N_1ZN_1Z$ process. Searches for pair productions of top ($t'$) and down ($b'$) fourth generation quarks were performed by CDF [7, 8] assuming $t'\bar{t} \to$

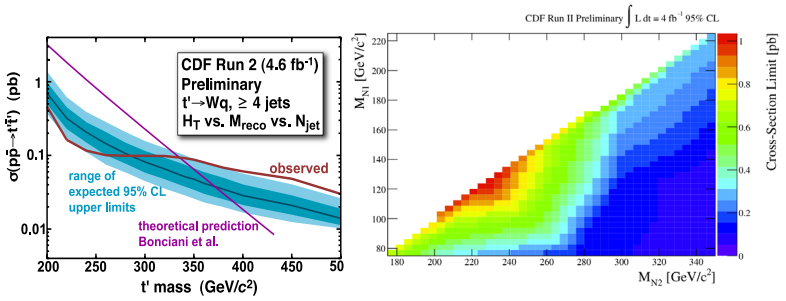


**(a)** **(b)**

Fig. 5: (a) The 95% C.L. limits on the pair production of the $4^{th}$ generation quarks $t'$, CDF [7]; (b) Plot of observed 95% C.L. cross section limits for spectrum of $M_{N2}$ and $M_{N1}$ mass points, CDF [10].

$WbW\bar{b} \rightarrow l\nu qqb\bar{b}$ and $b^{'}\bar{b}^{'} \rightarrow WtW\bar{t} \rightarrow WWbWW\bar{b} \rightarrow l\nu qq^{'}qq^{'}b$ decay cascades using respectively 4.8 fb$^{-1}$ and 5.6 fb$^{-1}$ data samples. In the $t^{'}$ analysis events were required to have exactly one high $p_T$ lepton, large $\not\!\!E_T$, and at least four energetic jets. One of these jets was required to be from $b$-quark decay ($b$-tagged). The $H_T = \sum_{jets} E_T + E_{T,l} + \not\!\!E_T$ and the reconstructed mass of the $t'$ were used to check for the presence of new high mass quarks. In the $b^{'}$ analysis events with a lepton ($e$ or $\mu$), $\not\!\!E_T > 20$ GeV at least five jets (one $b$-tagged) were selected and the $H_T$ was used as discriminator from SM top quark production. No excess of events over the SM predictions was observed and cross section limits at 95 % C.L. on the pair production of $t^{'}$, shown in Figure 5(a), and $b^{'}$ quarks were calculated. The production of fourth generation $t^{'}$ quarks with a mass below 358 GeV and $b'$ quarks with a mass below 372 GeV was excluded. A similar DØ search [9] for the $t^{'}$ quark using 5.6 fb$^{-1}$ data sample resulted in an exclusion of $M(t^{'})$ below 285 GeV.

Search for fourth generation neutrinos was conducted by the CDF collaboration using a 4.1 fb$^{-1}$ data sample [10]. The final state with two leptons, and two jets from $Z$ boson decay and large missing transverse energy was analyzed. No excess of data over the SM backgrounds were found and the 95% C.L limits were set of order 300 fb for the spectra of $M_{N1}$ and $M_{N2}$ mass points, shown in Figure 5(b).

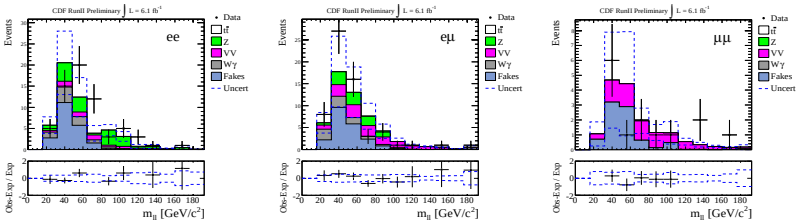


**(a)** **(b)** **(c)**

Fig. 6: The invariant mass distributions of $ee$ (a), $e\mu$ (b), and $\mu\mu$ (c) pairs, CDF [11].

# 4. Signature Based Searches in Rare SM Final States

## 4.1. Same-sign dileptons

The CDF collaboration performed a search for new physics in like sign dilepton events with a 6.1 fb$^{-1}$ dataset [11]. The results were examined via predictions of simplified SUSY or UED theories, same-sign top quark production models and the pair production of the generic doubly charged Higgs ($H^{++}$).

In the SM the like-sign signature is very rare, real like sign lepton events are largely from $WZ$ and $ZZ$ production. The dominant background comes from events in which the second lepton is due to the semi-leptonic decay of a $b$- or $c$-quark meson, largely from $W + jets$ production or $t\bar{t}$ production with semi-leptonic decays. The invariant mass distributions of $ee$, $e\mu$, and $\mu\mu$ pairs are shown in Figure 6. The $\not\!\!E_T$, $N_{jets}$, lepton $p_T$ and the $H_T$ were also examined. No deviation from the SM model predictions were observed and upper limits on the production cross section of the probed processes were calculated. Figure 7(a) shows the observed and expected limits on like-sign top quark production for the different chirality modes of the $tt$ pairs. Limits on supersymmetric quark production in the $(m_{\tilde{\chi}_1^{\pm}}, m_{\tilde{q}})$ plane are shown in Figire 7(b). Figire 7(c) shows the limit curves for the $H^{++} \to ee/e\mu/ee$ production. Depending on the theory model and the decay channel the $H^{++}$ analysis exclude m($H^{++}$) in the 190–245 GeV range.

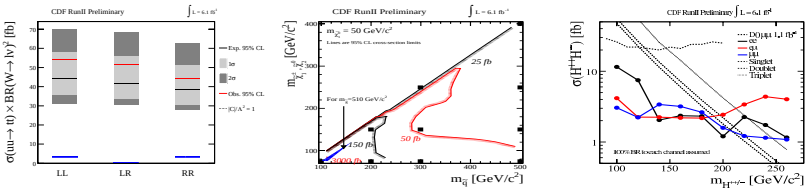


**(a)** **(b)** **(c)**

Fig. 7: Results of the CDF analyses [11] of the like sign dilepton events: (a) The observed and expected 95% limits on like-sign top quark production times for the different chirality modes of the $tt$ pairs; (b) The 95% limits on supersymmetric squark production in the $(m_{\tilde{\chi}_1^\pm}, m_{\tilde{q}})$ plane; (c) The 95% limit curves on the $H^{++} \to ee/e\mu/ee$ production cross section.

### 4.2. SUSY dileptons with taus

The CDF collaboration also analyzed the same sign dileptons final states with one hadronically decaying tau lepton using a 6.0 fb$^{-1}$ data sample [12]. This mode is important for SUSY models that allow the process $q\bar{q} \to \tilde{\chi}_1^\pm + \tilde{\chi}_2^0 \to \tilde{\tau}^\pm \nu_l + \tilde{l}^+ l^- \to \tilde{\chi}_1^0 \tau^\pm \nu_l + \tilde{\chi}_1^0 l^+ l^-$ where the decay of charginos and neutralinos to taus is dominant and $\tilde{\chi}_1^0$ is the stable lightest SUSY particle. The trilepton events with opposite signs leptons were used to validate the dominant SM backgrounds ($Z \to \tau\tau$ and $W + jets$), and the selection sensitivity to the same sign lepton events was optimized using a $\not\!\!E_T$ cut tuned for each $(M_{\tilde{\chi}_1^\pm}, M_{\tilde{\chi}_2^0})$ signal point. Figure 8(a) shows the $\not\!\!E_T$ distributions for the events with same sign $\tau\mu$ and $\tau e$. With a good agreement between data and backgrounds a 95% C.L. limits on signal production cross section were obtained for the analyzed SUSY models. Figure 8(b) shows the limit contours for the Simplified Gravity Model assuming $M_{\tilde{\chi}_1^0}$=120 GeV and Br$(\tilde{\chi}_1^\pm \to \tilde{\tau}^\pm + X)$=100%.

## 5. Tevatron Results Deviating from SM Predictions

### 5.1. Heavy resonance in the $W + 2jet$ final state

In the beginning of 2011 the CDF collaboration observed a peak in the dijet invariant mass distribution in the $W + 2jet$ final state us-

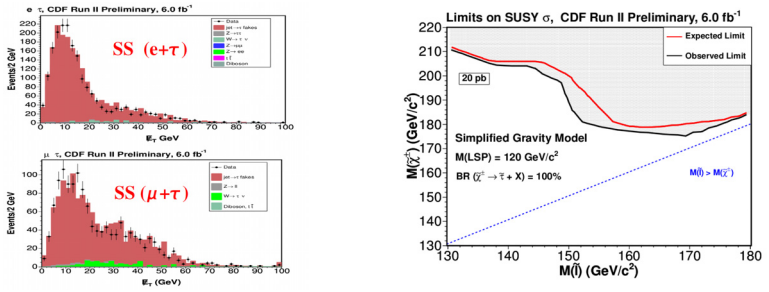


**(a)** **(b)**

Fig. 8: (a) The $\not\!\!E_T$ distributions for the events with same sign $\tau\mu$ (top) and $\tau e$ (bottom), CDF [12]; (b) The 95 C.L limit contours for the Simplified Gravity Model with $M_{\tilde{\chi}_1^0}$=120 GeV and Br($\tilde{\chi}_1^{\pm} \to \tilde{\tau}^{\pm} + X$)=100%.

ing 4.3 fb$^{-1}$ of data [13]. The number of events in the peak exceed the SM predictions by $3.2\sigma$ and can be assigned to production of an unknown particle $X$ with a mass near 145 GeV via $p\bar{p} \to XW$. This analysis has been later updated based on a 7.3 fb$^{-1}$ data sample [14], the obtained dijet invariant mass distribution is shown in Figure 9(a). The significance of the excess increased to $4.2\sigma$ with the estimated production cross section of $X$ particle of 3.0±0.7 fb. The D0 collaboration analyzed a 4.3 fb$^{-1}$ [15] dataset with selection criteria similar to those that were used in the CDF searches but does not confirm the result. No excess was observed and limits on the cross section were set as a function of $M_X$, shown in Figure 9(b). For $M_X = 145$ GeV DØ excludes production cross sections above 1.9 fb at 95% confidence level.

### 5.2. Forward-Backward asymmetry in $t\bar{t}$ production

The CDF and DØ experiments study the $t\bar{t}$ production asymmetry $A_{fb} = (N_f - N_b)/(N_f + N_b)$ where $N_f$ is the number of events with positive rapidity difference $\Delta y = y_t - y_{\bar{t}}$ between the top and anti-top quarks, and $N_b$ is the number of events with $\Delta y < 0$. The SM predicts a small positive asymmetry confirmed by the earlier measurements based on 1 fb$^{-1}$ datasets [16]. However in the 5.3 fb$^{-1}$ analysis of $t\bar{t}$ production in the lepton+jets channel [17] CDF found a $3.4\sigma$ discrepancy between measured $A^{fb} = 0.475 \pm 0.114$ and pre-

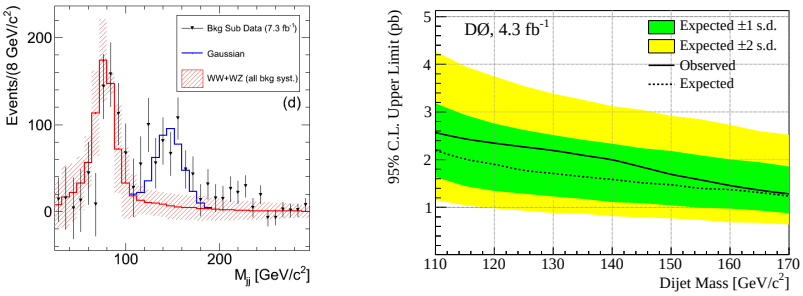


**(a)** **(b)**

Fig. 9: (a) The dijet invariant mass distribution, CDF [14]; (b) DØ limits [15] on the cross section for an excess as a function of dijet mass.

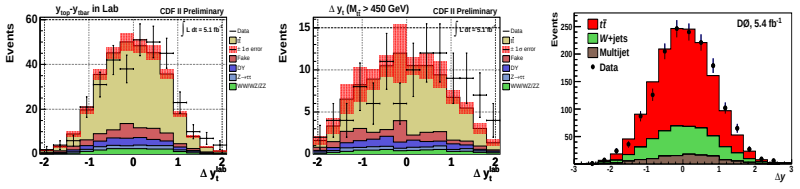


**(a)** **(b)** **(c)**

Fig. 10: (a),(b): Distributions of $\Delta y$ in $t\bar{t}$ events from CDF dilepton analysis [18] for $M_{t\bar{t}} < 450$ GeV and $M_{t\bar{t}} > 450$ GeV; (c) Distributions of $\Delta y$ from DØ [19] lepton+jets analysis.

dicted $A_{fb} = 0.088 \pm 0.013$ asymmetries. The asymmetry is larger for the subsets of events with the reconstructed $t\bar{t}$ mass, $M_{t\bar{t}}$, greater than 450 GeV and with large $\Delta y$. The recent CDF analysis of the $t\bar{t}$ production in the dilepton channel using a 5.1 fb$^{-1}$ dataset [18] reports a deviation of $2.3\sigma$: $A_{fb}(\text{measured}) = 0.42 \pm 0.15 \pm 0.05$, to be compared with $A_{fb}(\text{predicted}) = 0.06 \pm 0.01$. Again a larger asymmetry is observed at $M_{t\bar{t}} > 450$ GeV. In the DØ lepton+jets analysis of a 5.4 fb$^{-1}$ dataset [19] the measured $A_{fb}$ asymmetry disagree with SM predictions by up to $3\sigma$ but with no dependencies on $M_{t\bar{t}}$ or $\Delta y$. The distributions of $\Delta y$ from the CDF dilepton and from the DØ lepton+jets analyses are shown in Figure 10.

### 5.3. Dimuon charge asymmetry

The DØ collaboration updated the measurement [20] of the like-sign dimuon charge asymmetry in semi-leptonic decays of $b$ hadrons, $A_{sl}^b \equiv (N_b^{++} - N_b^{--})/(N_b^{++} + N_b^{--})$ using a 9.0 fb$^{-1}$ data sample [21]. $N_b^{++}$ and $N_b^{--}$ are the number of events containing two positively charged or two negatively charged muons, respectively, both of which are produced in prompt semi-leptonic $b$-hadron decays. The result, $A_{sl}^b = -0.787 \pm 0.172 \pm 0.093$ differs by $3.9\sigma$ from the $A_{sl}^b = (2.3 \pm 0.6) \times 10^{-4}$ prediction of the standard model, and provides evidence for anomalously large CP violation in semi-leptonic neutral $B$ decay.

## 6. Summary

Searches for physics beyond the standard model were performed in 4–9 fb$^{-1}$ data samples by the CDF and DØ collaborations. The measurements of the forward-backward asymmetry in $t\bar{t}$ production and of the like-sign dimuon charge asymmetry that deviate from the standard model predictions can be a signs of new physics, but need to be confirmed with the full Tevatron datasets analyses and results from the LHC experiments. The dijet invariant mass distribution peak is not confirmed by the DØ . Presented searches for the SM extensions show no excess in the analyzed final states and a set of 95% C.L. limits on the masses of the new particles and on the parameters of the examined models are obtained improving previous Tevatron results. The complete documentation on DØ and CDF BSM analyses can be found, respectively, at [22] and [23].

### Acknowledgements

We thank the staffs at Fermilab and collaborating institutions, and acknowledge support from the DOE and NSF (USA); CEA and CNRS/IN2P3 (France); FASI, Rosatom and RFBR (Russia); CNPq, FAPERJ, FAPESP and FUNDUNESP (Brazil); DAE and DST (India); Colciencias (Colombia); CONACyT (Mexico); KRF and KOSEF (Korea); CONICET and UBACyT (Argentina); FOM (The Netherlands); STFC and the Royal Society (United Kingdom); MSMT and GACR (Czech Republic); CRC Program and NSERC (Canada);

BMBF and DFG (Germany); SFI (Ireland); The Swedish Research Council (Sweden); and CAS and CNSF (China).

1. V.M. Abazov *et al.* (D0 Collaboration), Phys. Rev. Lett. **104**, 241802 (2010).
2. T. Aaltonen *et al.* (CDF Collaboration), Phys. Rev. Lett. **107**, 051801 (2011).
3. T. Aaltonen *et al.* (CDF Collaboration), Public Note 10479 (2011).
4. V.M. Abazov *et al.* (D0 Collaboration), Phys. Rev. Lett. **107**, 011801 (2011).
5. T. Aaltonen *et al.* (CDF Collaboration), Public Note 10163 (2011).
6. V.M. Abazov *et al.* (D0 Collaboration), Phys. Rev. Lett. **105**, 221802 (2010).
7. T. Aaltonen *et al.* (CDF Collaboration), Public Note 10395 (2011).
8. T. Aaltonen *et al.* (CDF Collaboration), Phys. Rev. Lett. **106**, 141803 (2010).
9. V.M. Abazov *et al.* (D0 Collaboration), Phys. Rev. Lett. **107**, 082001 (2010).
10. T. Aaltonen *et al.* (CDF Collaboration), Public Note 10539 (2011).
11. T. Aaltonen *et al.* (CDF Collaboration), Public Note 10464 (2011).
12. T. Aaltonen *et al.* (CDF Collaboration), Public Note 10611 (2011).
13. T. Aaltonen *et al.* (CDF Collaboration), Phys. Rev. Lett. **106**, 171801 (2011).
14. http://www-cdf.fnal.gov/physics/ewk/2011/wjj/7_3.html
15. V.M. Abazov *et al.* (D0 Collaboration), Phys. Rev. Lett. **107**, 011804 (2011).
16. V.M. Abazov *et al.* (D0 Collaboration), Phys. Rev. Lett. **100**, 142002 (2008); T. Aaltonen *et al.* (CDF Collaboration), Phys. Rev. Lett. **101**, 202001 (2008).
17. T. Aaltonen *et al.* (CDF Collaboration), Phys. Rev. D **83**, 112003 (2011)..
18. T. Aaltonen *et al.* (CDF Collaboration), Public Note 10436 (2011).
19. V.M. Abazov *et al.* (D0 Collaboration), arXiv:1107.4995 [hep-ex].
20. V.M. Abazov *et al.* (D0 Collaboration), Phys. Rev. D **82**, 032001 (2010); V.M. Abazov *et al.* (D0 Collaboration), Phys. Rev. Lett. **105**, 081801 (2010).
21. V.M. Abazov *et al.* (D0 Collaboration), Phys. Rev. D **84**, 052007 (2011).
22. http://www-d0.fnal.gov/Run2Physics/WWW/results/np.htm
23. http://www-cdf.fnal.gov/physics/exotic/exotic.html

# ATLAS OVERVIEW

A. Ventura[1]
on behalf of the ATLAS Collaboration

[1] *University of Salento and INFN Sezione di Lecce, via per Arnesano, 73100 Lecce, Italy*

**Abstract**

An overview of the ATLAS experiment running at the LHC is given. The detector main features are described, together with the reconstruction and trigger performance. Some results of searches for new phenomena beyond the Standard Model based on data collected during 2011 are briefly discussed as examples of the unprecedented ATLAS physics performance.

## 1. Introduction

The ATLAS experiment (A Toroidal LHC ApparatuS) [1] is a multi-purpose experiment running at the LHC (Large Hadron Collider), the main accelerator facility at CERN, the European Laboratory for Particle Physics in Geneva, Switzerland. At its design luminosity ($10^{34}$ cm$^{-2}$s$^{-1}$), the LHC will provide 23 inelastic proton-proton collisions for each bunch crossing at a center-of-mass energy of 14 TeV (presently this project value is set to 7 TeV).

The ATLAS program aims to reach important results over a wide range of physics processes, starting from known Standard Model processes (QCD, B-physics, gauge bosons, top quark, di-bosons) toward unknown processes predicted at (very) low cross-sections, such as Higgs searches, and other phenomena Beyond the Standard Model (BSM), like new $W'$ or $Z'$ bosons, Supersymmetry, Extra Dimensions and other Exotic physics processes. Two examples of searches for di-object resonances will be provided, to give an idea of the excellent detector performance in direct searches for new particles.

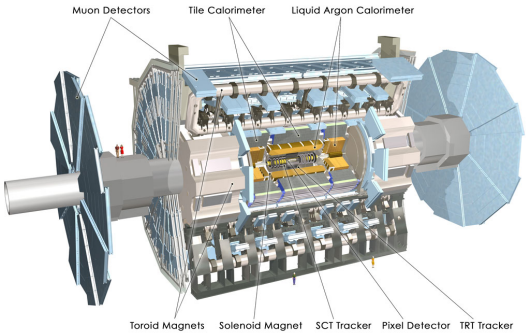


Fig. 1: A schematic view of the ATLAS detector

## 2. The ATLAS Detector

The detector of the ATLAS experiment is composed of concentric shells of specialized sub-detectors arranged in a cylindrical symmetry around the beam axis: an inner tracking detector inside a solenoidal magnetic field of about 2 T, a calorimetric system for energy measurements and a large air-core muon spectrometer that extends for about 44 m in length and 25 m in diameter. The detector has been designed to achieve high granularity, full coverage in solid angle, fast response and readout, radiation hardness especially near the interaction point. Its structure is shown in Fig. 1: the inner part of the apparatus is made up of a Pixel detector, a Silicon Central Tracker (SCT) and a Transition Radiation Tracker (TRT) which ensure a highly precise vertex reconstruction ($\sim$15 $\mu$m in the transverse plane) and transverse momentum ($p_T$) resolution ($\sigma_{p_T}/p_T \simeq 0.038\% p_T \oplus 1.5\%$). The electromagnetic (EM) calorimeter is made up of a liquid-Argon (LAr) based detector with accordion-shaped kapton electrodes and lead absorber plates; it is surrounded by a hadronic (Had) calorimeter which uses plastic scintillating tiles in the central region and additional liquid-Argon for higher $|\eta|$ (Fwd) with tungsten or copper absorber. Both calorimeters allow for very efficient particle identification and very good energy resolution up to $|\eta| < 4.9$: $\sigma_E/E \simeq 10\%/\sqrt{E} \oplus 0.7\%$ (EM) and $\sigma_E/E \simeq 50\%/\sqrt{E} \oplus 3\%$ (Had). The Muon Spectrometer is composed of four different types of gas-based chambers: Monitored

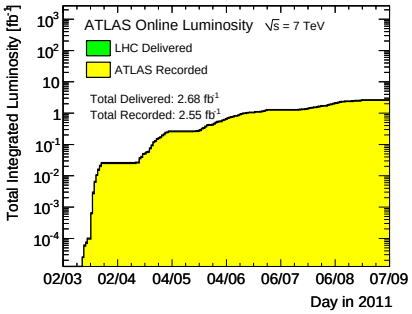


Fig. 2: Integrated luminosity collected by ATLAS until September 2011

Drift Tubes (MDT), Resistive Plate Counters (RPC), Cathode Strip Chambers (CSC) and Thin Gap Chambers(TGC); it is able to identify and reconstruct muon tracks up to $|\eta| < 2.7$ with a relative $p_T$ resolution better than 10% up to 1 TeV.

The experiment recorded about 45 $\text{pb}^{-1}$ of proton-proton collisions in 2010. Data taking resumed in March 2011, with a gradually increasing peak luminosity (reaching $2.5 \times 10^{33}$ $\text{cm}^{-2}\text{s}^{-1}$ by the summer). The total integrated luminosity at the time of writing is more than 2.5 $\text{fb}^{-1}$ (Fig. 2). In 2012, the LHC plans to continue to run in similar conditions at the same center-of-mass energy and then, after a long shutdown, a new run is foreseen at higher energy.

The ATLAS experiment collects the data delivered by the LHC with very high efficiency, as shown in Table 1, and the operational fractions for every single subdetector are very close to 1. Inefficiencies in the liquid-Argon calorimeters have been properly taken into account in the various physics analyses and have been partly recovered in the reprocessing of the data. The magnets were not operational for a 3-day period at the start of data taking in 2011. The exact data selection criteria applied depend on the subdetectors needed for each

**Table 1: Data taking efficiency, expressed in percentage, of all the ATLAS subdetectors during 2011**

| Inner Trackers | | | Calorimeters | | | |
|---|---|---|---|---|---|---|
| Pixel | SCT | TRT | LAr EM | LAr Had | LAr Fwd | Tile |
| 99.9 | 99.8 | 100 | 89.0 | 92.4 | 94.2 | 99.7 |

| Muon Detectors | | | | Magnets | |
|---|---|---|---|---|---|
| MDT | RPC | CSC | TGC | Solenoid | Toroid |
| 99.8 | 99.7 | 99.8 | 99.7 | 99.3 | 99.0 |

physics analysis: for this reason there are different possible selections of collected data, based on the quality of the data recorded by the subdetectors of interest.

The ATLAS trigger and data acquisition system, although designed to acquire 200 Hz, is presently capable of supporting a rate as high as 400 Hz. Especially depending on the increasing luminosity and on the purposes of the physics analyses, which can evolve as time passes, the definition of the *trigger menus* in ATLAS is very flexible and is continuously updated. During 2011, the *primary* triggers for each type of object have been based on increasing lowest unprescaled $p_T$ thresholds: for instance this is presently set to 22 GeV for electrons, 20 GeV for muons, 80 GeV for photons, 240 GeV for jets, 60 GeV for missing $E_T$. Tighter triggers will be used as the luminosity increases in the future. Reconstruction of raw data is first made at Tier-0 (CERN) and the outputs are then distributed to Tier-1 centers for physics analysis. At the end of every single run, a subset of the data is analyzed for calibration purposes in a fixed 36-hours period, after which the full reconstruction is performed. Finally, the data become available on the grid in usually less than one week. The number of jobs per day running on Tier-1 and Tier-2 centers is about one million: they concern physics analysis, simulation, reprocessing and other purposes.

## 3. ATLAS Physics Performance

The data collected in year 2010 have been very useful to measure and check ATLAS performance [2] on relevant physical quantities. The quality of lepton reconstruction is tested selecting events with $Z$ or $J/\Psi$ bosons decaying to $e^+e^-$ or $\mu^+\mu^-$, and measuring the width of the dilepton invariant mass peak: in the case of dileptons from $Z$, the Gaussian width of a resolution function (Crystal Ball) convolved with a Breit-Wigner line shape is found to be 1.7 GeV and 2.0 GeV for electrons and muons, respectively. In the left plot of Fig. 3 all the relevant di-muon mass peaks are visible over more than three orders of magnitude, with an impressive agreement with Monte Carlo [3].

The calorimeter systems allow the jet energy scale to be measured with a systematic error lower than 3% over a wide jet $p_T$ range.

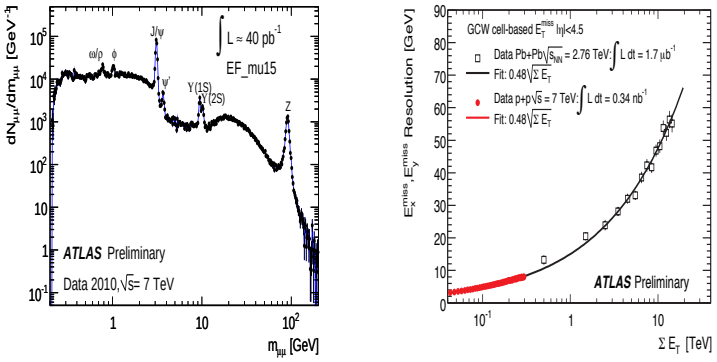


Fig. 3: Left: Di-muon invariant mass distribution as obtained on data (black points) and on simulation (blue line). Right: Resolution in $x$ and $y$ components of missing transverse energy (red points for proton-proton collisions and black squares for lead-lead) as a function of total transverse energy

The electromagnetic calorimeter features good resolution and linearity down to very low cluster energies (the width of the $\pi^0$ peak in the di-photon mass spectrum is $\sim$20 MeV). The missing transverse energy ($E_T^{\rm miss}$) is another quantity which ATLAS measures with very good accuracy: as shown in the right plot of Fig. 3, the resolution in its components is nicely fitted as a function of total transverse energy and is found to be lower than 10 GeV up to several hundred GeV [4]. Also b-tagging represents a crucial tool for studying Standard Model processes and beyond: the *SV0* algorithm, based on the significance of the signed decay length of the reconstructed secondary vertex, has been designed to reach a 40% to 60% efficiency on b-jets against 0.2% to 1% mistag rate coming from light flavour jets, for a jet $p_T$ in the range from 20 to 150 GeV.

## 4. Searches for Di-object Resonances

Among the many interesting recent ATLAS results concerning Standard Model [5] and beyond [6], in this section two examples of analyses performed with the ATLAS detector are shown, based on very simple signatures in which two physics objects are involved.

The first example concerns the search for resonances in the di-jet invariant mass spectrum [7]. The analysis is based on events

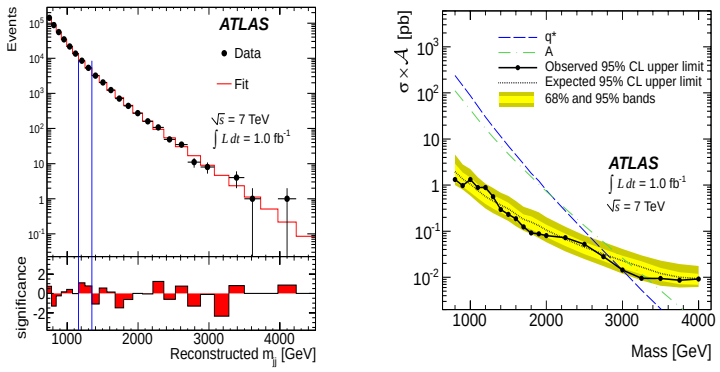


Fig. 4: Left: Observed di-jet mass distribution (points) fitted using a binned QCD background (fit) distribution described by the function $f(x) = p_1(1-x)^{p_2} x^{p_3+p_4 \ln x}$; in the lower panel the bin-by-bin significance of the data-background difference is shown. Right: Limit setting using $\sigma \times A$ theory curves for excited quarks (blue dashed) and axigluons (green dot-dashed); black circles are the 95% CL upper limit from data as a function of di-jet invariant mass, the black dotted curve shows the 95% CL upper limit expected from Monte Carlo and the light and dark yellow shaded bands represent the 68% and 95% contours of the expected limit, respectively

with at least two jets with $p_T > 30$ GeV in the region $|\eta| < 2.8$. The di-jet mass spectrum was analyzed by computing the Poisson probability in different mass regions covering at least two bins of the distribution (left plot of Fig. 4) and the most interesting peak was found in the interval [1.16, 1.35] TeV (vertical lines), but was found not significant. Three possible scenarios have been considered to account for new physics explaining di-jet resonances, in case they were found: Excited quarks (following quark-like quantum numbers from quark-gluon production models), Axigluons (high mass states with favored coupling to two quarks rather than two gluons) and Color Octet Scalars (like *s8*, a prototype for many possible exotic colored resonances). Using 0.81 fb$^{-1}$ of ATLAS data, both the expected and the observed 95% confidence level (CL) upper limits for these objects are brought to about 3 TeV for excited quarks and axigluons (as shown in the right plot of Fig. 4) and to ∼1.8 TeV for the *s8* scenario. For each new physics model considered in the figure, the observed (expected) limit occurs at the crossing of the theoretical curve (representing cross-section times acceptance, or $\sigma \times A$, in dashed

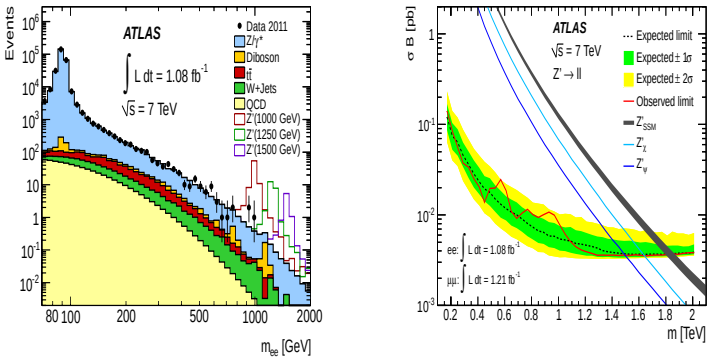


Fig. 5: Left: Di-electron invariant mass spectrum, compared to the stacked sum of all expected backgrounds, with three examples of SSM $Z'$ signals overlaid. Right: Expected (colored bands) and observed (red line) 95% CL limits on $\sigma$ $B$ and expected cross-sections for SSM production and two E6-motivated $Z'$ models with lowest and highest cross-section for the combination of the electron and muon channels. The uncertainties of theoretical curves are represented by the thickness of the corresponding curves.

colored lines) with the observed (expected) 95% CL upper limit curve. If systematic uncertainties were not included in this analysis, limits would have been 60 GeV higher.

Another important result is the search for dilepton resonances [8], coming from different possible theoretical scenarios, like a $Z'$ boson in the Sequential Standard Model (SSM) or in the E6 gauge group breaking up into SU(5) and two additional U(1) groups, motivated by Grand Unification Theory. The selection is based on exactly two opposite sign electrons (or muons) with $p_T > 25$ GeV and satisfying adequate selection criteria in order to optimize the rejection of the Standard Model background, dominated by $Z/\gamma^*$ going in two leptons, and including dibosons and dileptonic $t\bar{t}$. In the plot on the left of Fig. 5, the di-electron mass distribution obtained on more than 1 fb$^{-1}$ of data is superimposed on the Monte Carlo expectation, separated into all its relevant contributions, together with three possible simulated scenarios of SSM $Z'$ bosons. A similar plot is also obtained for di-muons. The Standard Model Monte Carlo is normalized to data in suitable control regions near the Z mass peak. In order to evaluate the 95% CL upper limits, the plot on the right of Fig. 5 shows,

as a function of di-lepton invariant mass, the expected cross-section times branching ratio ($\sigma\ B$) for the considered theoretical models superimposed on the expected and observed experimental limits (both electron and muon channels combined): the observed limits are 1.83 TeV for the SSM and range from 1.50 TeV to 1.64 TeV for the E6-motivated models. These results update a previous analysis obtained by ATLAS with 2010 data [9].

## 5. Conclusions

As of September 2011, the ATLAS experiment is smoothly running at the LHC and has collected more than 2.5 $\text{fb}^{-1}$ of data with very high efficiency and excellent physics performance of all of its subdetectors. Although there is still no definitive evidence of Higgs boson, excluded within Standard Model in a wide mass range [6], new mass limits are being set on Supersymmetry and on many other BSM phenomena, improving the results obtained by other collaborations so far or by ATLAS itself using 2010 data. As the integrated luminosity increases, ATLAS will continue to investigate unexplored regions to possibly discover new physics processes.

1. ATLAS collab., JINST **3**, S08003 (2008).
2. ATLAS collab., CERN-OPEN-2008-020, arXiv:0901.0512 (2009).
3. https://twiki.cern.ch/twiki/bin/view/AtlasPublic/MuonPerformancePublicPlots
4. https://twiki.cern.ch/twiki/bin/view/AtlasPublic/Approved2010HIPlotsJetEtMiss
5. F. Derue for the ATLAS collab., *Results on Standard Model and Heavy Ions physics of the ATLAS collaboration at the LHC*, these conference proceedings (2011).
6. N. Ruckstuhl for the ATLAS collab., *Search for Higgs and BSM physics with ATLAS*, these conference proceedings (2011).
7. ATLAS collab., New J. Phys. **13**, 053044 (2011).
8. ATLAS collab., CERN-PH-EP-2011-123, arXiv:1108.1582 [hep-ex], (2011).
9. ATLAS collab., Phys. Lett. B **700**, 163-180 (2011).

# ELASTIC PROTON-PROTON SCATTERING AT RHIC

Kin Yip for the STAR collaboration

*Brookhaven National Laboratory,*
*Collider-Accelerator Department,*
*Upton, NY 11973-5000, U.S.A.*
*e-mail: kinyip@bnl.gov*

**Abstract**

Here we describe elastic proton+proton (p+p) scattering measurements at RHIC in p+p collisions with a special optics run of $\beta^\star \sim 21$ m at STAR, at the center-of-mass energy $\sqrt{s} = 200$ GeV during the last week of the RHIC 2009 run. We present preliminary results of single and double spin asymmetries.

## 1. Introduction and Theoretical Formalism

Elastic scattering of polarized protons at small four momentum transfer squared $-t$ is described by interference of Coulomb and nuclear amplitudes. Coulomb amplitude is calculable by QED and such interference provides a unique opportunity to study the dynamics of the strong interaction in the nonperturbative region. The total cross section was measured to very high energy and turned out to be in a good agreement with the description by the Regge pole exchange. At ultra relativistic energies the main contribution comes from Pomeron or, in modern terms, multigluon exchange [1]. Most of the previous experiments were done with unpolarized beams and targets. The first measurement with polarized protons at high energies in the Coulomb nuclear interference (CNI) region ($\sqrt{s} = 19.4$ GeV was done in E704 experiment [2] with moderate precision. RHIC with its polarized beams [3] published a number of accurate measurements with

$\sqrt{s} = 6.8 - 21.7$ GeV [4, 5] in last few years. But only one measurement with a limited statistics exists so far in the collider energy range [7].

Elastic scattering of two identical particles with spin $\frac{1}{2}$ is described by 5 helicity amplitudes [8, 9]. Two amplitudes $\phi_1(s,t) = \langle ++|M|++\rangle$ and $\phi_3(s,t) = \langle +-|M|+-\rangle$ produce no spin-flip, two other $\phi_2(s,t) = \langle ++|M|--\rangle$ and $\phi_4(s,t) = \langle +-|M|-+\rangle$ produce double spin-flip and the last $\phi_5(s,t) = \langle ++|M|+-\rangle$ produces single spin-flip. Each of the amplitudes can be written as a sum of hadron and Coulomb amplitudes $\phi_i = \phi_i^{em} + \phi_i^h$. Electromagnetic part is calculable from QED. It is believed that the main hadron contribution to the cross section comes from non-flipping amplitudes so the optical theorem could be written as $\sigma_{\rm tot} = \frac{4\pi}{s}\mathrm{Im}(\phi_1+\phi_3)|_{t=0}$. Other hadron amplitudes are expected to be small and are parametrized in terms of $\mathrm{Im}\phi_+ = \mathrm{Im}(\phi_1+\phi_3)/2$:

$$\phi_2 = 2r_2\mathrm{Im}\phi_+, \quad \phi_4 = \frac{-t}{m^2}r_4\mathrm{Im}\phi_+, \quad \phi_5 = \frac{\sqrt{-t}}{m}r_5\mathrm{Im}\phi_+. \qquad (1)$$

The differential cross section and asymmetries can be written in terms of the amplitudes:

$$\frac{d\sigma}{dt} = \frac{2\pi}{s^2}(|\phi_1|^2 + |\phi_1|^2 + |\phi_2|^2 + |\phi_3|^2 + |\phi_4|^2 + 4|\phi_5|^2), \qquad (2)$$

$$A_N\frac{d\sigma}{dt} = -\frac{4\pi}{s^2}\mathrm{Im}\{\phi_5^*(\phi_1+\phi_2+\phi_3-\phi_4)\}, \qquad (3)$$

$$A_{NN}\frac{d\sigma}{dt} = \frac{4\pi}{s^2}\{2|\phi_5|^2 + \mathrm{Re}(\phi_1^*\phi_2 - \phi_3^*\phi_4)\},$$

$$A_{SS}\frac{d\sigma}{dt} = \frac{4\pi}{s^2}\{\mathrm{Re}(\phi_1\phi_2^* + \phi_3\phi_4^*)\}, \qquad (4)$$

where $A_N$ is the single spin asymmetry and $A_{NN}$ and $A_{SS}$ are the double spin asymmetries.

## 2. Experiment

The layout of the experiment is shown in Fig. 1. Protons scattered at very small angles at the interaction point (IP) travel inside the beam pipe utill they reach the Roman Pot (RP) detectors located in the

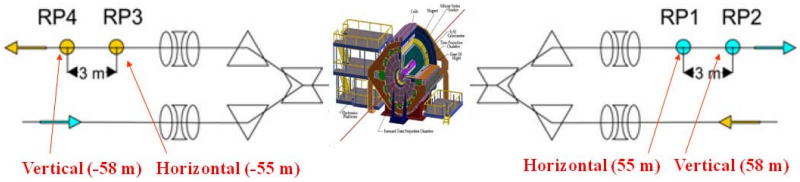


Fig. 1: Layout of the setup for small-t measurements with the STAR detector (in the center)

RHIC tunnel on both sides of the STAR detector. Each RP contains four silicon microstrip detectors and a trigger scintillation counter. During the 2009 run, we were able to insert RP detectors to be as close as 12 $\sigma$ ($\sigma$ being the beam size) from the center of the beam pipe. Two RP's with detectors inserted horizontally (at 55.5 m from IP) and another two RP's vertically (at 58.5 m) were used at each side of IP. More details of the detectors can be found in [11]. The coordinates measured by the detectors relate to the scattering angles at IP by the transport matrix:

$$\begin{pmatrix} x \\ y \end{pmatrix}_{\mathrm{RP}} = T_{\mathrm{RP}} \cdot \begin{pmatrix} \theta_x \\ \theta_y \end{pmatrix}_{\mathrm{IP}}, \tag{5}$$

where index $_{\mathrm{RP}}$ denotes a particular Roman Pot. The positions of the RP's were selected so that the error introduced by unknown position of the interaction point was minimal. More details on the detector layout, alignment and performance can be found at [12].

## 3. Analysis

Elastically triggered events were selected for rescontructions and the cuts are briefly described below.

**(A)** Clusters of consecutive strips with charge values above $5\sigma$ from their pedestals were found. We ignore rare clusters larger then 5 strips, because there were a lot of noise among them.

**(B)** A threshold depending on the cluster width was applied to the total charge of each cluster. This gave us better signal to noise ratio for clusters of 3 and 4 strips. After these cuts we had individual plane efficiencies above 99% as shown in Fig. 2.

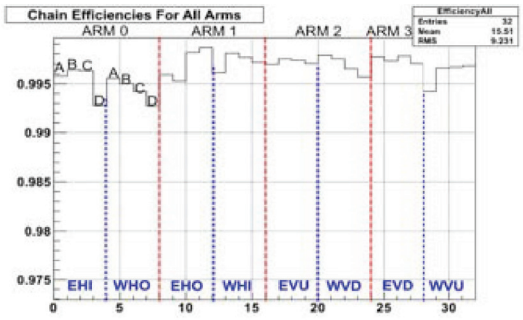


Fig. 2: Calculated efficiency of each Si detector plane/chain (A,B,C,D), in each elastic arm (end and dead strips excluded): Arm 0 (EHI-WHO or east horizontal inner – west horizontal outer detectors); Arm 2 (EVU-WVD or east vertical up and west vertical down detectors); Arm 1 and Arm 3 likewise

**(C)** Clusters in the planes of the same orientation (horizontal/$x$ or vertical/$y$) within the same RP were merged and we required that their coordinates were within 200 $\mu$m (2 strips) from each other.

**(D)** Clusters in $x$ and $y$ orientations form a track and opposite pairs of tracks formed from each side of the IP were chosen.

**(E)** Transport equation (5) was solved for each side.

**(F)** The strongest criteria of elastic events selection is the collinearity cut which was realized by requiring $\chi^2$, where $\chi^2 = (\theta_x^{\rm west} - \theta_x^{\rm east})^2/\sigma_x^2 + (\theta_y^{\rm west} - \theta_y^{\rm east})^2/\sigma_y^2$ and $\sigma_x$ and $\sigma_y$ are typically 0.057 mrad, to be $< 9$. The correlation between the angles can be seen in Fig. 3.

About 21 millions events out of about 33 million elastic triggers written during the run were selected for asymmetry calculations.

Using the square root formula [6, 7], raw asymmetry as function of azimuthal angle $\phi$ for only $++$ and $--$ bunch polarizations can be written as:

$$\epsilon_N(\phi) = \frac{(P_B + P_Y)A_N \cos(\phi)}{1 + \delta(\phi)} =$$

$$= \frac{\sqrt{N^{++}(\phi)N^{--}(\pi-\phi)} - \sqrt{N^{--}(\phi)N^{++}(\pi-\phi)}}{\sqrt{N^{++}(\phi)N^{--}(\pi-\phi)} + \sqrt{N^{--}(\phi)N^{++}(\pi-\phi)}}, \qquad (6)$$

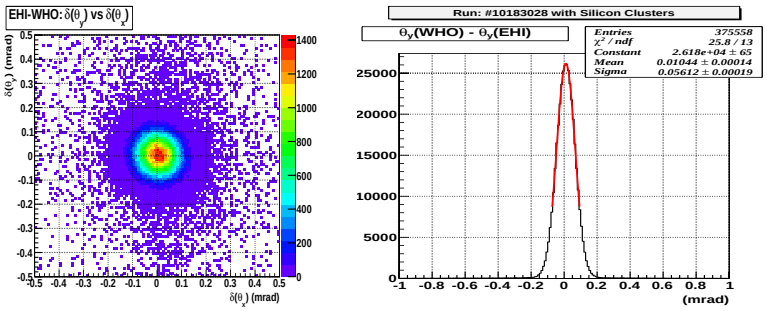


Fig. 3: Elastic correlation – difference in scattering angles at IP for particles scattered to the east and west in $x$ and $y$ in 2 dimensions (on the left) and 1 dimension (on the right)

where $\delta(\phi) = P_B P_Y (A_{NN} \cos^2(\phi) + A_{SS} \sin^2(\phi))$, $N^{ij}(\phi)$ – number of events with bunch polarization pattern $ij$ at the azimuthal angle $\phi$. $P_{B/Y}$ are polarizations of the blue and yellow beams, measured by HJET and pCarbon polarimeters [13]. The polarization values averaged for the time of our data taking were: $P_B + P_Y = 1.224 \pm 0.066$, $P_B - P_Y = -0.016 \pm 0.066$ and $P_B P_Y = 0.375 \pm 0.041$ (errors shown here include global systematic uncertainties). From double spin asymmetries measured by [7] we know that $\delta(\phi)$ is less than 0.01. Using other different bunch polarization combinations, other raw asymmetries can be introduced similarly to (6); particularly, the so-called "wrong combination" is shown here:

$$\epsilon'_N(\phi) = \frac{(P_B + P_Y) A_N \cos(\phi)}{1 - \delta(\phi)} =$$

$$= \frac{\sqrt{N^{+-}(\phi) N^{-+}(\pi - \phi)} - \sqrt{N^{-+}(\phi) N^{+-}(\pi - \phi)}}{\sqrt{N^{+-}(\phi) N^{-+}(\pi - \phi)} + \sqrt{N^{-+}(\phi) N^{+-}(\pi - \phi)}}. \qquad (7)$$

The preliminary results of $\epsilon_N(\phi)$ and $\epsilon'_N(\phi)$ are presented in Fig. 4 for $0.005 < |t| < 0.010$ $(\mathrm{GeV/c})^2$. Using (6), we fitted the raw asymmetry to extract $A_N$'s in 5 $t$-bins.

Double spin raw asymmetry is given by the equation:

$$\delta(\phi) = P_B P_Y (A_{NN} \cos^2(\phi) + A_{SS} \sin^2(\phi)) =$$

$$= \frac{(\frac{N^{++}}{L^{++}} + \frac{N^{--}}{L^{--}}) - (\frac{N^{+-}}{L^{+-}} + \frac{N^{-+}}{L^{-+}})}{(\frac{N^{++}}{L^{++}} + \frac{N^{--}}{L^{--}}) + (\frac{N^{+-}}{L^{+-}} + \frac{N^{-+}}{L^{-+}})}. \qquad (8)$$

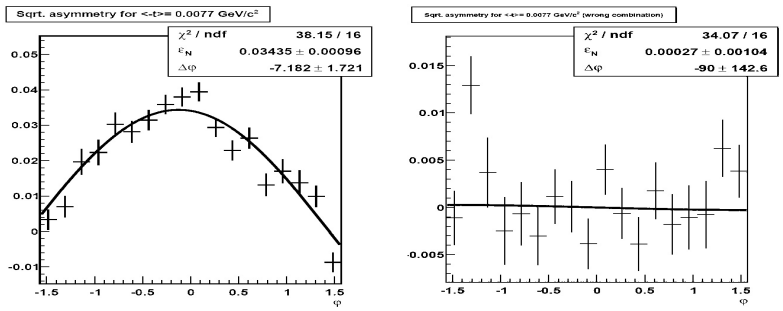


Fig. 4: STAR Preliminary: raw single spin asymmetries $\epsilon_N$ (left) and $\epsilon'_N$ (right) for $0.005 < |t| < 0.010$ $(\mathrm{GeV/c})^2$

Here $L^{ij}$ are relative luminosities for the corresponding polarization pattern. For the preliminary results we used relative luminosities obtained from counts of inelastic triggers produced by the vertex position detector (VPD) and beam-beam counters (BBC). The systematic uncertainty in the normalization can be estimated by the difference between VPD and BBC normalizations which turned out to be 0.25%. We hope to reduce this uncertainty taking advantage of other normalization sources.

## 4. Results

The preliminary results on the single spin asymmetry are shown in Fig. 5 in comparison with theoretical curve without hadron spin-flip (black line) and with the best fit allowing non zero hadron spin-flip (green line) (see [14] for formula). Only statistical errors have been included. Fig. 6 shows fitted value of $r_5$ with contours showing confidence levels of 1, 2 and $3\sigma$. No evidence for contribution of hadron spin-flip amplitude $\phi_5$ is seen.

The preliminary results on double spin asymmetries are shown in Fig. 7. Though some effects of the order of $10^{-3}$ could be seen, they are small and comparable with the normalization uncertainty. A careful study of systematic effects produced by normalization should be done before making any conclusions.

Our preliminary results agree with the hypothesis that only Pomeron exchange, which contributes only to spin non-flipping amplitudes $\phi_1$

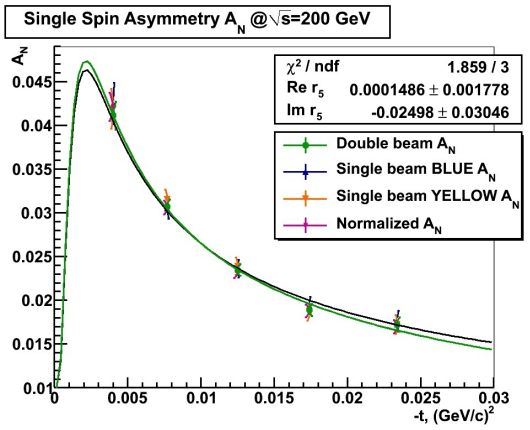


Fig. 5: STAR Preliminary: single spin asymmetry $A_N$

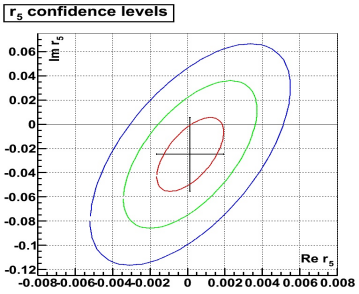


Fig. 6: STAR Preliminary: complex plane of parameter $r_5$ with contours of confidence level: 1, 2 and 3-$\sigma$

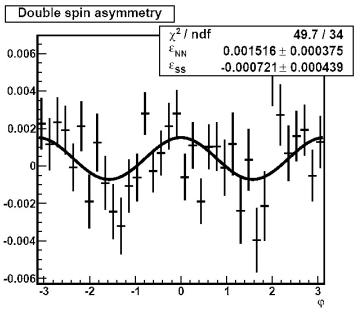


Fig. 7: STAR Preliminary results on raw double spin asymmetry

and $\phi_3$, survives at high energies. with other aforementioned measurements of the proton-proton elastic scattering with $\sqrt{s} > 10$ GeV, we see no evidence of contribution of other amplitudes.

## 5. Summary

We had a very successful run with the physics program with tagged forward protons at RHIC in 2009, in which nearly 33 million events

with elastic triggers were collected. We have so far focussed on data analyses in elastic scattering topics such as $A_N$, $r_5$, $A_{NN}$ and $A_{SS}$. We are finalizing our optimizations and systematic studies in our analyses and hope to have final results in near future. There is certainly more to do to fully explore physics potential and discovery possibilities at RHIC.

## Acknowledgments

This work is supported by Brookhaven Science Associates, LLC under Contract No. DE-AC02-98CH10886 with the U.S. Department of Energy. We thank the RHIC Operations Group and RCF at BNL, the NERSC Center at LBNL and the Open Science Grid consortium for providing resources and support. This work was supported in part by the Offices of NP and HEP within the U.S. DOE Office of Science, the U.S. NSF, the Sloan Foundation, the DFG cluster of excellence 'Origin and Structure of the Universe'of Germany, CNRS/IN2P3, FAPESP CNPq of Brazil, Ministry of Ed. and Sci. of the Russian Federation, NNSFC, CAS, MoST, and MoE of China, GA and MSMT of the Czech Republic, FOM and NWO of the Netherlands, DAE, DST, and CSIR of India, Polish Ministry of Sci. and Higher Ed., Korea Research Foundation, Ministry of Sci., Ed. and Sports of the Rep. Of Croatia, and RosAtom of Russia.

1. S. Nussinov, Phys. Rev. Lett. **34**, 1286 (1975);
   S. Nussinov, Phys. Rev. D **14**, 246 (1976).
2. N. Akchurin *et al.*, Phys. Rev. D **48**, 3026 (1993).
3. M. Bai *et al.*, Phys. Rev. Lett. **96**, 174801 (2006).
4. H. Okada *et al.*, Phys. Lett. B **638**, 450 (2005);
   I.G. Alekseev *et al.*, Phys. Rev. D **79**, 094014 (2009).
5. A. Bazilevsky, J. Phys. Conf. Ser. **295**, 012096 (2011).
6. G.G. Ohlsen and P.W. Keaton, Jr., Nucl. Instr. Meth. **109**, 41 (1973).
7. S. Bültmann *et al.*, Phys. Lett. B **632**, 167 (2006);
   S. Bültmann *et al.*, Phys. Lett. B **647**, 98 (2007).
8. N.H. Buttimore, E. Gotsman and E. Leader, Phys. Rev. D **18**, 694 (1978).
9. T.L. Trueman, (1996) arXiv:hep-ph/9610316.
10. K.H. Ackermann *et al.*, Nucl. Instr. Meth. A **499**, 624 (2003).
11. S. Bültmann *et al.*, Nucl. Instr. Meth. A **535**, 415 (2004).

12. D. Plyku, J. Phys. Conf. Ser. **295**, 012129 (2011).
13. http://www4.rcf.bnl.gov/~cnipol/pubdocs/Run09Offline/
14. N.H. Buttimore *et al.*, Phys. Rev. D **59**, 114010 (1999).

# II. PHENOMENOLOGY AND THEORY

# HIGHER-LOOP RESUMMATION IN QCD FRACTIONAL APT

Alexander P. Bakulev

*Bogoliubov Lab. of Theoretical Physics,*
*Joint Institute for Nuclear Research, 141980, Dubna, Russia,*
*e-mail: bakulev@theor.jinr.ru*

**Abstract**

We describe the development of Analytic Perturbation Theory (APT) in QCD, called Fractional APT (FAPT), which has been suggested to apply the renormalization group evolution and QCD factorization technique in the framework of APT. Then we show how to resum perturbative series in the one-, two- and three-loop FAPT. $P(t)$. At the end, we discuss the application of this resummation approach to the estimation of the Adler function $D(Q^2)$ in the $N_f = 4$ region of $Q^2$.

## 1. Short History of Analytic Approach in QCD

The QCD Analytic Perturbation Theory (APT) was initiated by N. N. Bogolyuov et al. paper of 1959 [1], where ghost-free effective coupling for QED has been constructed. Then in 1982 Radyushkin and Krasnikov and Pivovarov [2] using the same dispersion technique suggested regular (for $s \geq \Lambda^2$) QCD running coupling in Minkowskian region, the well-known $\pi^{-1}\arctan(\pi/L)$. The real realization of this technique into QCD was initiated by Igor Solovtsov and his co-authors in the mid-90s. In 1995 Jones and Solovtsov using variational approach [3] constructed the effective couplings in Euclidean and Minkowski domains which appears to be finite for all $Q^2$ and $s$ and satisfy analyticity integral conditions (1). Just in the same time Shirkov and Solovtsov [4], using the dispersion approach of [1], discovered

ghost-free coupling $\mathcal{A}_1[L]$, Eq. (4a), in Euclidean region and ghost-free coupling $\mathfrak{A}_1[L]$, Eq. (4b), in Minkowskian region, which satisfy analyticity integral conditions

$$\mathcal{A}_1(Q^2) = \hat{D}\left[\mathfrak{A}_1\right](Q^2) \equiv Q^2 \int_0^\infty \frac{\mathfrak{A}_1(\sigma)}{(\sigma+Q^2)^2} d\sigma; \tag{1a}$$

$$\mathfrak{A}_1(s) = \hat{R}\left[\mathcal{A}_1\right](s) \equiv \frac{1}{2\pi i} \int_{-s-i\varepsilon}^{-s+i\varepsilon} \frac{\mathcal{A}_1(\sigma)}{\sigma}\, d\sigma. \tag{1b}$$

The last coupling coincides with the Radyushkin one for $s \geq \Lambda^2$. Due to the absence of singularities in these couplings, Shirkov and Solovtsov suggested to use them for all $Q^2$ and $s$. Quite soon this construction was developed [5] in a closed scheme. See the history details in the recent review paper [6]. The whole construction is known since then as the Analytic Perturbation Theory.

The next step, made by Bakulev, Mikhailov, and Stefanis as an answer for a call of [7] (see below), generalizes the APT by including fractional powers of coupling, as well as products of coupling powers and logarithms [8] and for this reason, it was named the *Fractional APT*. At the same time, it appears possible to sum up nonpower series in the (F)APT [9–11].

## 2. Basics of APT in QCD

In the standard QCD PT we know the Renormalization Group (RG) equation in the $l$-loop approximation

$$\frac{da_{(l)}[L]}{dL} = -a^2_{(l)}[L]\left[1 + \sum_{k\geq 1}^{l-1} c_k\, a^k_{(l)}[L]\right] \tag{2}$$

for the effective coupling $\alpha_s(Q^2) = a_{(l)}[L]/\beta_f$ with $L = \ln(Q^2/\Lambda^2)$, $\beta_f = b_0(N_f)/(4\pi) = (11 - 2N_f/3)/(4\pi)$.[1] Then its one-loop solution generates Landau pole singularity, $a_{(1)}[L] = 1/L$. As a consequence, the perturbative power series for the Adler function, $D(Q^2) =$

[1] We use notations $f(Q^2)$ and $f[L]$ in order to specify the arguments we mean — squared momentum $Q^2$ or its logarithm $L = \ln(Q^2/\Lambda^2)$, that is $f[L] = f(\Lambda^2 \cdot e^L)$ and the QCD scale parameter $\Lambda$ is usually referred to $N_f = 3$ region.

$d_0 + \sum_{k\geq 1} d_k\, a^k[L]$, being reasonably good in the deep UV region of $Q^2$, at $Q^2 = \Lambda^2$ has the unphysical pole — in marked contrast to the analyticity property of the Adler function. Indeed, it should have a cut along the negative axis of $Q^2$, but can not have any poles in Euclidean domain, $Q^2 > 0$. APT was suggested as a resolution of this contradiction: From the very beginning we demand that improved coupling, as well as all its integer powers, should have the right analytic properties, i. e. be represented as dispersive integrals, see (3).

By the analytization in the APT for an observable $f(Q^2)$ we mean the Källen–Lehmann representation

$$\left[f(Q^2)\right]_{\rm an} = \int_0^\infty \frac{\rho_f(\sigma)}{\sigma + Q^2 - i\epsilon}\, d\sigma \tag{3}$$

with $\rho_f(\sigma) = \dfrac{1}{\pi}\,{\rm Im}\left[f(-\sigma)\right]$. Then in the one-loop approximation $\rho_1(\sigma) = 1/\sqrt{L_\sigma^2 + \pi^2}$ and

$$\mathcal{A}_1[L] = \int_0^\infty \frac{\rho_1(\sigma)}{\sigma + Q^2}\, d\sigma \;=\; \frac{1}{L} - \frac{1}{e^L - 1}\,, \tag{4a}$$

$$\mathfrak{A}_1[L_s] = 162 \int_s^\infty \frac{\rho_1(\sigma)}{\sigma}\, d\sigma \;=\; \frac{1}{\pi}\,\arccos\frac{L_s}{\sqrt{\pi^2 + L_s^2}}\,, \tag{4b}$$

whereas analytic images of the higher powers ($n \geq 2, n \in \mathbb{N}$) are:

$$\begin{pmatrix} \mathcal{A}_n[L] \\ \mathfrak{A}_n[L_s] \end{pmatrix} = \frac{1}{(n-1)!}\left[-\frac{d}{dL}\right]^{n-1} \begin{pmatrix} \mathcal{A}_1[L] \\ \mathfrak{A}_1[L_s] \end{pmatrix}. \tag{4c}$$

Note that at $L \gg 1$ the pole remover $\sim e^{-L} \approx e^{-1/a}$. In other words, Källen–Lehmann analyticity in the $Q^2$ plane generates nonperturbative $e^{-1/\alpha_s}$ correction. This correction guarantees the absence of spurious Landau-pole singularity and ensures the correspondence with perturbative $\alpha_s(Q^2)$ at $Q^2 \gg 1$ GeV$^2$.

In the left panel of Fig. 1, we show the so-called Distorting Mirror for analytic couplings in the Minkowski and Euclidean regions for $\mathfrak{A}_1(s)$ and $\mathcal{A}_1(Q^2)$. We see that in the IR domain one has universal finite IR values $\mathcal{A}_1(0) = \mathfrak{A}_1(0) = 1$. Moreover, starting from the two-loop level analytic couplings reveal loop stabilization of IR behavior.

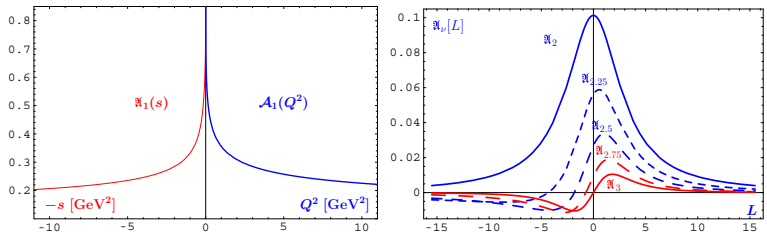


Fig. 1: Left panel: Distorting Mirror for analytic couplings in the Minkowski and Euclidean regions for $\mathfrak{A}_1(s)$ and $\mathcal{A}_1(Q^2)$. Right panel: Comparing $\mathfrak{A}_\nu[L]$ (right panel) vs. $L$ for fractional $\nu \in [2,3]$

This yields practical loop- and renormalization-scheme-independence of $\mathcal{A}_1(Q^2)$, $\mathfrak{A}_1(s)$, and higher expansion functions, for details see [6].

In the APT, in addition to the regular behavior of couplings, one has to have nonpower expansions for physical observables. Indeed, if in the standard pQCD for an observable $D$ we have[2]

$$D_{\rm PT}(Q^2) = d_0 + d_1\,\alpha_s(Q^2) + d_2\,\alpha_s^2(Q^2) + d_3\,\alpha_s^3(Q^2) + \ldots\,; \quad (5a)$$

$$R_{\rm PT}(s) = d_0 + d_1\,\alpha_s(s) + d_2\,\alpha_s^2(s) + r_3\,\alpha_s^3(s) + \ldots\,, \quad (5b)$$

then in the APT we should use the nonpower functional expansion

$$\mathcal{D}_{\rm APT}(Q^2) = d_0 + d_1\,\mathcal{A}_1(Q^2) + d_2\,\mathcal{A}_2(Q^2) + d_3\,\mathcal{A}_3(Q^2) + \ldots \quad (5c)$$

$$\mathcal{R}_{\rm APT}(s) = d_0 + d_1\,\mathfrak{A}_1(s) + d_2\,\mathfrak{A}_2(s) + d_3\,\mathfrak{A}_3(s) + \ldots\,. \quad (5d)$$

This provides the better loop convergence and practical renormalization-scheme independence of observables.

## 3. From APT to FAPT

At first glance, the APT is a complete theory providing tools to produce an analytic answer for any perturbative series in QCD. However, in 2001 Karanikas and Stefanis [7] suggested the principle of analytization "as a whole" in the $Q^2$ plane for hadronic observables, calculated perturbatively. More precisely, they proposed the analytization recipe for terms like $\int_0^1 dx \int_0^1 dy\,\alpha_{\rm s}\left(Q^2 xy\right) f(x) f(y)$ which

[2] Here $r_3$ and higher-order coefficients $r_n$ differ from $d_3$ and $d_n$ by the $\pi^2$ terms.

can be treated as an effective account for the logarithmic terms in the next-to-leading-order approximation of the pQCD. Indeed, in the standard pQCD one also has:
(i) the factorization procedure in QCD that gives rise to the appearance of logarithmic factors of the type: $a^\nu[L]\,L$;
(ii) the RG evolution that generates evolution factors of the type: $B(Q^2) = \left[Z(Q^2)/Z(\mu^2)\right]\,B(\mu^2)$ which reduce in the one-loop approximation to $Z(Q^2) \sim a^\nu[L]$ with $\nu = \gamma_0/(2\beta_0)$ being a fractional number.
All that means that in order to generalize the APT in the "analytization as a whole" direction, one needs to construct analytic images of new functions: $a^\nu$, $a^\nu\,L^m, \ldots$. This task was performed in the framework of the so-called FAPT suggested in [8]. Now we briefly describe this approach.

In the one-loop approximation, using recursive relation (4c) we can obtain explicit expressions for $\mathcal{A}_\nu[L]$ and $\mathfrak{A}_\nu[L]$:

$$\mathcal{A}_\nu[L] = \frac{1}{L^\nu} - \frac{F(e^{-L}, 1-\nu)}{\Gamma(\nu)}\,; \tag{6a}$$

$$\mathfrak{A}_\nu[L] = \frac{\sin\left[(\nu-1)\arccos\left(L/\sqrt{\pi^2+L^2}\right)\right]}{\pi(\nu-1)\left(\pi^2+L^2\right)^{(\nu-1)/2}}\,. \tag{6b}$$

Here $F(z,\nu)$ is the reduced Lerch transcendental function which is an analytic function in $\nu$. The couplings $\mathcal{A}_\nu[L]$ and $\mathfrak{A}_\nu[L]$ have very interesting properties, which we discussed extensively in our previous papers [8].

In the right panel of Fig. 1, we show in comparison how $\mathfrak{A}_\nu[L]$ and $\mathcal{A}_\nu[L]$ depend on $L$ for fractional values of $\nu$.

To demonstrate the importance of taking into account the FAPT, that is using $\mathcal{A}_\nu[L]$ and $\mathfrak{A}_\nu[L]$ instead of $(\mathcal{A}_1[L])^\nu$ and $(\mathfrak{A}_1[L])^\nu$, we show in the left panel of Fig. 2 the values of the normalized deviations $\Delta_{\rm M}(L,\nu) = 1 - (\mathfrak{A}_1[L])^\nu\,/\mathfrak{A}_\nu[L]$ in the Minkowski domain.

The construction of the FAPT with a fixed number of quark flavors, $N_f$, is a two-step procedure: we start with the perturbative result $\left[a(Q^2)\right]^\nu$, generate the spectral density $\overline{\rho}_\nu(\sigma)$ using Eq. (3), and then obtain analytic couplings $\mathcal{A}_\nu[L]$ and $\mathfrak{A}_\nu[L]$ via Eqs. (4). Here $N_f$ is fixed and factorized out. We can proceed in the same manner for $N_f$-dependent quantities: $\left[\alpha_s(Q^2;N_f)\right]^\nu \Rightarrow \overline{\rho}_\nu(\sigma;N_f) =$

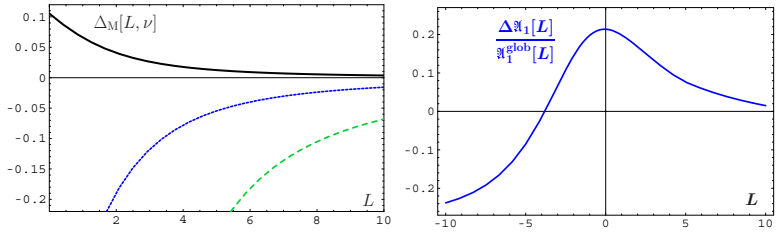


Fig. 2: Left panel: Comparing $\mathfrak{A}_\nu$ with $(\mathfrak{A}_1)^\nu$ for fractional $\nu = 0.62$ (solid line), 1.62 (dotted line) and 2.62 (dashed line). Right panel: Deviation $\Delta\mathfrak{A}_1[L]/\mathfrak{A}_1^{\rm glob}[L]$ of the global coupling relative to the fixed-$N_f$ coupling in the FAPT.

$\rho_\nu[L_\sigma; N_f] \equiv \rho_\nu(\sigma)/b_f^\nu \Rightarrow \overline{\mathcal{A}}_\nu[L; N_f]$ and $\overline{\mathfrak{A}}_\nu[L; N_f]$ — here $N_f$ is fixed but not factorized out.

The global version of the FAPT [8], (2009), which takes into account heavy-quark thresholds, is constructed along the same lines but starting from global perturbative coupling $\left[\alpha_s^{\rm glob}(Q^2)\right]^\nu$, being a continuous function of $Q^2$ due to choosing different values of QCD scales $\Lambda_f$, corresponding to different values of $N_f$. We illustrate here the case of only one heavy-quark threshold at $Q^2 = m_4^2$, corresponding to the transition $N_f = 3 \to N_f = 4$. Then we obtain the discontinuous spectral density

$$\rho_n^{\rm glob}(\sigma) = \theta\left(L_\sigma < L_4\right)\, \overline{\rho}_n\left[L_\sigma; 3\right] + \theta\left(L_4 \le L_\sigma\right)\, \overline{\rho}_n\left[L_\sigma + \lambda_4; 4\right]\,, \quad (7)$$

with $L_\sigma \equiv \ln\left(\sigma/\Lambda_3^2\right)$, $L_f \equiv \ln\left(m_f^2/\Lambda_3^2\right)$ and $\lambda_f \equiv \ln\left(\Lambda_3^2/\Lambda_f^2\right)$ for $f = 4$, which is expressed in terms of the fixed-flavor spectral densities with 3 and 4 flavors, $\rho_n[L_\sigma; 3]$ and $\rho_n[L_\sigma + \lambda_4; 4]$; note here that $L_\sigma + \lambda_4 = \ln(\sigma/\Lambda_4^2)$. However, it generates the continuous Minkowskian coupling

$$\mathfrak{A}_\nu^{\rm glob}[L] = \theta\left(L < L_4\right)\left(\overline{\mathfrak{A}}_\nu[L; 3] + \Delta_{43}\overline{\mathfrak{A}}_\nu\right) + \theta\left(L_4 \le L\right)\, \overline{\mathfrak{A}}_\nu[L + \lambda_4; 4] \quad (8a)$$

with $\Delta_{43}\overline{\mathfrak{A}}_\nu = \overline{\mathfrak{A}}_\nu[L_4 + \lambda_4; 4] - \overline{\mathfrak{A}}_\nu[L_4; 3]$ and the analytic Euclidean coupling $\mathcal{A}_\nu^{\rm glob}[L]$

$$\mathcal{A}_\nu^{\rm glob}[L] = \overline{\mathcal{A}}_\nu[L + \lambda_4; 4] + \int\limits_{-\infty}^{L_4} \frac{\overline{\rho}_\nu[L_\sigma; 3] - \overline{\rho}_\nu[L_\sigma + \lambda_4; 4]}{1 + e^{L - L_\sigma}}\, dL_\sigma\,. \quad (8b)$$

To demonstrate the magnitude of the threshold corrections, we show in the right panel of Fig. 2 the values of the normalized deviations $\Delta\mathfrak{A}_\nu[L] = \mathfrak{A}_\nu^{\rm glob}[L] - \overline{\mathfrak{A}}_\nu[L+\lambda_4; 4]$ in the Minkowski region (for more details see [10, 11]).

## 4. Resummation in the One-loop (F)APT

We consider now the perturbative expansion of a typical physical quantity, like the Adler function and the ratio $R$, in the one-loop APT. Due to limited space of our presentation we provide all formulas only for quantities in the Minkowski region:

$$\mathcal{R}[L] = \sum_{n=1}^{\infty} d_n\, \mathfrak{A}_n[L]\,. \tag{9}$$

We suggest that there exists a generating function $P(t)$ for the coefficients $\tilde{d}_n = d_n/d_1$:

$$\tilde{d}_n = \int_0^\infty P(t)\, t^{n-1} dt \quad \text{with} \quad \int_0^\infty P(t)\, dt = 1\,. \tag{10}$$

To shorten our formulae, we use for the integral $\int_0^\infty f(t)P(t)dt$ the following notation: $\langle\langle f(t)\rangle\rangle_{P(t)}$. Then the coefficients $d_n = d_1\, \langle\langle t^{n-1}\rangle\rangle_{P(t)}$ and, as has been shown in [9], we have the exact result for the sum in (9)

$$\mathcal{R}[L] = d_1\, \langle\langle \mathfrak{A}_1[L-t]\rangle\rangle_{P(t)}\,. \tag{11}$$

The integral in variable $t$ here has a rigorous meaning ensured by the finiteness of the coupling $\mathfrak{A}_1[t] \le 1$ and fast fall-off of the generating function $P(t)$.

In our previous publications [10, 11], we constructed generalizations of these results, first, to the case of the global APT when heavy-quark thresholds are taken into account. Then one starts with the series of type (9), where $\mathfrak{A}_n[L]$ are substituted by their global analogs $\mathfrak{A}_n^{\rm glob}[L]$ (note that due to different normalizations of global couplings, $\mathfrak{A}_n^{\rm glob}[L] \simeq \mathfrak{A}_n[L]/\beta_f^n$, the coefficients $d_n$ should also be changed). Then

$$\begin{aligned}\mathcal{R}^{\rm glob}[L] = {} & d_1\theta(L<L_4)\langle\langle \Delta_4\mathfrak{A}_1[t] + \mathfrak{A}_1\Big[L-\frac{t}{\beta_3}; 3\Big]\rangle\rangle_{P(t)} \\ & + d_1\theta(L\ge L_4)\langle\langle \mathfrak{A}_1\Big[L+\lambda_4-\frac{t}{\beta_4}; 4\Big]\rangle\rangle_{P(t)}\,;\end{aligned} \tag{12}$$

where $\Delta_4\mathfrak{A}_\nu[t] \equiv \mathfrak{A}_\nu\Big[L_4 + \lambda_4 - t/\beta_4; 4\Big] - \mathfrak{A}_\nu\Big[L_3 - t/\beta_3; 3\Big]$.

The second generalization has been obtained for the global FAPT. Then the starting point is the series

$$\mathcal{R}^{\rm glob}_\nu[L] = \sum_{n=1}^{\infty} d_n\, \mathfrak{A}^{\rm glob}_{n+\nu}[L] = d_1 \sum_{n=1}^{\infty} \langle\langle t^{n-1}\rangle\rangle_{P(t)}\, \mathfrak{A}^{\rm glob}_{n+\nu}[L] \qquad (13)$$

and the result of summation is a complete analog of Eq. (12) with the substitutions

$$P(t) \Rightarrow P_\nu(t) = \int_0^1 P\left(\frac{t}{1-x}\right) \frac{\nu\, x^{\nu-1} dx}{1-x}\,, \qquad (14)$$

$d_0 \Rightarrow d_0\, \mathfrak{A}_\nu[L]$, $\mathfrak{A}_1[L-t] \Rightarrow \mathfrak{A}_{1+\nu}[L-t]$, and $\Delta_4\mathfrak{A}_1[t] \Rightarrow \Delta_4\mathfrak{A}_{1+\nu}[t]$. All needed formulas have also been obtained in parallel for the Euclidean case, for details see [10,11].

## 5. Higher-loop Resummation in FAPT

Here we discuss the generalization of the FAPT resummation approach of the previous section for the case of the two- and three-loop QCD running coupling.

We start now with the non-power series ($\nu = 0$ corresponds to the APT case) of the type

$$\mathcal{S}_\nu[L; \mathcal{F}] = d_1 \sum_{n\geq 1} \mathcal{F}_{n+\nu}[L] = d_1 \sum_{n=1}^{\infty} \langle\langle t^{n-1}\rangle\rangle_{P(t)}\, \mathcal{F}_{n+\nu}[L]\,, \qquad (15)$$

where $\mathcal{F}[L]$ denotes one of the analytic quantities $\mathfrak{A}^{(l)}[L]$, $\mathcal{A}^{(l)}[L]$, or $\rho^{(l)}[L]$. So, actually we need to resum the series

$$\mathcal{W}_\nu[L; t; \mathcal{F}] = \sum_{n\geq 1} t^{n-1}\, \mathcal{F}_{n+\nu}[L]\,, \qquad (16a)$$

related to the original one in a simple way

$$\mathcal{S}_\nu[L; \mathcal{F}] = d_1\, \langle\!\langle \mathcal{W}_\nu[L; t; \mathcal{F}]\rangle\!\rangle_{P(t)}\ . \qquad (16b)$$

### 5.1. Two-loop FAPT

In the two-loop approximation we have more complicated recurrence relation as compared with the one-loop one, Eq. (4c):

$$-\frac{1}{n+\nu}\,\dot{\mathcal{F}}_{n+\nu}[L] = \mathcal{F}_{n+1+\nu}[L] + c_1\,\mathcal{F}_{n+2+\nu}[L] \tag{17}$$

with $c_1$ being the corresponding coefficient in Eq. (2). In order to resum the series $\mathcal{W}_\nu[L;t;\mathcal{F}]$ we need to introduce the "two-loop evolution" time

$$\tau_2(t) = t - c_1\,\ln\left[1+\frac{t}{c_1}\right]\;;\;\dot{\tau}_2(t) = \frac{1}{1+c_1/t}\,. \tag{18}$$

We obtained the following resummation recipe

$$\begin{aligned}\mathcal{W}_\nu[L,t;\mathcal{F}] &= \mathcal{F}_{\nu+1}[L] + \Delta(\nu)\,c_1\,\dot{\tau}_2(t)\,\mathcal{F}_2[L_{t,0}] \\ -\dot{\tau}_2(t)\int\limits_0^1 z^\nu &\left[t\,\dot{\mathcal{F}}_{\nu+1}[L_{t,z}] - \frac{c_1\,\nu}{z}\,\mathcal{F}_{\nu+2}[L_{t,z}]\right] dz\end{aligned} \tag{19}$$

with $L_{t,z} = L + \tau_2(t\,z) - \tau_2(t)$, $L_{t,0} = L - \tau_2(t)$, and $\Delta(\nu)$ being a Kronecker delta symbol. Interesting to note here that it is possible to obtain an analogous, but more complicated recipe for the case when $\mathcal{F}$ is the analytic image of the two-loop evolution factor $a^\nu(1+c_1 a)^{\nu_1}$, see in [11] for more detail.

### 5.2. Three-loop FAPT

We describe here the recently obtained results on resummation in the three-loop FAPT.[3] In this case the recurrence relation has three terms in the r.h.s.

$$-\frac{1}{n+\nu}\,\dot{\mathcal{F}}_{n+\nu}[L] = \mathcal{F}_{n+1+\nu}[L] + c_1\,\mathcal{F}_{n+2+\nu}[L] + c_2\,\mathcal{F}_{n+3+\nu}[L] \tag{20}$$

[3] These results have been obtained in collaboration with my Ph. D. student, Irina V. Potapova.

with $c_2$ being the corresponding coefficient in Eq. (2). We introduce the "three-loop evolution" time by

$$\tau_3(t) = t + \frac{c_1^2 - 2c_2}{\Delta} \arctan\left[\frac{t\,\Delta}{2\,c_2 + c_1\,t}\right] - \frac{c_1}{2}\,\ln\left[1 + \frac{c_1 + t}{c_2}\,t\right]; \quad (21)$$

$$\frac{d\tau_3(t)}{d\,t} \equiv \dot{\tau}_3(t) = \frac{1}{1 + c_1/t + c_2/t^2}\,.$$

Then our resummation recipe is

$$\mathcal{W}_\nu[L,t;\mathcal{F}] = \mathcal{F}_{\nu+1}[L] + \Delta(\nu)\,c_2\,\dot{\tau}_3(t)\,\mathcal{F}_3[L_{t,0}] + t\,\mathcal{F}_{\nu+2}[L]$$
$$-\dot{\tau}_3(t)\int_0^1 z^\nu \left[t\,\dot{\mathcal{F}}_{\nu+1}[L_{t,z}] - \frac{c_2\,\nu}{z}\,\mathcal{F}_{\nu+3}[L_{t,z}] + z\,t^2\,\dot{\mathcal{F}}_{\nu+2}[L_{t,z}]\right.$$
$$\left. +(\nu+1)\,t\,\mathcal{F}_{\nu+2}[L_{t,z}]\right] dz \quad (22)$$

with $L_{t,z} = L + \tau_3(t\,z) - \tau_3(t)$ and $L_{t,0} = L - \tau_3(t)$.

## 6. Resummation for Adler Function

Here we consider the PT power series of the vector correlator Adler function (labeled by the symbol V) [12]

$$D_{\rm V}[L] = 1 + \sum_{n\geq 1} d_n \left(\frac{\alpha_s[L]}{\pi}\right)^n\,. \quad (23)$$

Due to $d_1 = 1$ coefficients $\tilde{d}_n$ coincide with $d_n$. We suggested [11] the model for the generating function of the perturbative coefficients $d_n$ (see the first row in Table 1)

$$P_{\rm V}(t) = \frac{\delta\,e^{-t/c\delta} - (t/c)\,e^{-t/c}}{c\,(\delta^2 - 1)} \quad \text{with} \quad d_n^{\rm V} = c^{n-1}\,\frac{\delta^{n+1} - n}{\delta^2 - 1}\,\Gamma(n)\,. \quad (24)$$

Our prediction $d_4^{\rm V} = 27.1$, obtained with this generating function by fitting the two known coefficients $d_2$ and $d_3$ and using the model (24), is in a good agreement with the value 27.4, calculated in Ref.

**T a b l e 1: Coefficients $d_n$ for the Adler-function series with $N_f = 4$. The numbers in the square brackets denote the lower and the upper limits of the INNA estimates**

| | PT coefficients | $d_1$ | $d_2$ | $d_3$ | $d_4$ | $d_5$ |
|---|---|---|---|---|---|---|
| 1 | pQCD results with $N_f = 4$ [12] | 1 | 1.52 | 2.59 | 27.4 | — |
| $2^+$ | Model (24) with $c = 3.544, \delta = 1.3252$ | 1 | 1.53 | 2.80 | 30.9 | 2088 |
| 2 | Model (24) with $c = 3.553, \delta = 1.3245$ | 1 | 1.52 | 2.60 | 27.3 | 2025 |
| $2^-$ | Model (24) with $c = 3.568, \delta = 1.3238$ | 1 | 1.52 | 2.39 | 23.5 | 1969 |
| 3 | "INNA" prediction of [11] | 1 | 1.44 | [3.5, 9.6] | [20.4, 48.1] | [674, 2786] |

[12]. Note that fitting procedure, taking into account the fourth-order coefficient $d_4$, produces the readjustment of the model parameters in (24) to the new values $\{c = 3.5548,\ \delta = 1.32448\} \to \{c = 3.5526,\ \delta = 1.32453\}$. The corresponding values of coefficients $d_n^{\rm V}$ are shown in the third row labelled by 2 in Table 1.

In order to understand how important are the exact values of the higher-order coefficients $d_n$, we employed our model (24) with two different sets of parameters $c$ and $\delta$, shown in rows labelled by $2^+$ and $2^-$ in Table 1. One set, $2^+$, roughly speaking, enhances the exact values of the coefficients $d_3$ and $d_4$ by approximately $+8\%$ and $+13\%$, correspondingly, while the other one, $2^-$, — reduces them in the same proportion. All coefficients of these models are inside the range of uncertainties determined in [11] using the Improved Naive Non-Abelinization (INNA). Moreover, the difference between the analytic sums of the two models in the region corresponding to $N_f = 4$ is indeed very small, reaching just a mere $\pm 0.05\%$. This gives an evident support for our model evaluation.

Now we are ready to estimate the relative errors, $\Delta_N^{\rm V}[L]$, of the APT series[4] truncation at the $N$th term:

$$\Delta_N^{\rm V}[L] = \frac{\mathcal{D}_\infty^{\rm V}[L] - \mathcal{D}_N^{\rm V}[L]}{\mathcal{D}_\infty^{\rm V}[L]}\,; \quad \mathcal{D}_N^{\rm V}[L] = 1 + \sum_{n\geq 1}^{N} \frac{d_n}{\pi^n}\,\bar{\mathcal{A}}_n[L]\,. \qquad (25)$$

Here $\mathcal{D}_\infty^{\rm V}[L]$ is the resummed APT result in the corresponding $l$-loop approximation, see Eqs. (11), (19), and (22) with substitution $\nu \to 0$.

[4]Note that power series (23) has $\nu = 0$ — for this reason we use here the APT approach.

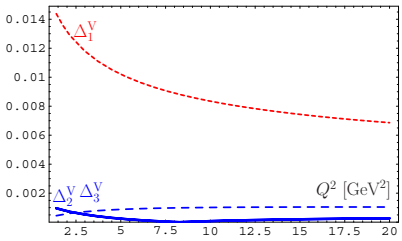


Fig. 3: The relative errors $\Delta_N^V(Q^2)$ evaluated for different values of $N$: $N = 1$ (short-dashed red line), $N = 2$ (solid blue line), and $N = 3$ (dashed blue line) of the truncated APT given by Eq. (25), in comparison with the exact result of the one- and two-loop resummation procedure represented by Eqs. (11) and (19)

In Fig. 3 we show these relative errors for $N = 1, 2, 3$, for the one- and two-loop cases (calculations for the three-loop case is not yet finished). The main result is in some sense surprising: The best order of truncation of the FAPT series in the region $Q^2 = 2 - 20$ GeV$^2$ is reached by employing the N$^2$LO approximation, i.e., by keeping just the $d_2$-term.

We may also compare the numerical values for the resummed quantities, obtained in different loop approximations. We take for this comparison the following $l$-loop QCD scale parameters at $N_f = 3$ flavors: $\Lambda_3^{(l=1)} = 201$ MeV, $\Lambda_3^{(l=2)} = 379$ MeV, and $\Lambda_3^{(l=3)} = 385$ MeV, which have been determined from the condition that the APT prediction for the ratio $R_{e^+e^-}(s = m_Z^2)$ should coincide with the "experimental" value 1.03904, determined in [12]. We obtain the following values of the resummed Adler functions $\mathcal{D}_\infty^{V,\,(l)}$ at $Q^2 = 2\,\text{GeV}^2$: 1.1221, 1.1223, and 1.1257 — for $l = 1$, $l = 2$ and $l = 3$, respectively. We see here a very good stability of our result with respect to loop-order variation. We can also compare our two-loop value (1.1223) with the recent estimate in [13], where the value $\mathcal{D}_\infty^V(Q^2 = 2\,\text{GeV}^2) = 1.1217$ has been obtained in the two-loop approximation using the so-called generalized Pade summation method, — we observe a good agreement of both methods.

## 7. Conclusions

We conclude with reminding that in the APT one has practical renormalization-scheme independence and quick loop convergence that

improves the situation with the role of higher-loop corrections. As a result of quick loop convergence, the two-loop level is practically sufficient. The Fractional APT (FAPT) provides an effective tool to apply the APT approach for renormgroup-improved perturbative amplitudes.

In both the APT and FAPT approaches we describe the resummation procedures that produce finite resummed answers for perturbative quantities if one knows the generating functions $P(t)$ for the perturbative coefficients.

Using quite simple model generating function $P(t)$ for the Adler function $\mathcal{D}(Q^2)$ we show that already at the $\mathrm{N^2LO}$, i. e. with taking into account the $d_2\,\mathfrak{A}_2$ term, being the analog of $d_2\,\alpha_s^2$ term, an accuracy is of the order 0.1%.

**Acknowledgements**

It is a pleasure to thank my collaborators Sergey Mikhailov, Dmitry Shirkov, and Nico Stefanis for numerous discussions and useful remarks. The fruitful remarks and discussions with Konstantin Chetyrkin, Andrey Grozin, Andrey Kataev, Alexey Pivovarov, and Oleg Teryaev are also greatly acknowledged. This work was supported by the RFBR grant No. 11-01-00182, the BRFBR–JINR grant (contract No. F10D-001) and the Heisenberg–Landau Program (grant 2011).

1. N. N. Bogoliubov, A. A. Logunov, and D. V. Shirkov, Sov. Phys. JETP **10**, 574 (1960).
2. A. V. Radyushkin, JINR Rapid Commun. **78**, 96 (1996) [JINR Preprint, E2-82-159, hep-ph/9907228]; N. V. Krasnikov and A. A. Pivovarov, Phys. Lett. B **116**, 168 (1982).
3. H. F. Jones and I. L. Solovtsov, Phys. Lett. B **349**, 519 (1995).
4. D. V. Shirkov and I. L. Solovtsov, JINR Rapid Comm. **2**[76], 5 (1996); Phys. Rev. Lett. **79**, 1209 (1997).
5. K. A. Milton and I. L. Solovtsov, Phys. Rev. D **55**, 5295 (1997); K. A. Milton, I. L. Solovtsov, and O. P. Solovtsova, Phys. Lett. B **415**, 104 (1997); Kimball A. Milton and Olga P. Solovtsova, Phys. Rev. D **57**, 5402 (1998); I. L. Solovtsov and D. V. Shirkov, Phys. Lett. B **442**, 344 (1998); A. P. Bakulev, A. V. Radyushkin, and N. G. Stefanis, Phys. Rev. D **62**, 113001 (2000); D. V. Shirkov, Theor. Math. Phys. **127**, 409 (2001); Eur. Phys. J. C **22**, 331 (2001).
6. D. V. Shirkov and I. L. Solovtsov, Theor. Math. Phys. **150**, 132 (2007).

7. A. I. Karanikas and N. G. Stefanis, Phys. Lett. B **504**, 225 (2001); *ibid.* **636**, 330–331(E) (2006).

8. A. P. Bakulev, S. V. Mikhailov, and N. G. Stefanis, Phys. Rev. D **72**, 074014, 119908(E) (2005); Phys. Rev. D **75**, 056005 (2007); **77**, 079901(E) (2008); A. P. Bakulev, A. I. Karanikas, and N. G. Stefanis, Phys. Rev. D **72**, 074015 (2005); A. P. Bakulev, Phys. Part. Nucl. **40**, 715 (2009); N. G. Stefanis, ArXiv:0902.4805 [hep-ph].

9. S. V. Mikhailov, JHEP **0706**, 009 (2007).

10. A. P. Bakulev and S. V. Mikhailov, in *Proceedings of International Seminar on Contemporary Problems of Elementary Particle Physics, Dedicated to the Memory of I. L. Solovtsov, Dubna, January 17–18, 2008.*, Eds. A. P. Bakulev *et al.* (JINR, Dubna, 2008), pp. 119–133 [ArXiv:0803.3013 [hep-ph]].

11. A. P. Bakulev, S. V. Mikhailov, and N. G. Stefanis, JHEP **1006**, 085 (2010).

12. P. A. Baikov, K. G. Chetyrkin, J. H. Kühn, Phys. Rev. Lett. **101**, 012002 (2008); Phys. Rev. Lett. **104**, 132004 (2010).

13. G. Cvetic, R. Kogerler, arXiv:1107.2902 [hep-ph] (2011).

# HARD SCATTERING ON LIGHT NUCLEI: A CONVENIENT WAY TO STUDY PARTON CORRELATIONS

Giorgio Calucci and Daniele Treleani

*Dipartimento di Fisica dell'Università di Trieste*
*INFN Sezione di Trieste, Italia*

**Abstract**

The one-body partonic distributions in the hadrons are well investigated using electromagnetic or weak interactions.

If we wish to exploit the same procedure to study the two-body distributions we should study the very rare events with multiple electromagnetic or weak interactions on the same hadron. The alternative is to study events with hard QCD double scattering of partons of the same hadron, such events become more and more abundant when the energy of the colliding hadrons grows. In fact at very high energies even the parton at small fractional momentum $x$ may suffer collisions with momentum transfer large enough to allow a perturbative treatment [1–14].

## 1. Motivation

What do we mean by `correlation?`. The word can express at least two properties of the multiparticle production: 1-uncorrelated production is described by Poisson distribution of the multiplicities, every deviation from this distribution represents a number correlation. 2-two parton can be correlated in phase space, *e.g.* in fractional light-cone momentum and transverse coordinate, this will result in a correlation of the final products, like jets.

Typical processes where correlations may show up and play a relevant role are the multiple partonic interaction that take place in hdronic high energy interactions. If the total energy is really high

even parton with small fractional momentum, and so large flux, can suffer scattering with large momentum transfer so that their interaction can be treated in perturbative QCD. An efficient tool to study correlations is given by the effective cross section and its generalizations: one defines the effective cross section as $\sigma_{\rm eff} = {\sigma_S}^2/(2 \cdot \sigma_D)$. $\sigma_S$ is the integrated inclusive cross section for one hard scattering, $\sigma_D$ is the integrated inclusive cross section for two hard scatterings.

This definition can be generalized for $K$-hard scatterings: in particular for triple scattering by defining the dimensionless parameters $\tau_3$ through $\sigma_3 = (\sigma_S)^3/[3!(\sigma_{\rm eff})^2\tau_3]$.

Intuitively: $\sigma_{\rm eff}$ is related to the size of the hadron, but this is not completely true there are possible concurrent effects from correlations among the partons and differences in multiplicity distribution.

This can be exemplified by two extreme situations:

1. Configurations with high multiplicity are frequent so many double collisions are produced and then $\sigma_{\rm eff}$ becomes small.
2. Partons are strictly correlated so that if one collides, another collides, again $\sigma_{\rm eff}$ becomes small.

Observing multiple collisions both on free nucleons and on nucleons bound in light nuclei helps in separating the different form of correlations.

## 2. Double Nucleon-Deuteron Collision

This process is described by the following `cut forward graphs`.

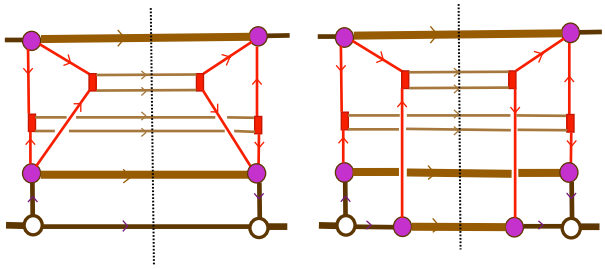

The graph *a*) describes a collision where one bound nucleon interacts twice and the other is a spectator, the information we get is essentially the same as we get from free-nucleon collision.

The graph *b*) describes a collision where both bound nucleon interact once, the multiplicity distribution and the possible correlations enter differently on the proton side and on the deuteron side, some new information is made available.

The cross sections when both nucleons interact and when only one nucleon interacts (twice) are respectively

$$\begin{aligned}
\sigma_{1,1} &= \frac{1}{(2\pi)^3}\int \Gamma(x_1,x_2,b_1,b_2)\Gamma(x_1'/Z,\beta_1)\Gamma(x_2'/(2-Z),\beta_2)\times \\
&\times \frac{d\hat{\sigma}(x_1,x_1')}{d\Omega_1}\frac{d\hat{\sigma}(x_2,x_2')}{d\Omega_2}\,\frac{|\Psi_D(Z,B)|^2}{Z(2-Z)}\times \\
&\times dBdZ\prod_{i=1,2} db_i d\beta_i dx_i dx_i' d\Omega_i/8\;\delta(B+b_1-b_2-\beta_1+\beta_2),\\
\sigma_{2,0} &= \frac{1}{(2\pi)^3}\int \Gamma(x_1,x_2,b_1,b_2)\Gamma(x_1'/Z,x_2'/Z,\beta_1,\beta_2)\times \\
&\times \frac{d\hat{\sigma}(x_1,x_1')}{d\Omega_1}\frac{d\hat{\sigma}(x_2,x_2')}{d\Omega_2}\,\frac{|\Psi_D(Z,B)|^2}{Z(2-Z)}\times \\
&\times dBdZ\prod_{i=1,2} db_i d\beta_i dx_i dx_i' d\Omega_i/8\;\delta(b_1-b_2-\beta_1+\beta_2).
\end{aligned}$$

The ingredients of these expression are: $\Gamma(x_1'/Z,\beta_1)$, $\Gamma(x_1,x_2,b_1,b_2)$, one and two parton structure function of the hadron, $\Psi_D(Z,B)$, deuteron wave function.

The variables are the fraction of light-cone momenta and the transverse position. There is a further graph describing a collision

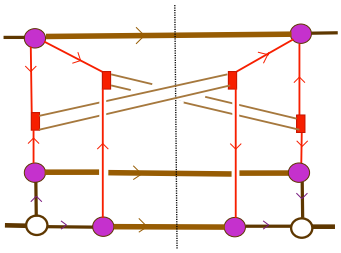

where both bound nucleon interact once, but the light-cone momenta carried away on the left are different from the same momenta carried away on the right, there is a mismatch on the nuclear wave function which makes the overall contribution smaller. If we look more closely to this graph we realize that the contribution is really small when the momenta carried out by the partons are different, it becomes more and more sizable when the light-cone momenta of the two partons approach the same value. Note finally that the same process can happens on Tritium or on $^3$He nucleus, in this case we have at least one spectator nucleon and so nothing really new is found in comparison with the Deuteron case.

## 3. Triple Collision

Here we find the following graphs (*drawn for the Triton case*). In the *first* graph we find two spectators (one spectator if the target is a Deuteron). In the *second* graph all three bound nucleons interact (*only Triton*). The *third and fourth* graph correspond both to two intercting bound nucleons; the *fourth* graph is an interference term. Also here we have for the interference terms a mismatch in the lon-

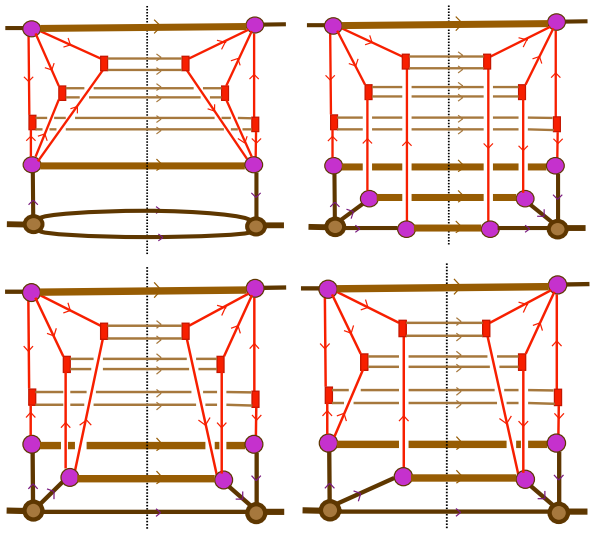

gitudinal variables of the nuclear wave function, the case where this contribution is relevant is now when the non diagonal parton carries away small momentum.[1]

From the graphs we get the analytical expression as before in the double-collision case. The most relevant new element is the three-body distribution $\Gamma_3(x_1, x_2, x_3, b_1, b_2, b_3)$. As an example we give the analytical expression for the diagonal contribution to the triple parton scattering cross sections on Deuteron when one nucleon interacts twice and another once, are thus expressed as:

$$\begin{aligned}\sigma_3^{PD}\big|_{2,d} = & \frac{2}{(2\pi)^3}\Gamma(x_1,x_2,x_3;s_1,s_2,s_3)\Gamma(z_1,z_2;b_1,b_2)\Gamma(z_3;,b_3)\times \\ & \times \frac{d\hat{\sigma}}{d\Omega_1}\frac{d\hat{\sigma}}{d\Omega_2}\frac{d\hat{\sigma}}{d\Omega_3}\Big|\frac{4\Phi_D(Z,B)}{M_D^2-2(\mu_1^2/Z_1+\mu_2^2/Z_2)}\Big|^2 dB \times \\ & \times ds_1 ds_2 ds_3\, db_1 db_2 db_3\, \delta(b_1-b_2-s_1+s_2)\,\delta(b_1-b_3-s_1+s_3)\times \\ & \times dx_1 dx_2 dx_3\, dz_1 dz_2 dz_3\, d\Omega_1 d\Omega_2 d\Omega_3/8^3\,\delta(Z_1+Z_2-2)\times \\ & \times dZ_1 dZ_2/Z_1 Z_2\ .\end{aligned}$$

We see explicitly wherefrom the correlations may find their origin: We have the size of the one-body, two-body, three-body distributions $\Gamma$, they control how much the final distribution in number deviates from a Poissonian distribution, and there is the dependence on $x_i, b_i$ of the $\Gamma$, in particular how much the two-body and three-body distributions differ from a factorized expression. If we look at the way in which these elements enter in the final expressions we see two relevant features: the combinations of the $\Gamma_i$ for light nuclei are different from the combination in nucleon-nucleon collision, the $\Gamma_i$ are integrated together with the nuclear wave functions, These facts can yield new informations about the partonic structure of hadrons, not only about one-body, but also about two-and-three-body distributions.

It is possible to give a more explicite form to the relevant elements of the partonic distribution, but at the price of being more model dependent.

[1] Moreover there are crossed graphs, as in the double collision.

## 4. Conclusions and Outlook

Light nuclei provide a tool to analyze the partonic structure of the hadrons. They allow multiple scatterings in conditions different from hadron-hadron collisions and so with a different role of the parameters of the distributions.They are sufficiently simple, they do not blur the fundamental aspects of the interaction: the main aim is to investigate the many-body aspects of the partonic distributions.

A relevant role in the analysis sketched here is played by the knowledge of the nuclear wave function. The relative motion of the nucleons within the nucleus is with good appoximation non relativistic, to use this kind of wave function in a highly relativistic process as the collision we are interested poses essentially a kinematical problem together with a problem of normalization. The nuclear wave function has a relevant role in the various interference terms: they become important when the fractional momentum (or the difference in momenta) of the outgoing partons are small with respect to the spread of the wave function, note the both quantities to be compared are measured by the variables $x, Z$ that are boost-invariant. In the cases we are considering the internal motion is nonrelativistic with good approximation; for heavier nuclei, where the relative motion requires a relativistic treatment further complications may arise.

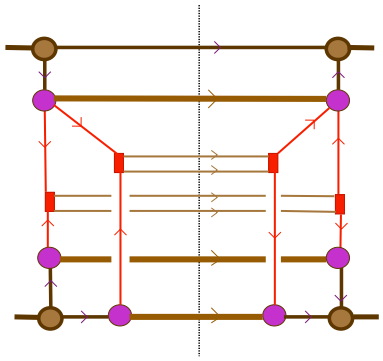

For experiments on light nuclei we can foresee also some sort of checks: in fact the Deuteron-Deuteron collison, (and possibly Deute-

ron-Triton and Triton-Triton) in the same kinematical condition would be described by the same set of parameters, and so in principle we would not get new information, but we could look for the consistency of the whole treatment (the graph gives an example of the D-D process).


1. T. Akesson *et al.* [Axial Field Spectrometer Collaboration], Z. Phys. C **34**, 163 (1987).
2. F. Abe *et al.* [CDF Collaboration], Phys. Rev. Lett. **79**, 584 (1997).
3. F. Abe *et al.* [CDF Collaboration], Phys. Rev. D **56**, 3811 (1997).
4. V. M. Abazov *et al.* [D0 Collaboration], Phys. Rev. D **81**, 052012 (2010) [arXiv:0912.5104 [hep-ex]].
5. V. M. Abazov *et al.* [D0 Collaboration], Phys. Rev. D **83**, 052008 (2011). [arXiv:1101.1509 [hep-ex]].
6. L. Frankfurt, M. Strikman, C. Weiss, Annalen Phys. **13**, 665-672 (2004). [hep-ph/0410307].
7. E. Cattaruzza, A. Del Fabbro, D. Treleani, Phys. Rev. D **70**, 034022 (2004). [hep-ph/0404177].
8. M. Strikman, W. Vogelsang, Phys. Rev. D **83**, 034029 (2011). [arXiv:1009.6123 [hep-ph]].
9. M. Strikman, D. Treleani, Phys. Rev. Lett. **88**, 031801 (2002). [arXiv:hep-ph/0111468 [hep-ph]].
10. N. Paver and D. Treleani, Nuovo Cim. A **70**, 215 (1982).
11. G. Calucci, D. Treleani, Phys. Rev. D **57**, 503-511 (1998). [hep-ph/9707389].
12. G. Calucci, D. Treleani, Phys. Rev. D **83**, 016012 (2011). [arXiv:1009.5881 [hep-ph]].
13. L. Frankfurt, M. Strikman, C. Weiss, Phys. Rev. D **69**, 114010 (2004). [hep-ph/0311231].
14. G. Calucci, D. Treleani, Proc XXIX ISMD World Scient, 2000, 436.

# WEAK NEUTRINOS-MATTER INTERACTIONS DUE TO CONTRACTION OF THE ELECTROWEAK MODEL

N.A. Gromov

*Department of Mathematics, Komi Science Center UrD RAS*

**Abstract**

The very weak neutrinos-matter interactions especially at low energies are explained at the level of classical fields with the help of the gauge group contraction of the standard Electroweak Model. The neutrinos-matter cross-sections change with the neutrino energy are connected with the energy dependence of the contraction parameter.

## 1. Introduction

The standard Electroweak Model based on gauge group $SU(2) \times U(1)$ gives a good description of electroweak processes. Due to this model the W- and Z-bosons was predicted and experimentally observed at the end of the last sentury. Higgs boson is now searched at the modern LHC. The gauge group of the model is the product of two simple groups. In physics it is well known the operation of group contraction [1], which is connected with introduction of special zero tending contraction parameter. This operation transforms, for example, a simple or semisimple group to a nonsemisimple one. Usually for better uderstanding of a physical system it is useful to investigate its limits for limiting values of its physical parameters. In this paper we discuss the modified Electroweak Model with the contracted gauge group $SU(2;j) \times U(1)$. We explain at the level of classical fields the vanishingly small interactions neutrinos with matter especially for low

energies and the decrease of the neutrinos-matter cross-section when energy tends to zero with the help of contraction of gauge group. We connect dimensionless contraction parameter $j \to 0$ with neutrinos energy.

## 2. Standard Electroweak Model

We shall follow the books [2]– [4] in description of standard Electroweak Model. The Lagrangian of this model is given by

$$L = L_B + L_L + L_Q, \tag{1}$$

where boson sector $L_B = L_A + L_\phi$ involve two parts:

$$L_A = \frac{1}{8g^2}\mathrm{Tr}(F_{\mu\nu})^2 - \frac{1}{4}(B_{\mu\nu})^2 =$$

$$= -\frac{1}{4}[(F^1_{\mu\nu})^2 + (F^2_{\mu\nu})^2 + (F^3_{\mu\nu})^2] - \frac{1}{4}(B_{\mu\nu})^2 \tag{2}$$

is the gauge field Lagrangian and

$$L_\phi = \frac{1}{2}(D_\mu\phi)^\dagger D_\mu\phi - \frac{\lambda}{4}\left(\phi^\dagger\phi - v^2\right)^2, \tag{3}$$

where $\phi = \begin{pmatrix} \phi_1 \\ \phi_2 \end{pmatrix} \in C_2$ are the matter fields, represents the matter field Lagrangian.

The fermion sector is the sum of the lepton $L_L$ and quark $L_Q$ Lagrangians. The lepton Lagrangian is taken in the form

$$L_L = L_l^\dagger i\tilde{\tau}_\mu D_\mu L_l + e_r^\dagger i\tau_\mu D_\mu e_r - h_e[e_r^\dagger(\phi^\dagger L_l) + (L_l^\dagger\phi)e_r], \tag{4}$$

where $L_l = \begin{pmatrix} \nu_l \\ e_l \end{pmatrix}$ is the $SU(2)$-doublet, $e_r$ is the $SU(2)$-singlet, $h_e$ is constant, $\tau_0 = \tilde{\tau}_0 = \mathbf{1}$, $\tilde{\tau_k} = -\tau_k$, $\tau_\mu$ are the Pauli matrices, $\phi \in C_2$ are the matter fields and $e_r, e_l, \nu_l$ are the two component Lorentzian spinors.

The quark Lagrangian is given by

$$L_Q = Q_l^\dagger i\tilde{\tau}_\mu D_\mu Q_l + u_r^\dagger i\tau_\mu D_\mu d_r -$$

$$-h_d[d_r^\dagger(\phi^\dagger Q_l) + (Q_l^\dagger \phi)d_r] - h_u[u_r^\dagger(\tilde{\phi}^\dagger Q_l) + (Q_l^\dagger \tilde{\phi})u_r], \qquad (5)$$

where left quark fields form the $SU(2)$-doublet $Q_l = \begin{pmatrix} u_l \\ d_l \end{pmatrix}$, right quark fields $u_r, d_r$ are the $SU(2)$-singlets, $\tilde{\phi}_i = \epsilon_{ik}\bar{\phi}_k, \epsilon_{00} = 1, \epsilon_{ii} = -1$ is the conjugate representation of $SU(2)$ group and $h_u, h_d$ are constants. All fields $u_l, d_l, u_r, d_r$ are two component Lorentzian spinors.

The covariant derivatives are given by the formulas:

$$D_\mu e_r = \partial_\mu e_r - ig'QA_\mu e_r \cos\theta_w + ig'QZ_\mu e_r \sin\theta_w,$$

$$D_\mu L_l = \partial_\mu L_l - i\frac{g}{\sqrt{2}}\left(W_\mu^+ T_+ + W_\mu^- T_-\right) L_l -$$

$$-i\frac{g}{\cos\theta_w} Z_\mu \left(T_3 - Q\sin^2\theta_w\right) L_l - ieA_\mu Q L_l, \qquad (6)$$

where $T_k = \frac{1}{2}\tau_k, k = 1,2,3$ are the generators of $SU(2)$, $T_\pm = T_1 \pm iT_2$, $Q = Y + T_3$ is the electrical charge, $Y$ is the hypercharge, $e = gg'(g^2 + g'^2)^{-\frac{1}{2}}$ is the electron charge and $\sin\theta_w = eg^{-1}$. The gauge fields

$$W_\mu^\pm = \frac{1}{\sqrt{2}}\left(A_\mu^1 \mp iA_\mu^2\right), \quad Z_\mu = \frac{1}{\sqrt{g^2 + g'^2}}\left(gA_\mu^3 - g'B_\mu\right),$$

$$A_\mu = \frac{1}{\sqrt{g^2 + g'^2}}\left(g'A_\mu^3 + gB_\mu\right) \qquad (7)$$

are expressed through the fields

$$A_\mu(x) = -ig\sum_{k=1}^{3} T_k A_\mu^k(x), \quad B_\mu(x) = -ig'B_\mu(x), \qquad (8)$$

which take their values in the Lie algebras $su(2)$ and $u(1)$, respectively.

From the viewpoint of electroweak interactions all known leptons and quarks are divided on three generations. Next two lepton and quark generations are introduced in a similar way to (4) and (5). Full lepton and quark Lagrangians are obtained by the summation over all generations. In what follows we shall regarded only first generations of leptons and quarks.

## 3. Modified Model

We consider a model where the contracted gauge group $SU(2;j) \times U(1)$ acts in the boson, lepton and quark sectors. The contracted group $SU(2;j)$ is obtained [5] by the consistent rescaling of the fundamental representation of $SU(2)$ and the space $C_2$

$$z'(j) = \begin{pmatrix} jz_1' \\ z_2' \end{pmatrix} = \begin{pmatrix} \alpha & j\beta \\ -j\bar{\beta} & \bar{\alpha} \end{pmatrix} \begin{pmatrix} jz_1 \\ z_2 \end{pmatrix} = u(j)z(j),$$

$$\det u(j) = |\alpha|^2 + j^2|\beta|^2 = 1, \quad u(j)u^\dagger(j) = 1 \tag{9}$$

in such a way that the hermitian form

$$z^\dagger z(j) = j^2|z_1|^2 + |z_2|^2 \tag{10}$$

remains invariant, when contraction parameter tends to zero $j \to 0$ or is equal to the nilpotent unit $j = \iota$, $\iota^2 = 0$. The actions of the unitary group $U(1)$ and the electromagnetic subgroup $U(1)_{em}$ in the fibered space $C_2(\iota)$ with the base $\{z_2\}$ and the fiber $\{z_1\}$ are given by the same matrices as on the space $C_2$.

The space $C_2(j)$ of the fundamental representation of $SU(2;j)$ group can be obtained from $C_2$ by substituting $z_1$ by $jz_1$. Substitution $z_1 \to jz_1$ induces another ones for Lie algebra generators $T_1 \to jT_1$, $T_2 \to jT_2$, $T_3 \to T_3$. As far as the gauge fields take their values in Lie algebra, we can substitute the gauge fields instead of transforming the generators, namely:

$$A_\mu^1 \to jA_\mu^1, \quad A_\mu^2 \to jA_\mu^2, \quad A_\mu^3 \to A_\mu^3, \quad B_\mu \to B_\mu. \tag{11}$$

For the gauge fields (7) these substitutions are as follows:

$$W_\mu^\pm \to jW_\mu^\pm, \quad Z_\mu \to Z_\mu, \quad A_\mu \to A_\mu. \tag{12}$$

The fields $L_l = \begin{pmatrix} \nu_l \\ e_l \end{pmatrix}$, $Q_l = \begin{pmatrix} u_l \\ d_l \end{pmatrix}$ are $SU(2)$-doublets, so their components are transformed in the similar way as components of the vector $z$, namely:

$$\nu_l \to j\nu_l, \quad e_l \to e_l, \quad u_l \to ju_l, \quad d_l \to d_l. \tag{13}$$

The right lepton and quark fields are $SU(2)$-singlets and therefore are not transformed.

After transformations (12), (13) and spontaneous symmetry breaking with $\phi^{vac} = \begin{pmatrix} 0 \\ \frac{v}{\sqrt{2}} \end{pmatrix}$ the boson Lagrangian (2),(3) can be represented in the form

$$L_B(j) = L_B^{(2)}(j) + L_B^{int}(j) =$$

$$= \frac{1}{2}(\partial_\mu \chi)^2 - \frac{1}{2}m_\chi^2 \chi^2 - \frac{1}{4}\mathcal{Z}_{\mu\nu}\mathcal{Z}_{\mu\nu} + \frac{1}{2}m_Z^2 Z_\mu Z_\mu - \frac{1}{4}\mathcal{F}_{\mu\nu}\mathcal{F}_{\mu\nu} +$$

$$+ j^2 \left\{ -\frac{1}{2}\mathcal{W}_{\mu\nu}^+ \mathcal{W}_{\mu\nu}^- + m_W^2 W_\mu^+ W_\mu^- \right\} + L_B^{int}(j), \qquad (14)$$

where as usual second order terms describe the boson particles content of the model and higher order terms $L_B^{int}$ are regarded as their interactions. So Lagrangian (14) include charded $W$-bosons with identical mass $m_W = \frac{1}{2}gv$, massless photon $A_\mu$, neutral $Z$-boson with the mass $m_Z = \frac{v}{2}\sqrt{g^2 + g'^2}$ and Higgs boson $\chi$, $m_\chi = \sqrt{2\lambda}v$. The lepton Lagrangian (4) in terms of electron and neutrino fields takes the form

$$L_L(j) = e_l^\dagger i\tilde{\tau}_\mu \partial_\mu e_l + e_r^\dagger i\tau_\mu \partial_\mu e_r - m_e(e_r^\dagger e_l + e_l^\dagger e_r) +$$

$$+ \frac{g\cos 2\theta_w}{2\cos\theta_w} e_l^\dagger \tilde{\tau}_\mu Z_\mu e_l - e e_l^\dagger \tilde{\tau}_\mu A_\mu e_l - g'\cos\theta_w e_r^\dagger \tau_\mu A_\mu e_r +$$

$$+ g'\sin\theta_w e_r^\dagger \tau_\mu Z_\mu e_r + j^2 \left\{ \nu_l^\dagger i\tilde{\tau}_\mu \partial_\mu \nu_l + \frac{g}{2\cos\theta_w}\nu_l^\dagger \tilde{\tau}_\mu Z_\mu \nu_l + \right.$$

$$\left. + \frac{g}{\sqrt{2}}\left[\nu_l^\dagger \tilde{\tau}_\mu W_\mu^+ e_l + e_l^\dagger \tilde{\tau}_\mu W_\mu^- \nu_l\right] \right\} = L_{L,b} + j^2 L_{L,f}. \qquad (15)$$

The quark Lagrangian (5) in terms of u- and d-quarks fields can be written as

$$L_Q(j) = d^\dagger i\tilde{\tau}_\mu \partial_\mu d + d_r^\dagger i\tau_\mu \partial_\mu d_r - m_d(d_r^\dagger d + d^\dagger d_r) -$$

$$- \frac{g}{\cos\theta_w}\left(\frac{1}{2} - \frac{2}{3}\sin^2\theta_w\right) d^\dagger \tilde{\tau}_\mu Z_\mu d - \frac{e}{3} d^\dagger \tilde{\tau}_\mu A_\mu d -$$

$$-\frac{1}{3}g'\cos\theta_w d_r^\dagger \tau_\mu A_\mu d_r + \frac{1}{3}g'\sin\theta_w d_r^\dagger \tau_\mu Z_\mu d_r -$$

$$+j^2\Big\{u^\dagger i\tilde{\tau}_\mu \partial_\mu u + u_r^\dagger i\tau_\mu \partial_\mu u_r - m_u(u_r^\dagger u + u^\dagger u_r) +$$

$$+\frac{g}{\cos\theta_w}\left(\frac{1}{2}-\frac{2}{3}\sin^2\theta_w\right)u^\dagger\tilde{\tau}_\mu Z_\mu u + \frac{2e}{3}u^\dagger\tilde{\tau}_\mu A_\mu u +$$

$$+\frac{g}{\sqrt{2}}\left[u^\dagger\tilde{\tau}_\mu W_\mu^+ d + d^\dagger\tilde{\tau}_\mu W_\mu^- u\right] + \frac{2}{3}g'\cos\theta_w u_r^\dagger\tau_\mu A_\mu u_r -$$

$$-\frac{2}{3}g'\sin\theta_w u_r^\dagger\tau_\mu Z_\mu u_r\Big\} = L_{Q,b} + j^2 L_{Q,f}, \qquad (16)$$

where $m_e = h_e v/\sqrt{2}$ and $m_u = h_u v/\sqrt{2}$, $m_d = h_d v/\sqrt{2}$ represents electron and quark masses.

The full Lagrangian of the modified model is the sum

$$L(j) = L_B(j) + L_Q(j) + L_L(j) = L_b + j^2 L_f. \qquad (17)$$

The boson Lagrangian $L_B(j)$ was discussed in [6], where it was shown that masses of all particles of the Electroweak Model remain the same under contraction $j^2 \to 0$. In this limit the contribution $j^2 L_f$ of neutrino, $W$-boson and $u$-quark fields as well as their interactions with other fields to the Lagrangian (17) will be vanishingly small in comparison with contribution $L_b$ of electron, $d$-quark and remaining boson fields. So Lagrangian (17) describes very rare interaction neutrino fields with the matter for low energies. On the other hand, contribution of the neutrino part $j^2 L_f$ to the full Lagrangian is risen when the parameter $j^2$ is increased, that again corresponds to the experimental facts. The dependence of $j$ on neutrino energy can be obtained from the experimental dates.

In the mathematical language the fields space of the standard electroweak model is fibered after the contraction in such a way that neutrino, $W$-boson and $u$-quark fields are in the fiber, whereas all other fields are in the base. In order to avoid terminological misunderstanding let us stress that we regard locally trivial fibering, which is defined by the projection in the field space. This fibering is understood in the context of semi-Riemannian geometry [7, 8] and has nothing to do with the principal fiber bundle. The simple and best

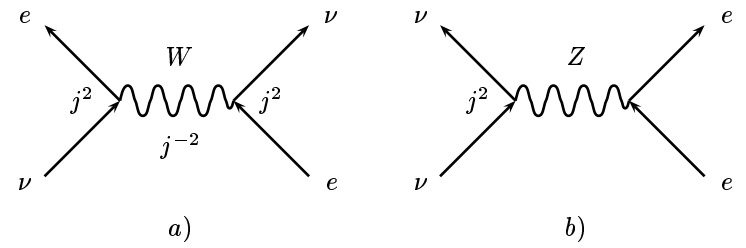


Fig. 1: Neutrino elastic scattering on electron.

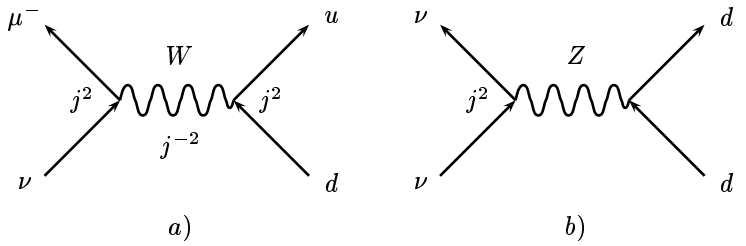


Fig. 2: Neutrino elastic scattering on quarks.

known example of such fiber space is the nonrelativistic space-time with one a dimensional base, which is interpreted as time, and a three dimensional fiber, which is interpreted as proper space. It is well known, that in nonrelativistic physics the time is absolute and does not depend on the space coordinates, while the space properties can be changed in time. The space-time of the special relativity is transformed to the nonrelativistic space-time when dimensionfull contraction parameter — velocity of light $c$ — tends to the infinity and dimensionless parameter $\frac{v}{c} \to 0$.

## 4. Rarely Neutrino-Matter Interactions

To establish the physical meaning of the contraction parameter we consider neutrino elastic scattering on electron and quarks. The corresponding diagrams for the neutral and charged currents interactions are represented in Fig. 1 and Fig. 2.

Under substitutions (12),(13) both vertex of diagram in Fig. 1,$a$) are multiplied by $j^2$, as it follows from lepton Lagrangian (15). The

propagator of virtual fields $W$ according to boson Lagrangian (14) is multiplied by $j^{-2}$. Indeed, propagator is inverse operator to operator of free field, but the later for $W$-fields is multiplied by $j^2$.

So in total the probability amplitude for charged weak current interactions is transformed as $\mathcal{M}_W \to j^2\mathcal{M}_W$. For diagram in Fig. 1,*b*) only one vertex is multiplied by $j^2$, whereas second vertex and propagator of $Z$ virtual field do not changed, so the corresponding amplitude for neutral weak current interactions is transformed in a similar way $\mathcal{M}_Z \to j^2\mathcal{M}_Z$. A cross-section is proportionate to an squared amplitude, so neutrino-electron scattering cross-section is proportionate to $j^4$. For low energies $s \ll m_W^2$ this cross-section is as follows [3]

$$\sigma_{\nu e} = G_{\mathrm{F}}^2 s f(\xi) = \frac{g^4}{m_w^4}\tilde{f}(\xi), \tag{18}$$

where $G_{\mathrm{F}} = 10^{-5}\frac{1}{m_p^2} = 1,17 \cdot 10^{-5}\ GeV^{-2}$ is Fermi constant, $s$ is squared energy in c.m. system, $\xi = \sin\theta_w$, $\tilde{f}(\xi) = f(\xi)/32$ is function of Weinberg angle. On the other hand, taking into account that contraction parameter is dimensionless, we can write down

$$\sigma_{\nu e} = j^4\sigma_0 = (G_{\mathrm{F}} s)(G_{\mathrm{F}} f(\xi)) \tag{19}$$

and obtain

$$j^2(s) = \sqrt{G_{\mathrm{F}} s} \approx \frac{g\sqrt{s}}{m_W}. \tag{20}$$

Neutrino elastic scattering on quarks due to neutral and charged currents are pictured in Fig. 2. Cross-sections for neutrino-quarks scattering are obtained in a similar way as for the lepton case and are as follows [3]

$$\sigma_\nu^W = G_{\mathrm{F}}^2 s\hat{f}(\xi)), \quad \sigma_\nu^Z = G_{\mathrm{F}}^2 s\, h(\xi). \tag{21}$$

Nucleons are some composite construction of quarks, therefore some form-factors are appeared in the expressions for neutrino-nucleons scattering cross-sections. The final expression

$$\sigma_{\nu n} = G_{\mathrm{F}}^2 s\hat{F}(\xi) \tag{22}$$

coincide with (18), i.e. this cross-section is transformed as (19) with the contraction parameter (20). At low energies scattering interactions make the leading contribution to the total neutrino-matter

cross-section, therefore it has the same properties (19),(20) with respect to contraction of the gauge group.

## 5. Conclusion

We have suggested the modification of the standard Electroweak Model by the contraction of its gauge group. At the level of classical (non-quantum) gauge fields the very weak neutrino-matter interactions especially at low energies can be explained by this model. The zero tending contraction parameter depend on neutrino energy in accordance with the energy dependence of the neutrino-matter interaction cross-section.

The limit transition $c \to \infty$ in special relativity was resulted in the notion of group contraction [1]. In our model on the contrary the notion of group contraction is used to explain the fundamental limit process of nature.

### Acknowledgements

I thank A.A. Slavnov for helpful discussions and the organizers of the conference, especially L.L. Jenkovszky, for hospitality. This work was supported by the program "Fundamental problems of nonlinear dynamics" of Russian Academy of Sciences.

1. E. Inönü, E.P. Wigner, Proc. Nat. Acad. Sci. USA **39**, 510 (1953).
2. V.A. Rubakov, *Classical Gauge Fields* (Editorial URSS, Moscow, 1999) [in Russian].
3. L.B. Okun', *Leptons and quarks* (Editorial URSS, Moscow, 2005) [in Russian].
4. M.E. Peskin, D.V. Schroeder, *An Introduction to Quantum Field Theory* (Addison-Wesley, 1995).
5. N.A. Gromov, Proc. Komi SC UrB RAS **1**(5), 5 (2010) (in Russian).
6. N.A. Gromov, Phys. Atom. Nucl. **73**, 326 (2010).
7. R.I. Pimenov, Vestnik Leningrad Univ. **1**, 137 (1965) (in Russian).
8. N.A. Gromov, Phys. At. Nucl. **72**, 794 (2009).

# LESSONS FROM THE FIRST MEASUREMENTS OF ELASTIC pp SCATTERING AT THE LHC

L. Jenkovszky[1] and D. Lontkovskyi[2]

[1]*Bobolyubov Institute for Theoretical Physics,*
*Nat. Acad. of Sci. of Ukraine,*
*Kiev, 03680 Ukraine, e-mail: jenk@bitp.kiev.ua*
[2]*Physics Department,*
*Taras Shevchenko National University of Kyiv,*
*01033 Kyiv, Ukraine, e-mail: dlont@mail.univ.kiev.ua*

**Abstract**

Recent data on elastic proton-proton scattering measured by the TOTEM Collaboration at the LHC are scrutinized with special emphasis on the dip-bump structure in the differential cross section.

First results on elastic proton-proton scattering from the LHC at 7 TeV appeared recently [1]. The data on the differential cross sections cover the range $0.36 < -t < 2.5$ GeV$^2$. In the measured range a single minimum at $-t = 0.53$ GeV$^2$ is clearly seen and no more dips are observed at larger $|t|$ (no recurrences). None of the existing models of elastic scattering succeeded to predict the value of the differential cross section in the dip region: they are off by a factor from 2 to 4, as seen in Fig. 4 of the TOTEM paper [1]. While the departure of the predictions for total cross section differ from the new data [2] only quantitatively, typically by about $(10-20)\%$, the dip (or dips), that can be created in many ways, deviate from the data

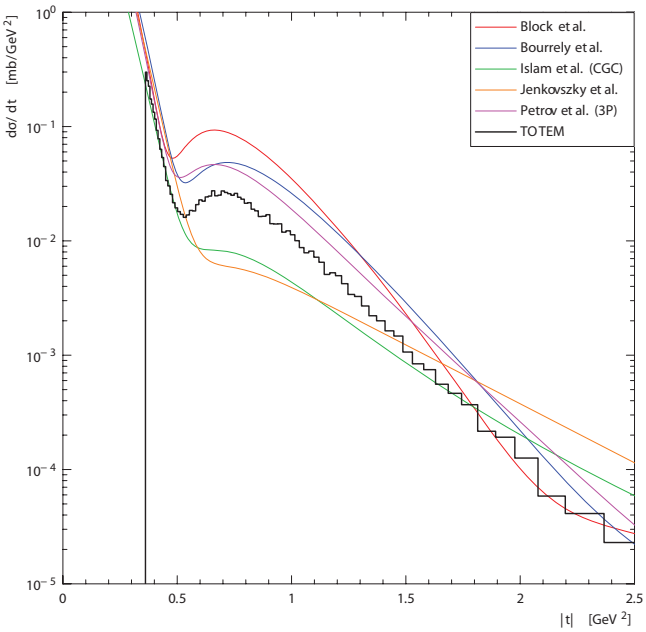


Fig. 1: $pp$ elastic differential cross section as measured recently by the TOTEM Collaboration [1] at the LHC. Our predictions are shown in orange

qualitatively, as seen from Fig. 4 of Ref. [1]. Thus, the dip-bump phenomenon is critical in understanding the dynamics of diffraction.

The existing models (for a recent review see, e.g. [3]) largely can be classified by the following criteria (implying also "mixed options"):

1. Models with or without the Odderon (apart from the Pomeron) making $pp$ and $\bar{p}p$ scattering different[1]);

2. The dip is created at the "Born" level, e.g. by geometrical consideration (sharp edge of a "black disc"-like profile function or a "hole" in its center – a "ring" replacing the "disc");

3. The diffractive pattern arises from unitarity correction to the otherwise smooth cone in $t$: e.g. in the Glauber-Sitenko approach to rescattering.

[1]The contribution from secondary Reggeons at the LHC can be neglected, see [5].

The experimental data on proton-proton elastic and inelastic scattering emerging from the measurements at the LHC, call for an efficient model to fit the data and identify their diffractive (Pomeron) component [3]. To this end, there is a need for a reasonably simple and feasible model of the scattering amplitude, yet satisfying the basic theoretical requirements such as analyticity, crossing and unitarity. In our opinion, the expected (dip-bump) structure in the differential cross section is most critical in discriminating models of high-energy diffraction, although other observables, such as the rate of the increase of the total cross sections, the ratio of the elastic to total cross section, details concerning the shape of the elastic cross section, such as its "break" at small $|t|$ and flattening at large $|t|$ are important as well.

In the present paper, rather than sticking to a particular model, we perform an "anatomic" analysis of the dip phenomena by means of a most general expression for the differential cross section suggested by Phillips and Barger (PB) [4] in analyzing the ISR data on $pp$ scattering, where the dip phenomenon was first observed in 1972. The approach of PB is the simplest universal way of modeling the phenomena: independent of the dynamics, the dip (diffraction minimum) arises from the interference of two (linear) exponentials in $t$ with a relative phase $\phi$:

$$\frac{d\sigma}{dt} = |\sqrt{A}\exp(Bt/2) + \sqrt{C}\exp(Dt/2 + i\phi)|^2, \tag{1}$$

where $\sqrt{A}$, $B$, $\sqrt{C}$, $D$ and $\phi$ were determined independently at each energy, i.e. energy dependence enters here parametrically.

We use this formula to fit the $pp$ elastic scattering data from the ISR energy region up to 7 TeV at the LHC. The PB formula fits the data reasonably, as shown in Fig. 2. The observed behavior of the extracted parameters $\sqrt{A}$, $B$, $\sqrt{C}$, $D$ may suggest simple Regge-type energy dependence, namely: the Donnachie-Landshoff [6] type parametrization for the rise of the cross sections with energy, $\sqrt{A} \to \sqrt{A(s)} = \sqrt{A_1}s^{\epsilon_1}$ and similarly $\sqrt{C} \to \sqrt{C(s)} = \sqrt{C_1}s^{\epsilon_2}$, next $B \to B(s) = B_0 + B_1 \ln s$ and $D \to D(s) = D_0 + D_1 \ln s$, where $s$ implies a dimensionless $s/1000$ GeV$^2$. In doing so a constant term can be added in (1), although its presence/importance may be a matter of

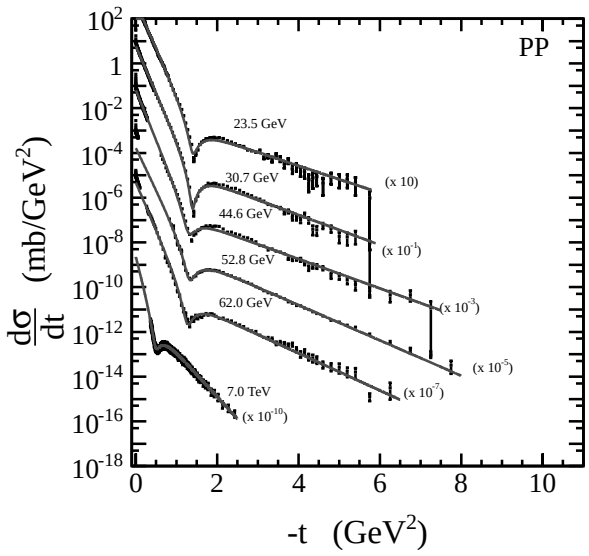


Fig. 2: Results of a fits to $pp$ data with the PB parametrization

debate [6]. In Fig. 3 the extracted parameters are compared to these simple parametrizations.

We proceed further by inserting the assumed energy dependence of the parameters directly into Eq. (1) and fitting the free parameters to the data. The results of this approach are shown in Fig. 4, and in Table 1.

To summarize, we have "translated" the experimental data on elastic $pp$ scattering from the ISR to the LHC from the $t$-dependent differential cross section, for fixed values of $s$, into a limited num-

**T a b l e 1: Parameters obtained from the fit to the $pp$ data**

| Parameter name | Value |
|---|---|
| $\sqrt{A}$ | 2.2 $10^1$ |
| $B_0$ | 1.4 |
| $B_1$ | 3.0 $10^{-1}$ |
| $\sqrt{C}$ | 7.0 $10^3$ |
| $D_0$ | 9.8 |
| $D_1$ | 4.6 $10-1$ |
| $\epsilon_1$ | 1.4 |
| $\epsilon_2$ | 1.1 |
| $\phi$ | 3.5 |

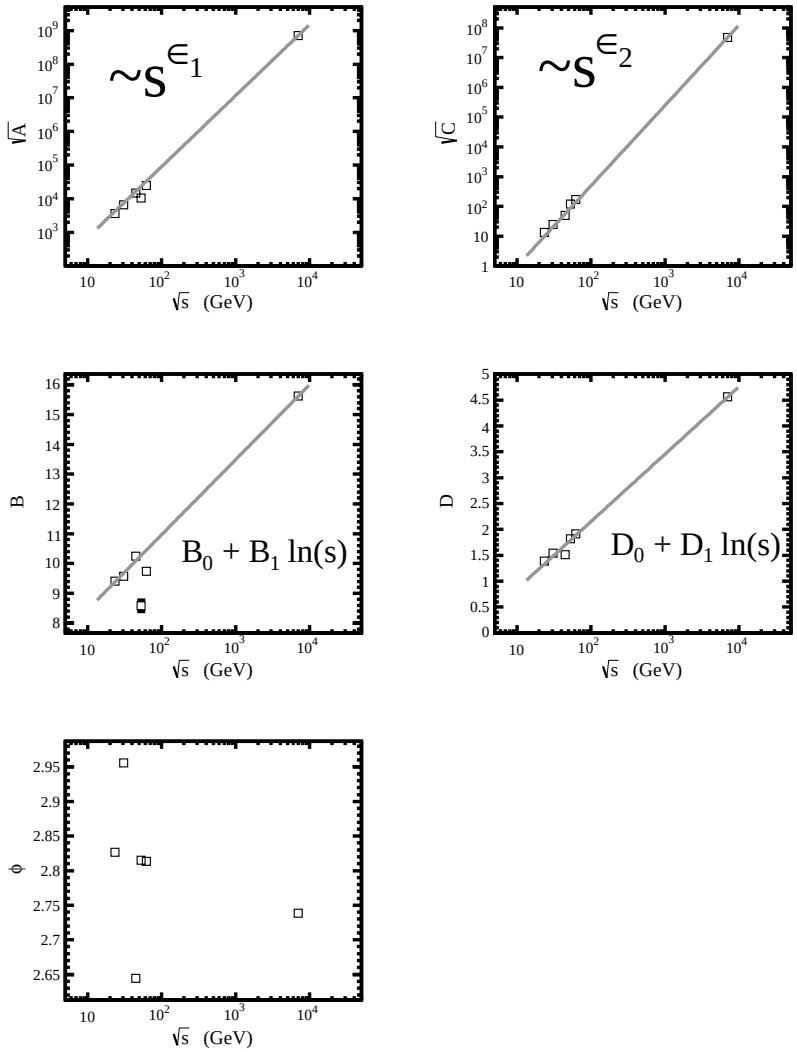


Fig. 3: Parameters obtained from fits to $pp$ data compared with the Donnachie-Landshoff type parametrization

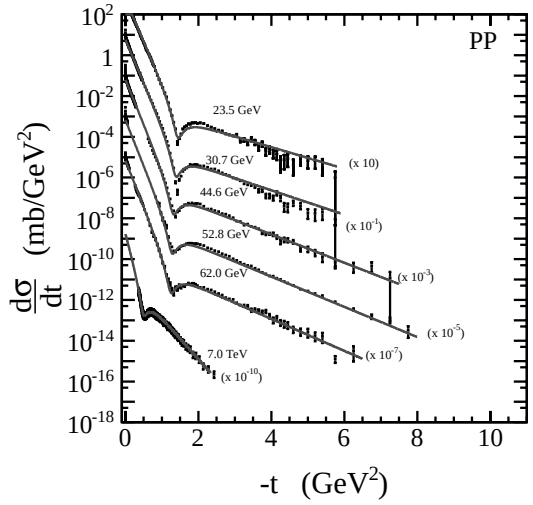


Fig. 4: Results of a fit to $pp$ data with the modified energy-dependent PB parametrization

ber of $s$-dependent parameters appearing in Eq. (1). Since this parametrization is simple and universal, the above results can be used in further modifications/generalizations, e.g. those of Regge-pole type, like those of Refs. [5] or [7]. Notice that the predictions of Ref. [7] are confirmed by the recent LHC data both on elastic differential and total cross sections. It should be also remembered that model-building is only a transitory, albeit important, stage in the study of the strong interaction. More ambitious are attempts to understand the phenomena by means of a physical picture, such as that of Ref. [8] based on (re)scattering of the constituents - quarks and gluons.

**Acknowledgements**

We thank Tamás Csörgő, Mario Deile and Jan Kašpar for useful discussions and correspondence.

1. P. Aspell *et. al.* (TOTEM Collaboaration), Europhys. Lett. **95**, 41001 (2011); arXiv:1110.1385.

2. G. Antchev *et al.* (TOTEM Collaboration), *First measurement of the total proton-proton cross section at the LHC energy of 7 TeV*, to be published in EPL; arXiv:1110.1395.

3. R. Fiore *et al.*, Int. J. Mod. Phys. A **24**, 2551-2559 (2009); arXiv:0810.2902.

4. R.J.J. Phillips and V. Barger, Phys. Lett. B **46**, 412 (1973).

5. L. Jenkovszky, D. Lontkovskyi, and A. Lengyel, *The Pomeron and Odderon in elastic, inelastic and total cross sections at the LHC*, Int. J. Mod. Phys., in press; arXiv:1105.1202.

6. S. Donnachie and P. Landshoff, Phys. Lett. B **123**, 345 (1983); Nucl. Phys. **267**, 690 (1985).

7. L.L. Jenkovszky, B.V. Struminsky and A.N. Shelkovenko, Yad. Fizika **46**, 1200 (1987) (English translation: Sov. J. Nucl. Phys.); see also: A.N. Vall, L.L. Jenkovszky and B.V. Struminsky, EChAYa **19**, 180 (1988) (English translation: Sov. J. Particles and Nuclei, **19**, 77 (1988)).

8. Seiichi Wakaizumi, Progress in Theor. Phys. **60**, 1040 (1978); R.J. Glauber and J. Velasco, *Multiple diffraction theory of pp scattering at* 546 *GeV*, CERN TH Preprint 3967/84.

# NON-COMMUTATIVE MODEL OF QUARK INTERACTIONS

V.V. Khruschov

*NRC "Kurchatov Institute", Moscow*

**Abstract**

A non-commutative model of quark interactions with the generalized O(2,6) symmetry in quantum phase space is considered. The model is based on the Snyder-Yang algebra, which includes in the relativistically invariant way two parameters $\mu_c$ and $\lambda_c$ with dimensionality of mass and length. The equations of motion obtained in the framework of the model contain the rising potentials which provide the confinement of color particles. The values of the parameters $\mu_c$ and $\lambda_c$, as well as the masses of constituent and current quarks are estimated.

## 1. Introduction

Now it is generally accepted that QCD is the theory of strong interaction of quarks and gluons. As is known QCD operates with quantum color fields of quarks and gluons defined in the conventional four dimensional Minkowski spacetime $M_{1,3}$ [1, 2]. QCD has considerable verification at high interaction energies, however some problems remain unsolved in the low energy region, such as a confinement of color particles and a violation of chiral invariance of the massless QCD lagrangian.

An origin of confinement, the interesting physical phenomenon, is under active study from the begining of the QCD era [3]. Today we have no rigorous proof of this fact in spite of considerable efforts. Color particle confinement is investigated in the frame of different approaches, for instance, such as the lattice QCD, the Schwinger-Dyson equations, massive transverse gluons, potential models, *etc*

[4–7]. In the present paper we consider a non-commutative model of quark interactions, that has the ability to solve the problem of color particle confinement. This model is based on the Snyder-Yang algebra (SYA) [8,9] for operators which have the meaning of angular momenta and generalized momenta and coordinates of color particle.

The SYA is dependent on two new fundamental constants with dimensionality of mass and length, which are responsible for non-commutativity of momenta and coordinates. The maximal non-commutativity of momenta and coordinates is accomplished in the frame of the generalized Snyder-Yang algebra (GSYA) with three new constants with dimensionality of mass, action and length, additional to the standard ones $c$ and $\hbar$ [10]. In the construction of non-commutative model of quark interactions, it is convenient to use an additional prerequisite, namely, the O(2,6) invariance in a phase space of a color particle, which have been proposed in Ref. [11].

## 2. Restrictions for Color Particle Motion Based on Extended Symmetry in Quantum Phase Space

Since we assume that coordinates and momentum components of a quantum color particle can be non-commutative in the general case, let us start with GSYA to be considered in the following form [8–11]:

$$
\begin{aligned}
&[F_{ij}, F_{kl}] = i(g_{jk}F_{il} - g_{ik}F_{jl} + g_{il}F_{jk} - g_{jl}F_{ik}),\\
&[F_{ij}, p_k] = i(g_{jk}p_i - g_{ik}p_j),\\
&[F_{ij}, q_k] = i(g_{jk}q_i - g_{ik}q_j),\\
&[F_{ij}, I] = 0, \quad [p_i, q_j] = i(g_{ij}I + \kappa F_{ij}),\\
&[p_i, I] = i(\mu^2 q_i - \kappa p_i), [q_i, I] = i(\kappa q_i - \lambda^2 p_i),\\
&[p_i, p_j] = i\mu^2 F_{ij}, \quad [q_i, q_j] = i\lambda^2 F_{ij},
\end{aligned}
\tag{1}
$$

where $c = \hbar = 1$, $F_{ij}$, $p_i$, $x_i$ are the generators of the Lorentz group and the operators of momentum components and coordinates, correspondingly, $I$ is the "identity" operator, $i, j, k, l = 0, 1, 2, 3$. The new quantum constants $\mu$ and $\lambda$ have dimensionality of mass and length correspondingly. The constant $\kappa$ is dimensionless in the natural system of units.

When applying the algebra (1) to the description of color particles the condition $\kappa = 0$ can be imposed. Actually it is known the nonzero $\kappa$ leads to the $CP-$violation [10], however strong interactions are invariant with respect to the $P$-, $C$- and $T$-transformations on the high level of precision, so $\kappa = 0$. In this case we obtain the reduction of GSYA to SYA with $\kappa = 0$ for strong interaction color particles. Denoting $\mu$ as $\mu_c$ and $\lambda$ as $\lambda_c$ we write the following commutation relations without the standard commutation relations with Lorentz group generators, which are shown above (see Eqs.(1)).

$$[p_i, q_j] = ig_{ij}I, [p_i, I] = i\mu_c^2 q_i, [q_i, I] = -i\lambda_c^2 p_i,$$
$$[q_i, q_j] = i\lambda_c^2 F_{ij}, \quad [p_i, p_j] = i\mu_c^2 F_{ij}. \tag{2}$$

We take into account difficulties arisen when one try to prove the confinement on the basis of only the QCD first principles, so we suppose that the nonperturbative OCD interaction have the property of an approximated or exact extended spacetime symmetry beyond the Poincare symmetry. In our model we turn from the Poincare symmetry in the Minkowski spacetime to the inhomogeneous O(2,6) symmetry in a phase space of a color particle [11].

In this way we consider the generalized model for a color particle motion, when coordinates and momenta are on equal terms and form an eight dimensional phase space: $h = \{h^A | h^A = q^\mu,\ A = 1,2,3,4,\ \mu = 0,1,2,3,\ h^A = \tau p^\mu, A = 5,6,7,8,\ \mu = 0,1,2,3\}$. $P = \{P^A | P^A = p^\mu,\ A = 1,2,3,4,\ \mu = 0,1,2,3,\ P^A = \sigma q^\mu,\ A = 5,6,7,8,\ \mu = 0,1,2,3\}$. The constants $\tau$ and $\sigma$ have dimensions of length and mass square, correspondingly. Their values can be chosen on the phenomenological ground or with the help of some functions of the quantum constants $\mu$, $\kappa$ and $\lambda$. So the generalized length square

$$L^2 = h^A h_A, \tag{3}$$

and the generalized mass square

$$M^2 = P^A P_A, \tag{4}$$

are invariant under the O(2,6) transformations, where $h_A = g_{AB}h^B$, $g_{AB} = g^{AB} = \mathrm{diag}\{1,-1,-1,-1,1,-1,-1,-1\}$.

Thus we propose that for strong interacting color particles the generalized differential mass squared has the physical meaning:

$$dM^2 = (dp_0)^2 - (dp_1)^2 - (dp_2)^2 - (dp_3)^2 +$$
$$+\sigma^2(dq_0)^2 - \sigma^2(dq_1)^2 - \sigma^2(dq_2)^2 - \sigma^2(dq_3)^2 =$$
$$= (dm)^2 + \sigma^2(ds)^2. \tag{5}$$

An important point is that the coordinates $q^\mu$ and the momentum components $p^\mu$ are the quantum operators satisfied Eqs.(1) or Eqs.(2) in the frame of this approach.

Under these conditions the new Dirac type equation for a spinorial field $\psi$ has the following form:

$$\gamma^A P_A \psi = M\psi, \tag{6}$$

where $\gamma^A$ are the Clifford numbers for the spinorial O(2,6) representation, i.e.

$$\gamma^A\gamma^B + \gamma^B\gamma^A = 2g^{AB}. \tag{7}$$

One can take the product of eq.(6) with $\gamma^A P_A + M$ and apply eqs.(1), then the following equation for $\psi$ can be obtained

$$(p^i p_i + \sigma^2 q^i q_i + 2\Sigma_{i<j} S^{ij} F_{ij} +$$
$$+2\sigma S^0 I)\psi = M^2\psi, S^0 = \frac{i}{2}C^0, S^{ij} = \frac{i}{2}C^{ij}, \tag{8}$$

where

$$C^0 = \gamma^1\gamma^5 g_{00} + \gamma^2\gamma^6 g_{11} + \gamma^3\gamma^7 g_{22} + \gamma^4\gamma^8 g_{33},$$
$$C^{01} = \gamma^1\gamma^2\mu^2 + \gamma^5\gamma^6\sigma^2\lambda^2 + (\gamma^1\gamma^6 - \gamma^2\gamma^5)\sigma\kappa,$$
$$C^{02} = \gamma^1\gamma^3\mu^2 + \gamma^5\gamma^7\sigma^2\lambda^2 + (\gamma^1\gamma^7 - \gamma^3\gamma^5)\sigma\kappa,$$
$$C^{03} = \gamma^1\gamma^4\mu^2 + \gamma^5\gamma^8\sigma^2\lambda^2 + (\gamma^1\gamma^8 - \gamma^4\gamma^5)\sigma\kappa,$$
$$C^{12} = \gamma^2\gamma^3\mu^2 + \gamma^6\gamma^7\sigma^2\lambda^2 + (\gamma^2\gamma^7 - \gamma^3\gamma^6)\sigma\kappa,$$
$$C^{13} = \gamma^2\gamma^4\mu^2 + \gamma^6\gamma^8\sigma^2\lambda^2 + (\gamma^2\gamma^8 - \gamma^4\gamma^6)\sigma\kappa,$$
$$C^{23} = \gamma^3\gamma^4\mu^2 + \gamma^7\gamma^8\sigma^2\lambda^2 + (\gamma^3\gamma^8 - \gamma^4\gamma^7)\sigma\kappa. \tag{9}$$

Eq.(8) contains the oscillator potential, which restricts a motion of a color quark. Besides that we broke the inhomogeneous O(2,6)

symmetry with the help of the commutation relations (1). In the special case $\kappa = 0$ and the commutation relations (2) for SYA we will obtain more simple expressions for the $C^0$ and $C^{ij}$, but the form of the Eq.(8) will remain unchanged.

Eq.(8) can also be applied for a description of a confinement of boson particles such as diquarks and gluons with the same confinement parameter $\sigma$. Moreover, in order to include interactions of quark with gluons, photons, $W^{\pm}$- and $Z$-bosons, one can use a generalized minimum interaction principle and makes the substitution: $P \to P - \sum g_i \widehat{A}_i$, where $g_i$ are interaction constants and $\widehat{A}_i$are matrix gauge fields.

## 3. Estimations of Quark Masses and the $\mu_c$ and $\lambda_c$ Constants

Let us consider some consequences of this approach for determination of color quark characteristics. From the relations (2) it immediately follows nonzero uncertainties for results of simultaneous measurements of quark momentum components. For instance, let $\psi_{1/2}$ is a quark state with a definite value of its spin component along the third axis. Consequently,

$$[p_1, p_2] = i\mu_c^2/2, \tag{10}$$

thus

$$\Delta p_1 \Delta p_2 \geq \mu_c^2/4 \tag{11}$$

and if $\Delta p_1 \sim \Delta p_2$, one gets

$$\Delta p_1 > \mu_c/2, \quad \Delta p_2 > \mu_c/2. \tag{12}$$

We see that the components of the generalized quark momentum $p_{\perp 1,2}$ cannot be measured better than one-half a value of $\mu_c$ [11].

One can get estimations of the $\mu_c$ and $\lambda_c$ values using the quark equation (8). As it is seen, $m^2$ and $p^2$ entered into Eq. (8) can be considered as current (q) and constituent (Q) quark masses squared, respectively. So Eq. (8) indicates that the conventional relation for a current quark $p^2_{\rm cur} = m^2$ in this case should be transform to

$$p^2 = k_*^2 + M^2, \quad M = m + \Delta \tag{13}$$

for a constituent quark, where $M$ is a constituent mass, $k_*$ is an effective value of the quark momentum. $\Delta$ and $k_*$ take into account the contributions from the additional terms of Eq. (8). To estimate the $\mu_c$ and $\lambda_c$ values with the help of the constituent quark mass $M$ and the current quark mass $m$, a ground state $\psi_0$ in a meson has been considered neglecting an orbital angular momentum contribution $L\psi_0$. We use the values of quark energies and its masses evaluated in the framework of the relativistic model of quasi-independent quarks [12] together with Eqs. (13). By this means we obtain the following parameters of the constituent and current $u$-, $d$-, $s$-, $c$-, $b$-quarks within a few percents of the relative uncertainty for these values (Table 1).

**T a b l e 1: Parameters of Q- and q-quarks in MeV's at $k_* = 130$ MeV**

| Quark | $u$ | $d$ | $s$ | $c$ | $b$ |
|---|---|---|---|---|---|
| Q energy | 335 | 339 | 486 | 1608 | 4950 |
| Q mass | 309 | 313 | 468 | 1603 | 4948 |
| q mass | 5 | 9 | 164 | 1299 | 4644 |

The quark parameters written in the Table 1 are not in contradiction with the values, which have been determined as in the frameworks of various models, as in the QCD frameworks [13,14]. Notice that the masses presented above are evaluated at the 130 MeV scale. Now that we have obtained the quark parameters, the $\mu_c$ and $\lambda_c$ values are readily evaluated: $\mu_c \approx 180$ MeV, $\lambda_c \approx 0.36$ Fm.

## 4. Conclusions

The convenience of the considered non-commutative model of quark interactions with the generalized O(2,6) symmetry resides in its ability to include the dimensional parameters, namely $\mu_c$ and $\lambda_c$, in the relativistically invariant way and in an explicit form. This model is able to describe a confining particle, since in the framework of the model the equations of motion (7) and (8) contain the rising potentials which provide the confinement of the particle.

It is interesting that $\mu_c$ value estimated above is approximately equal to the critical temperature $T_c$ of the deconfinement phase transition. If it is not accidental, then an adequate description of the quark-gluon plasma is impossible without incorporating the considered non-commutativity of dynamical observables of color particles.

The further investigation of properties of the model is being carried out at present.


1. N.N. Bogoliubov, A.A. Logunov, A.I. Oksak, and I.T. Todorov, *General principles of quantum field theory* (Nauka, Moscow, 1987) (in Russian).
2. F.J. Yndurain, *Quantum Chromodynamics*, (Springer-Verlag, New York–Berlin–Heidelberg–Tokyo, 1983).
3. R. Alkofer *et al.*, Panel discussion: What *don't* we know about confinement? arXiv:1012.3192[hep-th].
4. J. Greensite, Prog. Part. Nucl. Phys. **51**, 1 (2003).
5. E.S. Swanson, *Hadron Spectroscopy – Theory*, arXiv:0910.3704.
6. A.P. Szczepaniak and E.S. Swanson, Phys. Rev. D **65**, 025012 (2001).
7. R. Alkofer, C.S. Fischer and F.J. Llanes-Estrada, Mod. Phys. Lett. A **23**, 279 (2008).
8. H. Snyder, Phys. Rev. **71**, 38 (1947).
9. C.N. Yang, Phys. Rev. **72**, 874 (1947).
10. A.N. Leznov and V.V. Khruschov, *A general form of commutation relations of discrete space-time theory.* Prep. IHEP 73-38, Serpukhov (1973); V.V. Khruschov and A.N. Leznov, Grav. Cosmol. **9**, 159 (2007).
11. V.V. Khruschov, Grav. Cosmol. **15**, 323 (2009); arXiv:0906.5422[hep-th].
12. V.V. Khruschov, V.I. Savrin, and S.V. Semenov, Phys. Lett. B **525**, 283 (2002); V.V. Khruschov, and S.V. Semenov, Part. Nucl. Lett. **5** [114], 5 (2002); V.V. Khruschov, Proc. XLI Winter School of PNPI RAS, p. 139, arXiv:hep-ph/0702259.
13. V. Borka Jovanovic *et al.*, arXiv:1011.1749[hep-ph].
14. K. Nakamura *et al.* (Particle Data Group), J. Phys. G **37** 075021 (2010).

# THE PROJECT NICA

R. Lednický[1,2], V. Kekelidze[1], A. Kovalenko[1],
I. Meshkov[1], A. Sorin[1], G. Trubnikov[1]

[1] *Joint Institute for Nuclear Research, Dubna, Russia*
[2] *Institute of Physics ASCR, Prague, Czech Republic*

**Abstract**

The present flagship program of Joint Institute for Nuclear Research in Dubna assumes the experimental study of hot and dense strongly interacting QCD matter and polarization phenomena at the new home facility. This goal is proposed to be reached by (i) development of the existing 6 AGeV superconducting synchrotron – Nuclotron as a basis for generation of intense beams over atomic mass range from protons to gold and light polarized ions, (ii) design and construction of the Nuclotron-based Ion Collider fAcility (NICA) with the maximum nucleon-nucleon center-of-mass energy of $\sqrt{s_{NN}} = 11$ GeV and averaged luminosity $10^{27}$ cm$^{-2}$s$^{-1}$ for Au+Au collisions, and (iii) design and construction of the MultiPurpose Detector (MPD) and Spin Physics Detector (SPD) at intersecting beams. Realization of the project will lead to unique conditions for research activity of the world community in the field of relativistic nuclear and spin physics.

## 1. Introduction

The new Nuclotron-based Ion Collider fAcility (NICA) is under construction at the Joint Institute for Nuclear Research (JINR) in Dubna [1]. The research program of the planned experiments at this facility is relevant to understanding the key astrophysical phenomena like the evolution of the early Universe after the Big Bang, formation and structure of neutron stars or the origin of cosmic rays, as well as – to clarifying the physics of relativistic heavy ion collisions and spin phenomena [2–4].

Investigation of hot and dense nuclear matter produced in relativistic heavy ion collisions is a challenging task in modern physics.

It provides information on the in-medium properties of hadrons and nuclear matter equation of state, allows for a search of possible manifestations of the deconfinement and/or chiral symmetry restoration phase transitions, mixed phase and critical end-point by scanning various excitation functions in beam energy, atomic number and collision centrality. A number of new phenomena has already been discovered: strong stopping power of colliding nuclei, strong collective flows of secondary particles pointing to a formation of a new form of matter at top RHIC energies behaving like almost ideal and rapidly expanding liquid, constituent quark number scaling of the elliptic flow, a plateau in the apparent temperature at SPS energies and a broadening of transverse momentum distributions at higher energies, irregularities in the beam-energy behavior of the $K/\pi$ ratio, drastic enhancement of multistrange hyperon production, suppression of $J/\psi$ production at SPS energies, essential broadening of the vector meson spectral functions, strong in-medium modification of produced fast hadrons and jets pointing to jet quenching during propagation through the excited nuclear matter, indications on the chiral magnetic effect from three-particle correlations and their disappearance at $\sqrt{s_{NN}} < 20$ GeV.

Different phases of strongly interacting matter are shown in the phase diagram of Fig. 1. One may see that the heavy-ion experiments at RHIC and LHC probe the region of high temperature and low net baryon density where circumstantial evidence has been obtained for a new kind of QCD matter, the strongly interacting quark-gluon plasma (sQGP), existing above a critical temperature $T_c \approx 160 - 170$ MeV and behaving as an almost ideal liquid. In the other corner of the phase diagram, at a high net baryon density, the matter is deconfined even at a low temperature and, as predicted, correlated quark-antiquark pairs form a color superconductive phase. Such phase may be created in the interior of neutron stars. A fascinating peculiarity is offered in an intermediate region of the phase diagram, where the critical end-point is expected to be located and the phase transition of the excited nuclear matter becomes of the 1st order. The position of the critical end-point is strongly model dependent, the predictions lying in the region of temperature $T_E \sim 160$–$170$ MeV and baryon chemical potential $\mu_E \sim 200$–$700$ MeV. The comprehension of this part of the phase diagram is far from being complete due to the

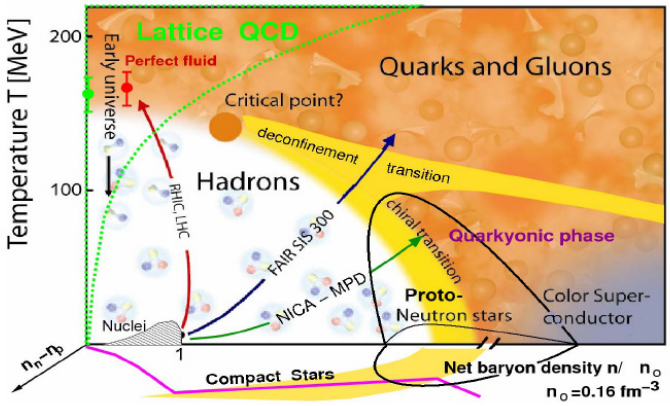


Fig. 1: The phase diagram of strongly interacting QCD matter, schematically showing the phase boundaries, critical end-point, and conjectured dynamical trajectories for an expansion stage

lack of sufficiently accurate data in the corresponding energy domain $\sqrt{s_{NN}} < 10$ GeV. Particularly, the absence of fluctuation and femtoscopic signals of the critical end-point and the onset of deconfinement is likely [4,5] due to expected dramatic decrease of the partonic phase in this energy range [6]. The search for these phenomena can thus be successful only in dedicated high statistics and precise experiments.

As a response to this quest, GSI declared construction of a big accelerator complex FAIR with the extracted heavy-ion beams at $E_{\rm lab} = 4$–$35$ AGeV, $\sqrt{s_{NN}} = 3$–$8$ GeV; the first stage SIS-100 ($E_{\rm lab} <$ 11 AGeV) to be available in 2019 and the second one SIS-300 – after 2020. At the BNL-RHIC, the pilot experiments have already been performed at the collider energies reduced from $\sqrt{s_{NN}} = 200$ GeV to 7.7, 11.5, 19.6 and 39 GeV despite the loss in the luminosity by 2-3 orders in magnitude at the lowest energies; the low energy scan program at RHIC will continue in 2012 by taking the data at the energy $\sqrt{s_{NN}} = 27$ GeV.

The NICA energy range $\sqrt{s_{NN}} = 4$–$11$ GeV is very much lower than those of the RHIC and the LHC, and partly overlaps with the lowest energies available in the RHIC energy scan and the energies of the fixed-target experiments at SPS and FAIR. It sits right on

top of the region where the net baryon density is expected to be the highest achievable in terrestrial experiments. In this energy range, the excited nuclear matter occupies the maximum space-time volume in the mixed quark-hadron phase (similar to that of the water-vapor coexistence phase).

Besides the heavy ion beams, the NICA will also provide the polarized proton and deuteron beams up to the c.m.s. energy of 27 GeV for pp collisions with the luminosity higher than $10^{30}$ cm$^{-2}$s$^{-1}$. The high intensity and high polarization ($> 50\%$) will provide a unique possibility for spin physics research, which is of crucial importance for the solution of the nucleon spin problem ("spin puzzle") – one of the main tasks of the modern hadron physics. Particularly, a study of the Matveev-Muradyan-Tavkhelidze-Drell-Yan (MMT-DY) processes, not requiring the input from the poorly known fragmentation functions, can be done in the kinematic region not available in other experiments.

## 2. NICA Layout

The NICA collider complex is shown on Fig. 2. The construction of this facility is based on the existing buildings and infrastructure of the Synchrophasotron/Nuclotron of the JINR Veksler-Baldin Laboratory of High Energy Physics. The accelerator chain includes heavy-ion and polarized particle sources (KRION-6T and SPP), RFQ injector, heavy- and light-ion linacs (HILac and LU-20), booster ring, Nuclotron and superconducting collider rings. The peak design kinetic energy of gold ions in the collider is 4.5 AGeV. Beam cooling and bunching systems are foreseen to achieve the average luminosity of $10^{27}$ cm$^{-2}$ s$^{-1}$ in the Au+Au collisions. The project design presumes the continuation of some of the fixed-target experiments, including those with polarized beams from the Nuclotron. The concept of the NICA project was first presented and discussed at the round table discussion in October 2006, the present project status is available in the Conceptual Design Report [2] and the Technical Design Report is close to its completion. Two interaction points are foreseen at the NICA collider, thus providing a possibility for two detectors to operate simultaneously. The MultiPurpose Detector (MPD) is optimized

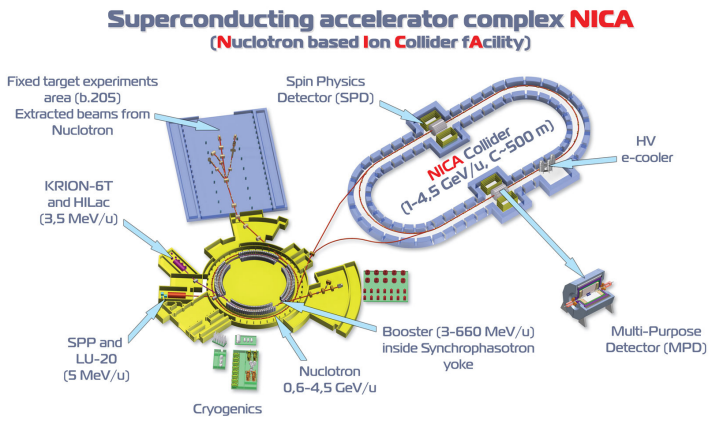


Fig. 2: Location of the NICA collider in the JINR accellerator complex area

for the study of properties of hot and dense nuclear matter produced in heavy-ion collisions and the Spin Physics Detector (SPD) – for the study of spin phenomena in the collisions of light polarized ions.

The NICA complex is aimed at the basic science research, yet beams of particles intended for physics experiments may find another applications. In particular, JINR has already accumulated essential experience in conducting biomedical research and in performing cancer therapy. The proton and ion beams from the linacs, booster and Nuclotron are well suited for applications and will greatly enhance the JINR capability in many important areas of applied sciences, radiation technology and medicine.

## 3. The Detectors: MPD and SPD

Due to the high complexity of the search for the critical end-point and mixed phase in relativistic heavy ion collisions and large uncertainties in the predicted signals, an accurate scanning of the considered phase diagram domain in the collision energy, impact parameter and system size is utterly needed. In this respect, it is important to provide a uniform detector acceptance over the whole energy range of inter-

est. The operation in the collider mode, as proposed in the NICA project and in the low-energy RHIC program (however, with the luminosity by several orders of magnitude lower than planned in the NICA project), naturally satisfies this demand and has an advantage as compared with the fixed-target mode (SPS, FAIR).

The MPD setup [2] is designed to explore the phase diagram of strongly interacting matter produced in heavy-ion collisions at NICA. It has to cover a large phase space, be functional at high interaction rates and comprise high efficiency and excellent particle identification capabilities in a high track multiplicity environment and allow for a controlled selection of the event centralities. The MPD detector concept matching these requirements comprises the central detector and two optional forward spectrometers, the latter covering the pseudorapidity region $2 < |\eta| < 3$.

The central detector consists of a barrel part and two end-cap trackers located inside the magnetic field. The latter are aimed for precise tracking over pseudorapidity range $1.2 < |\eta| < 2$. The barrel part covers the pseudorapidity region of $|\eta| \leq 1.2$. It consists of a tracker and particle identification system. The principal tracker is the time projection chamber (TPC) supplemented by the inner tracker (IT) surrounding the interaction region. Both IT (silicon strip detector as a baseline) and TPC have to provide precise track finding, momentum determination, vertex reconstruction and pattern recognition. The energy loss ($dE/dx$) measurements in the TPC gas will provide an additional capability for particle identification in low momentum region. The high performance time-of-flight (TOF) system must be able to identify charged hadrons and nuclear clusters in the broad rapidity range and up to total momentum of 2 GeV/c. The fast forward detectors will provide the TOF system with the start signal. In addition, the electromagnetic calorimeter will identify electrons, photons and measure their energy with high precision. Its high granularity together with excellent energy resolution and good timing performances will enhance the overall efficiency and particle identification capabilities of the MPD detector. Particles emitted in very forward/backward directions will be detected by fast forward detectors, beam-beam counters and zero degree calorimeters. They will be used for trigger definition, centrality determination and reconstruction of the position of the interaction point.

The following measurements will be done in the first stage: multiplicity and spectral characteristics of identified hadrons probing entropy production and system temperature at freeze-out; event-by-event fluctuations in multiplicities of various particle species, multiplicity ratios, charges and particle transverse momenta as generic properties of critical phenomena; collective flow effects, particle correlations and femtoscopy with identified particles characterizing collective phenomena and space-time evolution of the excited matter. In the second stage, the electromagnetic probes (photons and dileptons) will be measured.

The NICA facility will also give unique possibilities for spin physics. For this, the SPD setup [3] at the second interaction point is designed similar to the PAX setup at FAIR. It assumes nearly $4\pi$ acceptance, minimal radiation length to provide an effective detection of lepton pairs and a good angular resolution to allow for a measurement of azimuthal spin asymmetries in a wide kinematic region. The basic SPD parts are: a toroid magnet system with the integrated field of $\sim 0.4$ T·m, inner tracker (Silicon or MicroMega), main tracker (drift chambers or straw tubes), Cherenkov counter, electromagnetic calorimeter, trigger counters and EndCap detectors. Also considered is the possibility of so-called beam-dump muon detector.

The following measurements are assumed: MMT-DY and $J/\psi$ production processes with longitudinally and transversally polarized proton and deuteron beams for the extraction of unknown or poorly known parton distribution functions; spin effects in baryon, meson and photon production; spin effects in various exclusive reactions and diffractive processes; spin-dependent cross sections, helicity amplitudes and double spin asymmetries (Krisch effect) in elastic reactions; spectroscopy of quarkonia; polarimetry.

## 4. Conclusions

The project of the Nuclotron-based Ion Collider fAcility, NICA, is being realized in JINR. It will make it possible to study very important unsolved problems of the physics of strongly interacting matter and spin phenomena. The design and organizational work on this project started in 2006, and its realization assumes several stages: upgrade

of the Nuclotron facility, preparation of the NICA technical design report, start of the prototyping of the NICA, MPD and SPD elements (2007-2012); design, construction and assembling (2012-2016); commissioning (2017). Worldwide cooperation is anticipated at all stages of the project as well as – in the elaboration of the scientific program.

1. N. Agapov *et al.* (NICA Collaboration), *Design and Construction of Nuclotron-based Ion Collider fAcility (NICA), Conceptual Design Report* (Dubna, 2008); http://nica.jinr.ru.
2. Kh.U. Abraamyan *et al.* (MPD Collaboration), *The MultiPurpose Detector - MPD to study Heavy Ion Collisions at NICA (Conceptual Design Report)* (Dubna, 2011), http://nica.jinr.ru; Nucl. Instrum. Meth. A **628**, 99 (2011).
3. A. Efremov *et al.* (SPD Collaboration), *The Spin Physics Detector – SPD to study spin structure of the nucleon and polarization effects at NICA (Conceptual Design Report)* (Dubna, 2011), http://nica.jinr.ru/files/Spin_program/spd_cdr.htm.
4. http://theor.jinr.ru/twiki-cgi/view/NICA/NICAWhitePaper.
5. R. Lednicky, Nucl. Phys. Proc. Suppl. **198**, 43 (2010).
6. W. Cassing and E. Bratkovskaya, Nucl. Phys. A **831**, 215 (2009).

# THE SPIN-CHARGE-FAMILY-THEORY UNIFIES SPIN AND CHARGES AND OFFERS THE MECHANISM FOR GENERATING FAMILIES AND SCALAR FIELDS

Norma Susana Mankoč Borštnik

*Faculty of Mathematics and Physics,*
*University of Ljubljana, 1000 Ljubljana, Slovenia*

**Abstract**

The theory unifying the spin, charges and families predicts the number of families and their properties, explains the origin of the scalar and vector gauge fields and their properties, manifesting at low energies effectively the Higgs, Yukawa coupling and known gauge fields, respectively. The theory predicts that the fourth family could possibly be observed at the LHC, while the stable fifth family baryons might constitute the dark matter. It also predicts that searching for scalar fields will show up the differences between the Higgs and the scalar fields.

## 1. Introduction

The *standard model* of the electroweak and colour interaction, built on several assumptions for which we have no explanation yet, offered an elegant new step in understanding the origin of fermions and bosons. The next step models must, to propose relevant measurements, answer at least the questions:

- What is the origin of the families? How many families do we have?

- What is the origin of the scalar field (the Higgs) and the Yukawa couplings?

- Where does the dark matter originate?

There are also several other questions which need the urgent answers, like: What is the origin of the known charges and correspondingly of the gauge fields? Do all the charges originate in one charge? Where does the dark energy originate? What is the origin of the fermion-anti-fermion asymmetry? What is the dimension of space time and the origin of its signature? What is the role of symmetries, discrete, continuous, global and gauge? How do phase transitions determine properties of elementary fields – fermions and bosons? What is the origin of fields causing inflation? How can the vacuum energy of the second quantized fields be explained in the cosmological model? How can gravitational field be quantized? And others.

The authors of the *standard model* made the essential new step beyond the hadron physics by assuming that **i.** there are the colour, weak and hyper charges, **ii.** there are the family members, colour and colourless, left and right handed which differ in the weak and hyper charges, **iii.** and there is besides the vector gauge fields also the scalar field and the Yukawa couplings.

A lot of advises what to measure and how to observe the next step beyond the *standard model* are published. I don't see that proposals, which just continue the *standard model* ideas, by enlarging the number of families, or by explaining the appearance of families by the $SU(n)$ groups and the Yukawa couplings by the scalar dynamical fields in the (bi-) fundamental representations of the $SU(n)$ groups, or even by treating some of family members – the right handed neutrinos – independently of the other members, can have a chance to show the right way beyond the *standard model*.

That all the charges emerge from only one and might even unify with the spin is the idea which Kaluza and Klein started almost hundred years ago. For the unification of all the charges and correspondingly of the gauge fields speaks, in addition to the elegance and simplicity of such a theory, also that the scale of the colour phase transition (at which all the quarks would gain the same mass of $\approx 300$ MeV$/c^2$ if there would be no electroweak break) is connected with

(or even triggered by) the electroweak phase transition, otherwise we would have two completely independent measures for a meter.

The theory unifying the spin, charges and families (to be called the *spin-charge-family-theory*) explains the appearance of families, of the scalar and vector gauge fields and proposes the unification of spin and charges. It predicts the number of families, their properties and the properties of scalar and gauge fields. It predicts the fourth family at the low energy regime and explains the dark matter as clusters of the stable fifth family members.

## 2. Short Presentation of the Spin-Charge-Family-Theory

A simple starting Lagrange density [1, 2] for spinors in $d > (1+3)$, which carry two kinds of spin – the Dirac one (described by $\gamma^a$, $S^{ab} = \frac{i}{4}(\gamma^a\gamma^b - \gamma^b\gamma^a)$) and the additional one (described by $\tilde{\gamma}^a$, with the same Clifford algebra properties as $\gamma^a$ and anti commuting with $\gamma^a$, $\tilde{S}^{ab} = \frac{i}{4}(\tilde{\gamma}^a\tilde{\gamma}^b - \tilde{\gamma}^b\tilde{\gamma}^a)$, there exists no third kind of the spin) – no charges, and interact with only the gravitational field through the vielbeins and the two kinds of the spin connection fields, the gauge fields of $S^{ab}$ and $\tilde{S}^{ab}$,

$$\begin{aligned} \mathcal{L}_f &= \frac{1}{2}\,(E\bar{\psi}\,\gamma^a p_{0a}\psi) + h.c.\,, p_{0a} = f^{\alpha}{}_a p_{0\alpha} + \frac{1}{2E}\,\{p_\alpha\,, E f^{\alpha}{}_a\}_-\,, \\ p_{0\alpha} &= p_\alpha - \frac{1}{2}S^{ab}\omega_{ab\alpha} - \frac{1}{2}\tilde{S}^{ab}\tilde{\omega}_{ab\alpha}, \end{aligned} \tag{1}$$

manifests (after particular breaks of the starting symmetry) in $d = (1+3)$ two groups of four massless families. The gravitational gauge fields are assumed to appear in the action

$$S = \int d^dx\; E\; \mathcal{L}_f + \int d^dx\; E\; (\alpha\, R + \tilde{\alpha}\, \tilde{R}) \tag{2}$$

through the vielbeins ($f^{\alpha}{}_a$, $f^{\alpha}{}_a\, e^b{}_\alpha = \delta^b_a$) and the spin connection fields of two kinds ($\omega_{abc} = f^{\alpha}{}_c\,\omega_{ab\alpha}$ and $\tilde{\omega}_{abc} = f^{\alpha}{}_c\,\tilde{\omega}_{ab\alpha}$) as follows: $R = \frac{1}{2} f^{\alpha[a} f^{\beta b]}\,(\omega_{ab\alpha,\beta} - \omega_{ca\alpha}\,\omega^c{}_{b\beta})$, $\tilde{R} = \frac{1}{2} f^{\alpha[a} f^{\beta b]}\,(\tilde{\omega}_{ab\alpha,\beta} - \tilde{\omega}_{ca\alpha}\tilde{\omega}^c{}_{b\beta})$, with $f^{\alpha[a} f^{\beta b]} = f^{\alpha a} f^{\beta b} - f^{\alpha b} f^{\beta a}$. These gauge fields manifest in $d = (1+3)$ as the gauge fields of the observed charges

and as the scalar fields which contribute to the two successive breaks (from $SO(1,3)\times SU(2)_I \times SU(2)_{II} \times U(1)_{II} \times SU(3)$ into $SO(1,3)\times SU(2)_I \times U(1)_I \times SU(3)$ and further to $SO(1,3)\times U(1)\times SU(3)$), and determine, together with the gauge fields, the low energy properties of fermions and bosons.

A short overview of properties of the two kinds of scalar dynamical fields – one (the gauge fields of $S^{ab}$) distinguishing only among the members ($\alpha\,, \alpha \in (u\,, d\,, \nu\,, e)$) of a family, the other (the gauge fields of $\tilde{S}^{ab}$) only among the families – is made and the influence of scalar fields on properties of the mass matrices of twice (decoupled) four families and on the gauge fields presented. In the ref. [5] and the references cited there more information cane be found.

To see that the action of Eq. (1) manifests after the breaks of symmetries [2, 5, 6] all the known gauge fields, with the mass matrices included, let us rewrite formally the action for a Weyl spinor of (Eq.(1)) as follows

$$\begin{aligned} \mathcal{L}_f &= \bar{\psi}\gamma^m(p_m - \sum_{A,i} g^A \tau^{Ai} A^{Ai}_m)\psi + \\ &\Big\{ \sum_{s=7,8} \bar{\psi}\gamma^s p_{0s}\ \psi \Big\} + \\ &\text{the rest}, \end{aligned} \tag{3}$$

where $m = 0,1,2,3$ and $\tau^{Ai} = \sum_{a,b}\ c^{Ai}{}_{ab}\ S^{ab}$, $\{\tau^{Ai}, \tau^{Bj}\}_- = i\delta^{AB} f^{Aijk}\tau^{Ak}$. Index $A$ enumerates charges and $g^A$ is the coupling constant to a particular gauge vector field $A^{Ai}_m$. Before the electroweak break $A = 1$ stays for the weak charge, $A = 2$ for the hyper charge and $A = 3$ for the colour charge. The first row of Eq.(3) manifests the dynamical part, while the second row manifests the mass term. In the mass term ($\sum_{s=7,8}\ \bar{\psi}\gamma^s p_{0s}\ \psi$), in which the summation runs only over $s = 7, 8$, the operators $\gamma^s$ transform quantum numbers of the right handed members into those of the left handed partners. To the mass matrix two kinds of spin connection fields contribute $p_{0s} = f^\sigma{}_s p_{0\sigma} + \frac{1}{2E}\{p_\sigma\,, Ef^\sigma{}_s\}_-$, $p_{0\sigma} = p_\sigma - \frac{1}{2}S^{ab}\omega_{ab\sigma} - \frac{1}{2}\tilde{S}^{ab}\tilde{\omega}_{ab\sigma}$, and we have correspondingly also $\tilde{\tau}^{Ai} = \sum_{a,b}\ c^{Ai}{}_{ab}\ \tilde{S}^{ab}$, $\{\tilde{\tau}^{Ai}, \tilde{\tau}^{Bj}\}_- = i\delta^{AB} f^{Aijk}\tilde{\tau}^{Ak}$.

The scalar fields which originate in $\tilde{S}^{ab}$ and couple to only the upper four families are responsible with their nonzero vacuum expec-

tation values for mass matrices of the upper four families on the tree level. The lower four families stay massless up to the electroweak break, when the scalar fields which are orthogonal to the ones which determine mass matrices of the upper four families, gain nonzero vacuum expectation values. To the mass matrices of the lower four families also the scalar fields originating in $\omega_{abs}$ contribute.

While the mass matrices of different members of a family on the tree level are strongly correlated ($u$ has the same off diagonal matrix elements as $\nu$ and $d$ has the same off diagonal matrix elements as $e$ ), the so far evaluated one loop corrections [3] give a real hope that the loop corrections to all orders take care of the great differences in the properties of the family members for the lower four families. For neutrinos a Majorana like term appears, which might be to high extent responsible for the smallness of masses of the lower three families.

The influence of the loop corrections on the upper four families is expected to be much smaller than on the lower four families, since the scalar fields originating in the "Dirac kind" of the spin connection fields ($\omega_{ss's"}$ [1]), which distinguish among the family members (not among families [2]), gain nonzero vacuum expectation values at the electroweak break, while the upper four families gain masses at for several orders of magnitude higher scale [3].

The upper group of four families ($\Sigma = II$) do not couple to the lower one ($\Sigma = I$). Correspondingly the mass matrices of each family member ($\alpha \in (u, d, \nu, e)$) demonstrate twice four by four diagonal matrices

$$M^{\alpha} = \begin{pmatrix} M^{\alpha\, II} & 0 \\ 0 & M^{\alpha\, I} \end{pmatrix} . \tag{4}$$

[1] The scalar fields originating in the "Dirac kind" of spin $\gamma^s$ manifest after the electroweak break in terms $e\, Q\, A_s + g^1 \cos\theta_1\, Q'\, Z_s^{Q'} + g^2 \cos\theta_2\, Y'\, A_s^{Y'}$.

[2] The gauge scalar fields of $\tilde{\tau}^{Ai}$, which distinguish among families, are $\{[\tilde{g}^{\vec{N}_R}\, \vec{\tilde{N}}_R\, \vec{\tilde{A}}_s^{\tilde{N}_R} + \tilde{g}^{\tilde{Y}'}\, \tilde{Y}'\, \tilde{A}_s^{\tilde{Y}'} + \frac{\tilde{g}^2}{\sqrt{2}}(\tilde{\tau}^{2+}\, \tilde{A}_s^{2+} + \tilde{\tau}^{2-}\, \tilde{A}_s^{2-})] + [[\tilde{g}^{\vec{N}_L}\, \vec{\tilde{N}}_L\, \vec{\tilde{A}}_s^{\tilde{N}_L} + \tilde{g}^{\tilde{Q}'}\, \tilde{Q}'\, \tilde{A}_s^{\tilde{Q}'} + \frac{\tilde{g}^1}{\sqrt{2}}(\tilde{\tau}^{1+}\, \tilde{A}_s^{1+} + \tilde{\tau}^{1-}\, \tilde{A}_s^{1-})]]\}$. The term within the parentheses [ ] couples to the upper four families, while the term within the parentheses [[ ]] couples to the lower four families.

[3] Together with the upper four families also the vector gauge fields, which are the superposition of $\tilde{A}_m^2$ and $A_m^4$, gain masses when $SU(2)_{II} \times U(1)_{II}$ symmetry breaks into $U(1)_I$.

Accordingly there are two stable families of quarks and leptons: The first one $(u_1\,, d_1\,, \nu_1\,, e_1)$ and the fifth family one $(u_5\,, d_5\,, \nu_5\,, e_5)$. All the fifth family members are expected to have quite comparable masses due to the fact that the main dependence on the family members quantum number appears at the electroweak break, as explained above. It follows accordingly that the lightest baryon is very likely the neutron $(n_5)$ [4].

## 3. Estimation of Families Properties

Rough analyses (without loop corrections included) of the properties for the lower group of four families [2, 6] and for the fifth family members [7] were done by taking into account the so far observed properties of family members [5] and the dark matter observations. The prediction was made that the fourth family members can be possibly observed at the LHC or at somewhat higher energies.

The analyses with the loop corrections taken into account are in preparations [3] manifesting so far their strong dependence on family member quantum number. This gives correspondently a real hope that the loop correction will change the tree level mass matrices (which have the off diagonal matrix elements of $u$ equal to those of $\nu$ and equivalently for $d$ and $e$) in agreement with the observations.

The *spin-charge-family-theory* predicts the masses of the stable fifth family to be above the fourth family masses, let us say $> 10$ TeV, and pretty much below $10^{13}$ GeV, which is a possible scale of the first of the two $SU(2) \times U(1)$ breaks.

Following [7] the history of the stable fifth family members in the expanding universe from the time when they start to decouple from the cosmic plasma, through the freezing out procedure and the colour phase transition, up to the today's matter, we show that the fifth family members, the (colourless) baryons and anti-baryons and neutrinos and anti-neutrinos [6] are very likely the dark matter constituents.

[4] Properties of the fifth family members are under consideration [3, 4].

[5] The calculations of the lower four families properties were done under the assumption that loop corrections change the off diagonal matrix elements while keeping approximately the symmetry of mass matrices.

[6] Neutrinos and antineutrinos are expected to annihilate during the electroweak phase transition to the density which is in agreement with cosmological observations of the dark matter density.

We calculated the present number density of baryons and anti-baryons of the fifth family members ($n_{c_5}(T_0)$) as a function of the fifth family members mass. Taking into account the estimation inaccuracy the interval for the fifth family masses followed

$$10 \text{ TeV} < m_5\, c^2 < 4 \times 10^2 \text{ TeV}. \tag{5}$$

The estimated cross section for the fifth family neutrons ($\pi(r_{c_5})^2$): $10^{-8}$ fm$^2$ $< \sigma_{c_5} < 10^{-6}$ fm$^2$ manifests that the cross section of the fifth family "nuclear force" is at least $10^{-6}\times$ smaller than the cross section of the first family nuclear force, explaining why is the dark matter so inert.

We studied [7] also properties of the fifth family baryons and anti-baryons and neutrinos and anti-neutrinos in direct measurements done so far. My prediction is, after several discussions with the members of most of the groups performing direct measurements, that if DAMA/LIBRA measures our fifth family clusters, other direct measurements will confirm their results.

## 4. Conclusions and Discussions

The *spin-charge-family-theory* [1, 2, 5, 6] is offering the new way beyond the *standard model* by proposing the mechanism for generating families of quarks and leptons and consequently predicting the number of families at low energies and the mass matrices for each of the family member. It explains the origin of the *standard model* Higgs and the Yukawa couplings. It explains the appearance of charges by unifying all the charges and spin into only the spin and all the gauge fields into only gravity manifesting as spin connections of two kinds and vielbeins [7].

It predicts the fourth family to be possibly measured at the LHC or at some higher energies and the fifth family which is, since it is

[7] Let us comment at this point the last OPERA results about the velocity of neutrinos exceeding the light velocity. In the *spin-charge-family-theory* – which unifies all the charges and the gauge fields and treats all the family members in an equivalent way – the break of the electroweak symmetry would very hardly result in different velocities of the photon and the neutrino, which would consequently manifest in different Lorentz transformation properties.

decoupled in the mixing matrices from the lower four families and it is correspondingly stable, the candidate to form the dark matter [7].

There are two kinds of scalar fields, which interact with fermions – through the Dirac spin and through the second kind of the Clifford operators, which anti commutes with the Dirac one. The Dirac one distinguishes among the family members, the second one among the families. Beyond the tree level these two kinds of scalar fields and the vector massive fields start to contribute coherently, leading hopefully to the measured properties of the so far observed three families of fermions and to the observed weak gauge fields.

These scalar dynamical fields have all the charges in the adjoint representations of all the groups. Yet they manifest at low energies effectively as the *standard model* Higgs and Yukawa couplings. It is expected, however, that the differences will show up at least when searching for these scalar fields.

1. N.S. Mankoč Borštnik, Phys. Lett. B **292**, 25 (1992); J. Math. Phys. **34** 3731 (1993); Int. J. Theor. Phys. **40** 315 (2001); Modern Phys. Lett. A **10**, 587 (1995); hep-ph/0711.4681 p.94; arXiv:0912.4532 p.119; hep-ph/0711.4681, p. 94-113; arXiv:0912.4532, p.119-135; arxiv.org/abs/1005.2288.
2. A. Borštnik, N.S. Mankoč Borštnik, hep-ph/0401043, hep-ph/0401055, hep-ph/0301029, Phys. Rev. D **74**, 073013 (2006), hep-ph/0512062.
3. A. Hernández-Galeana, N.S. Mankoč Borštnik, in preparation, arXiv:1012.0224, p.166-176.
4. N.S. Mankoč Borštnik, M. Rosina, arXiv:1012.0224, p.203-210, paper in preparation.
5. N.S. Mankoč Borštnik, arXiv:.org/abs/1011.5765.
6. G. Bregar, M. Breskvar, D. Lukman, N.S. Mankoč Borštnik, New J. of Phys. **10** 093002 (2008).
7. G. Bregar, N.S. Mankoč Borštnik, Phys. Rev. D **80**, 083534 (2009); G. Bregar, R.F. Lang, N.S. Mankoč Borštnik, arXiv:1012.0224, p. 161-165.
8. R. Bernabei *et al.*, Int. J. Mod. Phys. D **13**, 2127 (2004); Z. Ahmed *et al.*, Phys. Rev. Lett. **102**, 011301 (2009); arXiv:0802.3530; M. Fich and S. Tremaine, Ann. Rev. Astron. Astrophys. **29**, 420 (1991); Z. Ahmed *et al.*, Phys. Rev. Lett. **102**, 011301 (2009), arXiv:0802.3530; E. Aprile *et al.*, Phys. Rev. Lett. **105**, 131302 (2010), arXiv:1005.0380.
9. R.S. Chivukula and H. Georgi, Phys. Lett. B **188**, 99 (1987); G. D'Ambrosio, G. Giudice, G. Isidori, and A. Strumia, Nucl. Phys. B **645**, 155–187 (2002), arXiv:hep-ph/0207036; R. Alonso, M.B. Gavela, L. Merlo, S. Rigolin, arXiv: 1103.2915v1[hep-ph].

# NEW FORMULATION OF ELECTRO-WEAK MODELS APPLICABLE BEYOND PERTURBATION THEORY

A.A. Slavnov

*Steklov Mathematical Institute,*
*Russian Academy of Sciences*
*Gubkina st.8, GSP-1, 119991, Moscow*
*e-mail: slavnov@mi.ras.ru*

**Abstract**

A new formulation of electro-weak models applicable beyond perturbation theory is reviewed.

## 1. Introduction

A discovery of a new symmetry usually allows to construct more transparent formulation of the theory. Recent examples are given by gauge theories. QED may be formulated in the Coulomb gauge, however much more transparent formulation is presented by the quantization in a manifestly covariant gauge, which is possible due to the gauge invariance of the theory. Yang–Mills theory became really popular only after its formulation in the Lorentz covariant terms and explicit proof of its renormalizability which was possible because of the gauge invariance. The gauge invariance of the Higgs model allows to give a manifestly renormalizable theory describing a massive gauge theory.

In this talk I wish to make a propaganda for a new class of symmetries, which were introduced in my paper rather long ago [1], but recently were applied successfully to the nonperturbative quantization of non-Abelian gauge theories.

This formulation is based on the so-called equivalence theorems for spectrum changing transformations. Equivalence theorems,which states that two different Lagrangians related with each other by some transformation of variables may give the same results for observable quantities were known long ago. Usually they refer to the canonical or point transformations:

$$\varphi = \varphi' + f(\varphi'). \tag{1}$$

However one may consider also more general transformations, including time derivatives of the fields:

$$\varphi = \frac{\partial^n \varphi'}{\partial t^n} + f\left(\frac{\partial^{n-1}\varphi'}{\partial t^{n-1}}, \dots \frac{\partial \varphi'}{\partial t}\right) = \tilde{f}(\varphi'). \tag{2}$$

After such transformation the spectrum of the theory obviously is changed. New excitations appear and one should worry about the unitarity of the new scattering matrix.

To answer this question it is instructive to consider the path integral formulation of the theory. The scattering matrix is given by the path integral

$$S = \int \exp\{i \int L(\varphi) dx\} d\mu(\varphi); \quad \lim_{t\to\pm\infty} \varphi(x) = \varphi_{\text{out,in}}(x). \tag{3}$$

If the change (2) does not change the asymptotic conditions, then the only effect of such transformation is the appearance of a nontrivial Jacobian

$$L(\varphi) \to \tilde{L}(\varphi') = L[\varphi(\varphi')] + \bar{c}^a \frac{\delta \varphi^a}{\delta \varphi'^b} c^b. \tag{4}$$

Here the ghost fields $\bar{c}, c$ are anticommuting variables reminding the Faddeev–Popov ghosts. If one postulates that the ghost fields satisfy the vacuum boundary conditions, one may integrate out explicitly all new excitations and return to the original theory. However it is far from obvious that one can impose vacuum boundary conditions

on the ghost fields, and the problem of physical unitarity requires more careful study. In solving this problem helps a new symmetry which possesses a transformed Lagrangian. The new Lagrangian is invariant with respect to the supertransformations

$$\delta\varphi'_a = c_a\varepsilon,$$

$$\delta c_a = 0; \quad \delta\bar{c}_a = \frac{\delta L}{\delta\varphi_a}(\varphi')\varepsilon. \tag{5}$$

Here $\varepsilon$ is a constant anticommuting parameter. On mass shell these transformations are nilpotent and generate a conserved charge $Q$. In this case there exists an invariant subspace of states annihilated by $Q$, which has a semidefinite norm [1]. For asymptotic space this condition reduces to

$$Q_0|\phi\rangle_{as} = 0. \tag{6}$$

The scattering matrix is unitary in the subspace which contains only excitations of the original theory. However the theories described by the $L$ and the $\tilde{L}$ are different, and only expectation values of the gauge invariant operators coincide. In gauge theories the transition from one gauge to another may be considered as such a change.

A very nontrivial generalization is obtained if one transforms the $\tilde{L}$ further shifting the fields $\varphi'$ by constants. It is not an allowed change of variables in the path integral as it changes the asymptotic of the fields. The unitarity of the "shifted" theory is not guaranteed and a special proof (if possible) is needed.

Using this method one can construct a renormalizable formulation of nonabelian gauge theories free of the Gribov ambiguity, and therefore applicable beyond perturbation theory [2–5].

## 2. Gribov Ambiguity

In spite of numerous efforts a problem of unambiguos quantization of nonabelian gauge theories beyond perturbation theory remains unsolved. Even in classical theory the equation

$$D_\mu F_{\mu\nu} = 0 \tag{7}$$

does not determine the Cauchi problem. Gauge invariance results in existence of many solutions of this equation. To define the classical

Cauchi problem and subsequently to quantize the model one imposes a gauge condition, e.g. Coulomb gauge $\partial_i A_i = 0$.

Normally the two classes of gauge conditions are used: Differential gauge conditions: $L(A_\mu, \varphi) = 0 \rightarrow$, which include the derivatives of the fields and are plagued as we shall show with Gribov ambiguity [6]. The second class includes so called algebraic gauge conditions: $\tilde{L}(A_\mu, \varphi) = 0 \rightarrow$ which do not involve derivatives of the fields and for that reason are not manifestly Lorentz invariant. They also are plagued with other problems, which will not be discussed here.

To understand better the problems arising when one uses differential gauges we consider in more details the Coulomb gauge $\partial_i A_i = 0$.

This gauge selects a unique representative in the gauge equivalent class, if the equation

$$A'_i = (A^\Omega)_i, \tag{8}$$

where $\Omega$ is an element of the gauge group, parametrised by the functions $\alpha$, vanishing at spatial infinity, has only trivial solutions. For infinitesimal $\alpha$ this equation looks as follows:

$$\triangle \alpha^a + ig\varepsilon^{abc}\partial_i(A^b_i \alpha^c) = 0. \tag{9}$$

This equation has nontrivial solutions decreasing at spatial infinity, which means that the Coulomb gauge does not fix uniquely a representative in the gauge equivalent class [6]. In the process of quantization of the theory it leads to vanishing of the Faddeev–Popov determinant at some large field and makes questionable the quantization procedure beyond perturbation theory. It is worth to mention that in perturbation theory the equation (9) has only trivial solution, and the Gribov ambiguity is absent. The similar result was obtained by I. Singer [7] for arbitrary differential gauge condition.

A similar problem arises in the theory of electro-weak interactions, described by the Weinberg–Salam model. The Lagrangian of the Weinberg–Salam model looks as follows:

$$\begin{aligned} L = -1/4F^a_{\mu\nu}F^a_{\mu\nu} - 1/4G^a_{\mu\nu}G^a_{\mu\nu} + i\bar{L}\gamma^\mu(\partial_\mu + \frac{ig}{2}\tau^a A^a_\mu + \frac{ig_1}{2}B_\mu)L + \\ + i\bar{R}\gamma_\mu(\partial_\mu + ig_1 B_\mu)R + |\partial_\mu\varphi + \frac{ig}{2}\tau^a A^a_\mu\varphi + \frac{ig_1}{2}B_\mu\varphi|^2 - \\ - G\{(\bar{L}\varphi)R + \bar{R}(\varphi^* L)\} + \frac{m^2}{2}(\varphi^*\varphi) - \lambda^2(\varphi^*\varphi)^2, \end{aligned} \tag{10}$$

where

$$\varphi(x) = (\varphi_1(x), \varphi_2(x)) = \sqrt{2}^{-1}(iB_1 + B_2, \sigma - iB_3 + \sqrt{2}\mu). \quad (11)$$

In perturbation theory all the predictions of the model fit the experiment very well. However there are certain questions to be answered.

1. Where is the Higgs meson?
2. Is the model valid beyond perturbation theory?
3. Is it possible to derive the Weinberg–Salam model from some grand-unified model?
4. Quantization of the Weinberg–Salam model beyond the perturbation theory?

The problems we discuss are mainly related to the quantization of the nonabelian gauge field. For that reason, to save the space we shall consider the $SU(2)$ Higgs–Kibble model.

## 3. Alternative Formulation of the $SU(2)$ Higgs–Kibble Model, Applicable Beyond the Perturbation Theory

The $SU(2)$ Higgs–Kibble model is usually described by the Lagrangian

$$L = -1/4F^a_{\mu\nu}F^a_{\mu\nu} + (D_\mu\varphi)^*(D_\mu\varphi) - \lambda^2(\varphi^*\varphi - \mu^2)^2. \quad (12)$$

It is known that the stable minimum of the Higgs potential corresponds to nonzero value of the field $\varphi$. So first of all we shift the fields $\varphi$ to the stable minimum, performing the transformation

$$\begin{aligned} &\varphi \to \varphi + \hat{\mu}, \\ &\hat{\mu} = \left(0, \frac{\mu}{g\sqrt{2}}\right). \end{aligned} \quad (13)$$

After this shift the vector field acquires the mass, the mass of the Higgs particle becomes real, and three unphysical Goldstone bosons arise. Simultaneously the field $\varphi$ also becomes a gauge field as under the gauge transformation it is shifted by an arbitrary function. The shifted theory remains gauge invariant, but the form of the gauge

transformations changes. For the fields $\varphi, A_\mu$ these transformations look as follows

$$\delta A^a_\mu = \partial_\mu \eta^a + g\varepsilon^{abc} A^b_\mu \eta^c,$$
$$\delta \varphi^a = \mu\sqrt{2}\eta^a + \frac{g}{2}\varepsilon^{abc}\varphi^b\eta^c + \frac{g}{2}\sigma\eta^a. \qquad (14)$$

Using the gauge freedom one can impose on the fields a gauge condition. One possibility is given by the so called unitary gauge: $\varphi^a = 0$. In this gauge only physical exitations are present. They include three components of the massive vector field $A_\mu$, and one neutral scalar meson (Higgs meson). The unitarity of the model is obvious, but unfortunately in this gauge the theory is not explicitly renormalizable, as the propagator of the vector field do not decrease at infinite momenta.

To construct a manifestly renormalizable formulation one can using the gauge invariance of the model pass to some differential gauge, for example the Lorentz gauge $\partial_\mu A_\mu = 0$. In this gauge the theory is manifestly renormalizable, but the spectrum includes a number of unphysical exitations. To prove the unitarity of the theory in the physical sector one can pass back to the unitary gauge. However the Lorentz gauge as any other differential gauge is plagued with the Gribov ambiguity, which makes such a transition possible only in the framework of perturbation theory.

To avoid this difficulty we propose an alternative formulation of the Higgs–Kibble model. We start with the gauge invariant Lagrangian

$$L = -\frac{1}{4}F^a_{\mu\nu}F^a_{\mu\nu} + (D_\mu\varphi^+)^*(D_\mu\varphi^-) + (D_\mu\varphi^-)^*(D_\mu\varphi^+) +$$
$$+(D_\mu\varphi)^*(D_\mu\varphi) - \lambda^2(\varphi^*\varphi - \mu^2)^2 - [(D_\mu b)^*(D_\mu e) + (D_\mu e)^*(D_\mu b)]. \qquad (15)$$

Here the field $\varphi$ is the complex doublet describing the Higgs meson, and the fields $\varphi^\pm$ are new auxiliary fields. The fields $b, e$ have a similar structure, but correspond to the anticommuting fields.

We shift both the Higgs field and the field $\varphi^-$:

$$\varphi \to \varphi + \hat{m}, \qquad (16)$$

$$\varphi^- \to \varphi^- + \hat{\mu}, \qquad (17)$$

where $\hat{m}$ and $\hat{\mu}$ are the coordinate-independent condensates

$$\hat{m} = (0, m/g); \quad \hat{\mu} = (0, \mu/g) \tag{18}$$

The shift of the Higgs field generates the mass term for the vector field, and the new Lagrangian looks as follows

$$\begin{aligned} L = -\tfrac{1}{4}F^a_{\mu\nu}F^a_{\mu\nu} + (D_\mu\varphi^+)^*(D_\mu\varphi^-) + (D_\mu\varphi^-)^*(D_\mu\varphi^+) - \\ -[(D_\mu\varphi^+)^*(D_\mu\hat{m}) + (D_\mu\hat{m})^* D_\mu\varphi^+] - \\ -[(D_\mu b)^*(D_\mu e) + (D_\mu e)^*(D_\mu b)] + (D_\mu\varphi)^*(D_\mu\varphi) - \\ -[(D_\mu\varphi)^*(D_\mu\hat{\mu}) + (D_\mu\hat{\mu})^*(D_\mu\varphi)] + \\ +(D_\mu\hat{\mu})^*(D_\mu\hat{\mu}) - \lambda^2[(\varphi-\hat{\mu})^*(\varphi-\hat{\mu}) - \mu^2]^2. \end{aligned} \tag{19}$$

After the shift both the fields $\varphi$ and $\varphi_-$ become the gauge fields. Under the gauge transformations they transform as follows:

$$\begin{aligned} \delta\varphi^a_- &= m\eta^a + \frac{g}{2}\epsilon^{abc}\varphi^b_-\eta^c + \frac{g}{2}\varphi^0_-\eta^a, \\ \delta\varphi^a &= \mu\eta^a + \frac{g}{2}\epsilon^{abc}\varphi^b\eta^c + \frac{g}{2}\varphi^0\eta^a. \end{aligned} \tag{20}$$

A gauge condition may be imposed on the fields $A^a_\mu, \varphi^a, \varphi^a$. We choose the gauge $\varphi^a_- = 0$. This is an algebraic gauge, which is manifestly Lorentz invariant and, as we shall see, renormalizable.

However this gauge still produce an ambiguity

$$\varphi^a_- = 0; \quad (\varphi^\Omega_-)^a = 0; \quad (\varphi^\Omega_-)^a = \varphi^a_- + (m + \frac{g}{2}\varphi^0_-)\eta^a. \tag{21}$$

For large $\varphi^0_-$ there is an ambiguity.

This ambiguity may be eliminated by a simple change of variables in the classical Lagrangian:

$$\begin{aligned} \varphi^0_- = \frac{2m}{g}\Big(\exp\Big\{\frac{gh}{2m}\Big\} - 1\Big); \quad \varphi^a_- = \tilde{M}\tilde{\varphi}^a_-, \\ \varphi^a_+ = \tilde{M}^{-1}\tilde{\varphi}^a_+; \quad \varphi^0_+ = \tilde{M}^{-1}\tilde{\varphi}^0_+, \\ e = \tilde{M}^{-1}\tilde{e}; \quad b = \tilde{M}\tilde{b}, \end{aligned} \tag{22}$$

where

$$\tilde{M} = 1 + \frac{g}{2m}\varphi^0_- = \exp\Big\{\frac{gh}{2m}\Big\}. \tag{23}$$

At the surface $\varphi^a_- = 0$, the equation $(\tilde{\varphi}^\Omega_-)^a = 0$ implies $\eta^a = 0$.

The divergency index of a diagram with $L_\Phi$ external lines of the field $\Phi$:

$$n = 4 - 2L_{\varphi^0_+} - 2L_{\varphi^a_+} - L_A - L_e - L_b - L_h - L_{\varphi^a} - L_{\varphi^0}. \qquad (24)$$

All the diagrams with more than four external lines are convergent. The model is explicitly renormalizable!

## 4. Physical Unitarity

The model includes many unphysical (ghost) fields: $\varphi^\alpha_+$, $(\alpha = 0, 1, 2, 3)$, $h$, $\varphi^a(B^a)$ $(a = 1, 2, 3)$, $e^\alpha$, $b^\alpha$, $A^a_0$. The unitarity in the physical subspace, including only $A^a_i, \varphi^0(\sigma)$ should be proven.

The Lagrangian $L$ was invariant with respect to the supersymmetry transformaions:

$$\begin{aligned}
&\delta\varphi^a_- = -b^a,\\
&\delta\varphi^0_- = -b^0,\\
&\delta e^a = \varphi^a_+,\\
&\delta e^0 = \varphi^0_+,\\
&\delta b = 0,\\
&\delta\varphi^\alpha_+ = 0,\\
&\alpha = 0, 1, 2, 3. \qquad (25)
\end{aligned}$$

This invariance induces the corresponding symmetry transformations of the variables $\tilde{\varphi}^\alpha_+$, $h$, $\tilde{e}$, $\tilde{b}$, which leave invariant the Lagrangian $\tilde{L}$. The asymptotic theory is invariant with respect to the supersymmetry transformations

$$\delta\tilde{\varphi}^a_- = 0; \quad \delta A^a_\mu = m^{-1}\partial_\mu \tilde{b}^a; \quad \delta h = -\tilde{b}^0; \quad \delta\varphi^a = 0. \qquad (26)$$

This invariance provides the conservation of the charge $Q$, and unitarity of the scattering matrix in the subspace of the states annihilated by $Q_0$: $Q_0|\psi\rangle_{as} = 0$

Together with the gauge invariance it guarantees the unitarity of the $S$-matrix in the space including only physical states $A^a_i, \sigma$.

## 5. Conclusion

1. A unique covariant quantization of the Higgs–Kibble (Weinberg–Salam) model beyond the perturbation theory is possible.

2. The model is renormalizable in the ambiguity free Lorentz invariant gauge.

3. The necessary counterterms preserve the symmetries, which provide the unitarity of the renormalized theory and preserve the gauge invariance. However a redefinition of the parameters and the fields is needed.

4. The crucial role for all this construction must be played by the nonperturbative calculations.

### Acknowledgements

This work was partially supported by RFBR under grant 11-01-12037-ofi-m-201109 and by the RAS program "Nonlinear dynamics".

1. A.A. Slavnov, Phys. Lett. B **258**, 391 (1991).
2. A.A. Slavnov, Theor. Math. Phys. **154**, 213 (2008).
3. A.A. Slavnov, JHEP **08**, 047 (2008).
4. A. Quadri, A.A. Slavnov, JHEP 1007 (2010).
5. A. Quadri, A.A. Slavnov, Theor. Math. Phys. **166**, 201 (2011).
6. V.N. Gribov, Nucl. Phys. B **139**, 1 (1978).
7. I. Singer, Comm. Math. Phys. **60**, 7 (1978).

# NEURAL NETWORK IN HIGH-ENERGY PHYSICS

G.N. Stelmakh

*National University "Kiev Polytechnical Institute",*
*Prospekt Pobedy 37, Kiev, Ukraine;*
*e-mail: lorenzo.bianco@me.com*

**Abstract**

A method for biased-free determination of the probability measure in the space of nucleon structure functions measured in deep-inelastic scattering, retaining information on experimental errors and correlations is discussed.

## 1. Introduction

Artificial neural networks constitute one of the most successful and multidisciplinary subjects, with applications ranging from images reconstruction to financial markets predictions. Artificial neural network methods are well established techniques for high energy physics too [2]. We start with a brief and general introduction to artificial neural networks (or simply neural networks).

The structure of biological nervous system started to be understood in 1888, when Dr. Santiago Ramón y Cajal succeeded in seeing the *synapses* between individual nervous cells, the *neurons*. This discovery was quite impressive as it proved that all the capabilities of the human brain rest not so much in the complexity of its constituents as in the enormous number of neurons and connections between them. To give an idea of these magnitudes, the usual estimate of the total number of neurons in the human central nervous system is $10^{11}$, with an average of 10000 synapses per neuron. The combination of both

numbers yields a total of $10^{15}$ synaptic connections in a single human brain.

In 1943 W.S. McCulloch and W. Pitts suggested a mathematical model for capturing some of the characteristics of the brain. First, an *artificial neuron* (or simply a *neuron*) is defined as a processing element whose state $\xi$ at time $t$ can take two different values only: $\xi(t) = 1$, if it is firing, or $\xi(t) = 0$, if it is at rest. The state of, say, the $i^{th}$ unit, $\xi_i(t)$, depends on the inputs from the rest of the N neurons. Then, a set of mutually connected McCulloch-Pitts units is what is called an *artificial neural network*.

The deeply inelastic scattering (DIS) cross section is expressed in terms of the nucleon structure function $F_2$, that carries informations about the inner structure of the nucleon. If we were able to solve QCD in the non-perturbative domain, we could calculate $F_2$. Unfortunately this is not the case. However, we need a more and more detailed knowledge of the structure of nucleons as they are essential ingredients for present and future hadron colliders. Note that the unpolarized structure function is necessary also to determine the polarized structure function from the spin asymmetry in polarized deep inelastic scattering. Although the accuracy of such experiments is not yet very high, it could be anyway useful for future tasks to minimize the sources of errors. We have thus to extract as much precise information as possible from experiments. For this purpose we present here an alternative approach to extract $F_2$ from data.

We consider the case where we have $M$ measurements of a nucleon structure function $F_2$. The central problem is to determine $F_2$ based on observations. Specifically, we can introduce a hypothesis for the structure function $F_2$ which depends on unknown parameters. The goal is then to estimate parameters by comparing the hypothesis with experimental data.

The Monte Carlo method is an alternative approach for calculating errors and correlations by using sequences of random numbers. A sequence of Monte Carlo generated values of $F_2$ may be used to evaluate estimators for errors and correlations of the values of the parameters of $F_2$. An important feature of properly constructed estimators is that their statistical accuracy improves as the number of values $N$ in the data sample increases.

A functional parametrization introduces an uncertainty due to the imposed dependence on $x$ and $Q^2$. However, nobody knows which is the real behavior of $F_2$, and any assumption on its functional form may be a source of uncertainty, whose exact size is very hard to assess. For this purpose one considers a fit with a neural network. Indeed, a neural network with a given architecture can describe a structure function as well as, say, a demographic distribution having very different behaviors: the difference only depends on the input and the output data which it is trained with. In this case however we will have a larger number of parameters than with the functional parametrization. The number of parameters included in a fit corresponds more or less at the number of terms included in a Taylor expansion of $F_2$. As nobody knows the exact expression of $F_2$, nobody also knows how many terms we have to include in its Taylor expansion or the exact number of parameter that we need to fit it. The space of parameters is an infinite dimensional space, and the arbitrary choice of a fixed number of parameters corresponds to an arbitrary reduction of this space without assessing the uncertainty with which this reduction is done. The number of neurons, and then of the parameters, in a neural network is chosen only by looking at the stability of the error function without making any theoretical assumption on their number. One observes that once the stability of a neural network is reached, information is maintained even in the case a neuron dies. In this way a neural networks guarantees a more robust and less arbitrary parametrization of a structure function. The only request is to determine the most stable and economic architecture for the problem at hand. Thus, a neural network fit of $F_2$ will avoid both theoretical assumptions on the functional behavior of the structure function and an arbitrary choice of the number of parameters used in the fit.

In this paper we present the results of a comparative analysis of different types of parametrizations: power-like and logarithmic.

It is generally believed that, at small $x$, the singlet SF increases monotonically, indefinitely, accelerating towards larger $Q^2$ (the Pomeron becomes more "perturbative"). We found evidence against this monotonic trend: moreover, we show that, at the highest $Q^2$, the rise of $F_2$ starts slowing down.

## 2. DIS Structure Functions

### 2.1. Small $x$ ($< 0.05$)

The following forms of the small $x$ singlet component $(S,0)$ of the SF are compared for $x < x_c$ and for each experimental $Q_i^2$ bin:

A. Power-like

$$F_2^{S,0}(x,Q_i^2) = a(Q_i^2)\left(\frac{1}{x}\right)^{\lambda(Q_i^2)}, \tag{1}$$

and

$$F_2^{S,0}(x,Q_i^2) = a_0(Q_i^2)\ \left(\frac{1}{x}\right)^{\epsilon_0} + a_1(Q_i^2)\ \left(\frac{1}{x}\right)^{\epsilon_1}, \tag{2}$$

where the exponents $\epsilon_0, \epsilon_1$ are fixed.

B. Logarithmic

$$F_2^{S,0}(x,Q_i^2) = b_0(Q_i^2) + b_1(Q_i^2)\ell n\left(\frac{1}{x}\right), \tag{3}$$

$$F_2^{S,0}(x,Q_i^2) = b_0(Q_i^2) + b_2(Q_i^2)\ell n^2\left(\frac{1}{x}\right) \tag{4}$$

and the combination of the two

$$F_2^{S,0}(x,Q_i^2) = b_0(Q_i^2) + b_1(Q_i^2)\ell n\left(\frac{1}{x}\right) + b_2(Q_i^2)\ell n^2\left(\frac{1}{x}\right). \tag{5}$$

In these equations, $a(Q_i^2)$, $a_{0,1}(Q_i^2)$, $b_{0,1,2}(Q_i^2)$ and $\lambda(Q_i^2)$ are parameters fitted to each $i^{\text{th}}$ $Q^2$ bin. More precisely, the free parameters are $a$ and $\lambda$ for (4), $a_0$ and $a_1$ for (5), $b_0$ and $b_1$ for (6), $b_0$ and $b_2$ for (7), $b_0$, $b_1$ and $b_2$ for (8).

The choice of the cut $x_c$ is obviously crucial, but subjective. Balancing between $x$ small enough, to minimize the large $x$ effects, and $x$ large enough to include as many data points as possible, we tentatively set, like in [6] $x_c = 0.05$ as a compromise solution.

### 2.2. Extension to all $x$ ($< 1.0$)

To ensure that our fits do not depend on the choice of the cut $x_c$, we extend the previous analysis to larger values of $x$ with relevant modifications of the SF. Namely, we multiply the singlet and subsequently the non singlet contributions by appropriate large $x$ factors [7]. The resulting SF becomes

$$F_2(x,Q_i^2) = F_2^{S,0}(x,Q_i^2)(1-x)^{n(Q_i^2)+4} + F_2^{nS,0}(x,Q_i^2)(1-x)^{n(Q_i^2)} \ , \tag{6}$$

where $F_2^{S,0}$ runs over all the cases considered in the previous section, and the exponent $n\left(Q_i^2\right)$ is either that of [7]

$$n\left(Q_i^2\right) = \frac{3}{2}\left(1 + \frac{Q_i^2}{Q_i^2+c}\right) \ , \ \text{with } c = 3.5489\,\text{GeV}^2 \ , \tag{7}$$

or is fitted to the data for each $Q_i^2$ value (see below).

### 2.3. Discussion of the results

We made two kinds of fits, one restricted to small $x$ only, ($x < x_c = 0.05$), the other one including large $x$ as well. In the first case ($x < x_c$) the experimental data are from [8]. Altogether 43 representative $Q^2$ values were selected to cover the interval $[0.2, 1200]$ GeV$^2$ and $x \in [2.10^{-6}, x_c]$. Including more (or all available) data points had little effect on the resulting trend of the results. The relevant values of $\chi^2$, with and without the non- singlet term, are given in Table 1. Notice, that we use the definition

$$\langle \chi^2/\text{dof} \rangle = \frac{\sum_{i=1}^{N_{\text{bin}}} \left( \frac{\chi_i^2}{n_{data_i} - m_{\text{para}}} \right)}{N_{\text{bin}}} \ , \tag{8}$$

where each $Q_i^2$ bin out of a total of $N$ bins contains $n$ data points and gives a resulting contribution to $\chi_i^2$ in fitting eqs. (4)–(8), each containing $m$ parameters.

The $Q^2$ dependence of the parameters was shown in Figs. 1–3. We exposed the most representative results from the small $x$ fit that may clarify asymptotic trends in the behaviour of the singlet SF (see [6] and the following discussion of the results). As already explained, the large $x$ extension was intended merely to support the small $x$ results.

**T a b l e 1: Results of the fits without or with non-singlet term (9) for small $x$ ($< 0.05$). The total number of experimental points is 508**

| Version | Power | Power | Logarithm | Logarithm | Logarithm |
|---|---|---|---|---|---|
| Eq. | (4) | (5) | (6) | (7) | (8) |
| Nb. of parameters | 2 | 2 | 2 | 2 | 3 |
| $\chi^2$ | 282 | 262 | 463 | 303 | 231 |
| $\langle\chi^2/\mathrm{dof}\rangle$ | 0.68 | 0.62 | 1.04 | 0.70 | 0.61 |
| Eqs. | (4),(9) | (5),(9) | (6),(9) | (7),(9) | – |
| Nb. of parameters | 3 | 3 | 3 | 3 | – |
| $\chi^2$ | 247 | 225 | 253 | 234 | – |
| $\chi^2/\mathrm{dof}$ | 0.67 | 0.60 | 0.67 | 0.62 | – |

Notice that in performing the small $x$ fit we profited from a large set of available data, while in the large $x$ extension a representative set of 30 $Q^2$ bins ($Q^2 \in [1.5, 2000]$ GeV$^2$) was used. The data are from [8,9]. The relevant $\chi^2$ values are shown in Table 2. Two options are presented : the first one relies entirely on the extension by [7], in the second one the exponent $n(Q^2)$ (see (10)) is fitted for each $Q^2$ bin.

**T a b l e 2: Results of the fits for all $x$ ($< 1.0$), when the parameters of the large $x$ extension $n$ is chosen as in [7] or fitted. The total number of experimental points is 545**

| Version | Power | Power | Logarithm | Logarithm | Logarithm |
|---|---|---|---|---|---|
| Eqs. | (4),(9)–(11) | (5),(9)–(11) | (6),(9)–(11) | (7),(9)–(11) | (8),(9)–(11) |
| Nb. of parameters | 3 | 3 | 3 | 3 | 4 |
| $\chi^2$ | 368 | 371 | 894 | 399 | 319 |
| $\langle\chi^2/\mathrm{dof}\rangle$ | 0.79 | 0.79 | 1.74 | 0.85 | 0.78 |
| Eqs. | (4),(9),(10) | (5),(9),(10) | (6),(9),(10) | (7),(9),(10) | – |
| Nb. of parameters | 4 | 4 | 4 | 4 | – |
| $\chi^2$ | 321 | 317 | 541 | 329 | – |
| $\chi^2/\mathrm{dof}$ | 0.76 | 0.75 | 1.25 | 0.780 | – |

## 3. Summary

The following comments are in order:

All the parametrizations (4)–(8), except (6), result in roughly equal quality fits. We may rule out the parametrization (6) giving the poorest (as expected) agreement with the data; so we do for the least economic (largest number of the free parameters), parametrization (8) (not shown in the figures).

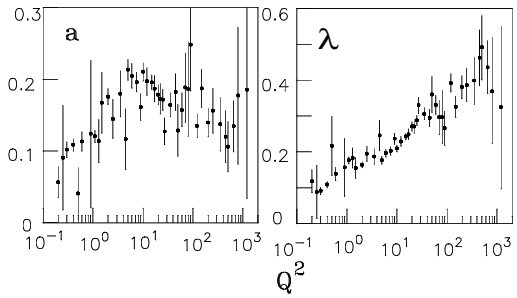


Fig. 1: Results of our analysis for $a\left(Q_i^2\right)$ and $\lambda\left(Q_i^2\right)$ entering in the parametrization (4): $F_2^{S,0} = a(\frac{1}{x})^{\lambda}$ of the small $x$ structure function ($x < x_c = 0.05$); they are fitted to the discrete values of $Q^2$ data from [8]; $Q^2$ is in GeV$^2$, the error bars are produced from the minimization program "Minuit"

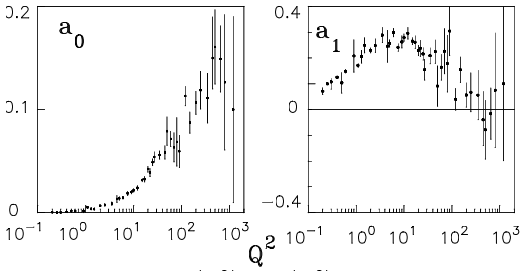


Fig. 2: Same as Fig .1 for $a_0\left(Q_i^2\right)$, $a_1\left(Q_i^2\right)$ and parametrization (5): $F_2 = a_0\left(\frac{1}{x}\right)^{0.418} + a_1(\frac{1}{x})^{0.0808}$

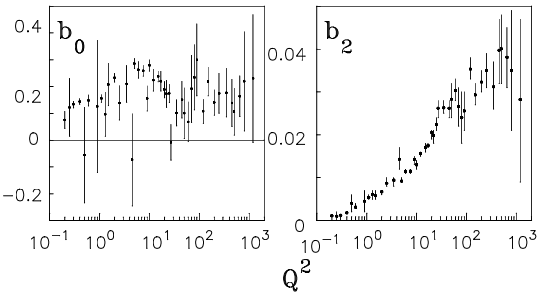


Fig. 3: Same as Fig .1 for $b_0\left(Q_i^2\right)$ and $b_2\left(Q_i^2\right)$ and parametrization (7): $F_2^{S,0} = b_0 + b_2 \ell n^2\left(\frac{1}{x}\right)$

The best results are achieved for the parametrization (8), giving the best value of the total $\chi^2$. Although fit (8) contains an extra free parameter with respect to the rest, the $\chi^2$/dof value is, nevertheless, better than in options (4)–(7). Notice that (8) leads to alternating signs of the coefficients as in the first few terms in an expansion of the supercritical Pomeron in an alternate series of logarithms.

**Acknowledgements**

I thank the Organizing Committee for inviting me and Andrey Deyneko for useful discussions on neural networks.

1. The NNPDF Collaboration (Luigi Del Debbio *et al.* arXiv: hep-ph/0501067; NNPDF Collaboration, R.D. Ball *et al.*, Nucl. Phys. B **838**, 136 (2010).
2. Krešimir Kumerički, Dieter Müller, and Andreas Schäfer, arXiv: 1106.2808 [hep-ph].
3. A.M. Cooper-Sarkar, R.C.E. Devenish, and A. De Roeck, Int. J. Mod. Phys. ABDI **13**, 3385 (1998).
4. A. Donnachie and P.V. Landshoff, Phys. Lett. B **437**, 408 (1998).
5. J. R. Cudell, A. Donnachie, and P.V. Landshoff, e-Print Archives: hep-ph/9901222, 1999.
6. L. Jenkovszky, A. Lengyel, and F. Paccanoni, Nuovo Cimento A **111**, 551 (1998).
7. A. Capella *et al.*, Phys. Lett. B **337**, 358 (1994).
8. M. Derrick *et al.*, ZEUS collaboration, Z. Phys. C **63**, 391 (1994); S. Aid *et al.*, H1 collaboration, Z. Phys. C **69**, 27 (1995); M. Derrick *et al.*, ZEUS collaboration, Z. Phys. C **72**, 399 (1996); J. Ahmed *et al.*, H1 collaboration, Nucl. Phys. B **470**, 3 (1996); M.R. Adams *et al.*, E665 collaboration, Phys. Rev. D **54**, 3006 (1996); C. Adolf *et al.*, H1 collaboration, Nucl. Phys. B **497**, 3 (1997); J. Breitweg *et al.*, ZEUS collaboration, Phys. Lett. B **407**, 432 (1997); J. Breitweg *et al.*, ZEUS collaboration, ZEUS Results on the Measurement Phenomenology of F2 at Low x and Low $Q^2$, DESY-98-121, e-Print Archives: hep-ex/9809005 (1998).
9. A.C. Benvenuti *et al.*, BCDMS collaboration, Phys. Lett. B **223**, 485 (1989); M. Arneodo *et al.*, NMC collaboration, SLAC-PUB 317 (1990); L.W. Whitlow *et al.*, Phys. Lett. B **282**, 475 (1992); M. Arneodo *et al.*, NMC collaboration, Nucl. Phys. B **483**, 3 (1995).
10. Yu. Iljin and A. Lengyel *Alternating series fit to the total cross sections*, ITP-93-25E, Kiev (1993).
11. H. Navelet, R. Peschanski, and S. Wallon, Mod. Phys. Lett. A **9**, 3393 (1994); L. Schoeffel, Univ. Paris XI / Orsay, Dissertation thesis (12-1997), http://www-h1.desy.de/
12. A. De Roeck, E.A. De Wolf, Phys. Lett. B **388**, 188 (1996).

# MASSES OF FUNDAMENTAL PARTICLES

Hidezumi Terazawa

*Center of Asia and Oceania for Science(CAOS),*
*3-11-26 Maesawa, Higashi-kurume,*
*Tokyo 203-0032, Japan*
*and*
*Midlands Academy of Business & Technology(MABT),*
*Mansion House, 41 Guildhall Lane,*
*Leicester LE1 5FR, United Kingdom*

**Abstract**

Not only the masses of fundamental particles including the weak bosons, Higgs scalar, quarks, and leptons, but also the mixing angles of quarks and those of neutrinos are all explained and/or predicted in the unified composite model of quarks and leptons successfully. In addition, both of the two anomalies recently found by the CDF Collaboration are suggested to be taken as evidences for the substructure of the fundamental particles.

## 1. Introduction

In 1953, Nakano and Nishijima, and independently Gell-Mann [1] found "strangeness", the new quantum number for particles, which is the beginning of hadron physics in the third quarter of the twentieth century. Then, Gell-Mann and independently Zweig [2] introduced the quark model for hadrons, and Nambu and the others [3] proposed QCD(quantum chromodynamics), the Yang–Mills gauge theory of color $SU(3)$ for strong interactions of quarks and gluons. Furthermore, Glashow, Salam, and Weinberg [4] proposed QFD (quantum flavor dynamics), the $SU(2) \times U(1)$ gauge theory for electroweak interactions of quarks and leptons. Thus, in the last quarter of the

last century, the Standard Model of all elementary particle forces consisting of QCD and QFD, had already been not only proposed theoretically but also confirmed experimentally. Therefore, although the Higgs scalar is yet to be found experimentally, what is left in quark-lepton physics is to explain or predict not only all the masses of fundamental particles including the weak bosons, Higgs scalar, quarks, and leptons, but also all the mixing angles of quarks [5] and those of neutrinos [6]. A main purpose of this paper is to discuss how to predict all of these fundamental parameters in the Standard Model successfully in the unified composite model of quarks and leptons [7, 8].

## 2. Unified Composite Model

In 1977, we proposed the unified composite model of fundamental particles and forces in which not only quarks and leptons but also gauge bosons and Higgs scalars are composites of subquarks, the most fundamental form of matter [7, 8]. The minimal supersymmetric composite model of quarks and leptons consists of an isodoublet of spinor subquarks with charges $\pm 1/2$, $w_1$ and $w_2$ (called "wakems" standing for weak and electromagnetic), and a Pati–Salam color-quartet of scalar subquarks with charges $+1/2$ and $-1/6$, $C_0$ and $C_i (i = 1, 2, 3)$ (called "chroms" standing for colors). The spinor and scalar subquarks with the same charge $+1/2$, $w_1$ and $C_0$, may form a fundamental multplet of $N = 1$ supersymmetry [9]. Also, all the six subuarks, $w_i$ $(i = 1, 2)$ and $C_\alpha$ $(\alpha = 0, 1, 2, 3)$, may have "subcolors", the additional degrees of freedom, and belong to a fundamental representation of subcolor symmetry [10]. Although the subcolor symmetry is unknown, a simplest and most likely candidate for it is $SU(4)$. Therefore, for simplicity, all the subquarks are assumed to be quartet in subcolor $SU(4)$. Also, although the confining force is unknown, a simplest and most likely candidate for it is the one described by quantum subchromodynamics(QSCD), the Yang–Mills gauge theory of subcolor $SU(4)$ [10]. Note that the subquark charges satisfy not only the Nishijima–Gell-Mann rule of $Q = I_{w3} + (B - L)/2$ but also the "anomaly-free condition" of $\sum_i Q_{w_i} = \sum_\alpha Q_{C_\alpha} = 0$. The

Lagrangian for QSCD is simply given by

$$L_{\rm QSCD} = \sum_i \overline{w}_i[i\gamma^\mu(\partial_\mu - ig\frac{\lambda^a}{2}A^a_\mu) - M_i]w_i +$$

$$+ \sum_\alpha [|(\partial_\mu - ig\frac{\lambda^a}{2}A^a_\mu)C_\alpha|^2 + m^2_\alpha|C_\alpha|^2] -$$

$$-\frac{1}{4}(\partial_\mu A^a_\nu - \partial_\nu A^a_\mu + gf^{abc}A^b_\mu A^c_\nu)^2,$$

where $g$ is the coupling constant of $SU(4)_{sc}$ gauge fields, $A^a_\mu$ $(a = 1,2,3...,15)$, $\lambda^a$ and $f^{abc}$ are the extended Gell-Mann matrices and structure constants of $SU(4)$, respectively, and $M$'s and $m$'s are the wakem and chrom masses.

In the minimal supersymmetric composite model, we expect that there exist at least $36(=6\times 6)$ composite states of a subquark and an antisubquark which are subcolor-singlet. They include 1) $16(=4\times 2\times 2)$ spinor states corresponding to one generation of quarks and leptons, and their antiparticles of

$$\nu = \overline{C}_0 w_1, \quad l = \overline{C}_0 w_2, \quad u_i = \overline{C}_i w_1, \quad d_i = \overline{C}_i w_2$$

or 2) $4(=2\times 2)$ scalar states corresponding to the Higgs scalars of

$$\phi_{ij} = \begin{pmatrix} \overline{w}_1 w_1 & \overline{w}_2 w_1 \\ \overline{w}_1 w_2 & \overline{w}_2 w_2 \end{pmatrix}$$

$(i,j=1,2)$ and 3) $16(=4\times 4)$ vector states corresponding to a) the gluons, "leptogluon", and "barygluon" of

$$G^a = \overline{C}_i \frac{\lambda^a_{ij}}{2} C_j; \quad G^0 = \overline{C}_0 C_0; \quad G^9 = \overline{C}_i C_i$$

$(i,j=1,2,3)$, where $\lambda^a$ $(a=1,2,3,...,8)$ is the Gell-Mann matrix of $SU(3)_c$, and b) the "vector leptoquarks" of

$$X_i = \overline{C}_0 C_i$$

and the hermitian conjugates $(i=1,2,3)$, or $16(=4\times 4)$ scalar states corresponding to the "scalar gluons", "scalar leptogluon", "scalar barygluon", and "scalar leptoquarks" of

$$\Phi_{\alpha\beta} = \overline{C}_\alpha C_\beta$$

$(\alpha, \beta = 0, 1, 2, 3)$. Quarks and leptons with the same quantum numbers but in different generations can be taken as dynamically different composite states of the same constituents. In addition to these "meson-like composite states" of a subquark and an antisubquark, there may also exist "baryon-like composite states" of 4 subquarks which are subcolor-singlet. These exotic quarks, leptons, and gauge bosons are new forms of quark-lepton matter, which is a subject to discuss later in the next Section.

In the unified subquark model of quarks and leptons [8], it is an elementary exercise to derive the Georgi-Glashow relations [11],

$$\sin^2 \theta_w = \sum (I_3)^2 / \sum Q^2 = 3/8$$

and

$$f^2/g^2 = \sum (I_3)^2 / \sum (\lambda^a/2)^2 = 1$$

for the weak-mixing angle ($\theta_w$), the gluon and weak-boson coupling constants ($f$ and $g$), the third component of the isospin ($I_3$), the charge ($Q$), and the color-spin ($\lambda^a/2$) of subquarks, without depending on the assumption of grand unification of strong and electroweak interactions. The experimental value is $\sin^2 \theta_w(M_Z) = 0.23116(13)$ [12]. The disagreement between the value of $3/8$ predicted in the subquark model and the experimental value might be excused by insisting that the predicted value is viable as the running value renormalized *a la* Georgi, Quinn, and Weinberg at extremely high energies (as high as $10^{15}$ GeV), given the "desert hypothesis" [13].

## 3. Quark Mixing Matrices

In the unified composite model of quarks and leptons [14], the CKM quark-mixing matrix $V$ [5] is given by the expectation value of the subquark current between the up and down composite states as

$$V_{us} \sim \langle u|\overline{w}_1 w_2|d\rangle, ...$$

[15-17].

To sum up, we have succeeded in predicting all the magnitudes of the CKM matrix elements except for a single element, say, $V_{us}$.

## 4. Quark and Charged Lepton Masses

For the last quarter century, we have been trying to complete an ambitious program for explaining all the quark and lepton masses by deriving many sum rules and/or relations among them and by solving a complete set of the sum rules and relations [18–26].

Now I am ready to discuss new forms of quark-leptonic matter such as exotic quarks, leptons, and gauge bosons [27, 28].

## 5. Weak Boson and Higgs Scalar Masses

In the unified $SU(2) \times U(1)$ gauge theory of electroweak interactions [4], the masses of weak bosons, $W^{\pm}$ and $Z$, are given as

$$m_W = m_Z \cos\theta_w = (\pi\alpha/\sqrt{2}G_{\rm F})^{1/2}/\sin\theta_w$$

(where $\alpha$ and $G_{\rm F}$ are the fine structure and Fermi coupling constants) so that they can be predicted if the weak mixing angle $\theta_w$ is fixed by any means. In 1969, the weak boson mass was predicted for the first time to be of the order of 100 GeV by myself, provided that the self-masses of leptons be finite [29]. In the grand unified $SU(5)$ gauge theory of strong and electroweak interactions of Georgi and Glashow [11] or in the unified composite model of quarks and leptons [14], the weak angle is fixed as $\sin^2\theta = 3/8$ so that the weak boson masses, $m_W$ and $m_Z$, may be predicted.

In 1980, the mass of the physical Higgs scalar in QFD, $m_H$, was first predicted by myself in the composite model of Higgs scalars [30]. To be more precise, it has been predicted in three ways [31].

## 6. Future Prospects

What can we expect to find in future high-energy experiments and astroparticle observations, especially at the Large Hadron Collider? Firstly, most of us, high-energy physicists, may expect that the Higgs scalar, the only fundamental particle that has not yet been found in the Standard Model, will be found. The predictions for the Higgs scalar mass in the composite models are presented in details in the last Section.

Secondly, many of us may expect that superparticles [9], the superpartners of fundamental particles, will be found if the energy scale of SUSY breaking is of the order of 1 TeV. In the unified supersymmetric composite model, there may exist superpartners of any fundamental particles containing $w_1$ or $C_0$, which can be made by replacing either $w_1$ by $C_0$ or $C_0$ by $w_1$. However, there is no reason for expecting that any superparticles be as light as hundreds GeV. All of them must be as heavy as the compositeness energy scale, say 1 TeV.

Thirdly, some of us (in particular, string theorists) may expect that Kaluza–Klein extra dimensions of the space-time [32] would be found if the size of extra dimensions is as small as of the order of 1 TeV$^{-1}$, which has recently been emphasized by Arkani–Hamed *et al.* [33]. However, it seems to me that there is no compelling reason for expecting that the size of extra dimensions is so large as the LHC energy is enough high to see an evidence for the extra-dimensions, if any.

Fourthly, some of us (in particular, composite modelists) may expect that the substrucure of fundamental particles would be found if the energy scale of compositeness is of the order of 1 TeV. It would be the most exciting to find an evidence for the substructure in search for anomalous events due to excited quarks, leptons, gauge bosons, and Higgs scalars [34], or due to exotic particles such as the barygluon, leptoquark, and color-ball discussed in the Section 4. In fact, everytime when new colliders reached new energy scales in the last decade in the last century, some anomalies had been reported for possible evidence for the substructure at LEP [35], Tevatron [36], and HERA [37], although those anomalies have either disappeared or not been confirmed by later experiments. Very lately, however, the CDF Collaboration has reported two new anomalies: 1) in a $t\bar{t}$ production asymmetry [38] and 2) in the spectrum of the invariant mass of the pair of hadronic jets associated with a $W$ boson [39]. The former may be taken as an evidence for the existence of an excited Higgs scalar ($H^*$) or neutral weak boson ($Z^*$) while the latter as another for that of excited weak bosons ($W^*$ or $Z^*$). About a quarter century has past since $W$ and $Z$ were discovered for evidence for the Standard Model. I hope that LHC [40] will soon provide us enough high energy and luminosity not only to produce $H$ for establishing the Standard Model but also to lead us to subquark physics in the

first quarter of the 21st century [41]. The time has come when we are about to be able to give an answer to both of the following questions which Einstein seemed to ask by himself: "What is the Universe?" and "What is the electron?" [42].

## 7. Appendix-Neutrino Masses and Mixing Matrices [43]

In 1997, the Super-Kamiokande Collaboration [44] found an evidence for the non-vanishing mass for the muon and/or tau neutrinos in the analysis based on neutrino oscillation due to the neutrino mixing among three generations of neutrinos [6] $(\nu_e, \nu_\mu, \nu_\tau)$, breaking lepton-number conservation which Nishijima, Schwinger, and Bludman had introduced four decades earlier in 1957 [45]. See the details in Ref. [43].

### Acknowledgements

The author would like to thank Professor Laszlo L. Jenkovszky and all the other organizers of International Summer School and Conference, "New Trends in High-Energy Physics", Alushta, Crimea, Ukraine, September 3-10, 2011, for their invitation of him to the School and Conference and for their acceptance of this contributed paper for publication in this Proceedings although he could not attend the School and Conference unfortunately. He also wishes to thank the late Professor Kazuhiko Nishijima, to whom this lecture has been dedicated, for so many helpful advices and helps which he had received since 1967 during his graduate study in University of Tokyo. In addition, he thanks Professor Keiichi Akama for very useful helps in correcting errors in the original manuscript.

1. T.Nakano and K.Nishijima, Prog. Theor. Phys. **10**, 581 (1953); M.Gell-Mann (1953), for a review, see J. Phys. **43**, 395 (1982).
2. M.Gell-Mann, Phys. Lett. **8**, 214 (1964); G.Zweig (1964), for a review, see Int. J. Mod. Phys. **A25**, 3863 (2010).
3. Y.Nambu, in *Preludes in Theoretical Physics*, edited by A.de Shalit (North-Holland, Amsterdam, 1966); H.Frizsch and M.Gell-Mann, in *Proc. XVI International Conf. on High Energy Physics*, edited by A.Roberts (NAL, Batavia, 1973), Vol.2, p.135.

4. S.L.Glashow, Nucl. Phys. **22**, 579 (1961); A.Salam, in *Elementary Particle Physics*, edited by N.Svartholm (Almqvist and Wiksell, Stockholm, 1968), p.367; S.Weinberg, Phys. Rev. Lett. **19**, 1264 (1967).

5. N.Cabibbo, Phys. Rev. Lett. **10**, 531 (1963); S.L.Glashow, I.Iliopoulos, and L.Maiani, Phys. Rev. D **2**, 1285 (1968); M.Kobayashi and T.Maskawa, Prog. Theor. Phys. **49**, 652 (1973); H.Terazawa, Prog. Theor. Phys. **63**, 1779 (1980).

6. B.Pontecorvo, Zh. Eksp. Teor. Fiz. **33**, 549 (1957) [Soviet Phys. JETP **6**, 429 (1958)]; **34**, 247 (1958) [**7**, 172 (1958)]; **53**, 1717 (1967) [**26**, 984 (1968)]; Z.Maki, M.Nakagawa, and S.Sakata, Prog. Theor. Phys. **28**, 870 (1962); H.Terazawa, Prog. Theor. Phys. **57**, 1808 (1977); H.Terazawa, Prog. Theor. Phys. **63**, 1779 (1980).

7. J.C.Pati and A.Salam, Phys. Rev. D **10**, 275 (1974); H.Terazawa, Y.Chikashige, and K.Akama, Phys. Rev. D **15**, 480 (1977); H.Terazawa, Phys. Rev. D **22**, 184 (1980).

8. For a classical review, see H.Terazawa, in *Proc. XXII International Conf. on High Energy Physics*, Leipzig, 1984, edited by A.Meyer and E.Wieczorek (Akademie der Wissenschaften der DDR, Zeuthen, 1984), Vol.I, p.63. For more recent reviews, see, for example, H.Terazawa, in *Proc. International Conf. "New Trends in High-Energy Physics"*, Alushta, Crimea, 2003, edited by P.N.Bogolyubov, L.L.Jenkovszky, and V.K.Magas (Bogolyubov Institute for Theoretical Physics, Kiev, 2003), Ukrainian J. Phys. **48**, 1292 (2003); in *Proc. XXI-st International Conf. "New Trends in High-Energy Physics"*, Yalta, 2007, edited by P.N. Bogolyubov, L.L.Jenkovszky, and M.K.Magas (Bogolyubov Institute of Theoretical Physics, Kiev, 2007), p.272.

9. H.Miyazawa, Prog. Theor. Phys. **36**, 1266 (1966); Yu.A.Gol'fand and L.P.Likhtman, ZhETF Pis. Red. **13**, 452 (1971) [JETP Lett. **13**, 323 (1971)]; D.V.Volkov and V.P.Aklov, ibid. **16**, 621 (1972) [*ibid.* **16**, 438 (1972); Phys. Lett. **46B**, 109 (1973); J.Wess and B.Zumino, Nucl. Phys. **B70**, 39 (1974).

10. G.'t Hooft, in *Recent Developments in Gauge Theories*, edited by G.'t Hooft (Plenum, New York, 1980), H.Terazawa, Prog. Theor. Phys. **64**, 1763 (1980).

11. H.Georgi and S.L.Glashow, Phys. Rev. Lett. **32**, 438 (1974).

12. K.Nakamura *et al.* (Paticle Data Group), J. Phys. G **37**, 075021 (2010).

13. H.Georgi, H.R.Quinn, and S.Weinberg, Phys. Rev. Lett. **33**, 451 (1974).

14. H.Terazawa, T.Chikashige, and K.Akama, Phys. Rev. D **15**, 480 (1977).

15. H.Terazawa, Prog. Theor. Phys. **58**, 1276 (1977); V.Visnjic-Triantafillou, Fermilab Report No. FERMILAB-Pub-80/34-THY, 1980 (unpublished); H.Terazawa, Prog. Theor. Phys. **64**, 1763 (1980); O.W.Greenberg and J.Sucher, Phys. Lett. **99B**, 339 (1981); H.Terazawa, Mod. Phys. Lett.**A7**, 3373 (1992).

16. H.Terazawa, Phys. Rev. D **22**, 184 (1980).

17. H.Terazawa, Mod. Phys. Lett. **A7**, 3373 (1992); **A11**, 2463 (1996). Recently, a deviation of $\Delta = 0.0083(28)$, which is 3.0 times the stated error, was found from the unitarity condition for the first row of the CKM matrix. This may be taken as an evidence for the substructure of quarks. See H.Abele *et al.*, Phys. Rev. Lett. **88**, 211801 (2002).

18. H.Terazawa, Mod. Phys. Lett. **A7**, 1879 (1992).

19. H.Terazawa, Prog. Theor. Phys. **64**, 1763 (1980).

20. W.Buchmuller, R.D.Peccei, and T.Yanagida, Phys. Lett. **B124**, 67 (1983); R.Barbieri, A.Masiero, and G.Veneziano, *ibid.* **B124**, 179 (1983); O.Greenberg, R.N.Mohapatra, and M.Yasue, *ibid.* **B128**, 65 (1983).

21. H.Terazawa, J. Phys. Soc. Jpn. **55**, 4249 (1986); H.Terazawa and M.Yasue, Phys. Lett. **B206**, 669 (1988); H.Terazawa, in *Perspectives on Particle Physics*, edited by S.Matsuda *et al.* (World Scientific, Singapore, 1988), p.193.

22. H.Terazawa and M.Yasue, Phys. Lett. **B307**, 383 (1993); H.Terazawa, Mod. Phys. Lett. **A10**, 199 (1995).

23. For a review, see, for example, J.Gasser and H.Leutwyler, Phys. Rep. **87**, 77 (1982).

24. Y.Nambu and G.Jona-Lasinio, Phys. Rev. **122**, 345 (1961).

25. Y.Nambu, Nucl. Phys. **A629**, 3c (1998); **A638**, 35c (1998).

26. A.Davidson, T.Schwartz, and K.C.Wali, J. Phys. G **24**, L55 (1998).

27. H.Terazawa, Mod. Phys. Lett. **A13**, 2427 (1998).

28. H.Terazawa, Prog. Theor. Phys. **79**, 738 (1988).

29. H.Terazawa, Phys. Rev. Lett. **22**, 254 (1969); *ibid.* **22**, 442 (E) (1969); Phys. Rev. D **1**, 2950 (1970); J.Pestieau and P.Roy, Phys. Rev. Lett. **23**, 349 (1969); S.Weinberg, Phys. Rev. Lett. **29**, 388 (1972); Phys. Rev. D **7**, 2887 (1973).

30. H.Terazawa, Phys. Rev. D **22**, 2921 (1980); **41**, 3541 (E) (1990).

31. H.Terazawa, Mod. Phys. Lett. **A5**, 1031 (1990).

32. T.Kaluza, Sitzker. Preuss. Akad. Wiss. **K1**, 966 (1921); O.Klein, Z. Phys. **37**, 896 (1926).

33. N.Arkani-Hamed, S.Dimopoulos, and G.Dvali, Phys. Lett. **B429**, 263 (1998); Phys. Rev. D **59**, 086004 (1999); I.Antoniadis *et al.*, Phys. Lett. **B436**, 257 (1998); L.Randall and R.Sundrum, Phys. Rev. Lett. **83**, 3370 (1999); **83**, 4690 (1999). Note that superstring theories at the Fermi mass scale $G_{\rm F}^{-1/2}(\sim$ 300 GeV) instead of the Planck mass scale $G^{-1/2}(\sim 10^{19}$ GeV) was first suggested by myself by a decade earlier. See H.Terazawa, Prog. Theor. Phys. **79**, 734 (1988).

34. H.Terazawa, M.Yasue, K.Akama, and M.Hayashi, Phys. Lett. **112B**, 387 (1982).

35. K.Akama and H.Terazawa, Phys.Lett. **B321**, 145 (1994), and references therein.

36. K.Akama and H.Terazawa, Phys. Rev. D **55**, R2521 (1997). Recently, the rare events of 2 electrons + 2 photons + missing transverse energy whose rate was 2.7 sigma above the Standard Model predictions had been reported by the CDF Collaboration. This may be taken as an evidence for the existence of excited leptons or weak bosons. See A.Loginov (for the CDF Collaboration), Report-No. FERMILAB-CONF-05-598-E, hep-ex/0604036, 2006.

37. K.Akama, K.Katsuura, and H.Terazawa, Phys. Rev. D **56**, R2490 (1997), and references therein. Recently, the analysis of events with isolated leptons and missing transverse momentum in $e^+p$ collisions by the H1 Collaboration had observed an excess over the Standard Model expectation 3.4 sigma significance. This may be taken as an evidence for the existence of excited leptons or weak bosons. See G.Brandt (for the H1 Collaboration), hep-ex/0701050, 2007.

38. T.Aaltonen et al. (CDF Collaboration), Phys. Rev. D **83**, 112003 (2011). Very lately, the CDF Collaboration measured a $t\bar{t}$ production asymmetry of $48 \pm 11\%$ for an invariant mass of the $t\bar{t}$ pair larger than 450 GeV/c$^2$, which is three standard deviations above the Standard Model expectation, $9 \pm 1\%$. This may be taken as an evidence for the existence of an excited Higgs scalar ($H^*$) or weak boson ($Z^*$).

39. T.Aaltonen *et al.* (CDF Collaboration), Phys. Rev. Lett. **106**, 171801 (2011). Very lately, the CDF Collaboration found an unexpected peak in the spectrum of the invariant mass of the pair of hadronic jets associated with a $W$ boson. The excess of approximately 250 events appeared as a bump around 144 GeV/c$^2$. This may be taken as an evidence for the existence of excited weak bosons ($W^*$ or $Z^*$). For other interpretations, see, for example, B.A.Dobrescu and G.Z.Krnjaic, arXiv:1104.2893, April 2011; P.Ko, Y.Oura, and Chachyun Yu, arXiv:1104.4066, April 2011; T.Plehn and M.Takeuchi, arXiv:1104.4087, April 2011; P.J.Fox, J.Liu, D.Tucker-Smith, and N.Weiner, arXiv:1104.4127, April 2011.

40. For the latest searches for the substructure of quarks at LHC, see the CMS Collaboration, Phys. Rev.L ett. **106**, 122003 (2011); arXiv:1102.2020, February 2011; the ATLAS Collaboration, arXiv:1104.4398, April 2011.

41. H.Terazawa, in *Proc. XXI International Conf. on High Energy Physics*, Paris, 1982, edited by P.Petiau and M.Porneuf, J.de Phys. **C3**-191 (1982).

42. H.Terazawa, in *"What is the electron?"*, edited by V.Simulik (Apeiron, Montreal, 2005), p.29.

43. For a review, see H.Terazawa, in *Proc.International Conf. on Modern Developments in Elementary Particle Physics*, Cairo, Helwan and Assyut, 1999, edited by A.Sabry (Ain Shams University, Cairo, 1999), p.128.

44. Y.Fukuda *et al.* (Super-Kamiokande Collaboration), Phys. Rev. Lett.**81**, 1562 (1998).

45. K.Nishijima, Phys. Rev. **108**, 907 (1957); J.Schwinger, Ann. Phys. **2**, 407 (1957); S.Bludman, Nuovo Cimento **9**, 433 (1958).

# HIGGS SEARCHES AT CMS[1]

Antonio Branca[2] for the CMS Collaboration

[2] *University and INFN of Padova*

**Abstract**

The results of the Standard Model (SM) Higgs boson searches performed by the CMS Collaboration are presented for eight different decay channels. The overall combination leads to a 95% exclusion in three mass ranges: 145-216, 226-288 and 310-400 GeV. The expected exclusion in the absence of a signal is 130-440 GeV. The results of the Minimal Super Symmetric Standard Model (MSSM) Higgs boson searches are also presented for the neutral states decaying in the $\tau\tau$ channel. A large area of the parameters space of the model is excluded. Depending on the analysis, the amount of data used corresponds to 1.1-1.7 fb$^{-1}$ of integrated luminosity.

## 1. SM Higgs Boson Searches

The main contribution to the SM Higgs boson production at LHC come from gluon fusion, followed by the vector boson fusion (VBF), the production in association with a vector boson and the production in association with a $t\bar{t}$ pair. The overall production cross section goes from about 20 pb for a Higgs boson of mass $m_H = 120$ GeV to $10^{-2}$ pb for a Higgs boson of mass $m_H = 1$ TeV.

At high masses, $m_H > 135$ GeV, the branching ratio is dominated by the decay into a pair of vector bosons, while at low masses, $m_H < 135$ GeV, the $b\bar{b}$ channel overcome the $\gamma\gamma$ and $\tau\tau$ channels. At CMS [1] in the low mass range the $\gamma\gamma$ channel gives the best sensitivity, followed by $b\bar{b}$ and $\tau\tau$, whereas in the high mass interval the sensitivity depends on the final state channel of the bosons pair.

[1] Received after the dead-line.

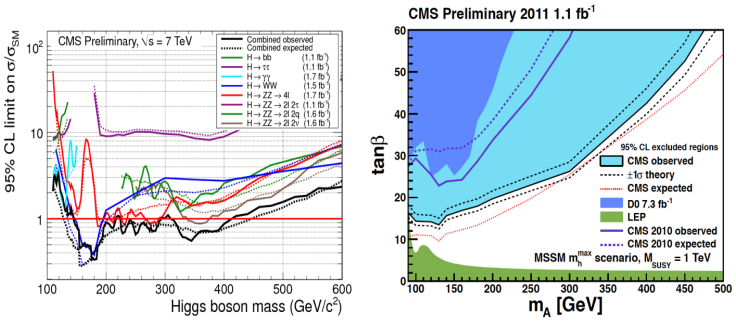


(a) (b)

Fig. 1: (a) The expected and observed 95% of CL upper limits on the $\sigma/\sigma_{SM}$ as a function of the SM Higgs mass for the eight analysis and their combination. (b) Region in the MSSM parameter space of $tan\beta$ versus $M_A$ excluded at 95% of CL , with the effect of $\pm 1\sigma$ theoretical uncertainties shown. The other shaded region show the 95% CL excluded region from LEP and Tevatron experiments

### 1.1. $H \to \gamma\gamma$ channel

The $\gamma\gamma$ channel [2] ensure good sensitivity at low masses ($110 < m_H < 150$ GeV). The invariant mass can be fully reconstructed with a good resolution (from 2.4% up to 6.5%).

The dominant source of background comes from events with two real prompt photons or one prompt and a fake from a jet. Photon isolation and ECAL cluster shape requirements efficiently suppress these backgrounds. The background modeling is obtained from a polynomial fit to the data. For the signal the shape is taken from Monte Carlo (MC) by smearing of the photon energy to account for differences between data and simulation.

To gain sensitivity the events are divided in eight different classes, according to mass resolution and signal to background probability. The analysis performed for each class are combined obtaining the limit shown in fig. 1. The expected limit at 95% of CL is about three up to four times the SM expectation in the considered mass range, whereas the observed limit is within $2\sigma$ from the expected one.

### 1.2. $H \to \tau\tau$ channel

The $\tau\tau$ channel [3] has good sensitivity in the mass range $110 < m_H < 140$ GeV. Four different final states are considered depending on the $\tau$ decay channel. The best discrimination power is given by the visible mass distribution, reconstructed with a resolution of about 20%, which is used to obtain the limit reported in fig. 1.

The dominant irreducible background is $Z \to \tau\tau$ production followed by electroweak ($W(l\nu) + jets$, $Z(ll) + jets$), $t\bar{t}$, and QCD, in which one or both leptons are fake. Cut on the missing transverse energy ($E_T^{miss}$) and the event topology are performed to reject $t\bar{t}$ and $W(l\nu) + jets$ backgrounds. Data driven techniques and MC are used for the background estimation.

Events with a pair of forward-backward jets are analyzed separately from the rest of selected events to gain sensitivity from the VBF production. The limit is obtained by fitting the visible mass distributions for the two categories and combining the results. The expected and observed limits at 95% CL, shown in fig. 1, are about nine up to ten times the SM expectation.

### 1.3. $H \to b\bar{b}$ channel

To suppress the QCD background in this analysis [4], that gives sensitivity for $110 < m_H < 135$ GeV, events where the Higgs boson is produced in association with a vector boson ($V$) decaying leptonically are selected. Other backgrounds are $t\bar{t}$, $V + light\ quarks$, and the irreducible $ZZ(b\bar{b})$, $W(l\nu)Z(b\bar{b})$, $V + b\bar{b}$. Different discriminating variables have been identified, taking into account the presence of jets originated from $b$ quarks, the provenance of the $b\bar{b}$ pair from a resonance, the back to back production of the Higgs boson and $V$ with significant transverse momentum.

The discriminating variables are used as input for the Boosted Decision Tree ($BDT$) algorithm implemented in the $TMVA$ framework [5]. A $BDT$ analysis is performed for each selected final state, where the backgrounds estimation is obtained from control regions identified in data. The results are combined to produce the limits in fig. 1 on Higgs production cross section. At $m_H = 115$ GeV the observed upper limit is 8.3 times the SM expectation, where the expected one was 5.7.

### 1.4. $H \to W^+W^- \to 2l2\nu$ channel

This channel [6] is characterized by two oppositely charged isolated leptons and large missing transverse energy arising from neutrinos in $W$ decays. The best sensitivity is achieved at intermediate mass range ($130 < m_H < 200$ GeV).

The analysis is based on the cut-and-count approach. The main sources of background are the irreducible $W^+W^-$ and the reducible $W + jets$, QCD, $Z/\gamma^* \to l^+l^-$, $t\bar{t}$, $tW$ and the diboson $W\gamma$, $WZ$, $ZZ$. Cuts made on the transverse invariant mass of the two leptons and $E_T^{miss}$ suppress the irreducible background. Other requirements are placed on the transverse momenta of the harder and softer leptons, the dilepton mass, and the azimuthal angle between the two leptons. The reducible backgrounds is suppressed requiring well reconstructed isolated leptons and rejecting events with at least one of these characteristics: low $E_T^{miss}$, invariant mass of two same-flavor leptons around the $Z$ mass, b-tagged jets, more than two leptons, $\gamma$ conversion.

The selected events are divided in three categories: one sensitive to the $VBF$ production mechanism and the other two where cuts on discriminating variables are effective to reduce the backgrounds.

The remaining backgrounds are estimated from data, apart for the reducible electroweak di-bosons, for which MC simulated events are used. The observed limit reported in fig. 1 permit to exclude an Higgs boson with mass $147 < m_H < 194$ GeV at 95% of CL, while the expected exclusion was $136 < m_H < 200$ GeV.

### 1.5. $H \to ZZ^{(*)}$ channel

For the $ZZ$ decay, four different final states are analyzed: the $4l$ [7], the $2l2\nu$ [8], the $2l2q$ [9] and the $2l2\tau$ [10]. For the $4l$ final state the sensitivity is in the whole mass range $110 < m_H < 600$ GeV, whereas for the remaining channels a good sensitivity is obtained at high masses.

In the $4l$ final state the main backgrounds are the irreducible electroweak $ZZ^{(*)}$ production, the reducible $t\bar{t}$, $Zb\bar{b}$, and the instrumental $Z + jets$, $WZ + jets$, QCD. Events with two pairs of

opposite charge same flavor leptons, compatible with $Z$ mass, are selected. These selections together with isolation and impact parameter requirements suppress effectively the reducible and instrumental backgrounds, which become negligible or small. The remaining background is the irreducible di-boson production. In the $2l2\nu$ final state the main background contributions come from the resonant $Z+jets$, the non resonant $t\bar{t}$, $tW$, $WW$, $W+jets$, and the irreducible $ZZ$ and $WZ$. Requiring events with large $E_T^{miss}$ suppress almost all these contributions. This is particularly crucial for the $Z+jets$, which is five order of magnitude larger than the signal (before any cuts applied) but contains little real $E_T^{miss}$. To suppress background where $E_T^{miss}$ is due to jet mismeasurements, events where the $E_T^{miss}$ is aligned with a jet are rejected. In the $2l2q$ final state the main background contributions come from resonant $Z+jets$, non resonant $t\bar{t}$, $tW$ and electroweak $ZZ$, $WZ$ and $WW$. Background suppression is primarily based on the di-lepton and di-jet invariant masses, $m_{ll}$ and $m_{jj}$. Requiring $m_{jj}$ and $m_{ll}$ compatible with $Z$ mass reduce the $Z+jets$ and backgrounds without a real $Z$. The topology of the signal and the flavor of the jets are exploited in two likelihood discriminants used to separate signal from background. In the $2l2\tau$ final state there are small background contributions, coming from the irreducible $ZZ$ and reducible $WZ$ in association with jets and $t\bar{t}$.

A shape analysis is performed for the $4l$, $2l2q$ and $2l2\tau$ final states: the signal is parametrized by a convolution between a Breit-Wigner and a Crystall-Ball or is taken from MC. The backgrounds shape are obtained from MC, fitting the distribution or taking the shape of the simulated events, while the normalization are taken from data driven techniques. For the $2l2\nu$ a cut and count approach is used: a data driven estimation of the backgrounds is performed, apart for the irreducible one that is taken from MC. The observed and expected limits at 95% of CL are shown in fig. 1: they are between one up to two times the $SM$ expectation in the range $150 < m_H < 420$ GeV for the $4l$ final state. The Higgs mass range $340 < m_H < 375$ GeV is excluded with the $2l2\nu$ analysis. For the $2l2q$ final state the limits are approaching those of the SM expectation. Finally, for the $2l2\tau$ analysis the expected and observed limits are about ten up to twelve times the SM expectation for $200 < m_H < 400$ GeV.

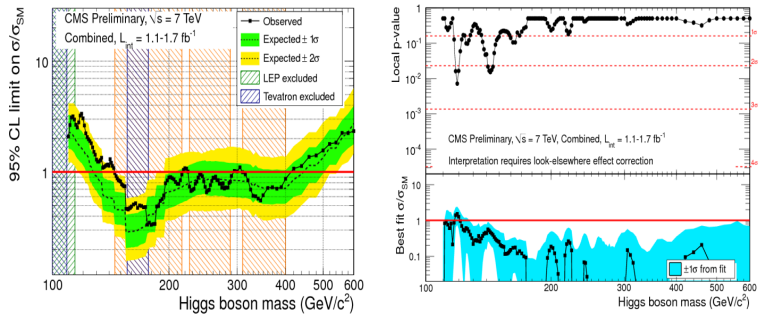


(a) (b)

Fig. 2: (a) The combined 95% CL upper limits on the $\sigma/\sigma_{SM}$, as a function of the SM Higgs mass. (b) Local p-values (top) and observed best fit to $\sigma/\sigma_{SM}$ (bottom) as a function of the SM Higgs mass.

### 1.6. SM Higgs combination results

The observed and expected limits at 95% of CL that result combining all eight analysis [11] are presented in fig. 2. The observed limit leads to an exclusion of the SM Higgs boson at 95% of CL in three mass intervals: 145-216, 226-288, and 310-400 GeV, where the expected limit in absence of signal was 130-440 GeV. This reduces the allowed mass range for the SM Higgs boson remained unrestricted by the direct searches performed by the past LEP [12] and Tevatron [13] experiments, as well as in comparison to the limits reported by the CMS and ATLAS Collaborations at the EPS conference [14, 15].

The two gaps between the three excluded mass ranges observed in data are consistent with statistical fluctuations. The limits are about $2\sigma$ larger than the expectation for low mass values ($m_H < 150$ GeV), which makes the observed limits in this range less restrictive than expected.

In fig. 2 is shown also the local *p-value*, the probability of the background to fluctuate and give an excess as large or larger than the observed one. One can see that the *p-value* curve dips downward over a broad range of low mass, driven by the $WW$, $ZZ$, and $\gamma\gamma$ analysis. The deeper value would correspond to a $2.3\sigma$ excess. Taking into account the probability of observing the excess anywhere in the full

search range, the so called *look elsewhere effect*, the probability to observe such an excess is about 40%. The excesses at low masses are not significant with the amount of data available for the discussed analysis.

## 2. MSSM Higgs Boson Searches

The minimal supersymmetric extension to the standard model (MSSM) requires the presence of two Higgs doublets. This leads to a more complicated scalar sector, with five massive Higgs bosons: three neutral (h, H, A) and two charged ($H^{\pm}$) states. The model is described by two parameters at tree level: $tan\beta$ and the mass of one scalar $M_A$. There are two main production channels at LHC for the scalar states: the gluon fusion and the production in association with a $b\bar{b}$ pair.

### 2.1. $\phi \to \tau\tau$ channel

The analysis main stream for this channel [3] is the same as for the SM $H \to \tau\tau$, discussed in section 1.2: same final states selected, same background rejection and estimation. To increase the sensitivity the production in association with a $b\bar{b}$ pair is exploited for the analysis. The events are divided in two categories, defined by the presence or not of at least one b tagged jet. The limits in fig. 1 are obtained from a fit to the visible invariant mass distribution and set in the parameter space of the model ($\tan\beta$, $M_A$). A large region of the MSSM parameters is excluded at 95% of CL, reaching $\tan\beta = 14.2$ at $M_A = 120$ GeV. This is a good improvement with respect to the 2010 data.

## 3. Conclusions

The results obtained by the CMS Collaboration in the search for the SM Higgs boson have been shown in eight distinct Higgs decay final states. Higgs boson mass range covered by these analysis spans from 110-600 GeV. The overall combinations of the eight analysis leads to an exclusion at 95% of CL in three mass ranges: 145-216, 226-288, and 310-400 GeV. The expected exclusion in absence of a signal is 130-440 GeV. The largest excursion of the observed limit from the

expected one has a probability of 40% after taking into account the *look elsewhere effect*. The results for the search of a neutral MSSM Higgs boson decaying in a $\tau\tau$ pair have also been shown. A large area of the parameter space of the MSSM model has been excluded. The amount of data used for these searches corresponds to 1.1-1.7 $\text{fb}^{-1}$ of integrated luminosity.


1. CMS Collaboration, *The CMS experiment at the CERN LHC*, JINST 3:S08004 (2008).
2. CMS Collaboration, *Search for a Higgs boson decaying into two photons in the CMS detector*, CMS PAS **HIG-11-021** (2011).
3. CMS Collaboration, *Search for Neutral Higgs Bosons Decaying to Tau Pairs in pp Collisions at* $\sqrt{s} = 7$ TeV, CMS PAS **HIG-11-009** (2011).
4. CMS Collaboration, *Search for the Standard Model Higgs Boson decaying to Bottom Quarks and Produced in Association with a W or a Z Boson*, CMS PAS **HIG-11-012** (2011).
5. A. Hoecker *et al.*, *TMVA – toolkit for multivariate data analysis*, arXiv:0703039.
6. CMS Collaboration, *Search for the Higgs Boson Decaying to* $W^+W^-$ *in the Fully Leptonic Final State*, CMS PAS **HIG-11-014** (2011).
7. CMS Collaboration, *Search for a Standard Model Higgs boson in the decay channel* $H \to ZZ^{(*)} \to 4l$, CMS PAS **HIG-11-015** (2011).
8. CMS Collaboration, *Search for the Higgs boson in the* $H \to ZZ \to 2l2\nu$ *channel in pp collisions at* $\sqrt{s} = 7$ TeV, CMS PAS **HIG-11-016** (2011).
9. CMS Collaboration, *Search for the standard model Higgs Boson in the decay channel* $H \to ZZ \to l^+l^-q\bar{q}$ *at CMS*, CMS PAS **HIG-11-017** (2011).
10. CMS Collaboration, *Search for a Standard Model Higgs boson produced in the decay channel* $H \to ZZ \to 2l2\tau$ *with CMS detector at* $\sqrt{s} = 7$ TeV, CMS PAS **HIG-11-013** (2011).
11. CMS Collaboration, *Search for the standard model Higgs boson in pp collisions at* $\sqrt{s} = 7$ TeV *and integrated luminosity up to* $1.7fb^{-1}$, CMS PAS **HIG-11-022** (2011).
12. R. Barate and others (LEP Working Group for Higgs boson searches and ALEPH, DELPHI, L3, and OPAL Collaborations), *Search for the standard model Higgs boson at LEP*, Phys. Lett. B **565**, 61 (2003).
13. CDF and D0 Collaborations, Combined CDF and D0 upper limits on Standard Model Higgs Boson production, CDF Note 10606 and D0 Note 6226 (July, 2011).
14. CMS Collaboration, *Search for standard model Higgs boson in pp collisions at* $\sqrt{s} = 7$ TeV, CMS PAS **HIG-11-011** (July, 2011).
15. ATLAS Collaboration, *Combined Standard Model Higgs Boson Searches in pp Collisions at* $\sqrt{s} = 7$ TeV *with the ATLAS Experiment at the LHC*, ATLAS-CONF-2011-2012 (July, 2011).

# AUTHOR'S INDEX